Distribution Agreement

Signature:

__________________________________ ________________

Orion Paul Keifer, Jr. Date

The Development and Application of *Ex Vivo* Magnetic Resonance Imaging Techniques to Understand the Neural Basis of Pavlovian Fear Conditioning and Extinction.

By

Orion Paul Keifer, Jr.
Doctor of Philosophy

Graduate Division of Biological and Biomedical Science
Neuroscience

Kerry Ressler, M.D., Ph.D.
Advisor

Nicholas Boulis, M.D.
Committee Member

Shannon Gourley, Ph.D.
Committee Member

Kim Huhman, Ph.D.
Committee Member

Shella Keilholz, Ph.D.
Committee Member

Todd Preuss, Ph.D.
Committee Member

James Zheng, Ph.D.
Committee Member

Accepted:

Lisa Tedesco, Ph.D.
Dean of the James T. Laney School of Graduate Studies.

Date

The Development and Application of *Ex Vivo* Magnetic Resonance Imaging Techniques to Understand the Neural Basis of Pavlovian Fear Conditioning and Extinction.

By

Orion Paul Keifer, Jr.
B.S., Applied Psychology *with Highest Honors*, Georgia Institute of Technology
B.S., Applied Biology *with Highest Honors*, Georgia Institute of Technology
B.S., Biomedical Engineering *with Highest Honors*, Georgia Institute of Technology
M.S., Psychology – Brain and Cognitive Sciences, Georgia Institute of Technology

Advisor: Kerry J Ressler, M.D., Ph.D.

An abstract of a dissertation submitted to the Faculty of the James T. Laney School of
Graduate Studies of Emory University in partial fulfillment of the requirements for the
degree of Doctor of Philosophy in Neuroscience
2014

Abstract

The Development and Application of *Ex Vivo* Magnetic Resonance Imaging Techniques to Understand the Neural Basis of Pavlovian Fear Conditioning and Extinction.

By Orion Paul Keifer, Jr.

Pavlovian fear conditioning is the pairing of a neutral stimulus (conditioned stimulus) with an aversive stimulus (unconditioned stimulus) until the presentation of the neutral stimulus results in fear behaviors (conditioned response). Conversely, extinction is the process of presenting the conditioned stimulus until it no longer elicits fear behaviors. The power of these paradigms is the simplicity of execution and the translational validity with human physiology (emotional memory) and pathophysiology (fear and anxiety disorders). In fact, decades of cat, rat, and monkey fear conditioning studies have led to an anatomically constrained hypothetical fear circuit. Concomitantly, magnetic resonance imaging (MRI) allows for unparalleled study of the structure and function of the brain. While most MRI work is human focused, it is notable that MRI is one of a few research tools that can be directly translated between humans and experimental animals. This dissertation reports on the development, application, and validation of *ex vivo* MRI methods to study brain structure, especially in the context of the fear circuit in mice. First, connections of the olfactory bulb and the amygdala were evaluated using *ex vivo* diffusion weighted imaging (DWI) and were compared to the results from *in vivo* manganese enhanced MRI. Second, the projections of the infralimbic and prelimbic cortices were compared and contrasted using a combination of *ex vivo* DWI and anterograde tracing with biotinylated dextran amine (BDA). Third, the projections of the posterior thalamic group (medial geniculate, paraintralaminar, and suprageniculate nucleus) were analyzed with *ex vivo* DWI, and those results were validated using BDA tracing and were also compared to *in vivo* DWI results in humans. Fourth, *ex vivo* voxel-based morphometry analysis (VBM) was performed on structural scans of *Thy1*-YFP mice after auditory fear conditioning with followup confocal analysis of the dendritic density and morphology in areas of VBM significance. The results across all four approaches are broadly impactful as they validate the use of *ex vivo* MRI, refine underlying mechanisms of DWI and VBM signals, are a proof of concept for the translational utility of MRI, and provide much needed anatomical and structural evidence for the fear circuit in mice.

The Development and Application of *Ex Vivo* Magnetic Resonance Imaging Techniques to Understand the Neural Basis of Pavlovian Fear Conditioning and Extinction.

By

Orion Paul Keifer, Jr.
B.S., Applied Psychology *with Highest Honors*, Georgia Institute of Technology
B.S., Applied Biology *with Highest Honors*, Georgia Institute of Technology
B.S., Biomedical Engineering *with Highest Honors*, Georgia Institute of Technology
M.S., Psychology – Brain and Cognitive Sciences, Georgia Institute of Technology

Advisor: Kerry J Ressler, M.D., Ph.D.

A dissertation submitted to the Faculty of the James T. Laney School of Graduate Studies
of Emory University in partial fulfillment of the requirements for the degree of Doctor of
Philosophy in Neuroscience
2014

Acknowledgements

"Victory at all costs, victory in spite of all terror, victory however long and hard the road may be; for without victory, there is no survival." - Winston Churchill

It may be both melodramatic and unintentionally brash to draw parallels between earning a PhD and rousing the House of Commons for the Battle of France, but the acknowledgements section is one of the few sections of this dissertation where I am able to write fully at my discretion. So I do draw the parallel because, almost without the thought of the historical reference, I have often told the undergraduates who wish to enter science that it only takes "blood, toil, tears and sweat". Of course, it is naïve to think that is enough. It truly takes a bulwark of outside support in nearly every aspect of life or else one is likely to fall off the ledge. In that regard, to be complete my list of thanks and acknowledgements must be far longer than the dissertation itself, however space is limited so to those not specifically acknowledge below I say a becausere thank you (I trust you know who you are, except Kenneth McCullough who insisted on being mentioned by name).

In my personal life, unlimited thanks must go to my infinitely supportive and understanding parents, Orion and Patricia Keifer. Even with my early struggles with getting "b" and "d" correct, somehow you still convinced me that I could be "*knowlebgeadle"* enough to be a doctor (or even a double doctor). Thanks must also go to my three older sisters, Rachel, Megan and Dorion, who, while correctly assessing that I was "crazy", still would listen to my rants and support my goals. I should also say that Erin Hecht is good.

In my academic life, many thanks must go to Dr. David Gutman, soon to be Dr. Mary Horton, and Dr. John Rolston who were the triumvirate that ultimately led me to the MD/PhD path. In the same manner, I have a tremendous amount of gratitude and reverence for the rule of seven (code name for my committee). They have invested countless hours in my development, the development of my projects, and the development of my dissertation - my becausere hope is that I have risen to their lofty expectations. In particular, Dr. Nicholas Boulis has been instrumental in fostering my interest and experience with neurosurgery (first scrub–in, first craniotomy, first Bovie work, and many other OR firsts), while also supporting my growth as a critical thinker both as a clinician and researcher. Dr. Shannon Gourley, though she failed me on my oral qualifying exam, was also the one who would absolutely not let me leave the PhD program. I believe she has certainly seen the error of her earlier ways because she is now one of my biggest pillars of support (thank you open door policy). Dr. Kim Huhman has been a staunch supporter, believer, and cheerleader at all times – especially in the effort to "get it done"; much of the development of the MRI work was done in collaboration with Dr. Huhman. Dr. Shella Keilholz has provided her time, the time of her students, and her expertise to drag me out from my past state of "ignorant of MRI" to my current state of "MRI novice" (that is a lot of progress); without her this dissertation would likely not involve any MRI work. Dr. Todd Preuss has served as a perfect example of a thoughtful, thorough, and passionate scientist, with our brainstorming sessions always leading to new and exciting ideas. Dr. James Zheng has always had high expectations of my work and during committee meetings has asked the most poignant and elegant questions that have substantially improved my work, my scientific thinking, and this dissertation. Lastly, but certainly not least, Dr. Kerry Ressler must be acknowledged for his unlimited capacity for encouragement, support, and confidence in all of our work. He was an untiring defender (which is good because I occasionally did get in trouble) who could clearly see my strengths while also working on my numerable weaknesses. I am a far better person, friend, colleague, scientist, and clinician for having worked with Kerry, and he will always have my unending appreciation.

Finally, to those undergraduates (Robert Hurt, Le Zhong, Michael Baron, Cheng-Wei Lo, Jacob Garrett, and on and on) that have served under me (a cruel and demanding master), thank you for helping me become a better mentor, supervisor, and scientist. I would have never learned the breaking point of Emory undergraduates if you would have not sacrificed your time and energy under my guidance. For those that survived the break and were reborn in my image, thank you for the help you provided in ensuring that all my projects would at least have a chance to be piloted and executed.

Table of Contents

Chapter 1: General Overview and Framework

Chapter 2: The Development and Refinement of *Ex vivo* Magnetic Resonance Imaging

<u>Chapter 3: A Review of the Pertinent Literature for the Relevant Neurobiology of Fear Conditioning and Extinction</u>

Chapter 4: Mapping of the Mouse Olfactory System with Manganese-Enhanced Magnetic Resonance Imaging and Diffusion Tensor Imaging

Chapter 5: A DTI Tractography analysis of Infralimbic and Prelimbic Connectivity in the Mouse using High-throughput MRI

Chapter 6: A Comparative Analysis of Mouse and Human Medial Geniculate Nucleus Connectivity: A DTI and Classical Tracing Study

Chapter 7: Parallel Macroscopic and Microscopic Increase in Brain Structure After Learning: Voxel-Based Morphometry Predicts Shifts in Dendritic Spine Density and Morphology with Auditory Fear Conditioning

Chapter 8: Overall Discussion and Future Directions

Appendix

Figure Index

Chapter 1:

General Overview and Framework

1.1 An Overall Perspective on the Dissertation

The following dissertation represents the intersection of technical development and scientific application. On the technical development side, the dissertation presents the process of development and refinement of *ex vivo* magnetic resonance imaging (MRI) using a high field MRI scanner (Chapter 2). Further, with the successful development of the imaging methodology, the work here presents the technical adaptations of existing analysis software (built almost exclusively to analyze human MRI data) to analyze *ex vivo* mouse brains (Chapter 4-7). Finally, on the technical development side, much of the MRI research results presented here are compared against a more traditional or "“gold standard"” approach to allow for both a validation of the MRI approach and to provide a better understanding of the underlying cellular mechanisms of MRI signal (Chapter 5-7).

From a scientific application perspective, the dissertation presents work that highlights the strengths of using *ex vivo* MRI to answer scientifically meaningful questions. Broadly speaking, the dissertation lies within the fields of memory and emotion. More specifically, the scientific questions are focused on the field of fear conditioning and extinction, which is thought to reflect the intersection of memory and emotion. Of particular interest here is the neurobiological basis for fear conditioning and extinction (Chapter 3). Specifically, the work shows the utility of using diffusion weighted imaging (DWI) to generate probabilistic tractography of the connections in the mouse brain, especially with respect to the proposed fear circuits (Chapter 4-6). Further, it shows how the application of DWI based probabilistic tractography can be used as a tool for comparative work between humans and mice (Chapter 6). Finally, the work shows how the application of voxel-based morphometry to *ex vivo* high-resolution structural scans can yield meaningful results about structural changes in the brain, which can be further complemented by confocal analysis of cellular structure (Chapter 7).

1.1.1 The Particulars of the Technical Development

The historical perspective of the use of *ex vivo* imaging is presented in Chapter 2. Additionally, within that chapter is a presentation of the development and refinement of the *ex vivo* method that was used for the dissertation work and the work of collaborators. The following briefly highlights the importance of the work. While the *ex vivo* technique that was employed in these studies is a modification of previous work, it is notable that there were several improvements. First, the protocol used here involved acquiring MRI scans of multiple *ex vivo* brains simultaneously. Second, the protocol used here involved doping the agarose (used for embedding the extracted brains) with gadolinium (III) oxide. In doing so, the MRI signal from background was significantly reduced, allowing for easier processing. Third, the protocol used here is easy to learn and implement, cost-efficient to use, and has no long term effects on brain tissue. Fourth, the protocol used here has been successfully used across the brains of multiple species with different scanners and imaging protocols. In sum, this protocol is efficient, robust, scalable, and generalizable across species, techniques, and brain sizes.

With regards to the adaptation of existing software to analyze MRI images of mouse brains, Chapters 4-7 provide the details for the modifications to the FSL software (FMRIB, Oxford, UK) package that were necessary to successfully extract the brains from their imaging volumes, pre-process those images for analysis, and then finally process and analyze the probabilistic tractography and voxel-based morphometry data. These modifications were necessary because most software packages are designed to pre-process and analyze human brains.

Finally, while MRI techniques are usually designed to answer questions about the structure and function of human brains, it is important to note that, most commonly, they are based on theoretical frameworks that must be validated. For example the application of functional MRI was in widespread use before there was experimental validation that neuronal activity leads to increased blood flow which in turn causes shifts in the magnetic environment that can be detected by the MRI scanner (discussed briefly at the start of Chapter 7). Therefore, conspicuous in the work presented in Chapters 5-7, which employ the use of DWI probabilistic tractography and voxel-based morphometry, are attempts to validate and understand the underlying neurobiological mechanisms for the MRI signal of these analyses. For the DWI probabilistic tractography, the underlying theory holds that water is more likely to diffuse along the length of an axon as opposed to across the length of an axon, and therefore measurements of water diffusion can act as a proxy for the direction of axonal projections. Thus, in the DWI tractography research presented in Chapter 5 and 6, the results were always compared to anterograde tracing results using biotinylated dextran amine. In doing so, not only did the results provide impactful information about the connectivity of the mouse brain, but they also served to test and validate that DWI tractography reflects the anatomical substrates it is purported to detect. Likewise for the VBM work presented in Chapter 7. VBM is thought to capture cellular structural changes in the areas of interest. These changes are thought to potentially include differences in the glial and neuronal density or differences in the neuronal dendritic spine density and/or morphology. To address this, the VBM results presented were also complemented by analysis of nuclear density (a proxy for neuronal and glial density) and neuronal dendritic spine density, width, and length.

In considering the broader impacts of these technical developments, there are several points to be made. The first is that the *ex vivo* method presented here will be published and will allow many imaging cores to use that as a base of information to launch their own *ex vivo* imaging programs, because because the methods presented here do not require specialized hardware or software to complete the studies (detailed in Chapter 2). Second, with the success of the application of the *ex vivo* imaging method to answer scientific questions, this dissertation highlights its enormous potential. Finally, as noted, these results are beginning to bridge the theories of the underlying source for MRI signal and the experimental “ground truth” in terms of cellular structure.

1.1.2 The Particulars of the Scientific Application

The context of the scientific work presented in this dissertation is the field of fear conditioning and extinction. A particular focus is on the neurobiological underpinnings that are thought to explain the mechanism of fear conditioning and extinction. In particular, as the field stands there is a generalized fear circuit that is proposed to account for the process of fear conditioning and extinction (Chapter 3). Within that framework, there are four points of interest that have been investigated in the following dissertation. These are the projections from the olfactory bulb to the amygdala in mice using DWI probabilistic tractography and manganese enhanced magnetic resonance imaging (Chapter 4), the projections of the infralimbic and prelimbic cortex in mice using DWI probabilistic tractography and BDA anterograde tracing (Chapter 5), the projections from the posterior thalamus with an emphasis on the medial geniculate nucleus in mouse and human brains using DWI probabilistic tractography, with BDA anterograde tracing in mice (Chapter 6), and the role of the auditory cortex in auditory fear conditioning as assessed with voxel-based morphometry and confocal analysis of nuclei density, dendritic spine density, width, and height (Chapter 7). The broader historical perspectives and literature for these pathways are reviewed in Chapter 3.

In considering the broader impact of these scientific applications, there are several important points to be made. The results of the tractography and tracing work establish evidence for the presence of the fear circuit in mice (there is a paucity of anatomical tracing work in mice). Further, the work comparing the projections from the medial geniculate nucleus in humans and mice provides a much-needed first proof of concept to open up the tremendous opportunity to use the technique comparatively for physiological or pathophysiological applications. The same is true for the VBM work presented here. While VBM is used quite commonly in humans, there are only a couple of papers that have applied the technique to rodents. Further, our combined confocal - VBM work has also shed light on part of the cellular mechanism that may account for the changes detected in MRI signal. This would aid the human VBM literature tremendously, as there are only untested hypotheses about what causes this signal change.

Chapter 2:

The Development and Refinement of *Ex Vivo* Magnetic Resonance Imaging

2.1 Context, Author’s Contribution, and Acknowledgement of Reproduction

The following chapter presents an introduction to *ex vivo* imaging, the development of the *ex vivo* protocol used for the work in the dissertation, and the presentation of many different species' brains that have undergone MRI scanning using the methodology presented. The work presented here was conceptualized, organized, researched, and written by the dissertation author. Of the data presented all, except for the sea lion brain, was collected by the author under the guidance of Dr. Ressler, Dr. Keilholz, and many collaborators. The chapter is reproduced with minor edits from Keifer, Jr., O.P., Gutman, D.A., Hecht, E.E., McCann, K.E., Walker, L.C., Preuss, T.M., Huhman, K.L., Ressler, K.J., and Keilholz, S.D. (Under Revision for Submission). “The Methodology and Application of *Ex Vivo* Magnetic Resonance Imaging to a Diversity of Species’ Brains.”

2.2 Introduction

The vast majority of neuroscientifically and neurologically focused magnetic resonance imaging (MRI) studies examine the human brain *in vivo*. These studies have had a tremendous impact on our understanding of the function and structure of the human brain. However, the smaller and often overlooked field of post-mortem or *ex vivo (*or *in vitro* imaging - the terminology is still unfortunately mixed) has also yielded a wealth of data to improve our understanding of the function and structure of the brain of many species. For clarity herein, post-mortem imaging will refer to work involving human brain, whereas *ex vivo* imaging will refer to MRI use in other animals. The field most predominantly employs the use of very high strength magnetic resonance scanners to investigate post-mortem human brain tissue and *ex vivo* laboratory animals (Driehuys, Nouls et al. 2008, Badea and Johnson 2012). There are numerous reasons why studies in this area are fewer than the *in vivo* counterpart, including a lack of standardized approaches and limited expertise, fewer high strength magnetic resonance scanners, the belief that the method requires custom hardware and sequences, and practical/infrastructural issues with using the MRI scanner. Here we examine the strength of *ex vivo* / post-mortem imaging while also providing our experience to develop and refine *ex vivo* imaging in a research-dedicated Bruker 9.4T MRI scanner (Bruker Corp, Billerica, MA). The approach presented here uses standard Bruker sequences (Paravision 4 and 5) and standard Bruker hardware (S/R coils and gradient sets) to gather post-mortem and *ex vivo* scans to help ensure that the methods are generalizable. Further, it ensures that the scans do not require specialized knowledge of MRI hardware building (e.g., custom coils, custom cooling setups), sequences programming, or MRI physics - albeit all of those skills certainly facilitate pushing scanners to their very limits (Papp, Leergaard et al. 2014). Further, all efforts were made to minimize cost while maximizing the quality of the data to facilitate entry into the field.

Some of the earliest MRI-based studies applied to post-mortem human brains were focused on learning more about the neurobiological causes of human disease and disorders like schizophrenia (Roberts and Bruton 1990), multiple sclerosis (Macchi and Cioffi 1992), and Alzheimer's disease (Besson, Best et al. 1992, Narkiewicz, de Leon et al. 1993). Soon, clinically observed lesions on MRI were ascribed to particular causes after using a combination of pre- and post-mortem MRI imaging and autopsy/histological analysis, such as pontine lesions (Kleinschmidt-DeMasters, Anderson et al. 1997) and brainstem pathology (Maurer, Mitrovics et al. 1998). More recently, a considerable effort has gone into using post-mortem MRI as an autopsy substitute for cases of fetus/newborn death (parents often decline autopsy yet wish to know cause of death). Interestingly, this factor has also allowed for the refinement of *in utero* MRI diagnosis of developmental disorders (Griffiths, Paley et al. 2005). These pioneering studies highlight some of the strengths of post-mortem/*ex vivo* imaging. First, it is possible to conduct pre- and post-mortem imaging on patients, helping to validate the clinical use of MRI imaging in diagnostics. Second, post-mortem imaging offers an opportunity to scan for extended times, thereby improving signal to noise, resolution, and contrast, which facilitates the detection of only very slight differences in brain structure. Third, post-mortem imaging usually involves fixed tissue (e.g., the cellular structure of the tissue at the time of imaging is preserved and static), which can undergo histological analysis for comparison and quantitative correlation to the MRI scans (so called "ground truth" (Osechinskiy and Kruggel 2009)). The latter point is illustrated by studies like that by Bobinski and colleagues that correlated hippocampal volume and neuronal counts in Alzheimer's disease (Bobinski, de Leon et al. 2000), or Nijeholt's study of post-mortem spinal cords from patients with multiple sclerosis, which showed strong correlations between MRI and histopathological lesion size (Nijeholt, Bergers et al. 2001). Clearly there are strengths to post-mortem imaging in human brains, and the majority of the post-mortem/*ex vivo* MRI field lies in this direction. However, the application of the e*x vivo* imaging of laboratory animals has grown drastically in the last two decades (Johnson, Benveniste et al. 1997, Badea and Johnson 2012).

The span of *ex vivo* imaging has been just as long as that of post-mortem work, with Buonanno and colleagues studying isolated cat heads as a model of ischemic stroke (Buonanno, Pykett et al. 1982). *Ex vivo* work would go on to expand into studies using rats (Ford, Ceckler et al. 1990, Lanens, Van der Linden et al. 1994), mice (Smith, Johnson et al. 1994, Benveniste, Kim et al. 2000), and macaques (D'Arceuil, Westmoreland et al. 2007). Beyond looking at multiple species, the applications of the *ex vivo* MRI techniques have been broad. They include (but are certainly not limited to) developing relevant MRI based 3-D atlases (Benveniste, Kim et al. 2000, Zhang, van Zijl et al. 2002), monitoring neural development (Mori, Itoh et al. 2001, Anaby, Duncan et al. 2013), studying transgenic pathological model animals (Lee, Falangola et al. 2004), studying injury models (Nishi, Liu et al. 2007), neural stem cell graft tracing (Magnitsky, Watson et al. 2005), and methods of tracing connectivity in the brain (Gutman, Keifer et al. 2012, Gutman, Magnuson et al. 2013). These studies all highlight further important strengths of *ex vivo* imaging. First, both *in vivo* and *ex vivo* MRI techniques provide powerful tools for translational work between human patients and the laboratory animals used to model them. Second, *ex vivo* imaging allows for extended scanning times (with all the benefits discussed above) which also allows for the collection of multiple imaging modalities on one sample. Third, *ex vivo* allows for imaging multiple brains at a time, thereby helping to offset the increased scan time (Gutman, Keifer et al. 2012, Gutman, Magnuson et al. 2013). Fourth, it allows for the scanning of species, like a whale shark (Yopak and Frank 2009), that otherwise could not be placed in conventional MRI scanners *in vivo*.

Clearly there are tremendous advantages to using a post-mortem/*ex vivo* approach; however, there are also notable weaknesses. First, *ex vivo* work, for obvious reasons, does not allow for a real-time assessment of functional activity of the brain as in the case of *in vivo* fMRI. Second, longitudinal work requires the sacrifice of multiple animals at different time points as opposed to following the same cohort of animals over time. Third, while the technique allows for high quality and high-resolution images, this benefit comes at the cost of increased scan time. Fourth, the brains must be embedded to provide stability (some sequences can cause motion in the scanner leading to movement of the brain) and to protect the brains from dehydration, while also making it possible to extract the brains later for histological processing. Fifth, the scans and parameters used for imaging *ex vivo* brains are naturally different than those of *in vivo* scanning (i.e., clinical and research scanners run very standardized sequences), which requires testing sequences with different parameter settings to optimize the data quality. Clearly, the first two weaknesses are impossible to address with the technique. The three other weaknesses are problematic in that it may prevent the widespread adoption of post-mortem/*ex vivo* imaging because the approach has not benefited from widespread application and therefore standardized techniques have not been presented. We maintain that the latter weaknesses are addressable, at least to some extent.

Here we present our experience with *ex vivo*, high-resolution magnetic resonance imaging. We include a detailed description of our embedding techniques across a diversity of species, problems encountered with the technique and commensurate troubleshooting steps, a listing of our successful high-throughput imaging methods for smaller animal species (mice, rat, and hamsters), and our high-resolution acquisitions of larger species (rhesus monkeys, squirrel monkeys, fox, and sea lions) and human brain sections.

2.3 Methods and Results

2.3.1 Practical Considerations

Before beginning *ex vivo* there are a few important practical considerations. First, given the cost and importance of high field MRI scanners, it is paramount that the scanners have fail-safes in place to protect equipment. Nearly all modern scanners have a temperature sensor with cut-off in place, which is of the first importance for high intensity long duration scans (note that many of our imaging parameters where dictated more by temperature control than by the limits of the sequences or scanner). When running any scanning parameter for the first time, the temperature of the scanner should be closely monitored until it plateaus (the heuristic employed in our center is no change in temperature for one hour). Once the sequence has been tested for temperature stability, then it can then be run overnight unmonitored.

A second consideration is the available gradients and send/receive coils available for imaging. Particular attention should be paid to the inner diameter of the send and receive coil and the size of the sensitivity range for a coil. These factors will determine the size of the embedding chamber that can be used and also the size of the sample that can be imaged with particular gradient and coil combinations.

A third consideration is the placement of the sample within the bore of the scanner, particularly within the coil. While this last consideration seems the most trivial, it is often the most time consuming portion of the scanning process for the operator. For larger coils there are often cradles used for imaging, though those are designed for *in vivo* imaging. While these cradles can be used for *ex vivo* imaging, there are a number of difficulties. First is rotation; if 16 brains are placed in a single plane when embedding them for scanning, ideally that plane is not rotated with respect to the y-axis in the coil because it can put the sample in a non-ideal position with respect to coil sensitivity (the operator will either have to pull the sample back out and rotate it or will have to acquire more slices to cover the area of the brains or will have to rotate the image using software, which can complicate post imaging processing). Second is centering in the magnet. Ideally, the sample is in the middle of the sensitive range of the coil with respect to each plane in 3 dimensions. Cradle adjustments in the z-direction are as simple as moving the cradle into and out of the bore. However, adjustments in the x-axis require pulling the sample out and repositioning. Likewise, positioning in the y axis means moving the sample, but often there is less room for adjustment (the position in the y-axis is dictated by the depth of the sample in the embedded chamber and also the size of the cradle and height of the coil). For samples without cradles that must rest in the coil (e.g., smaller coils like the Bruker RF Volume Coils 1H/X with 35 mm inner diameter), the sample's position (with the exception of the z-axis) is exclusively dictated by the embedding procedure, and great care must be exercised to ensure the sample to be imaged is centered in the x and y axis of the embedding chamber (e.g., a 50ml falcon tube).

2.3.2 Brain Perfusion, Fixation, and Extraction

Integrity of neural tissue is paramount for successful magnetic resonance imaging. For brain extraction that can occur on a schedule (e.g., small animals that are euthanized after the experimental manipulation), it is important to ensure consistency across animals as degradation of neural tissue through autolysis is rapid and can lead to signal differences (Benveniste and Blackband 2002). To combat autolysis and tissue destruction, we and many others employ a formalin fixation protocol which crosslinks proteins to each other and proteins to nucleic acids (Werner, Chott et al. 2000). For our mouse, rat, and hamster studies, intravascular perfusions consisted of intra-cardiac injection of 10-200ml of phosphate buffered saline (the volume used corresponds to the amount need to clear blood from the vasculature) followed by the same amount of 4% paraformaldehyde in phosphate buffered saline with the range of volumes reflecting the range of animal size. The rate of perfusions was controlled either by hand (predominantly) or by pump. In our experience, the pump introduced significant air into the vasculature, whereas when perfusing by hand there was the potential to rupture the venous side of the vasculature in the brain. Each technique can cause artifacts (air bubbles are the most notable as they lead to susceptibility artifacts). An injection rate of about 10ml of fluid per 1-2 minutes is our goal when working with mice (the most common animal used).

Following perfusion, the brain is carefully extracted and is immersed in formalin for between 24 hours for smaller brains like mice or for or 48 hours for larger brains like hamsters and rats. For our larger specimen brains (e.g., non-human primates and sea lions), their extraction was rarely a scheduled event. Therefore, it was not always possible to for them to undergo a perfusion procedure. Typically the brains presented here, and many other brains that are banked, are extracted as soon as possible after death and are then immersed in 10% formalin for approximately 1 month. In some of the cases, the brains also underwent a cryopreservative sequence (a series of immersions in sucrose solutions ranging from 5-30%). Based on our experience, these brains had less signal than did fixed tissue. Therefore, we reversed the cryopreservation series and noted success in increasing the signal, though not typically fully to the level of fixed tissue.

2.3.3 Evolution of the Embedding Procedure

The major advantage of *ex vivo* or post-mortem imaging is the length of time available to run the scanner for data acquisition. Such time allows for the acquisition of high-resolution volumes with multiple averages yielding data of unparalleled signal-to-noise (SNR) and contrast-to-noise ratios (CNR). Additionally, as our work has shown, it also allows for the acquisition of between 1 and 16 brains per scanning session (Gutman, Keifer et al. 2012, Gutman, Magnuson et al. 2013). However, it also introduces the problem, as; that outside of the skull, the brains are not protected from the environment and therefore will, amongst other things, dehydrate. Placing the brains in a liquid solution has the advantage that the solution is able to fill many of the cavities of the brain, but has the downside that the brain is still allowed to drift (i.e., some sequences like diffusion weighted protocols create a vibration in the scanner and the brains will move during the acquisition). There have been several solutions (with varying of success and cost) to the problem including paraffin oil (Beaulieu, Zhou et al. 1993), agarose (Smith, Johnson et al. 1994), agarose doped with magnetite (Dhenain, Michot et al. 2000), and fluorocarbon (Dhenain, Ruffins et al. 2001). Of these, the cheapest is agarose, while the most expensive is fluorocarbon. For us, the considerations that are important for the selection of the medium include ease of the embedding and extraction, cost, availability, impact on brain tissue, stability of the brain tissue, and background/artifacts on the acquired data. Here, we describe our experiences with agarose (RXA-2500LE, Phenix Research Products, Candler, NC) doped with gadolinium (III) oxide (12064-62-9, Acros Organics, NJ).

2.3.4 Embedding Iteration 1

Based on the aforementioned characteristics, our first scanning sessions followed the methods of Smith and colleagues, using an agarose based embedding medium (Smith, Johnson et al. 1994) with the exception that we doped the agarose with 1 mM gadolinium (III) oxide. At first, we added 2% w/v molecular grade agarose and the gadolinium (III) oxide to distilled water, brought to a boil, and cooled the solution till it was slightly viscous but not hard. From there a portion was poured into a 50 ml Falcon tube that was then turned on its side and allowed to harden. Moving rapidly (to beat the hardening of the gel), the brains were dipped in the liquid one at a time (using a spatula) and slid into the falcon tube onto the previously dried gel (once the gel around the brain hardened it was harder for it to float with the later addition of more agarose solution). Once all brains were in place, additional liquid agarose solution was poured over the top to fill the Falcon tube completely, and the top was then fastened in place. The first acquisition (**Figure 2.3-1**) using this method contained 6 rat brains using the standard Bruker spin echo diffusion weighted sequence ("DTIstandard", 60 diffusion directions, b= 2000 s/mm^2, 4 b0 images, 230 µm isotropic, 256 x 128 x 45 slices, TE = 27.1 ms, TR = 25000ms, 56 hours) using the standard Bruker RF Rat Body Volume Coils 1H/X with 70 mm inner diameter.

The result of the first round of scanning effort quickly revealed a couple of notable problems. First, given the high signal of the background, it was thought that the concentration of gadolinium (III) oxide was too low and that the distribution was also unequal. This resulted in difficulty parsing the brains away from the background for analysis. Second, it highlighted the potential for points of high signal intensity near the cortex and cerebellum of the brains that would result in Gibbs ringing (Archibald and Gelb 2002) in the images (indicated by arrows in **Figure 2.3-1a**). Third, despite all six brains being in the reported sensitive range of the coil, there is a clear exponential signal drop off within that range (**Figure 2.3-1a**, loss of signal at the top and bottom of the image).

2.3.5 Embedding Iteration 2

For the next iterations of scanning (**Figure 2.3-2**) the gadolinium (III) oxide concentration was increased to 2 mM. Further, to ensure that the distribution of gadolinium (III) oxide was equal throughout the agarose mixture, it was mixed constantly using a stir bar during the embedding procedure. Given location of the Gibbs ringing around the olfactory bulbs, we thought it might result from entrapment of fixative solution, so we dried the brains before adding them to the embedding mixture. Also, unlike the first iteration, the brains were allowed to swirl in the agarose gadolinium (III) oxide solution. **Figure 2.3-2a,b** presents a horizontal section of the b0 image of the Bruker spin echo diffusion weighted sequence (DTIstandard, 60 diffusion directions, b= 2000, 4 b0 images, 200 μm isotropic, 256 x 128 x 45 slices, TE = 26.9 ms, TR = 20000 ms, 62 hours) and the Bruker RARE T2 weight sequence (RARE,12 averages, TE=20 ms, TR = 15000 ms, 512 x 256 x 120 slices, 0.1 mm isotropic). Further, we reduced the number of rat brains that we were embedding down to 4 given the coil sensitivity and the difficulty with spacing the brains.

Notable in these images are the intermittent appearance of “scallops” (indicated with arrows on the b0 images in **Figure 2.3-2a,b** - note they are smaller in the T2 RARE acquisitions) around certain portions of the cortex (these brains were un-embedded and there was no damage to the cortex in these areas). Further, there was reduced but still noticeable persistence of Gibb’s ringing especially around the olfactory bulb and cerebellum.

2.3.6 Embedding Iteration 3

We observed that the scalloping of the images only appeared after increasing the gadolinium (III) oxide concentration and allowing the brains to swirl within the agarose gadolinium (III) oxide solution. These changes, along with the scalloping artifact, suggested that this represented a susceptibility artifact, potentially generated by either tiny bubbles or the presence of a fluid interface layer (initially brains were pulled from the refrigerator and immediately embedded). This artifact can vary significantly in effect (see **Figure 2.3-3** for the artifact on 9 mouse brains all RARE, 10 averages, TE = 28.61, TR = 10000, 2048 x 512 x 70, 0.081 x 0.081 x0.161, 14 hours). Thus, we next attempted to mitigate the potential for bubbles in the agarose-gadolinium (III) oxide solution by keeping the temperature of the solution stable at approximately 40-45 degrees celsius during the embedding procedure and also taking care to eliminate bubbles on the surface of the brain when placing them in the falcon tube. Further, all brains were taken from the refrigerator (stored individually in scintillation vials) and were brought to embedding temperature using a water bath. Additionally, the presence of Gibbs ringing around the olfactory bulbs suggested two possible solutions. The first solution was the removal of the olfactory bulbs (if not relevant for the study in question) or specifically paying attention to that area during drying and embedding (shifting the olfactory bulbs and cerebellum while applying small amounts of the embedding mixture).

Figure 2.3-4 shows the results of these modifications. In this case, we have both mice (**Figure 2.3-4a-d**) and rat brains (**Figure 2.3-4e**). With the mice brains we attempted to embed as many brains as possible into the tube (11 in **Figure 2.3-4a-c** and 16 in **Figure 2.3-4d**). The area marked by a white box in **Figure 2.3-4d** shows how a collection of brains floated in the tube before the gel hardened. The images were acquired with the standard Bruker RARE T2 weight sequence (RARE, 20 averages, 512 x 256 x 65 (100 for rat) slices, 0.161 mm isotropic, TE = 25, TR = 10000 ms, 13 hours) and the Bruker spin echo diffusion weighted sequence (DTIstandard, 60 diffusion directions, b= 3000, 3 b0 images, 0.250 mm isotropic, 256 x 128 x 55 slices, TE = 27.1, TR = 27500, 62 hours).

The images in **Figure 2.3-4** have excellent signal to noise, excellent contrast to noise, and very few if any of the artifacts noted above. However, as is made clear by the portion of **Figure 2.3-4d**, a more standardized and easier way of placing the brains was still necessary. So, the last major revision to the process involves placement of the brains in the embedding container. In this case, we moved towards cutting a portion of the falcon tube or the larger sealing plastic imaging tube used for scanning (Hinge Top Vials, SKS Bottle and Packaging, Inc., Watervliet, NY), which allowed for more accurate and precise placement/spacing of the brains avoiding the problem of brains either moving in the tube during embedding or not being aligned during placement (Gutman, Keifer et al. 2012). For example, **Figure 2.3-5a**, shows our typical results with our 3x3 and 4 x 4 grid of mouse brains (RARE, TE = 13.40, TR = 10000.00, 10 Averages, 512 x 512 x 65, 100 µm in-plane, 160 micron slice thickness, 14 hours). A final proof of the overall method comes in the form of imaging mouse brains with glioblastomas (**Figure 2.3-5d,e**). These brains have irregular edges, many convolutions, and areas of necrosis yet there are minimal issues with Gibbs ringing or susceptibility artifacts with these brains.

2.3.7 Application to Other Species and Modifications

2.3.7.1 Small Animal Species

Similarly sized brains are easily amendable to the procedures already describe. **Figure 2.3-5c** shows how Syrian hamster brains underwent scanning using the same approach with equal success.

2.3.7.2 Large Animal Species

In addition to the utility of high-resolution imaging of multiple smaller animal brains, there is also great utility for this methodology to study larger species like the sea lions, foxes, and non-human primates at high-resolution. In general, these brains require the same embedding procedure and tend to have the same overall results. Importantly, however, there are a few caveats. The most notable hurdle that had to be overcome was the volume of material that was being imaged. Larger brains, like that of rhesus macaque, were a challenge because the volume of the brain plus the volume contributed by the agarose-gadolinium (III) oxide gel often resulted in an inability to tune and match the coil and MRI scanner. As a result, we modified our conventional use of the plastic hinge, top sealing tube and instead approached the problem of minimizing the volume of the sample to be imaged. The best solution was the dipping of the brain into the agarose-gadolinium (III) oxide solution, allowing that to harden (note that the brains were handled in the solution ensuring that the solution was able to reach many of the involutions of the brain). Then, the brain was re-dipped into the solution until about a 3-4 mm coat of the gel was surrounding the brain (e.g., the “candy apple” method). The embedded brain was then placed inside a latex balloon or wrapped in plastic wrap to prevent any dehydration.

Images of the rhesus are presented **Figure 2.3-6a-c** (**Figure 2.3-6a,b** - RARE, TE = 13.4, TR = 11750 ms, 10 Averages, 512 x 256 x 200, 250 µm isotropic, 8.5 hours; **Figure 2.3-6b,c** GEFC, TE = 10.4 ms, TR = 9000 ms, 6 averages, 512 x 512 x 140, 130 µm in plane, 350 micron slice thickness, 8 hours). However, not all brains required the candy apple method; for example, we were able to run three different sequences on several squirrel monkey brains, which are presented in **Figure 2.3-6d-i** (RARE, TE = 13.4 ms, TR = 10000 ms, 10 averages, 512 x 512 x 160, 100 μm in plane, 200 μm slice thickness, 14.5 hours; DTIstandard, TE = 27.1 ms, TR=32000 ms, 128 x 128 x 64 slices, 0.500 mm isotropic, 12 gradient direction, 3 b0, b = 3000, 18 hours; GEFC, TE= 10.63 ms, TR = 9000 ms, 10 average, 512 x 512 x 160, GEFC sequence, 100 μm in plane, 328 micron slice thickness, 13 hours; GEFC, TE = 10.5, TR = 7000, 512 x 512 x 92 slices, 100 micron in-plane, 350 micron slice thickness, 10 averages, 10 hours).

2.3.7.3 Unique Species

As mentioned above, *ex vivo* imaging provides exciting opportunities to scan animals that are rare, unique, or are not easily compatible with *in vivo* imaging. Here we present two examples of animals that fall into these categories. The first is our work with the silver fox that has undergone selection to create two lines of foxes (Belyaev, Plyusnina et al. 1985, Kukekova, Trut et al. 2004), where we have acquired T2 high-resolution and DWI sequences on fox hemispheres (**Figure 2.3-7a-d**, DTIstandard, TE = 27.1 ms, TR =42500 ms, b = 3000, 3 b0, 256 x 128 x 85, 300 μm isotropic, 52 hous; **Figure 2.3.7e,f** - RARE, TE = 13.4 ms, TR = 10000 ms, 10 averages, 512 x 512 x 150, 125 μm in plane, 180 μm slice thickness, 14.5 hours).

There are certain animal species that do not immediately lend themselves for *in vivo* imaging. Within this category, we have collaborators who are currently employing the embedding technique presented here while scanning sea lion brains within a Siemens 3T scanner (Miller, McNab et al. 2012). Preliminary results showing the generalizability of the method are shown in **Figure 2.3-7g-j**.

2.3.7.4 Post-Mortem Human Brain Sections

Because the bore diameter and coil sizes available for most high strength MRI machines is smaller than an entire human brain, magnetic resonance microscopy on human brain tissue often involves only examining discrete sections of the brain. Like the small and large animal brains, these sections lend particularly well to our *ex vivo* imaging method as there is less concern about the agarose-gadolinium (III) oxide filling the numerous cavities of a complete or hemisected brain. Admittedly, imaging only sections leads to an incomplete picture of the whole brain at high-resolution, but each section alone still provides robust data for analysis and histological comparison. **Figure 2.3-7k,l** shows some preliminary results imaging human sections that were approximately 2.5 cm thick (RARE, TE = 28.6, TR = 10000, 10 Averages, 1024 x 512 x 75, 80 µm in plane, 160 µm slice thickness, 7 hours).

2.4 Discussion

The applications of the methods discussed here are both broad and impactful, including being uniquely useful in biomedical research. For example, the rat data presented in Figure 4e was part of a larger study looking at the consequences of microembolisms (Nemeth, Gutman et al. 2014). The mouse data have been used to look at diffusion based tractography in the medial prefrontal cortex and the olfactory with concomitant comparison to retrograde tracing results (Gutman, Keifer et al. 2012, Gutman, Magnuson et al. 2013). The mouse data have also been used in a study of comparative tractography of the medial geniculate in humans and mice. The mouse data have also been used in a voxel based morphometry study of auditory fear conditioning with correlations to dendritic spine density and morphology. Finally, the mouse tumor data in

Figure 5d,e are part of a broader program focused on glioblastomas and its different subtypes (Cooper, Kong et al. 2012, Gutman, Cooper et al. 2013). While the data are not shown, there is also on-going work with a sickle cell mouse model using the techniques presented here (Keegan, Keifer et al. 2013). The Syrian hamster work is part of an on-going effort to study the neurobiology of conditioned defeat (Markham, Taylor et al. 2010, McCann and Huhman 2012). The rhesus and squirrel monkey brains, plus the human sections, are part of a broader effort to understand iron deposition in the brain (arrows in Figure 6i) and Alzheimer's disease (Elfenbein, Rosen et al. 2007). Such research in monkeys is also useful for comparative anatomical work (Hecht, Gutman et al. 2013, Hecht, Murphy et al. 2013) and for aging studies (Yan, Li et al. 2014). The fox work is part of a larger study on the genetics and neurobiology of domestication (Belyaev, Plyusnina et al. 1985, Kukekova, Trut et al. 2004). The sea lion brains are part of a larger study attempting understand particular facets of domoic acid toxicosis in these animals in an attempt to improve diagnosis, prognosis and treatment (Goldstein, Mazet et al. 2008, Cook, Reichmuth et al. 2011). Together, it is clear that a standardized, cost-effective, and easily reproducible methodology for *ex vivo* imaging across sites and species is important for understanding neurobiology and neuropathology across species and models.

While others have published additional methods, they often involved customized MRI coils or other hardware, custom-written scanning sequences, or expensive methods of embedding brains (Johnson, Benveniste et al. 1997, Benveniste, Kim et al. 2000, Badea and Johnson 2012, Papp, Leergaard et al. 2014). While these methods certainly provide compelling and meaningful results, the very nature of the customization limits the general applicability of the technique to the broader scientific world. In an attempt to make the use of *ex vivo* high-resolution magnetic resonance imaging more accessible and affordable we present our methods here. The use of gadolinium (III) oxide as a doping agent to reduce the background noise in an agarose gel is extremely cost effective, preserves the brains well, does not appear to alter the magnetic resonance data, and does not negatively affect the tissue quality of the many brains we have scanned. Additionally, we have used standard sequences and hardware, and we have presented our sequence parameters to serve as a starting point for any imaging facility attempting to start a high-resolution *ex vivo* MRI project. In this same vein, we have also detailed many of the most common problems encountered with our methods and the current solutions that have worked for us to facilitate quick and efficient trouble shooting, thereby mitigating wasted time and resources.

In a broader sense, anyone considering conducting *ex vivo* high-resolution imaging must consider that the enormous strengths of the imaging come with notable costs. First and foremost, there are considerable time commitments associated with scanning (higher resolution scans take longer and averaging helps to significantly increase SNR, but also adds time). There are two ameliorating factors that should be considered when discussing the time commitments options for scanner use. The first is that most scanners are not run overnight or over the weekend. These times offer 12 hour blocks and 48 hour blocks over which to scan, often at a significantly reduced price. The second is that once vetted, the scans can be run without the presence of an MRI tech or scientist to monitor anesthesia to the animal (both are significant contributions to the cost of *in vivo* imaging). Additionally, it should be mentioned that many imaging groups are actively developing, refining and sharing imaging sequences that are able to acquire *ex vivo* data faster and, at times, of higher caliber than the standard sequences included with the Bruker Paravision software (Muller, Vernikouskaya et al. 2012, Muller, Kassubek et al. 2013, Papp, Leergaard et al. 2014). The second cost is also related to the issue of time.

Studies seeking to use MRI data from small or larger animals often require multiple animals to draw statistical conclusions. Scanning one brain at a time, one day at a time makes using the technique prohibitive. In a partial solution to this limitation, we have presented our approaches to simultaneously scanning multiple small animal brains in a high throughput approach. However, with larger brains there are still significant hurdles to overcome in terms of time commitment. The current solution appears to be scanning a section of the brain that has an area of interest. In a similar problem, brains larger than any available coil will have to be divided to accomplish scanning. This in turn means that that the power of looking across the whole brain is lost, though gaining very high-resolution images of even subsections of brains could far outweigh the benefits of deferring to a larger bore magnet (e.g., 3T scanners).

In conclusion, we have made substantial progress in identifying techniques that allow high-throughput, simultaneous scanning of multiple small animal brains for structural MRI. However, not all problems with this or other post-mortem or *ex vivo* methods have been solved. Consider that something as simple as positioning of the sample in the most ideal 3 dimensional center of the magnet is still a challenge and is a time consuming process. Additionally, there are still some sources of Gibbs ringing, most notable in areas that are internal to the brain including the ventricular spaces. On-going work is attempting to solve these two problems, but the future is bright in that these are solvable problems. Utilizing high-throughput structural imaging in combination with small models, such as genetically modifiable mouse lines, will continue to provide powerful new ways to understand brain structure and function.

Figure. 2.3-1 Preliminary *Ex Vivo* Scans of Rat Brains.

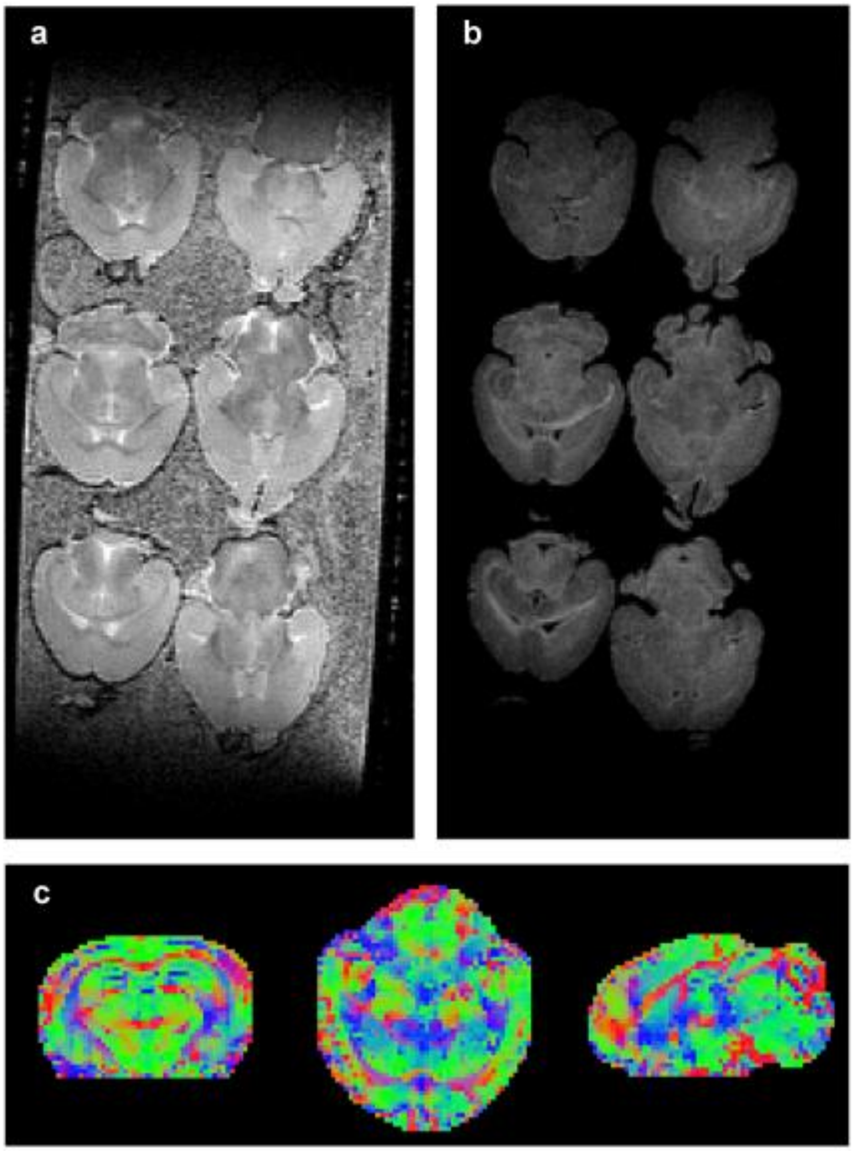

(**a**) The image shows the b0 image from the Bruker DTIstandard sequence, most notable in the image is the relatively high background despite the presence of gadolinium (III) oxide and the arrow pointing to an instance of Gibbs ringing. (**b**) The image shows the same section of the image but for one of the diffusion weighted directions. (**c**) The primary eigenvectors for the diffusion tensor analysis shown in red-green-blue (RGB) color coding of FSL (http://fsl.fmrib.ox.ac.uk/fsl/fslwiki/FSLVBM/UserGuide, Oxford, UK).

Figure. 2.3-2 Subsequent *Ex Vivo* Scans of Rat Brains with Refinements

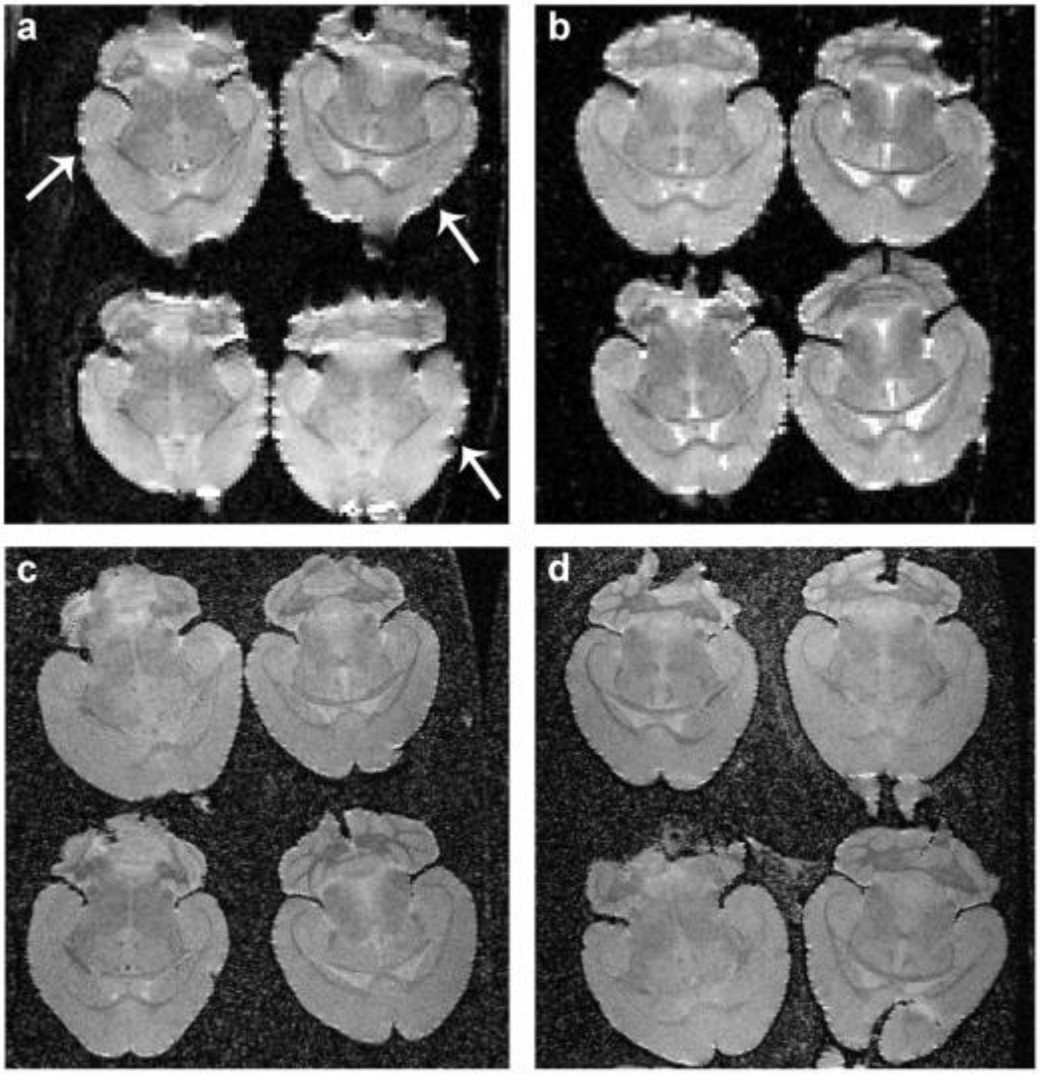

(**a**) The image shows the b0 image from the Bruker DTIstandard sequence with the refinements discuss in *Iteration 2* of the methods section. Most notable in the image is the relatively lower background compared to Figure 1a. The arrows on the image are pointing to an instance of susceptibility artifact. (**b**) The image shows another b0 image with less of the scalloping susceptibility artifact despite using the same imaging parameters. (**c,d**) Show the respective T2 RARE image of the same brains (re-embedded, hence they are not in the same orientation); there is notably less susceptibility in this sequence series.

Figure. 2.3-3 Spectrum of Susceptibility Artifact on a 3 x 3 Mouse Brain Grid

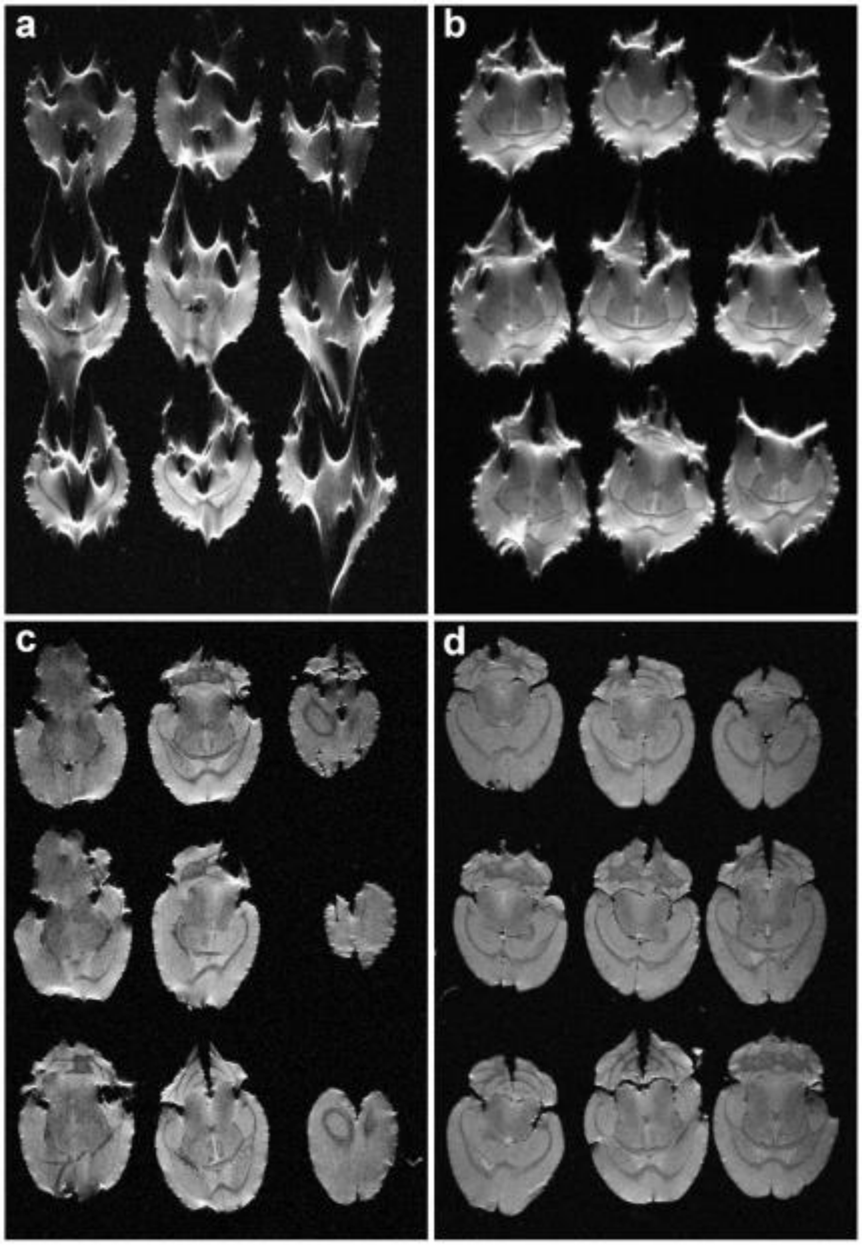

(**a-d**) These four images highlight the range of susceptibility artifacts (worst in **a**, best in **d**) that we observed in our T2 RARE 3 x 3 grid scanning of mouse brains. We noted remarkable improvement when brains where raised to embedding temperature and the surface of the brain was dried before the embedding procedure.

Figure. 2.3-4 High-Throughput MRI Imaging of Mouse and Rat Brains

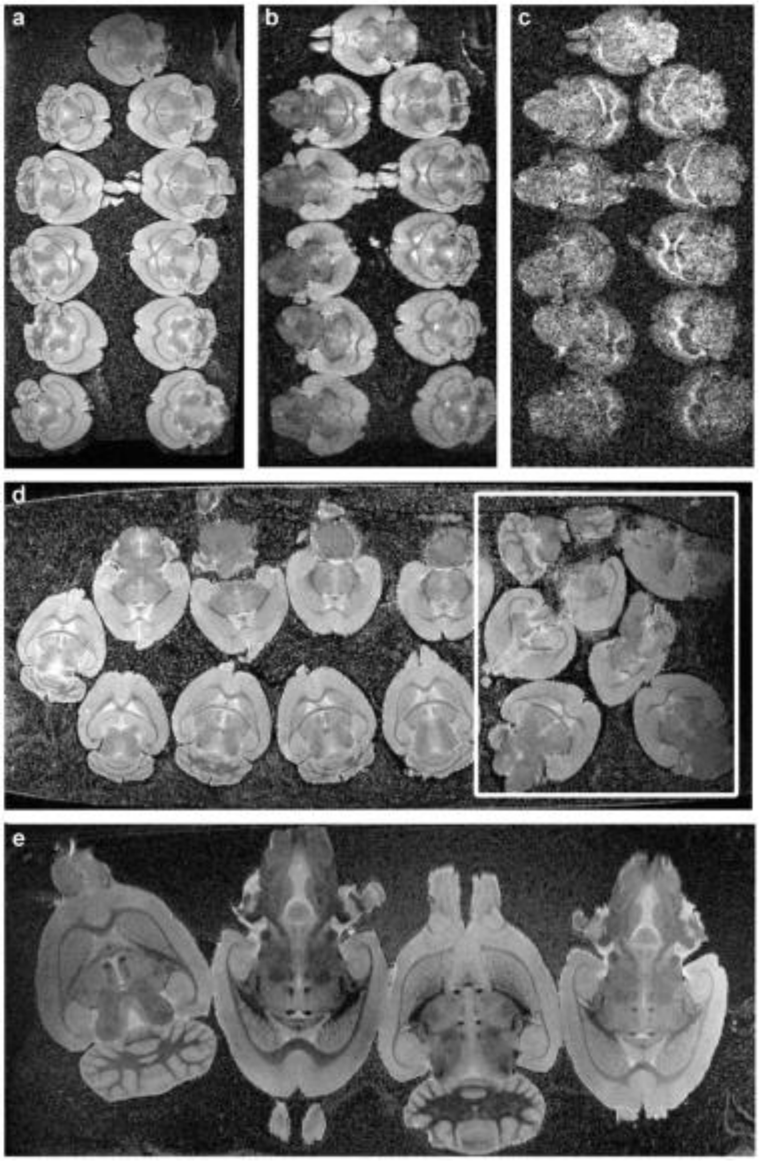

(**a**) This image presented the T2 Rare images of 11 mouse brains, (**b**) shows the b0 images from the DTIstandard sequence, and (**c**) shows one of the diffusion directions for these brains. (**d**) This image represented our attempt to image 16 brains, most notable here is the area highlighted by the white box. During the embedding procedure these brains were not fixed to the embedding layer and began to float before the gel hardened. (**e**) This image shows our results with the RARE sequence in rat brains, this should be compared to our first and second efforts in Figure 1 and 2.

Figure. 2.3-5 Refinement of the Embedding Container and Mouse Tumor Brains

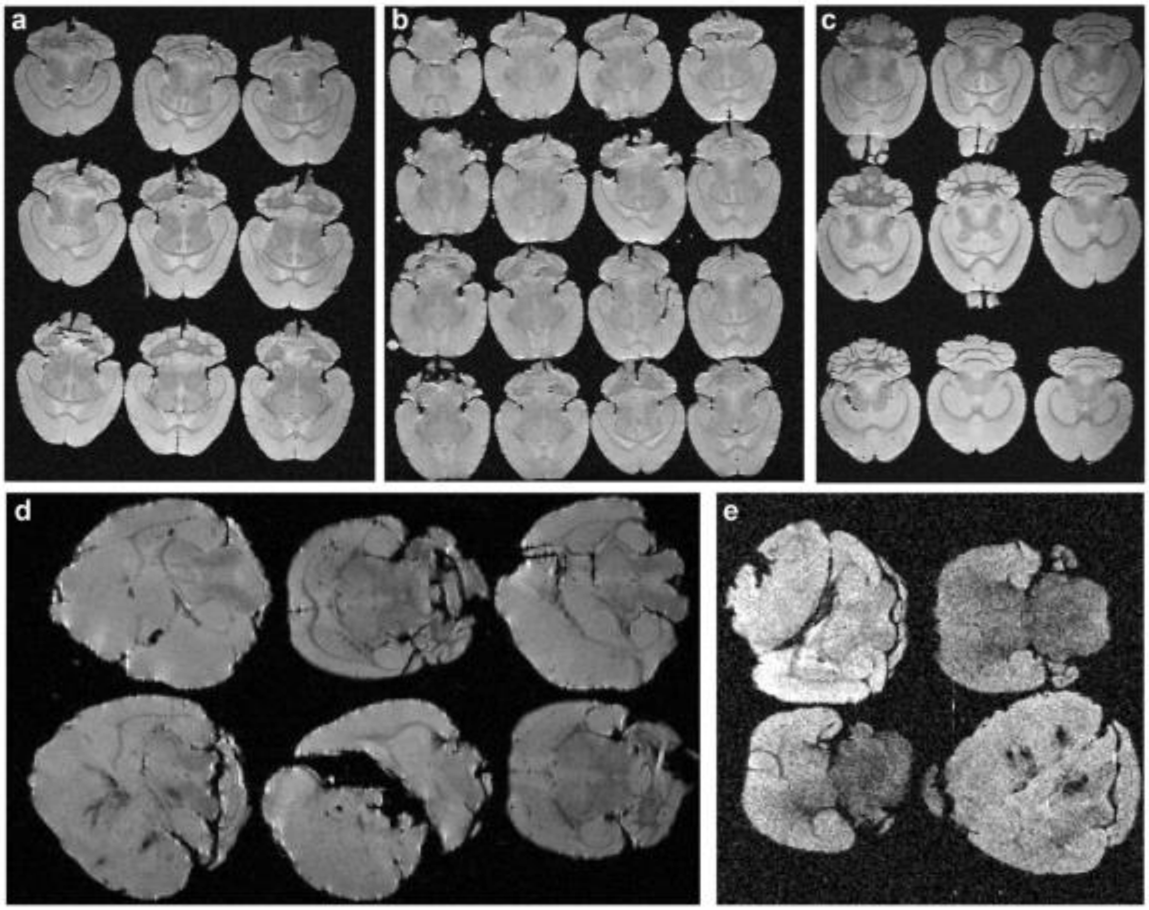

(**a,b**) Representative images of the T2 RARE acquisition of the 3 x 3 and 4 x 4 grid of mouse brains with accurate and precise placement with the modification of the embedding chamber (discussed in the methods). (**c**) A similar acquisition as a,b except this shows the application to Syrian hamster brains. (**d-e**) Representative images of mouse brains that are growing glioblastomas (T2 RARE and DTIstandard respectively).

Figure. 2.3-6 Application of Method to Large Animal Brains

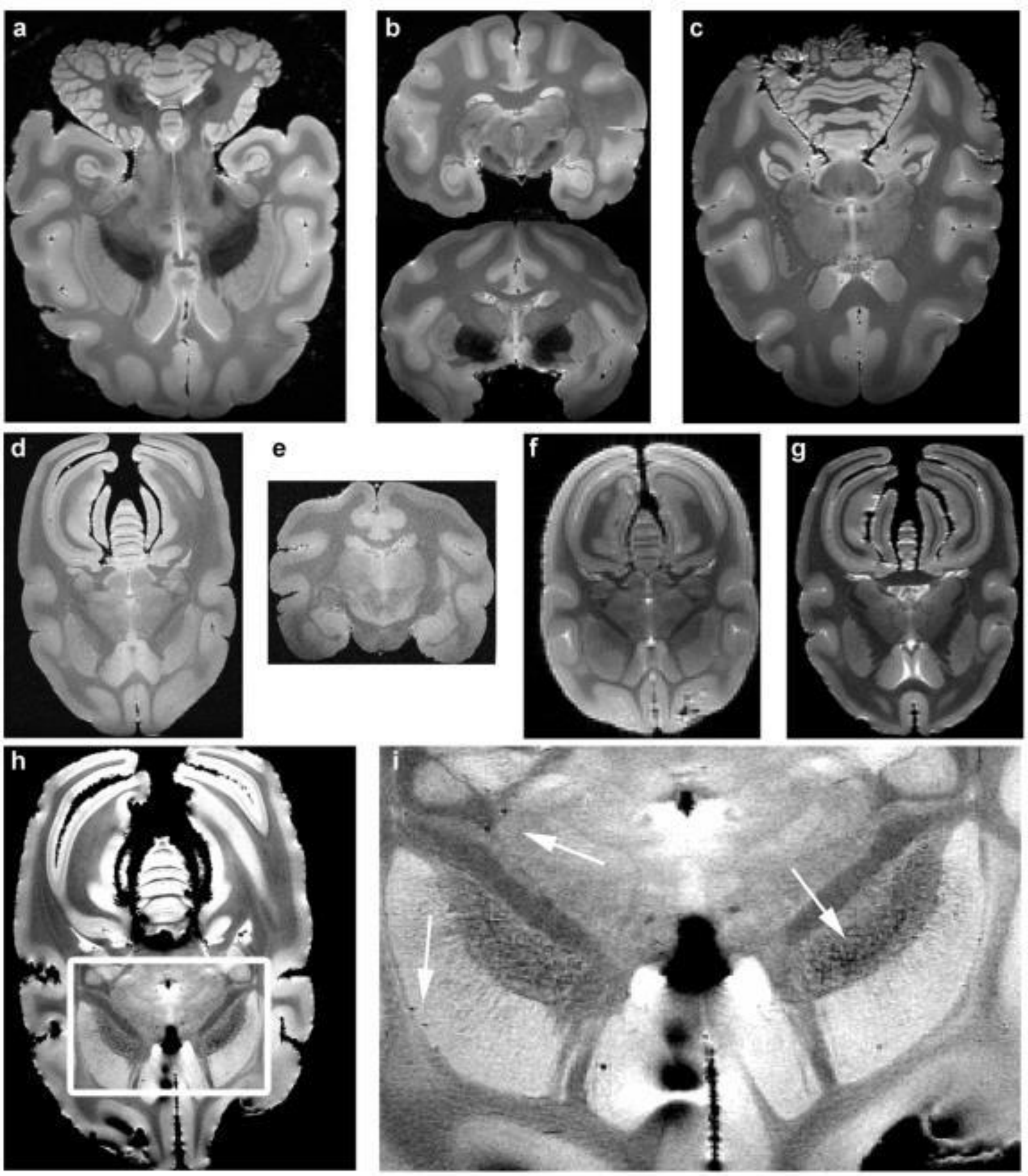

(**a-c**) Representative images of the T2 Rare and T2* GEFC images of a rhesus monkey brain. (**d-e**) Representative horizontal and coronal images of the T2 RARE acquisition of a squirrel monkey brain. (**f**) Representative images of the b0 for the squirrel monkey and (**d,h**) showing separate acquisitions of the GEFC imaging of the squirrel monkey. (**i**) The arrows highlight the artifact created on T2* imaging that relates to iron deposition.

Figure. 2.3-7 Human Brain Sections and Rare and Unique Brains

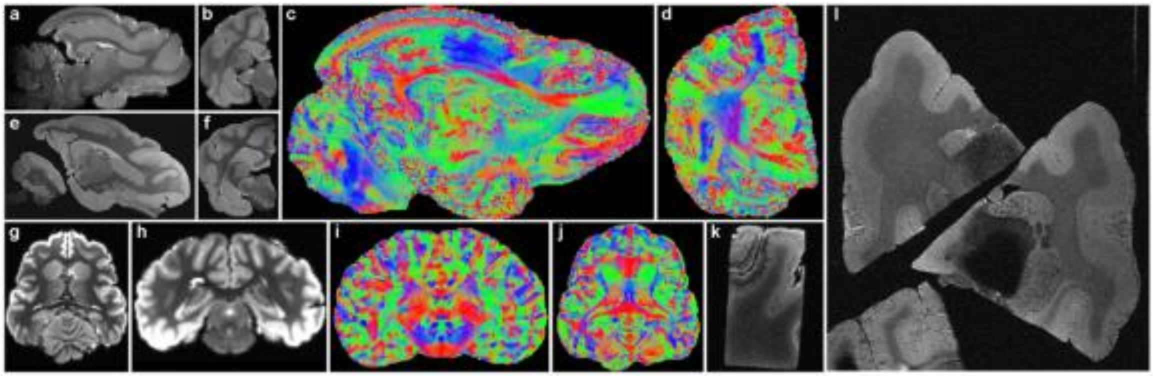

(**a-d**) Shows the sagittal and coronal b0 (DTIstandard) and primary eigenvector RGB maps of a silver fox brain. (**e-f**) Shows a sagittal and coronal image of the T2 RARE acquisition of a silver fox brain. (**g-j**) Shows a sagittal and coronal image of the sea lion brain from a diffusion weight acquisition on a Siemens 3T scanner using our embedding methods (sequence details are discussed in the methods). (**k-l**) Representative T2 RARE images of sections of human brain tissue.

Chapter 3:

A Review of the Pertinent Literature for the Relevant Neurobiology of Fear Conditioning and Extinction

3.1 Context, Author's Contribution, and Acknowledgement of Reproduction

The following chapter presents an introduction to the neurobiology of fear conditioning with a special emphasis on the circuits and brain areas that are the focus of the remaining dissertation chapters. The work presented here was conceptualized, organized, researched, and written by the dissertation author under the guidance of Dr. Ressler and many collaborators. The chapter is reproduced with from sections with minor edits from Keifer, Jr., O.P., Hurt, R.C., Marvar, P.J., Ressler, K.J.. (Under Revision for Submission). "Afferents to the Amygdala and Their Role in Fear Conditioning and Extinction." *Physiology*

3.2 Introduction

Within the domain of neuroscience there are many broad fields of study. Of these broad categories the work of this dissertation falls within both the memory and emotion field. In particular, the work focuses on Pavlovian fear conditioning and extinction which is thought to be at the intersection of memory and emotion. Pavlovian fear conditioning (Pavlov 1927, Pavlov 2003) is the process by which a neutral stimulus (conditioned stimulus – CS) is paired with an aversive stimulus (unconditioned stimulus – UCS), until the presentation of the neutral stimulus leads to threat-induced defensive reactions (a behavior that is often used as a surrogate for the conscious emotion of fear in humans (LeDoux 2014); conditioned responses – CR). Such pairing is thought to reflect the intersection of memory and emotion, providing a simple and elegant paradigm to study the interaction of the two systems and determining the underlying circuits and mechanisms of the formation of the pairing. Conversely, extinction is the process by which, after conditioning, the conditioned stimulus is presented in isolation repeatedly until it no longer results in the threat induced defensive reactions. This equally elegant and simple paradigm is important for determining how memory and emotion are uncoupled or inhibited and the processes involved. Because these methods are powerful and yet simple, and also reflect human emotional learning, they have become a ubiquitous model to study anxiety/fear related disorders in humans (e.g., post-traumatic stress disorder, phobias, social anxiety disorder) and potential treatments for these disorders (e.g., exposure therapy) (Rasmusson and Charney 1997).

The rise of the importance of this behavioral paradigm is perhaps best exhibited by **Figure 3.2-1**, which shows the number of entries on pubmed.gov (US National Library of Medicine, NIH – Bethesda, Maryland) that contain "fear conditioning". Clearly, a great deal of work has attempted to address various aspects of the mechanisms of fear conditioning and extinction. Looking into the different approaches using the fear conditioning and extinction behavior paradigms, we see that the fields follow along the sensory modality (auditory, gustatory, olfactory, tactile, and visual) of the conditioned stimulus (Maren 2001, Rodrigues, LeDoux et al. 2009) with the addition of context conditioning (Maren 2008). Further it is clear, from reviews that span across these fields (Maren 2001, Maren 2008, Rodrigues, LeDoux et al. 2009), that the current theories about the neurobiological circuits of fear conditioning and extinction all have a similar pattern and often involve common pathways (**Figure 3.2-2**, adapted from (Medina, Repa et al. 2002, Quirk and Mueller 2008, Rodrigues, LeDoux et al. 2009, Sotres-Bayon and Quirk 2010)). However, despite these similarities, there is also an extensive and long standing history, often with its own terminology, in each of these fields – auditory (LeDoux 1993), visual (Maren 2001), olfactory (Otto, Cousens et al. 2000), gustatory (Welzl, D'Adamo et al. 2001), and contextual (Maren 2008).

Because a review of all of these fields in the context of neurobiology, behavior and brain function would be massive and beyond the scope of this dissertation, the focus of the following chapter is to review a subset of this literature with an emphasis on the neural circuitry that is integral to the chapters following this one. Further, each section covering a particular neurobiological connection will also outline some of the studies that have been conducted to understand the role of the connection. The contents of this chapter will include a brief review of the role of the amygdala, followed by the four main sections covering neuroanatomical pathways between the olfactory bulb and the amygdala (olfactory fear conditioning), between the medial geniculate nucleus and the amygdala (relevant to auditory fear conditioning), between the auditory cortex and the amygdala, and between the infralimbic and prelimbic prefrontal cortices and the amygdala (relevant to conditioning and extinction behavior).

Before delving into the research studies, the following will detail the use of anatomical terminology for the sake of clarity (at least as much as possible with the diversity of neuroanatomical nomenclatures within and between species). Broad terms like amygdala and medial geniculate nucleus will be used either in cases of general discussion or when the study did not disambiguate between the nuclei. At all times there is an understanding that these areas are further subdivided into anatomically and functionally distinct nuclei, which will be made explicit when both possible and pertinent to the discussion section. Further, neuroanatomical terms are almost as diverse within species as they are across species, in order to not misrepresent results of studies, the terminologies from the original papers have been used in place of attempting to bring all terms to a common standard.

3.3. A Brief Discussion of the Amygdala

As shown in **Figure 3.2-2,** the amygdala is often placed at the center of the neurobiological circuit for any type of fear conditioning. The prominence of the amygdala in this circuit is directly related to the large number of studies that have suggest that the amygdala is the major site of plasticity for the pairing of the UCS and CS (lateral amygdala) and thus serves as the controlling output path (LA to BLA to central amygdala) for generating the conditioned response. While much of the literature establishing these pivotal roles for the amygdala are extensively reviewed elsewhere (LeDoux 1993, LeDoux 2000, Maren 2001, Medina, Repa et al. 2002, Maren 2008, Rodrigues, LeDoux et al. 2009), it is worth highlighting the results from the now classic studies as complimented by recent and relevant modern studies.

Like most fields of study, it is hard to put a birth date on the study of the amygdala. Contemporary accounts often cite the work of Kluver and Bucy (Kluver and Bucy 1937) who were placing lesions in the temporal lobes of lip smacking rhesus monkeys (the lip smacking of the monkeys resulted from their being high on peyote). After lesioning the whole temporal lobe, Kluver and Bucy documented, amongst many profound behavioral changes, that the lesioned monkeys no longer exhibited the same level of fear (e.g., to an experimenter entering the monkey area). However, it is worth emphasizing that the damage was to the entire temporal lobe, which is now known to contain many important additional brains regions. It would take nearly 20 years for follow-up work in rhesus macaque to show that the damage to the amygdala specifically resulted in the loss of behaviors that typified a fear response (Weiskrantz 1956). Advancing another two decades, the intersection of the amygdala and fear conditioning would occur when rats with lesions to their amygdala failed to show appropriate contextual conditioning

(Blanchard and Blanchard 1972). Advancing yet another two decades, the work of Ledoux would establish that the basolateral complex of the amygdala (particularly the lateral amygdala - LA) was the site of termination of auditory input from the medial geniculate and that lesions of the lateral amygdala (but not immediately surrounding nuclei) disrupted auditory fear conditioning (LeDoux, Sakaguchi et al. 1984, LeDoux, Sakaguchi et al. 1985, LeDoux, Cicchetti et al. 1990, LeDoux, Farb et al. 1990). These results suggested that projections to the BLA would generalize to visual (Campeau and Davis 1995), olfactory (Cousens and Otto 1998), and contextual (Cousens and Otto 1998) fear conditioning. Within the BLA, further evidence would suggest that the LA was the site of convergence of the UCS and CS. For example, there is electrophysiological evidence that single neurons of the LA respond to auditory and shock stimuli (Romanski, Clugnet et al. 1993) and that neurons in the LA show short-latency plasticity with auditor fear conditioning (Quirk, Repa et al. 1995). It should be noted, that in addition to the papers discussed here, there is a much broader literature that further supports the LA as a site of plasticity and CS and US pairing. Like all healthy scientific fields, however, there is some skepticism that the LA is the only site of the CS-UCS pairing (Weinberger 2011).

The lateral amygdala is of course not the only nucleus of the amygdala that figures prominently in most proposed fear conditioning circuits. The central amygdala (CeA) is often posited as the “receiving station” of the output of processing in the LA (through the BLA). The CeA is further thought to then be the distribution center of that signal to several other brains areas that would lead to the downstream threat-induced defensive behaviors. At least a few lines of work have been central (pardon the pun) to determining the role of the CeA. To establish that the central amygdala leads to the downstream conditioned response behaviors seen in fear conditioning, researchers directly stimulated the CeA and noted changes in the cardiovascular tone of the animal (Kapp, Gallagher et al. 1982). Lesioning the CeA entirely mitigated nearly all stress related behavior and blocked the acquisition/expression of fear conditioning (Hitchcock and Davis 1986, Roozendaal, Koolhaas et al. 1991). Finally, efferent targets of the central amygdala, including the lateral hypothalamus (cardiovascular regulation) and the periaqueductal grey (freezing behavior), when lesioned, results in selective loss of particular aspects of the threat-induced defensive behaviors associated with fear conditioning (LeDoux, Iwata et al. 1988).

Given that the predominance of evidence suggests that the amygdala is the point of convergence, processing, and output of the fear circuit, two questions now arise - how does sensory information reaches the amygdala? And is the amygdala regulated by other brain areas?

3.4 Olfactory Fear Conditioning – Main Olfactory Bulb to the Amygdala

The following discussion on olfactory conditioning is rather brief compared to the other sections, this reflects the overall dominance of contextual and auditory fear conditioning as paradigms used in the field, however, much insight has been gained using olfactory fear conditioning (Jones, Heldt et al. 2005, Jones, Stanek-Rattiner et al. 2007, Jones, Choi et al. 2008, Dias and Ressler 2014). Olfactory fear conditioning follows the same overall paradigm discussed above - a neutral odorant is presented and paired with a foot shock until the presentation of the odorant results in an animal displaying threat-induced defensive behaviors (as extensively reviewed by (Otto, Cousens et al. 2000)). Interestingly, unlike the CS pathways to the amygdala with auditory (discussed below), visual, and contextual fear conditioning, olfactory information does not pass through the thalamus. Instead, based on rather limited evidence on the connectivity of the olfactory bulbs, it would appear that olfactory information can reach the amygdala through a few direct or indirect paths (**Figure 3.4-1**, from (Otto, Cousens et al. 2000)). The direct path is the MOB projecting directly onto the corticomedial amygdala which then directly projects onto the BLA. There are also several indirect paths, such as the MOB projecting to the piriform cortex and then to the corticomedial amygdala, the MOB projecting to the piriform cortex which then projects to the perirhinal cortex which connects to the LA, or finally the projection from the MOB to the perirhinal cortex then to the LA (Krettek and Price 1978, Ottersen 1982, Russchen 1982, Luskin and Price 1983). There is only now emerging evidence as to which of these paths are important in fear conditioning. Lesioning studies of the amygdala have shown the expected impairment of olfactory conditioning (Cousens and Otto 1998). Further, lesioning of the perirhinal cortex leads to loss of olfactory conditioning, though notably without loss of contextual fear conditioning or the ability to perceive odor (Otto, Schottler et al. 1991, Herzog and Otto 1997, Herzog and Otto 1998).

3.5 Auditory Fear Conditioning – Medial Geniculate Nucleus (and closely adjacent suprageniculate and posterior intralaminar nucleus) to the Amygdala

Like olfactory fear conditioning, auditory fear conditioning uses an auditory cue as the initially neutral unconditioned stimulus and it is normally paired with a foot shock as the conditioning stimulus. For example, a rat is played a simple tone (one frequency) which then co-terminates with a brief electrical shock for 5 iterations, and then that animal is tested later (often 24 hours) with the presentation of the tone (which if continued to be played iteratively would lead to extinction). It is expected that upon playing the tone during the test, the animal will display threat-induced defensive reactions (most commonly used is “freezing” behavior – or the cessation of all motion except for basal survival functions, but there are also autonomic measures that can be recorded, such as heart rate and corticosterone levels (Blanchard and Blanchard 1969)). In such a model the brain must have inputs and pathways for the auditory stimulus to reach the amygdala. The example case presented in **Figure 3.2-2** covers a generalization of the input of auditory information into the amygdala. In particular, it details two paths that auditory information uses to arrive at the amygdala. The first path is the direct projection from the medial geniculate nucleus (particularly the medial portion) to the amygdala. The second is the indirect projection of auditory information from the medial geniculate nucleus (particularly the ventral portion) to the auditory cortex and then finally to the amygdala. The focus of this section will be the projections of the medial geniculate nucleus to the amygdala and its relevance for auditory fear conditioning whereas the next section will focus on the projections of the auditory cortex to the amygdala.

Because the earliest identifiable role of the medial geniculate nucleus was in the realm of auditory sensory processing, it is not surprising that tracing work has predominantly focused on projections to the auditory cortex (Rose and Woolsey 1949, Diamond and Neff 1957, Diamond, Chow et al. 1958). However, in parallel to these tracing studies, a body of work was also growing with a focus on the connections of the medial geniculate nucleus (and other members of the posterior thalamic group such as the suprageniculate and posterior intralaminar nuclei) to the amygdala. Of the notable firsts, early work would use fiber staining techniques on sections of human brains to reconstruct the path between the medial geniculate nucleus and amygdala (Hilpert 1928, Papez 1945, Marburg 1948). Further comparative and converging evidence would accumulate for a direct projection from the medial geniculate nucleus to the amygdala when degeneration techniques were applied in the opossum and cat (Ebner 1967, Graybiel 1973). Using the more accurate and precise application of horseradish peroxidase (HRP - retrograde transport), attempts would be made to determine which subdivisions of the medial geniculate nucleus projected to the many subdivisions of the amygdala in rats and cats (Carter and Fibiger 1977, Veening 1978, Ottersen and Ben-Ari 1979). Of the studies, the work of Ottersen and Ben-Ari would be the first to attempt to determine the correspondence of projections between the posterior thalamic nuclei and the amygdala, noting a particularly strong projection between the medial division of the medial geniculate nucleus (mMGN) and most of the nuclei of the amygdala. These results in the cat would be echoed by Russchen, using retrograde HRP and florescent bisbenzimide and nuclear yellow tracers (Russchen 1982). Using wheat-germ agglutinin-horseradish peroxidase (WGA-HRP), Ledoux would further add to the medial geniculate tracing literature in the rat brain by showing a connection between the mMGN and the central and lateral amygdala, the caudate-putamen, subparafasicular nucleus, and the ventromedial hypothalamus (LeDoux, Sakaguchi et al. 1984, LeDoux, Sakaguchi et al. 1985). Pushing the analysis further with anterograde and retrograde WGA-HRP tracing techniques, he would go on to show the mMGN and suprageniculate nucleus (SG) projected to the amygdala and caudate-putamen, while the posterior area surrounding the mMGN accounted for the projections to the subparafasicular thalamic nucleus and the ventromedial nucleus of the hypothalamus (LeDoux, Ruggiero et al. 1985). Further work by Ledoux would add the posterior intralaminar nucleus (PIN) into the consideration of auditory input pathway to the amygdala. He showed that in addition to the mMGN and SG, the PIN also receives input from the inferior colliculus and also projections to the lateral amygdala. He also determined that the projections to the central, medial and basomedial nuclei of the amygdala likely arose from the medial posterior complex (POM), which did not receive input from the inferior colliculus

(LeDoux, Farb et al. 1990). In a similar expansion, later work would also show that the dorsal division of the medial geniculate and the lateral posterior thalamic nucleus also send substantial projection to the lateral amygdala (Doron and Ledoux 1999). The current state of literature holds that the projections from the mMGN and PIN are the sources of direct auditory input into the amygdala for auditory fear conditioning. Hence nearly all follow-up work has focused on these connections. For example, the follow-up work has established the ultrastructure of these synapses (LeDoux, Farb et al. 1991), which are shown to contain glutamate (LeDoux and Farb 1991), and they also overlap with projections from the auditory cortex to the amygdala (LeDoux, Farb et al. 1991) .

From a functional perspective, while Ledoux and colleagues were conducting the tracing work in rats, they united the tracing work with lesioning and functional studies to determine which of the connections of the posterior thalamic group (mMGN, SG, and PIN) and the amygdala were important for auditory fear conditioning. The first question was whether the medial geniculate nucleus or the auditory cortex was primarily responsible for relaying the simple tone to the amygdala. The results of this early study suggested that lesions of the auditory cortex did not prevent the acquisition or expression of auditory fear conditioning, but that damage to the inferior colliculus and medial geniculate nucleus did cause notable disruptions (LeDoux, Sakaguchi et al. 1984). In a similar effort, he noted that in addition to projecting to the amygdala, the MGN also projected to the caudate-putamen of the striatal system. He therefore proceeded with lesioning studies aimed at determining whether that system is important for auditory fear conditioning. Again MGN-to-amygdala pathway destruction would lead to disruption of auditory fear conditioning and expression, but destruction of striatal projections did not have an effect. Further, these effects where shown to be specific to destruction of the neurons of the mMGN (and not damage to the fibers of crossing), for auditory but not visual fear conditioning (LeDoux, Iwata et al. 1986). Moreover, stimulation of the mMGN results in responses evoked in the amygdala (Clugnet, LeDoux et al. 1990), likewise neurons in the amygdala are responsive to both auditory and shock inputs (Romanski, Clugnet et al. 1993). Additionally, this pathway was shown to have LTP plasticity mediated by NMDA and AMPA receptors and the ERK/MAO kinase signaling pathway (Farb and LeDoux 1997, Apergis-Schoute, Debiec et al. 2005).

3.6 Auditory Fear Conditioning – The Auditory Cortex to the Amygdala

The first lines of evidence of that projections of the auditory cortex to the amygdala are involved in fear conditioning are anchored in early rhesus macaque work using silver impregnation/autoradiographic tracing and degeneration work. These studies would provide evidence that the super temporal gyrus, the anterior middle and inferior temporal gyri, and the temporal pole of the monkey send projections to the lateral and basal amygdala (Nauta and Whitlock 1956, Herzog and Van Hoesen 1976, Turner, Mishkin et al. 1980). These methods would be improved upon when HRP tracing approaches were used in the rhesus macaque, which showed heavy projections from the superior temporal sulcus to the lateral amygdala (Aggleton, Burton et al. 1980).These results generalize when investigations began in the rat, where a WGA-HRP study would show connections of the TE1 and TE3 (TE1 is considered primary auditory cortex for the rat), showed connections to the amygdala in a fashion similar to projection from the mMGN (LeDoux, Farb et al. 1991). These results, especially the direct projection between the primary auditory cortex and lateral amygdala, would be further confirmed and refined with the application of *Phaseolus vulgaris* leukoagglutinin (PHA-L) tracing work in the rat (Romanski and LeDoux 1993), wheat germ agglutinin-conjugated horseradish peroxidase (WGA-HRP) in the rhesus macaque (Yukie 2002), and the application of fluorescent tracers and biotinylated dextran amine in dogs (Kosmal, Malinowska et al. 1997) and gerbils (Budinger, Laszcz et al. 2008).

With regard to the functional role of the auditory cortex in auditory fear conditioning, one of the earliest studies (discussed in the MGN section) would show that lesions to the auditory cortex did not disrupt fear conditioning to a simple tone, while lesions to the medial geniculate nucleus did disrupt fear conditioning and expression (LeDoux, Sakaguchi et al. 1984). From this study, the assertion that the auditory cortex is not critically involved in auditory fear conditioning would remain for about a decade, with the exception of a report that suggested the presence of shifts in frequency specific receptive fields in the auditory cortex after auditory fear conditioning in the guinea pig (Bakin and Weinberger 1990). Right around this time, another study lesioning the auditory cortex and the perirhinal cortex would again show that this manipulation did not affect auditory fear conditioning (Romanski and LeDoux 1992).

The discordance between lesion studies of the auditory cortex which showed no effect on auditory fear conditioning and the study showing the auditory cortex shifts receptive fields with fear conditioning would become clear with another study by the Ledoux group. Using a double-dissociation lesioning strategy, the results of the study showed that the pathway from the auditory cortex to the amygdala could be used for the acquisition of fear conditioning in the absence of the path from the mMGN to the amygdala (Romanski and LeDoux 1992). In other words, auditory information from the mMGN-to -amygdala projection or from the mMGN-to-auditory cortex-to-amygdala projection can be used for the acquisition of auditory fear conditioning. These results are not discordant with previous results, because the previous study eliminated much of the medial geniculate nucleus (hence both paths were knocked out), whereas elimination of the auditory cortex still left the direct mMGN to amygdala pathway intact. This would lead to the growth of a body of studies attempting to understand the role of the auditory cortex in auditory fear conditioning, and also a debate about which pathway was of primary importance (Boatman and Kim 2006).

Evidence from these studies has provided some interesting details regarding input to the amygdala from the auditory cortex. Not surprisingly, given the indirect path from the auditory cortex, the arrival of the information, as measured electrophysiologically, into the amygdala from auditory cortex comes after the direct input from the auditory thalamus (Li, Stutzmann et al. 1996). Additionally, both the input from the auditory cortex and auditory thalamus allow for generalization (responding to tones with frequencies near that of the trained tone) in a fear conditioning paradigms (Armony, Servan-Schreiber et al. 1997). Further, the auditory cortex appears to have neurons that are resistant to extinction – suggesting a role for the auditory cortex in the memory of auditory fear conditioning (Quirk, Armony et al. 1997). The projection from the auditory cortex are glutamatergic and are complimented by NMDA and AMPA receptors within the lateral amygdala (Farb and Ledoux 1999). These findings supported a later study that confirmed the formation of LTP in the auditory cortex to amygdala projection with auditory fear conditioning (Tsvetkov, Carlezon et al. 2002). Looking at even a finer resolution, very recent work has suggested that the auditory cortex contains disinhibitory microcircuits that are important for auditory fear conditioning (Letzkus, Wolff et al. 2011). At the dendritic level, the auditory cortex has also shown shifts in spine formation, elimination and persistence with fear conditioning (Moczulska, Tinter-Thiede et al. 2013). Finally, a new and growing literature is suggesting a more prominent role for the auditory cortex in processing auditory cues that are more complicated than simple tones (Peter, Scheuch et al. 2012). Clearly, the auditory cortex is involved in fear conditioning, though despite all these studies, its precise role remains unclear, especially when considering that there is the more direct (and seemingly just as capable) projection from the medial geniculate nucleus and the amygdala.

3.7 Fear Expression and Extinction – The Infralimbic and Prelimbic Cortex Pathway to the Amygdala

For the following discussion, the term medial prefrontal cortex (mPFC) will be used to refer to the infralimbic (IL), prelimbic (PL), and anterior cingulate cortices (ACC). Because the focus in this section is on the evidence and potential function of the connectivity of from the infralimbic (IL) and prelimbic (PL) cortices to the amygdala, where possible from the results of reviewed study, IL or PL will be stated explicitly. Some of the earliest work to examine the projections of the IL and Pl were done by Ottersen, who used HRP to show, for the rat, that both the IL and the PL projected to the lateral and central amygdala (Ottersen 1982). In the same year, these projections would also be shown in the cat using HRP (Russchen 1982). While these initial results were in agreement, further work in the cat would suggest that the IL distributes projections only to the medial and central amygdala, while the PL distributes its projections to the basolateral, basomedial, and central nuclei (Room, Russchen et al. 1985). Such differences in projections between the IL and PL would appear in the rat literature as well, with a WGA-HRP and fluorescent tracers study showing that the IL connects to the anterior amygdaloid area, whereas the PL sent projections to the basolateral amygdala (Cassell and Wright 1986). Increasing focus on the IL, work with PHA-L and WGA-HRP showed the rat IL had a prominent ventral projection to the central, medial, basomedial nuclei, and the periamygdaloid cortex (Hurley, Herbert et al. 1991). Though, interestingly, in the same year another study also using PHA-L would suggest that the IL projected to the whole of the amygdaloid complex with a particularly prominent branch to the central amygdala (Takagishi and Chiba 1991).

As is growing apparent, the connectivity of the IL and PL remains contentious at this point, leading to further tracing studies with more tracing techniques and more species. The projections of the IL and PL in the rabbit appeared to follow previous results with both the PL having projections to basolateral, basomedial, and lateral amygdala and the IL having projections to the central amygdala (Buchanan, Thompson et al. 1994). In a study focused exclusively on the connectivity of the rat IL and PL with the amygdala, it was reported that the IL connects to the central, corticomedial, lateral, accessory basal nuclei of the amygdala, and the anterior amygdaloid area. In contrast, the PL was reported to project to the basal, lateral, and central nuclei of the amygdala (McDonald, Mascagni et al. 1996). In a strange reverse of the normal sequence of species used for tracing experiments, the first monkey study would show that both the IL and PL projected strongly to the magnocellular accessory basal nuclei of the amygdala, and moderately-to-weakly to the lateral basal and lateral amygdala (Chiba, Kayahara et al. 2001). Clearly, there was still considerable disagreement on where the IL and PL precisely projected both within and between species. In a readdress, Vertes (2004) would provide the most comprehensive analysis of the similarities and differences of IL and PL connectivity. In particular, for the IL, projections included the medial, basomedial, central and cortical nuclei of the amygdala, whereas the PL was noted to connect to the capsular part of the central nucleus and the basolateral nucleus (Vertes 2004). In most respects, it appears that the Vertes work is now the gold standard for the connectivity of the IL and PL. The most recent notable addition is the projection of the IL to the very small intercalated region of the amygdala (Pinard, Mascagni et al. 2012).

It is certainly clear from the preceding reports that the IL and PL project to the amygdala with different patterns. What is less clear (at least with respect to the more obvious role for sensory input into the amygdala), is the role of these connection in conditioning or extinction. Further it is also unclear if there are species differences that are coming into play with regards to determining the patterns of connectivity. As the roles of the IL and PL in fear extinction and expression have been reviewed extensively by Sotres-Bayon and Quirk (2010), the following will provide a brief summary of their conclusions (**Figure 3.7-1**, from (Sotres-Bayon and Quirk 2010)).

The current overall thinking on the role of infralimbic cortex is that it is involved in the process of extinction, particularly the retention of extinction learning (Quirk and Mueller 2008). However, much like the tracing literature of the PL and IL, the studies of the role of the IL are somewhat conflicting, though a convergence of evidence is occurring. The origin of the IL (and PL) literature starts broadly with studies of the role of the frontal cortex. Early monkey studies showed that when the frontal cortex was damaged there was a tendency for the monkeys to develop response perseveration (that is an inability to inhibit inappropriate responses) during experimental tasks (Sotres-Bayon, Cain et al. 2006). Tapering to a more focused task and area of the brain, lesioning of the ventromedial prefrontal cortex (vmPFC) in the rat would result in a failure of the animal to extinguish to the CS appropriately (the animal's freezing behavior did not decrease as drastically as controls when repeatedly presented the CS-tone in the absence of the UCS-shock). However, there was a failure to demonstrate the effect by another group who lesioned the mPFC and looked at fear-potentiated startle and freezing measures for both visual and auditory CS paradigms (Gewirtz, Falls et al. 1997). These conflicting reports would continue with reports suggesting that vmPFC lesions lead to no differences in any aspects of extinction (Garcia, Chang et al. 2006), or that the while the area may be involved it was certainly not critical (Farinelli, Deschaux et al. 2006).

How can these discrepancies be explained? Looking to studies that showed an effect, it becomes clear that animals with a lesion to the vmPFC would actually extinguish normally after training (within a session, animals would decrease their freezing to the CS), but if required to undergo another round of extinction training the next day, it would appear as if they did not retain the previous extinction memory (i.e., their freezing levels during the second round of extinction training returned to the initial levels of fear seen during the first round of extinction) like the controls (Lebron, Milad et al. 2004). Further, it also became clear that the time of the lesioning mattered. If the lesion was made prior to fear conditioning then the extinction deficit was more pronounced, whereas one made after fear conditioning only had subtle effects (Morgan, Schulkin et al. 2003). Perhaps most importantly, it was also suggested that lesions that spare the IL of the vmPFC would result in normal extinction behavior. The later finding would lead the field to explore the potential that the IL was the source of the extinction deficits. The use of pharmacological agents (e.g., tetanus toxin, NMDA antagonists, PKA inhibitors, MAPk inhibitors, and protein synthesis blockers) in the IL would all show that while extinction on day 1 would proceed normally, on day 2 the animals had impaired retention of extinction – the animals acted as if they had never received any extinction training (Santini, Muller et al. 2001, Hugues, Deschaux et al. 2004, Santini, Ge et al. 2004, Burgos-Robles, Vidal-Gonzalez et al. 2007). These data have also been complemented by electrophysiological studies suggesting an important role for the IL in the retention of extinction (Herry and Garcia 2002, Milad and Quirk 2002, Burgos-Robles, Vidal-Gonzalez et al. 2007).

Interestingly, the much smaller body of research focused on the PL has suggested that it plays a complementary role in facilitating fear (Sotres-Bayon and Quirk 2010).

Using microstimulation in both the IL and the PL, it was shown that PL stimulation increased the expression of conditioned fear and the IL reduced the expression of conditioned fear (Vidal-Gonzalez, Vidal-Gonzalez et al. 2006). In turn, when the PL was inactivated, conditioned animals showed overall reduced fear behavior across extinction trials (Laurent and Westbrook 2009). Like the IL, the PL has had its role confirmed using electrophysiological measures in response to the conditioned stimulus (Knapska and Maren 2009), which are notable in that they are often sustained over several seconds during the presentation of the conditioned stimulus (Burgos-Robles, Vidal-Gonzalez et al. 2009) and the magnitude of these measures are responsive to pharmacological interventions that lead to reductions in the expression of threat-induced defensive behaviors (Rodriguez-Romaguera, Sotres-Bayon et al. 2009, Lemos, Resstel et al. 2010). The combination of findings of relatively specific, but opposing, roles of the IL and PL in fear expression and extinction help clarify why lesions of the entire vmPFC initially were inconsistent and controversial, but more localized lesions and molecular / physiological manipulations of IL or PL alone have produced much more consistent results.

3.8 Discussion

There are several points of interest that span the discussion of all four sensory paths and their potential function in fear conditioning and extinction. The first notable point is that tracing data – whether in the earliest forms with degeneration studies or the more recent use of microinjected fluorescent tracers – have notable limitations in their accuracy and precision. Ensuring that the tracer is injected both accurately (covering the size of the area of interest and no other areas) and precisely (placed in the same accurate way across animals) is highly improbable, which accounts for the often discrepant results across studies. The second notable point is that many of these studies are conducted in only a few species of experimental animals (earlier and less plentiful work often used monkeys, cats, and rabbits, with the majority of studies in rats). It has been argued, not unreasonably, that this fear circuit and its function is general and fundamental to brains across species (including humans which are purportedly modeled by these animals), yet it is important, when and where possible, to ensure that these results are confirmed across species (especially in the nearly ubiquitous mouse and, where possible, humans). Third, while studies are certainly elucidating roles for these pathways and the respective brain areas; it is interesting to note that a systems level understanding has yet to emerge from all the pieces (e.g., consider that it is still not understood why there are two paths of auditory information into the amygdala - the brain, and biological systems, are not well known for unutilized redundancy). The later point is concerning considering that current efforts in science are geared towards analyzing a theory at incrementally smaller levels of detail even in the absence of understanding higher or large-scale levels of analysis (this is exemplified here in the discussion of progress in research for each of the circuit pieces). Fourth and finally, though nearly every paper and review of fear conditioning reports that the fear circuits and the function of each area is well understood, there is still much work to be done and many hypothetical assumptions of the circuit that must be researched.

The work presented in the following dissertation attempts to address these points. First, through the use of MRI based diffusion weighted imaging with probabilistic tractography, we show that the method is both a precise and accurate way to looking at tractography. Second, by conducing out work in mice, the work helps to generalize the proposed fear circuit and fills in needed gaps in the anatomical literature. Third, through asking scientific questions at a systems level, the hope is to start integrating the results in a holistic manner to understand the dynamics of the fear circuit. Finally, by continuing work that is focused on elucidating the fear circuit, the hope is to continue to increasing the current understanding of the fear system.

Figure. 3.2-1 Pubmed Count, by year, of "Fear Conditioning" Literature

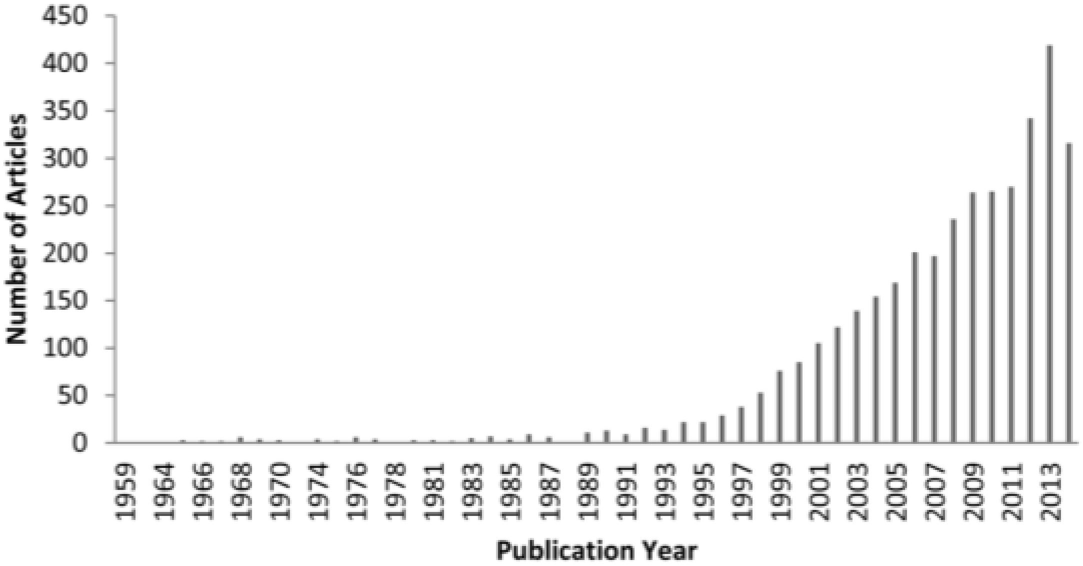

The graph shows the tremendous surge in interesting in fear conditioning over the last two decades. This drastic increase is directly related to the simplicity, utility, and translational capacity of fear conditioning as a model of emotional memory and the pathophysiology therein.

Figure. 3.2-2 Neurobiological Circuit of Fear Conditioning and Extinction.

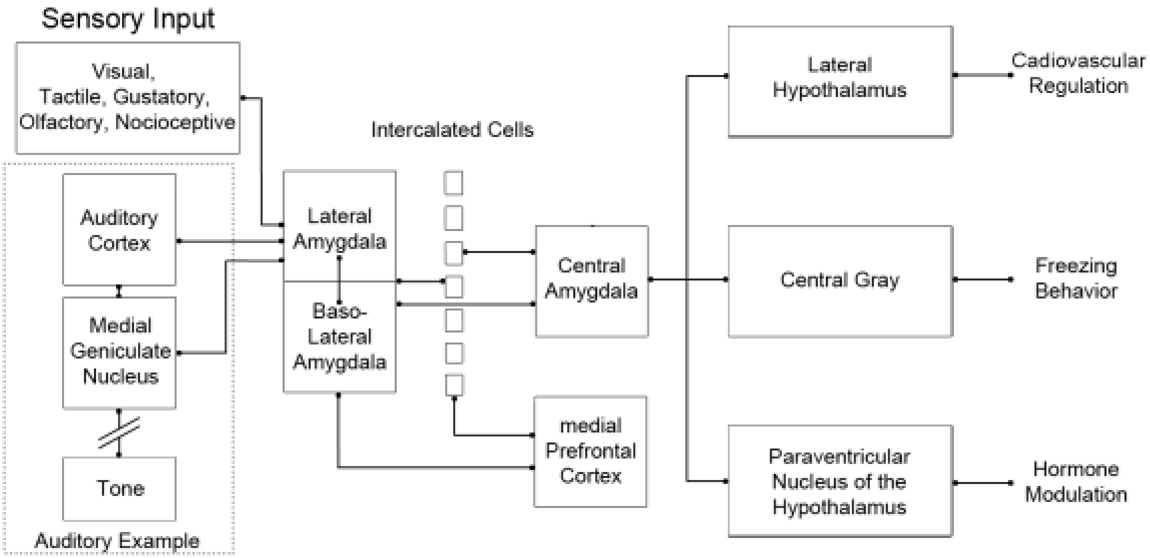

The figure presents an integrated hypothetical circuit (adapted from (Medina, Repa et al. 2002, Quirk and Mueller 2008, Rodrigues, LeDoux et al. 2009, Sotres-Bayon and Quirk 2010), that accounts for the neurobiological substrates that are thought to mediate fear conditioning and extinction. The low of information follows a left to right pattern, though the diagram is draw without direction as many of these connections are reciprocal.

Figure. 3.4-1 Neurobiological Circuit of Olfactory Fear Conditioning

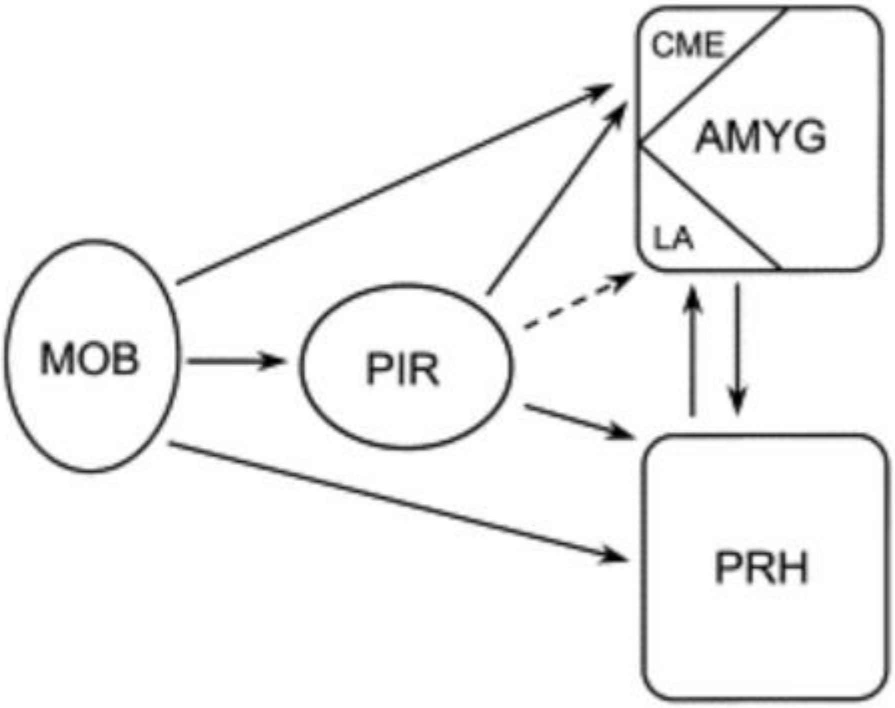

The figure presented above is from (Otto, Cousens et al. 2000), who proposed the olfactory fear conditioning circuit based on the confluence of evidence from lesion and tracing studies. MOB – main olfactory bulb, PIR – piriform cortex, AMY – amygdala, LA – lateral amygdala, PRH - perirhinal cortex, CME – corticomedial amygdala.

Figure. 3.7-1 Neurobiological IL/PL Circuit of Fear Conditioning and Extinction

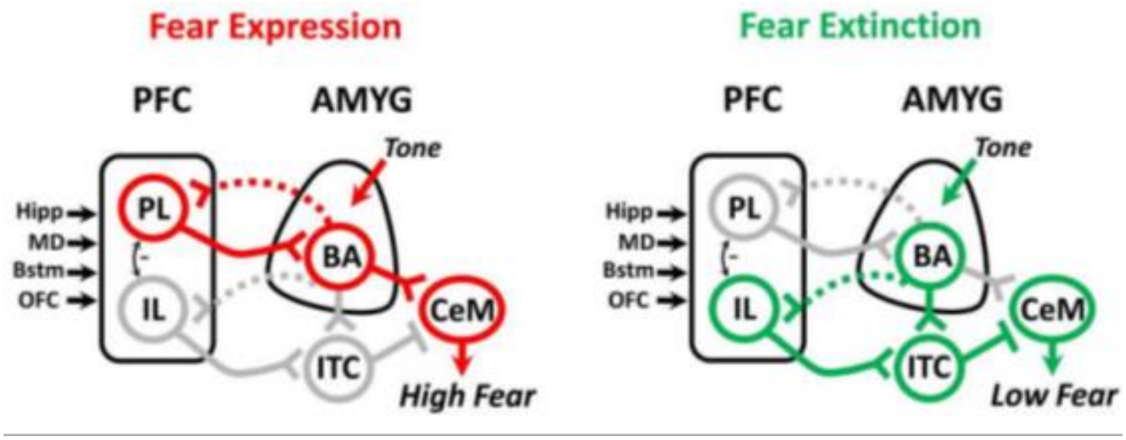

The figure presented above is from (Sotres-Bayon and Quirk 2010), who proposed the PL-IL fear conditioning and extinction circuit based on the confluence of evidence from lesion, tracing, and electrophysiological studies. PL – prelimbic cortex, IL – infralimbic cortex, BA – basolateral amygdala, ITC – intercalated cells, CeM – Central Amygdala.

Chapter 4:

Mapping the Mouse Olfactory System with Manganese-Enhanced Magnetic Resonance Imaging and Diffusion Tensor Imaging

4.1 Context, Author's Contribution, and Acknowledgement of Reproduction

The following chapter presents the first application of *ex vivo* DWI probabilistic tractography to the mouse brain. The context of the study was an effort to better understand the connections of the olfactory bulb, especially with the amygdala. The results of the probabilistic tractography were compared to a parallel study using *in vivo* manganese enhanced magnetic resonance imaging (MEMRI). Both the DWI probabilistic tractography and MEMRI tracing technique are discussed in the introduction. The dissertation author contributed to the paper by preparing the *ex vivo* brains, imaging those brains with the DWI scan, pre-processing that data, and contributing to the writing of the paper. The chapter is reproduced with minor edits from Gutman, D.A., Magnuson, M., Majeed, W., Keifer Jr, O.P., Davis, M., Ressler, K.J., and Keilholz, S.D. (2013) Mapping of the Mouse Olfactory System with Manganese-Enhanced Magnetic Resonance Imaging and Diffusion Tensor Imaging.
Brain Structure and Function. 218 (2), 527-537

4.2 Introduction

As the power of mouse genetics and behavior push the limits of neuroscience, neuroimaging approaches which can optimally and efficiently utilize these same mouse models are critically needed to determine the strength and pattern of connectivity of different brain systems. The application and development of anterograde and retrograde tracing techniques have been instrumental in understanding structural connectivity of the brain (Raju and Smith 2006, Callaway 2008, Ugolini 2010). However, classical histological techniques, while both feasible and a gold standard, present a number of difficulties. In particular, such tracing can take weeks to produce results, are limited by animal and surgical resources, allow for tracing from only one or at most a few areas in any individual animal (depending on the number of different tracers used), require sacrificing the animal, and, especially in the case of the mouse, require highly accurate injections into brain areas that are relatively minute and closely spaced (leading to mice with “missed” or diffuse injections). Subsequently, in a partial redress of these limitations, a number of MRI based techniques have been developed to allow computation of anatomic/structural connections between regions of the brain. Among these are methodologies based on diffusion-tensor imaging (DTI), which rely on the diffusion of water along the lengths of axons in the brain, as well as techniques that use exogenous contrast agents (such as manganese enhanced MRI,MEMRI) that are preferentially taken up by neurons in proximity to where the contrast agent is applied. However, these tools have yet to be sufficiently validated within the mouse brain.

DTI has been extensively used in both human (Wedeen, Wang et al. 2008, Gutman, Holtzheimer et al. 2009, Douaud, Jbabdi et al. 2011) and nonhuman primate studies (Rilling, Glasser et al. 2008, Wedeen, Wang et al. 2008, Li, Preuss et al. 2010) to compare and contrast the structural connectivity of brain regions. Additional studies, particularly in the porcine brain, have directly compared the results of diffusion tensor tractography to the gold standard tracer-injection studies and have generally shown a high concordance between the histologically defined pathways and those defined based on MRI tractography results (Dyrby, Sogaard et al. 2007, Dyrby, Baare et al. 2011). However, at this juncture the use of DTI in mice is limited, and validation of the technique is still underway. For example, Moldrich and colleagues have recently published an analysis using different DTI processing algorithms to assess general patterns of direct thalamocortical connections (Moldrich, Pannek et al. 2010).

A complementary technique, manganese-enhanced MRI (MEMRI), has been the subject of increasing interest among the MRI community during the last few years because of the unique dual function of manganese (Mn^{2+}) as a powerful T1 shortening agent and a biological calcium analogue (Koretsky and Silva 2004). Manganese is taken up by depolarized neurons through voltage-gated calcium channels and transported by a microtubule transport system through axons to the synaptic cleft, where it is released along with neurotransmitters and taken up post-synaptically. Therefore, manganese acts as an anterograde tracer that can map an entire neuronal pathway by traveling trans-synaptically (Pautler, Silva et al. 1998). By using manganese, contrast can be observed in T1 weighted images as a result of activity dependent uptake and transport of Mn^{2+} (Lin 1997). These properties have made MEMRI a valuable tool for *in vivo* neuronal activity dependent tract tracing (Pautler 2004).

Pautler and colleagues were first able to detect enhancement in the olfactory tract after injecting $MnCl_2$ into the naris of mice (Pautler, Silva et al. 1998). A similar study demonstrated enhancement of the optical tract after manganese was injected into the vitreous body of the eye of a rat (Watanabe, Michaelis et al. 2001). These two neural tracts have been the focus of several MEMRI studies (Lin, Tseng et al. 2001, Cross, Minoshima et al. 2004, Takashi Watanabe 2004, Marte Thuen 2005, Thuen, Singstad et al. 2005, Øystein, Marte et al. 2008, Chuang and Koretsky 2009). Other studies have also demonstrated tract-tracing after intracerebral injection (Saleem, Pauls et al. 2002, Van der Linden, Verhoye et al. 2002, Leergaard, Bjaalie et al. 2003, Robia G. Pautler 2003, Takashi Watanabe 2004, Dyrby, Sogaard et al. 2007, Canals, Beyerlein et al. 2008). However, intracerebral approaches are limited in ways analogous to the classical tracing studies including manganese diffusion outside of the injection site.

While the results of aforementioned studies are promising, most of the published work is not in mice. Additionally, DTI has not been assessed in mice for complex and long tracts in the mouse brain. Furthermore, there has been little work focusing on whether MEMRI and DTI provide corroborating evidence for complex anatomical pathways in the mouse (the closest work is in rats (Lin, Tseng et al. 2001, Lin, Wedeen et al. 2003, Thuen, Singstad et al. 2005). Because the mouse model is the standard mammalian tool for genetic manipulation, there is the potential for the combination of these methods with genetically targeted approaches as well as following behavioral and developmental manipulations. Therefore, it is imperative that these techniques be validated in a known neural pathway in the mouse brain, which will then allow future studies combining genetic manipulation with neuroimaging approaches for quantitatively and qualitatively comparing connectivity patterns and strength.

Specifically, further understanding the pathways involved in olfactory coding and connectivity in the mouse are particularly important and exciting given the enormous increase in understanding of the molecular mechanisms underlying olfactory processing in recent years (Buck and Axel 1991, Ngai, Chess et al. 1993, Ressler, Sullivan et al. 1993, Dulac and Axel 1995). The discovery of the odorant receptor family of genes has led to breakthroughs in understanding the connectivity between neurons in the nose with the olfactory bulb as well as other olfactory areas (Ressler, Sullivan et al. 1994, Vassar, Chao et al. 1994, Mombaerts, Wang et al. 1996). A much more detailed understanding of the specific mapping of olfactory information (Sosulski, Bloom et al. 2011), as well as changes that occur with olfactory learning (Jones, Choi et al. 2008), are on the horizon; however progress has been hampered by limited neuroimaging methodology in the mouse.

The aims of this study were to further validate and also directly compare the MEMRI and DTI approaches within the olfactory system of the mouse. The olfactory tract of the mouse was selected for analysis due to its ease of access through the naris (MEMRI), the more complicated geometry and known pattern of functional connections (relative to the aforementioned optic pathway and thalamocortical pathways), as well as for the burgeoning progress in the molecular organization of this system. For MEMRI, manganese was administered to the nasal epithelium and the corresponding enhancement patterns were compared to DTI tracts calculated using a probabilistic tractography algorithm in the FSL analysis suite (Oxford, www.fmrib.ox.ac.uk/fsl). In order to efficiently utilize MRI scanner time, DTI data were acquired using a high throughput *ex vivo* method (scanning 6 perfused mouse brains) to maximize the spatial resolution and minimize partial volume effects. The results indicate that manganese delivered via the nasal epithelium enhances a large subset of the olfactory network (of known anatomical connections) that was also detected using DTI probabilistic tractography, indicating that MEMRI and DTI have complimentary capabilities for the delineation of known complex white matter pathways. Our data demonstrate the feasibility of probabilistic tractography and MEMRI in small animal imaging, which establishes a foundation for exploring novel networks within the brain with the combined power of mouse genetics tools.

4.3 Methods

4.3.1 *Animal Preparation and Imaging*

All animals used in this study were treated humanely following a procedure approved by the Institutional Animal Care and Use Committee at Emory University. A total of 6 adult CFW (Carworth Farms White) Swiss Webster mice were used in the experiments for MEMRI and 10 C57BL6 (Jackson Labs) for the DTI probabilistic tractography.

Group 1 (MEMRI): All imaging experiments were performed on a Bruker 9.4T horizontal scanner using a 35 mm volume coil (Bruker, Billerica, MA). The 6 mice in Group 1 were imaged before (baseline control) and 42 hours after Mn^{2+} administration (experimental group) using the following protocol. $MnCl_2$ pellets were weighed and then dissolved into saline via a vortex mixer. Each mouse was anesthetized with 5% isoflurane initially and maintained on 1.5% isoflurane (30% oxygen) during the imaging procedures. The mice were restrained in a plastic cradle (Bruker, Billerica, MA) with ear and bite bars. Care was taken to align each mouse into the cradle and scanner in a consistent manner. 3D T1 weighted images were obtained using a 3D FLASH sequence with the following parameters: Flip angle = 30 degrees, field of view = $1.92 \times 1.92 \times 1.92$ cm^3, acquisition matrix size = $96 \times 96 \times 96$, reconstruction matrix size = $128 \times 128 \times 128$, TR = 70 ms, TE = 4 ms, NEX = 2, imaging time = 21 minutes.

After the pre-contrast image was obtained, the mice were anesthetized with 5% isoflurane, laid in a supine position, and injected with 5 µl of 1M MnCl2 solution into each nostril using a 50 µl Hamilton syringe inserted at a depth of ~3 mm into the nostril. The MnCl2 mixture was administered in 1-2 µl portions to ensure that it did not overflow from the nostril. After manganese injection the animals were placed back into the anesthesia chamber under 2% isoflurane for an additional 5 minutes, allowing the manganese to be absorbed (when the mice wake up immediately after injection they typically sneeze, expelling the manganese solution). The animals were then returned to their home cage and the post-contrast image was acquired approximately 42 hours after Mn^{2+} exposure. Following recovery, the animals appeared healthy with no obvious indication of Mn^{2+} toxicity.

The 42 hour delay was determined empirically based on preliminary studies by our group, as well as by data presented in (Pautler, Silva et al. 1998). We imaged several mice repeatedly at time points ranging from 24 to 48 hours, and found that the 42 hour time mark provided a nice compromise between extent of enhancement (e.g., the Mn^{2+} traveling further over time) and signal washout (loss of Mn^{2+} over time). The goal of our optimization was to image the greatest extent of the olfactory pathway that we could.

Group 2 (DTI): The mice were euthanized using pentobarbital, and brains were perfused with 4% paraformaldehyde, the brains were extracted from the skull and were rinsed in PBS and then stored at 4˚C until embedding in an agarose matrix. Two sets, one of four and another of six mouse brains were embedded in a matrix of 2% agarose (Sigma) doped with an insoluble mixture of 1 mM gadolinium (III) oxide (Fisher Scientific), all contained within a plastic 25 mL tube. Doping with gadolinium (III) oxide serves to suppress the signal (shortens the T1 relaxation time) from the agarose/water solution, providing better separation of the brains from the background.

For each tube of brains, T2-weighted images were first acquired at 100 micron isotropic resolution (TE = 26ms, matrix 256 x 512, 20 averages, scan time ~ 16 hours). Diffusion-weighted images were then acquired using a 2-D spin-echo based sequence with 161 micron isotropic resolution (TE = 26.9 ms, TR=10000 ms, matrix size of 256 x 128, 60 axial slices collected/tube, 60 gradient directions with a diffusion weighting b=2000, and 3 b=0 images). We used the Massachusetts General Hospital (MGH) 60 direction DTI gradient sequence, and obtained the BVECS from the built-in gradient tables in trackvis.org (Wedeen et al. 2008). The ability to image multiple brains in a single session is the crucial feature that makes this experiment practical. Because the readout direction of the MRI scanner can be increased with no increase in imaging time, brains can be aligned along this direction, allowing 6 brains to be acquired in the same length of time as 2 brains (60 hours in the present study).

4.3.2 Image Processing

MEMRI: One control image was chosen to serve as the standard space for registration. All of the other images were registered to the standard image using automated intensity-based registration, aimed at finding the optimal 9-parameter affine transformation. Normalized cross correlation was used as the objective function.

The standard image was cropped and all the images were normalized to the cropped standard image using the method described by Venot and colleagues (Venot, Lebruchec et al. 1983). Individual images were scaled to maximize the number of zero crossings in the image obtained by subtracting the scaled image from a reference image (without any enhancement). This method assumes that most of the brain is not enhanced, which is expected to be true for the methods/parameters we used. This method has been used previously by Cross et al (Cross, Minoshima et al. 2004) in Mn^{2+} enhanced images.

Two tailed, unpaired t-tests were performed between control and contrast-enhanced images on a voxel by voxel basis. Percentage enhancement (PE) relative to the control group was calculated for each significantly enhanced voxel ($p < 0.01$). The enhanced voxels were clustered based upon their connectivity with the olfactory bulb, and the enhancement maps were overlaid on the average image of all the control images.

DTI: Prior to further processing, the diffusion images from each scan (with one image containing multiple brains) were manually segmented into individual files. For both the T2 weighted scan and the DTI-scans, the brains were isolated from the background using the Brain Extraction Toolkit (BET) (FSL, www.fmrib.ox.ac.uk/fsl). A study-specific high-resolution mouse template was generated by nonlinearly registering each mouse brain to a single reference image, and then creating a composite image (FNIRT, www.fmrib.ox.ac.uk/fsl). A transformation matrix for each mouse DTI dataset to this mouse-standard space was subsequently generated (FLIRT, www.fmrib.ox.ac.uk/fsl) using a 12-DOF affine warp. A conservative olfactory bulb (OB) ROI was defined, with anatomical landmarks from the Allen Mouse Brain atlas (http://mouse.brain-map.org/), on this reference image and tractography results were generated for each individual mouse brain (i.e., the ROI was placed in the anterior section of the OB, and did not span the entire cross-section or depth of the olfactory bulb).

The DTI probabilistic tractography was performed using the FSL imaging suite on a Linux workstation. As part of the standard FSL pipeline, the standard OB ROI is projected onto each individual mouse's DTI scan, tractography is computed for each voxel within the seed mask (using n=25000 streamline fibers/voxel and curvature threshold of 0.2) and then back-transformed into the mouse-standard space. For all tractography, a multi-fiber reconstruction algorithm was implemented in the FSL bedpostx algorithm, which allows reconstruction of more geometrically complex pathways, including regions of crossing fibers (Behrens et al. 2007).

Following tractography, each individual's raw tract map was subsequently smoothed (s=0.167 mm gaussian kernel), thresholded at 1% of the robust mean intensity value, and finally binarized. A composite image was then generated by combining the results from each binarized individual tract map. The value of the composite map at a given voxel corresponds to the number of individual mice with a probabilistic tract passing through that voxel (i.e., the ratio of mice with a tract through that voxel to the total number of mice).

Registration and Comparison of *in vivo* and ex vivo templates: To allow direct comparison of the MEMRI and tractography results, a 12 DOF affine registration was generated between the reference brains used for the MEMRI and DTI probabilistic tractography. The results from the MEMRI experiments were subsequently registered to the reference image used for the tractography results using nearest-neighbor interpolation.

In order to quantify the overlap of the MEMRI and DTI probabilistic tractography results, a percentage overlap method was selected. The calculations were made for increasing statistical thresholds of the MEMRI analysis ($p<0.05$, $p<0.01$, $p<0.005$, $p<0.001$, $p<0.0001$) and increasing concordance of DTI tractography across subjects (from 6 of 10 to 10 of 10 animals showing a particular tract through a voxel).

The DTI Tractography was used as the reference image with the percentage of MEMRI voxels matching those contained in the DTI tractography. Unilateral seeding of the DTI tractography vs. a bilateral intranares manganese injection for the MEMRI allowed for both an ipsilateral and contralateral comparison.

4.4 Results

4.4.1 MEMRI Results

T_1-weighted images were obtained from all mice pre- and post-manganese injection. The post-contrast images exhibited a strong increase in signal in the olfactory bulb along with enhancement throughout the olfactory tract. All images were registered to the standard image (normalized correlation coefficient > 0.75). **Figure 4.4-1** shows representative slices from the average pre- and post-contrast images obtained after registration.

Maps of voxels in the post-contrast images with statistically significant enhancement compared to pre-contrast images were created and are shown in **Figure 4.4-2**, thresholded at a p-value of 0.01. Maximum enhancement was observed in the olfactory bulb, with a gradual decrease in the intensity of enhancement in the rostral-caudal direction. Statistically significant enhancements, based on comparison to the Allen Brain Atlas, were observed in olfactory bulb (OB), anterior olfactory nucleus (AON), piriform cortex (Pir), olfactory tubercle (OT), anterior commissure (AC), nucleus accumbens (Acc) and basolateral amygdala (BLA). Enhancement was more intense in the outer layers of the OB, as compared with the inner part, comprising axons. The average percentage enhancement for these anatomical regions was also measured and is shown in **Figure 4.4-3**.

In order to estimate the sensitivity of the MEMRI analysis, the minimum percentage difference was measured in brain areas where significant enhancement was observed. For a threshold of $p < 0.05$, the minimal detectable percent enhancement was 4.1%; for $p < 0.01$, it was 5.0%.

4.4.2 Probabilistic Tractography

High-resolution T2 and DTI scans were obtained *ex vivo* on all mouse brains. A composite image showing voxels that were found to have a consistent connection in at least 7 of the 10 mice included in this study is shown in **Figure 4.4-4** (The placement of the seed (in red) and resulting fiber tracts (in blue) are shown below in **Figure 4.4-5g**). Regions shown to be consistently connected to the olfactory bulb seed included the AON, anterior commissure, nucleus accumbens, and BLA, and a projection to the entorhinal cortex.

4.4.3 Overlap of DTI and MEMRI

Figure 4.4-5 provides a direct comparison between MEMRI and DTI-based tractography. The results for the two techniques were largely consistent and included areas with known anatomical connections to the olfactory bulb such as the anterior olfactory nucleus, piriform cortex, amygdala, and entorhinal cortex. The most notable differences between the two were that the DTI-tractography also showed a connection through the olfactory limb of the anterior commissure; and the connection to the entorhinal cortex, which is quite caudal from the injection site.

As expected, the percentage of MEMRI overlap with DTI varied considerably depending on the statistical threshold of MEMRI and the between subjects concordance of DTI (presented in supplementary table 1). However, use of a high statistical threshold in MEMRI (e.g., $P<0.00001$) and a lower DTI concordance threshold (6 of 10 mice matching), resulted in an overlap percentage of approximately 75%.

4.5 Discussion

This work has demonstrated reproducible and consistent connectivity of the mouse olfactory bulb using two techniques, DTI probabilistic tractography and MEMRI. MEMRI and DTI probabilistic tractography provide complementary information about the network organization of the mouse brain. In MEMRI, contrast is based on both structural integrity and functional synaptic transmission, with the transfer of manganese across synapses dependent upon the existence of activity of the neurons. It is an anterograde tracer, so that enhancement indicates the directionality as well as the functional integrity of the pathway. However, nonspecific enhancement can also occur, either from manganese that is taken up into the blood via the nasal epithelium (Chuang and Koretsky 2009), or via localized diffusion near synapses. In contrast, DTI probabilistic tractography is sensitive only to the diffusion of water based on the structural properties of white matter, so that tracts can be delineated regardless of their directionality or the level of activity.

One of the primary challenges of DTI tractography is following tracts through a complex pathway. It is often difficult to resolve crossing fibers, although recent advances in crossing fiber algorithms (Behrens, Berg et al. 2007) have somewhat ameliorated this problem. In addition, issues related to partial volume effects, selection of thresholds for the tractography results, scan quality, and distance from the seed for a given region, can also significantly influence the results (Moldrich, Pannek et al. 2010). Despite these limitations, the results from both MEMRI and DTI-based probabilistic tractography are largely consistent with expected neuroanatomical connectivity. Using classic orthograde and retrograde tracing methodology in mice, Shipley and Adamek (1984) described connectivity from the main olfactory bulb to the ipsilateral anterior olfactory nucleus, the anterior aspects of the hippocampus, olfactory tubercle, and parts of the medial part of the entorhinal cortex. Of note, contralateral connectivity was noted only to the anterior olfactory nucleus, as well as a connection to the posterolateral and medial amygdala. More recently, (Miyamichi, Amat et al. 2011) used a trans-synaptic tracing method and showed similar connectivity from the olfactory bulb to the anterior olfactory nucleus, piriform cortex, and cortical amygdala. These classic tracing methods support the data presented herein. Importantly, now that the two techniques are validated for the olfactory system they can be used to provide a quantifiable change in strength and patterns of connectivity with experimental manipulations in genetically modified mice (e.g., Jones et al. 2008).

The results in this study were very similar between MEMRI and DTI probabilistic tractography (up to 75% overlap). The most notable difference was in the caudal portions of the brains, particularly along the corpus callosum and the lateral entorhinal cortex, where DTI probabilistic tractography shows connectivity but MEMRI does not. There are a few technical reasons that may account for the observed difference. First, because the signal enhancement produced by manganese is dependent on the transport of $MnCl_2$ injected, more caudal areas will receive proportionally less manganese resulting in a reduced signal. It is expected that either higher initial volume, higher concentration of $MnCl_2$, or allowing for a longer time period of anaesthesia before the animal awakens and expels the solution should increase caudal enhancement signal. Second, the sensitivity profile of the coil used to maximize signal for *in vivo* studies may also impact MEMRI data from caudal portions of the brain; therefore, increasing the number of averages may improve MEMRI's sensitivity to distal connections. Finally, from an experimental model perspective, two different mouse species (C57BLJ vs Swiss Webster) were used in these two studies, although this unlikely accounts for any major differences in the main pathways of the olfactory system which appear to be highly conserved across mammals (Scalia and Winans 1975).

With regard to MEMRI, it is worth noting that significantly higher resolution was obtained in this study than in most previous related work in rodents (Leergaard, Bjaalie et al. 2003, Cross, Minoshima et al. 2004). Cross et al. (Cross, Minoshima et al. 2004) created 3D enhancement maps with a spatial resolution of 0.273 x 0.273 x 0.5 mm^3 after interpolation (0.273 x 0.437 x 1 mm^3 without interpolation) with an imaging time of 7 minutes (NEX = 4). Leergaard et al. (Leergaard, Bjaalie et al. 2003) used a spatial resolution of 0.390 x 0.390 x 0.390 mm^3 for 3D stereotaxic registration, each scan lasting 5.5 minutes (NEX = 1). The MEMRI resolution presented here was 0.200 mm isotropic (0.144 mm isotropic after interpolation) within 20 minutes (NEX = 2). Higher spatial resolution is particularly important for applications which require registration because partial volume effects associated with low spatial resolution will result in registration errors and information loss along the edges. Such errors in registration and data loss make it not feasible to have all the images in a standard space for analysis / comparison within group and across different modalities.

One of the key developments that made this study feasible was the method for obtaining high-resolution DTI data from multiple brains during a single scan. Both high spatial resolution and high spectral resolution are important for DTI studies in small animals because the high spatial resolution reduces partial volume effects that reduce the signal from small white matter tracts, and the high spectral resolution facilitates the identification of twisting or crossing white matter pathways. However, to obtain the desired resolution, scan times become quite long (e.g., 60 hours). Therefore, the protocol presented here is designed to take advantage of the fact that acquiring more data points in the readout direction is nearly free in terms of acquisition time, so that an entire tube of six brains could be scanned over a single weekend. Dyrby et al. (2011) describe a similar *ex vivo* setup, but due to the larger size of the porcine brain, only one brain was imaged in each scan which contrasts with our ability to acquire 6 mouse brains within one imaging session, with the potential to acquire more based on the MRI coil setup.

4.6 Conclusions

This study demonstrates high-resolution 3D statistical tract mapping for the mouse olfactory system using MEMRI and DTI probabilistic tractography. Progress in mouse molecular genetics and behavior make this a particularly important model for advanced neuroimaging approaches. Additionally, advances in understanding its molecular architecture have made the olfactory system particularly amenable to applying high-resolution neuroimaging techniques. The mouse olfactory system contains multiple pathways and more complicated fiber tract geometries than the optical or thalamocortical systems, where the majority of previous studies using MEMRI or DTI probabilistic tractography were performed. Furthermore, the two techniques provided accurate information in the smaller mouse brain volume compared to previous studies using mostly rat or porcine models. The two modalities map similar pathways, although probabilistic tractography may be more sensitive for detecting distal connections. The results confirm that MEMRI and probabilistic tractography provide a similar quality of complementary and accurate information about the function and structure of white matter pathways in the complex mouse olfactory sensory system. The results also lay the foundation for use of these two techniques in experimental questions manipulating the genetics and, therefore, connectivity of the mouse olfactory system.

Figure. 4.4-1 MEMRI of Olfactory System Following Mn^{2+} Infusion into the Nose

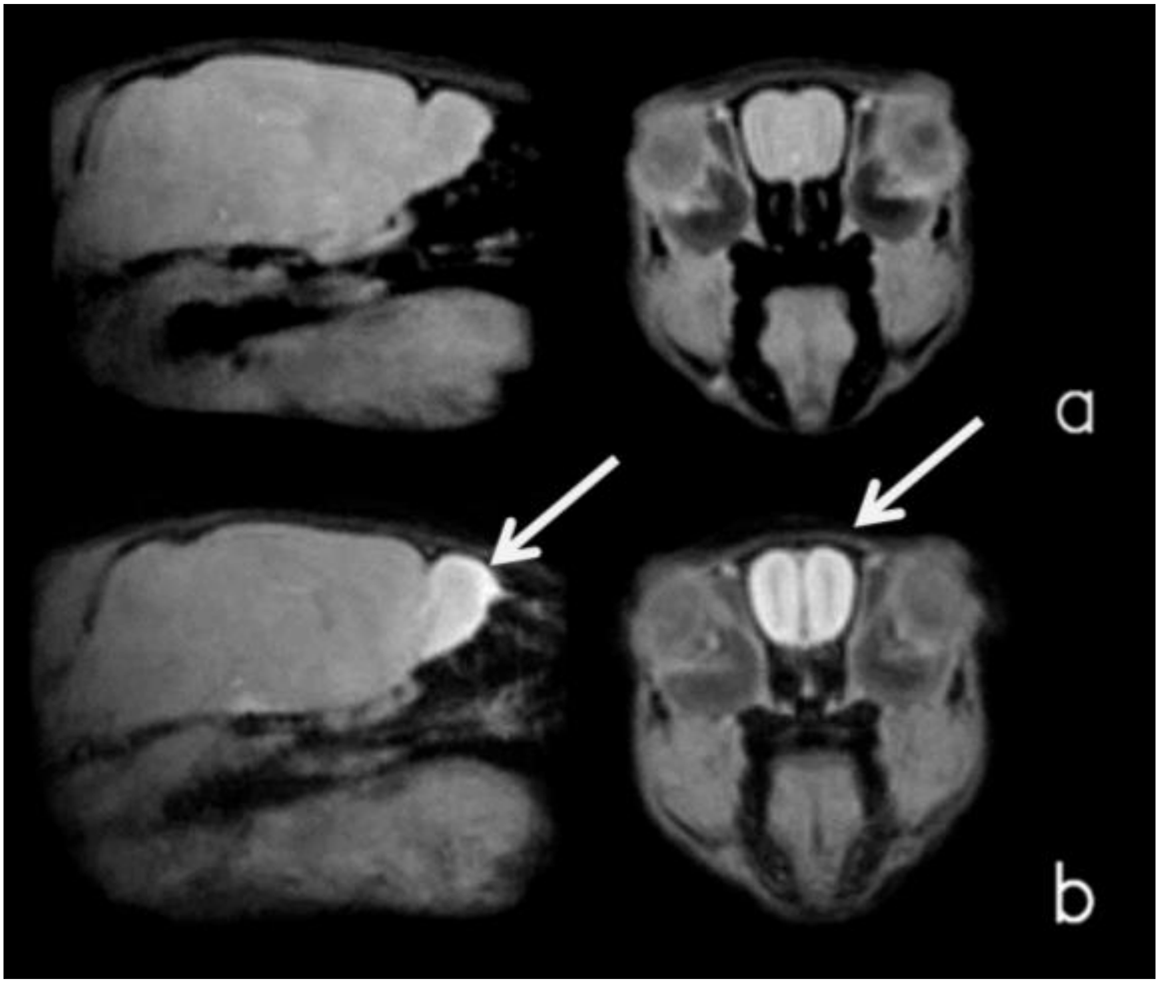

Representative sagittal (left) or coronal (right) slices from average MEMRI images obtained (**a**) pre- and (**b**) post-contrast. Each image is the average of 6 individual images. The edges of the images are crisp and there is no blurring, which suggests accuracy of the registration process. The olfactory bulb and tract are enhanced compared to the rest of the brain in the post-contrast images (arrows).

Figure. 4.4-2 Imaging of Mn^{2+} Enhanced Signal throughout the Olfactory System

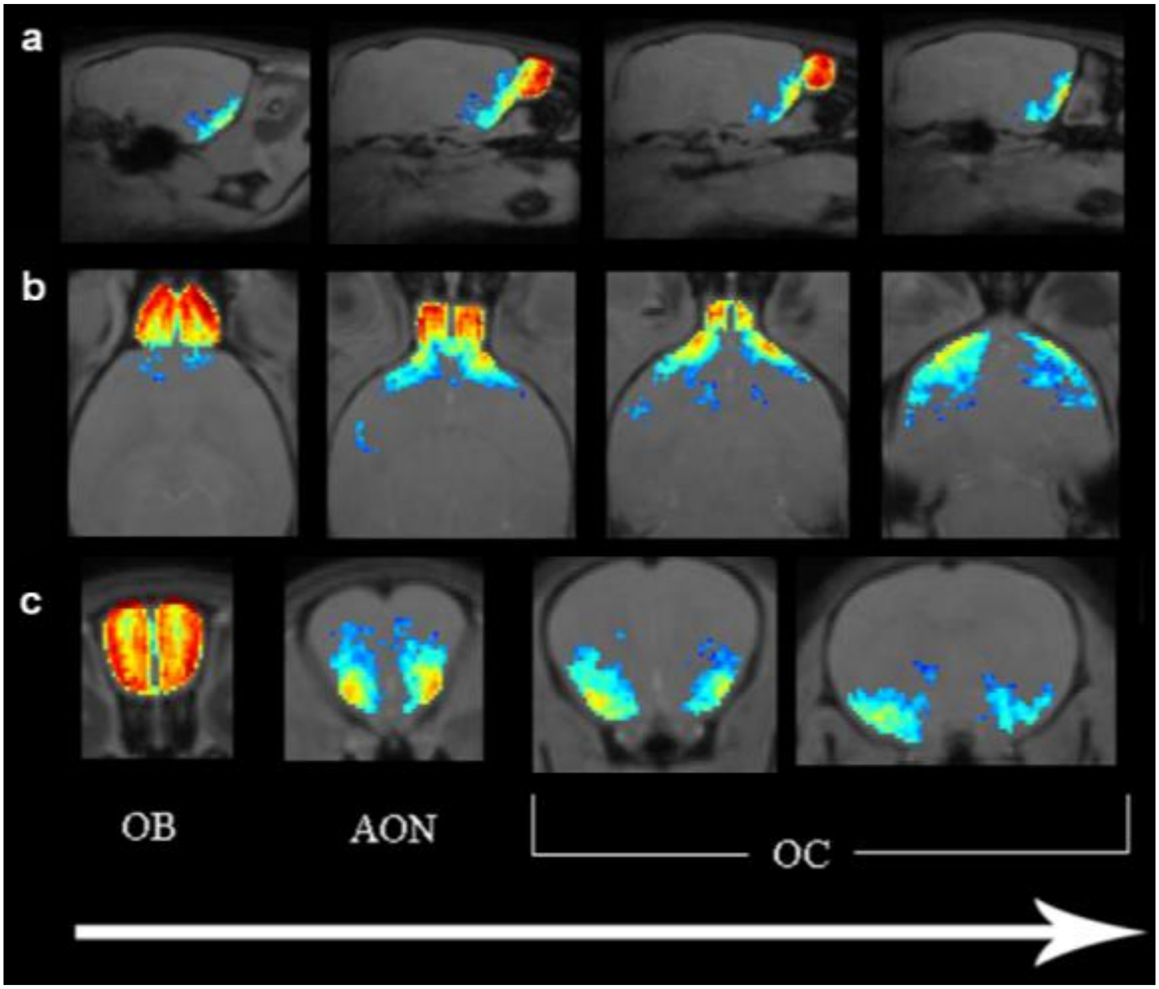

(**a**) sagittal, (**b**) horizontal, and (**c**) coronal slice maps of statistically significant enhancement in the MEMRI data, thresholded at 0.01. The olfactory bulb (OB), anterior olfactory nucleus (AON), and olfactory cortex (OC) are labeled. The direction of the arrow corresponds to anterior to posterior progression through coronal slices, dorsal to ventral progression through horizontal slices, and left to right progression through the sagittal slices.

Figure 4.4-3 Quantification of Mn^{2+} Enhanced Signal Across Brain Regions

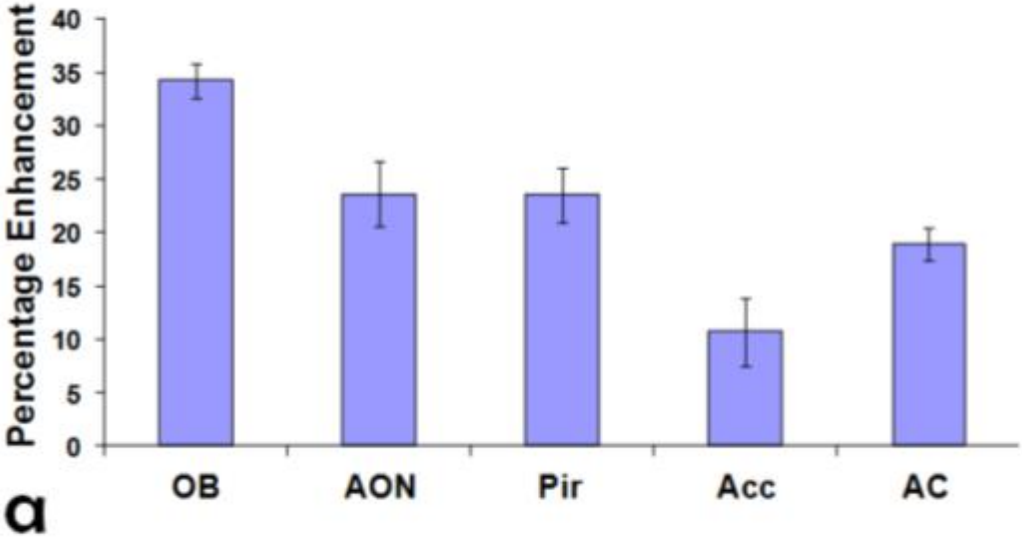

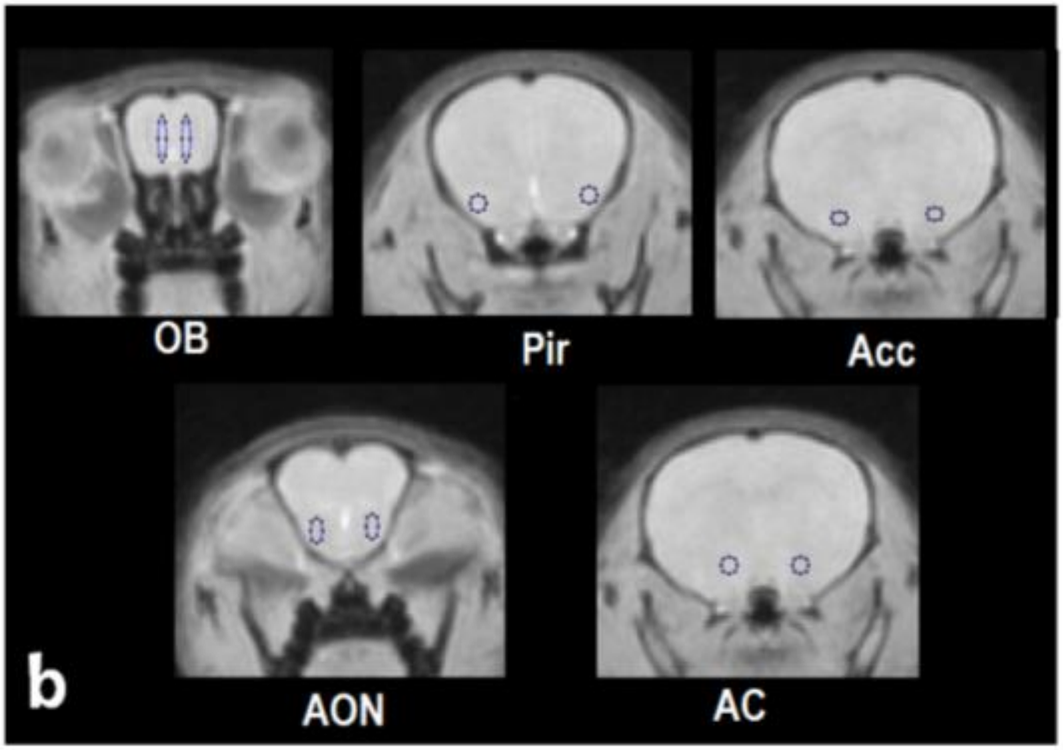

(**a**) Average percent enhancement measured from manually drawn regions of interest in the olfactory bulb (OB), anterior olfactory nucleus (AON), piriform cortex (Pir), anterior commissure (AC), and nucleus accumbens (Acc), based on maps thresholded at $p<0.05$. Standard deviations across mice are indicated by the error bars. (**b**) Specific regions of interest quantified above are identified on coronal brain images.

Figure 4.4-4 DTI Probabilistic Tractography with Unilateral Olfactory Bulb Seed

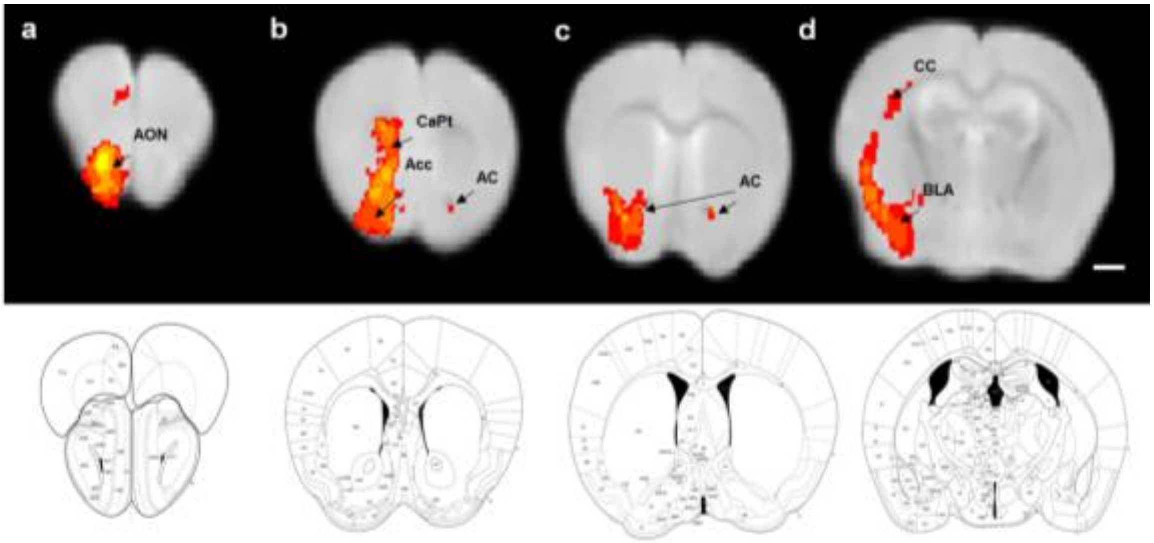

A composite image showing voxels that were common to at least 7/10 mice imaged with DTI probabilistic tractography. DTI images are shown above respective diagrams of mouse coronal sections (Paxinos and Watson, 2001). Connections to the anterior olfactory nucleus and a frontal areas (**a**), olfactory tubercle, accumbens, and septum (**b**), pallidum and bilateral connectivity via the anterior commissure (**c**), as well as connections to the BLA and along the corpus callosum (**d**) were noted. AON: Anterior Olfactory Nucleus; AC: Anterior Commissure. CC: Corpus Callosum; BLA: Basolateral Amygdala; Acc: accumbens; CaPt: Caudate/Putamen; Scale Bar = 1mm.

Figure 4.4-5 Comparison of Results from MEMRI and Probabilistic Tractography

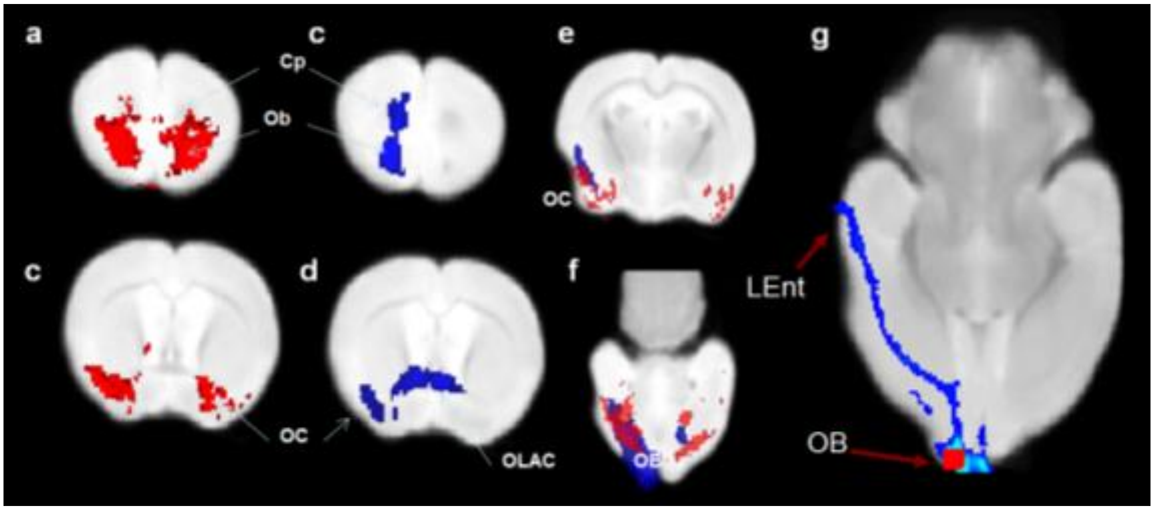

Significant enhancement (p>0.05) in the MEMRI data set is shown on two coronal slices in red (**a,c**) and the DTI probabilistic tractography common to at least 7/10 mice are shown in blue scale with dark blue representing 7 mice and light blue representing 10 mice (**b,d**). It should be noted that tractography was seeded unilaterally, whereas the Mn solution was injected bilaterally. Panels (**e**) and (**f**) show both images superimposed on the same map, demonstrating the high degree of overlap between the two methods. An axial view that better depicts the seed region (in red) for the DTI tractography (shown in blue) shown in (**g**). A distal connection to the entorhinal cortex can be seen as well as proximal connections to the anterior olfactory nucleus adjacent to the olfactory bulb seed. LEnt: Lateral Entorhinal Cortex; OB: Olfactory Bulb seed ; OC- Olfactory Cortex; Cp- Caudate-putamen; OLAC- Olfactory limb of the anterior commissure

Chapter 5:

A DTI Tractography analysis of Infralimbic and Prelimbic Connectivity in the Mouse using High-throughput MRI

5.1 Context, Author's Contribution, and Acknowledgement of Reproduction

The following chapter presents the application of *ex vivo* DWI probabilistic tractography to the mouse brain to study the similarities and difference of the projections of the infralimbic and prelimbic cortices. The context of the study was an effort to better understand the connections of the infralimbic and prelimbic cortices especially with the amygdala. The results of the probabilistic tractography were compared to a parallel study using the anterograde tracer biotinylated dextran amine in the infralimbic and prelimbic cortices. The dissertation author contributed to the paper by preparing the *ex vivo* brains, imaging those brains with the DWI scan, pre-processing and analyzing the data, conducting the injections of the anterograde tracer and the followup tracing work, and was a main contributor to the writing of the paper. The chapter is reproduced with minor edits from Gutman, D.A.*, Keifer Jr, O.P.*, Magnuson, M., Choi, D.C., Keilholz, S.D., Ressler, K.J. (2012) A DTI tractography analysis of infralimbic and prelimbic connectivity in the mouse using high-throughput MRI. Neuroimage 63 (2), 800-811. * denotes equal contributions to the work.

5.2 Introduction

An increasing focus has been placed on differential functions of the medial prefrontal cortex (mPFC) in mammals. This region is involved in a number of regulatory functions in humans, and in rodents has been most associated with regulation of behavior related to appetitive and aversive processing (Milad and Quirk 2002, Milad, Vidal-Gonzalez et al. 2004, Corcoran and Quirk 2007, Peters, LaLumiere et al. 2008). The processing of conditioned fear is among the most well-understood neural circuits related to a specific behavior, and recently the mPFC has been shown to intimately regulate the amygdala in the modulation of learned fear (Vidal-Gonzalez, Vidal-Gonzalez et al. 2006, Corcoran and Quirk 2007). The prelimbic (PL) component of the mPFC in mice and rats has been associated with the learning and expression of conditioned fear, but with no effect on innate fear behavior (Powell, Skaggs et al. 2001, McLaughlin, Skaggs et al. 2002). In contrast, the infralimbic (IL) component of the mPFC appears to have an opposite function, with its requisite involvement in the inhibition of learned fear behavior (Quirk, Russo et al. 2000, Milad and Quirk 2002, Nieuwenhuis and Takashima 2011). Similarly, with appetitive behaviors, the PL appears to drive drug seeking while the IL suppresses such behaviors after extinction. What is particularly interesting about the mPFC regions is that despite their apparently opposite functions in emotion regulation, they are adjacent, sharing a thin cortical region of only a few hundred μm within the rodent mPFC. Furthermore, although the PL/IL connectivity has been examined in the rat (Vertes 2004), these connections have not been described in the mouse, which is increasingly used for understanding the molecular genetic mechanisms of brain function.

Therefore, it is critical to better understand the complementary and differential roles of these regions, as well as their connections with other brain regions. However, classical anatomical techniques, while feasible and serving as the gold standard, are slow - often requiring weeks from injection to image generation, low throughput - being limited by the number of stereotaxic setups and animal surgery time, are limited to a few injections of tracer in regions of interest in each animal, and are not easily applied in small animal models. For example (and in the case of this paper), when working with a mouse brain, the injection targets are significantly smaller (leading to a high "miss" rate) and the diffusion of the tracer may impact surrounding regions of interest unless the volume of tracer injection is reduced (also reducing the neural tracing fidelity).

Besides classical tracing are other methods including Magnetic Resonance Imaging (MRI), which provides an excellent and powerful set of customizable methodologies to allow non-invasive *in vivo* and *ex vivo* analysis of the mouse brain. A number of different MRI methods have been developed and implemented to allow high-throughput *ex vivo* imaging of fixed tissue or *in vivo* samples. Several groups have developed sophisticated workflows that allow rapid *in vivo* analysis in mice, although this often requires the construction of custom enclosures, receiver coils, or modifications to the underlying hardware. For anatomical scans and morphometric analysis of brain structures, many of the studies focus on T2 and T2* weighted pulse sequences, which provide a good balance of tissue contrast, signal-to-noise ratio (SNR) and resolution. The choice of optimal scan parameters of course remains a tradeoff, as there is inherently a tradeoff between SNR, image resolution, scan time, and sample preparation which can be a particular problem in diffusion tensor imaging which requires multiple acquisition volumes.

Diffusion Tensor Imaging (DTI) is a MRI technique that generates its signal and contrast primarily based on the degree and direction that water diffuses along neuronal axons (Zhang, Richards et al. 2003). DTI has had some preliminary success when used to characterize the developing mouse embryo (Zhang, Richards et al. 2003). DTI has also been extensively used in both human (Wedeen, Wang et al. 2008, Gutman, Holtzheimer et al. 2009, Douaud, Jbabdi et al. 2011) and non-human primate studies (Rilling, Glasser et al. 2008, Wedeen, Wang et al. 2008, Li, Preuss et al. 2010) to compare and contrast the structural connectivity of brain regions between the model species imaged. Using computation techniques, it is possible to reconstruct putative connections *in silico* via various computational algorithms. A few studies have also directly compared the results of tractography to the gold standard tracer-injection studies in the porcine model and have generally shown a high concordance between the histologically defined pathways and those defined based on MRI Tractography results (Dyrby, Sogaard et al. 2007, Dyrby, Baare et al. 2011). Furthermore, one study has compared the DTI analysis of the tracts of the murine olfactory bulb to corresponding MRI based tracing conducted using MEMRI (Gutman et al., 2012).

The generation of high-throughput MRI DTI presents a number of challenges in mice—largely related to the small size of the mouse brain. For example, the resolution required to gather isotropic voxels less than a fifth of a millimeter (or about the size of the smaller nuclei in the mouse brain) makes a high field magnet (e.g., 7 or greater Tesla) with a complimentary gradient and RF coil set ideal. Additionally, the higher resolution increases the length of the scan tremendously. Furthermore, in order to compute probabilistic tractography, a minimum of 30 gradient directions is recommended (although technically only 6 are required to compute a 'tensor'), necessitating the collection of at least 31 separate volumes (when including at least one B0), which dictates and even longer scanning session. Considering both the resolution and number of gradients such work is often not feasible with *in vivo* models. Importantly, the addition of 30 or more directions and higher resolution are imperative as it allows estimations of a more sophisticated tensor model that allows tracking through regions of "crossing fibers" (Behrens, Woolrich et al. 2003, Johansen-Berg and Behrens 2006, Behrens, Berg et al. 2007).

In this study, we report our implementation of a high-throughput *ex vivo* diffusion tensor imaging protocol that allows for both high-resolution and a high number of diffusion weighted directions. For these studies, groups of fixed *ex vivo* mice brains were scanned in a single acquisition session. We then tested the feasibility and fidelity of using probabilistic tractography in the mouse by analyzing the connectivity of the IL and PL cortices (areas separated by less than a millimeter) with the results validated against previous tract-tracing experiments in rats, and also against our own BDA tracing of the mouse PL and IL projections. Comparisons to rat anatomy are important a major theme of this paper as there is an assumed homology. Furthermore, a comparison to the traditional tracing results within mice provides a validation of the DTI technique. Specifically, the mPFC region was chosen as it has received both increasing interest within the neuroscience community (Maddux and Holland 2011, Nieuwenhuis and Takashima 2011), as well as provides some of the technical challenges in terms of proximity.

Our DTI and classical tracing data suggest that IL and PL share a majority of projections but also have unique connectivity as well. More importantly, it demonstrates that these methods can be utilized to examine differential connectivity of mPFC (and other regions of interest) in genetically modified models as well as pre- and post-experimental manipulation, e.g., following stress, fear conditioning, drug sensitization, etc. In this paper, we demonstrate the feasibility of tracking complicated pathways in the mouse through the use of probabilistic tractography, and we compare these results using a comparative anatomy approach of known anatomical connections of the rat IL/PL (Vertes 2004) and also using a preliminary tracing study of the mouse IL/PL. Finally, our data provides a preliminary comparison of rat and mouse IL/PL connectivity, often assumed to be homologous.

5.3 Methods

5.3.1 Animals

All animals used in this study were treated humanely following a procedure approved by the Institutional Animal Care and Use Committee at Emory University. A total of 18 C57BL6 mice (Jackson Labs) were used for the MRI imaging presented in the study. Animals were ~ 100 days at old at time of fixation. A total of 24 C57BL6 mice (Jackson Labs) were used to conduct a preliminary anterograde tracing study of IL and PL.

5.3.2 Fixation Procedure

Mice were euthanized using pentobarbital, and brains were perfused with 10 ml Phosphate Buffered Saline (PH 7.4) followed by 10 ml 4% paraformaldehyde (PF)/PBS. The brains were then extracted from the skull (to ensure a close interface between the brain and embedding matrix as discussed below) and were post-fixed (for 24 hours) in the same 4% PF/PBS, then rinsed in PBS and stored at 4˚C in PBS until they were embedded in an agarose-gadolinium (III) oxide matrix for imaging. No exogenous contrast agent was used for this study.

5.3.3 Mounting procedure

Following at least 24 hours of post-fixation, the brains were embedded in a 50 ml falcon tube (Fisher Scientific), with an approximate outer diameter of 3.0 cm and a length of 11.5 cm from cap to tip, arranged in a 2 x 3 matrix (see **Figure 5.3-1**). Brains were embedded in 2% agarose (Phenix Research Products Low EEO, Molecular Biology Grade Agarose) doped with an insoluble mixture of 2 mM gadolinium (III) oxide (Acros Organics Fisher Scientific). Of note, several iterations of T2 scans with different gadolinium concentrations were conducted with the 2x3 configuration to optimize integration with the Bruker coil, minimizing signal drop-off and maximizing SNR. Doping with gadolinium (III) oxide serves to robustly reduce the T1 relaxation time in the agarose/water solution, providing better separation of the brains from the background.

The mounting procedure is simple and straightforward providing both accurate and precise *ex vivo* imaging. The lid is cut from a 50mL Falcon Tube with a Dremel Tool using a Dremel Plastic Cutting Wheel (Model 4000 and EZ476 respectively, Bosch Tools). The first cut is made along the length of the falcon tube at the point of maximum diameter connecting each cut on the side at the tip of the tube, a perpendicular cut is made through the long axis near the cap (**Figure 5.3-1a**). The lid section then has two 0.5 cm holes cut into it using a Dremel high speed cutting bit (192, Bosch Tools). Concurrently, a solution of deionized water containing 2% (by weight) agarose and 2 mM Gadolinium (III) Oxide (note: Gadolinium III Oxide is not soluble and needs to be maintained in suspension) is mixed on a stir plate until homogenous and then heated in a microwave. Following heating, the solution is placed back onto the stir plate, to ensure homogeneity; the solution is then poured into the tube, until the level of the solution is approximately 2 mm below the edge created when cutting out the top (replace the beaker onto the stir-plate). The tube containing the agarose/Gadolinium III oxide is then placed into a 4°C freezer (to accelerate the setting of the agarose before the gadolinium forms a concentration gradient due to gravity), until the agarose is firm. Next, a thin layer of the agarose/gadolinium mixture is formed by filling the remaining space of the tube (up to the edge, ~2 mm), and the perfused brains are placed into the layer immediately (this layer is necessary to ensure the mixture can get into the ventral spaces at the interface of the cerebellum, brainstem, and forebrain else air pockets form creating an artifact when imaging; it is also possible to submerge the brains in the mixture then place them onto the hardened layer). Once that layer has firmed, the lid is then hot glued into it original orientation, creating a water tight seal. Upon the glue hardening, the remaining Agarose Gad (III) oxide solution is used to fill the remaining volume of the tube using the two 0.5 cm holes previously drilled (one serving as a point of pipette tip insertion, and the other as an air escape). The whole tube is then allowed to set. The two holes are then covered with hot glue to prevent dehydration of the agarose/gadolinium gel. Because the contrast in DTI is based on the diffusion rate of water, the tube is then allowed to equilibrate with ambient room temperature for a minimum of six hours prior to scanning.

5.3.4 Imaging Parameters

High-resolution DTI with multiple gradient directions can result in a scanning sequence that lasts several days. Therefore the ability to image multiple brains in a single session is the crucial feature that makes this experiment practical. All imaging was performed on a 9.4 T 20 cm horizontal bore scanner (Bruker, Billerica, MA) interfaced with an ACANCE console (Bruker, Billerica, MA). To obtain maximum resolution for the DTI/tractography experiments, a 6cm gradient insert (150 G/cm) was used with a 35 mm transmit/receive volume coil. The data were collected in the axial orientation with the read-out direction oriented to the long axis of the tube. For each tube of brains, T2-weighted images were first acquired at 100 micron isotropic resolution (10 averages, TE = 26ms, matrix 256 x 512, 20 averages, scan time ~ 16 hours). Diffusion-weighted images of the 6 mouse brains were then acquired using a 2-D spin-echo based sequence with 161 micron isotropic resolution. (1 average, TE = 26.9 ms, TR=10000 ms, matrix size of 256 x 128, ~ 55-60 axial slices collected/tube, 60 gradient directions with a diffusion weighting b=2000 s/mm^2, and 3 b=0 s/mm^2 images, scan time ~ 60 hrs). The Massachusetts

General Hospital (MGH) 60 direction DTI gradient sequence was used for data acquisition; the calculated tensors were verified using the built-in gradient tables in trackvis.org (Wang, Benner et al. 2007, Wedeen, Wang et al. 2008).

5.3.5 ROI Selection

For each T2 high-resolution brain scan, two 10 x 4 x 5 voxel cubed (1.0 mm x 0.4 mm x 0.5 mm) ROIs were drawn, and were only inclusive of the IL and PL volumes, respectively, see **Figure 5.3-2,** based on the atlas of Paxinos and Franklin (Paxinos and Franklin 2004).

5.3.6 DTI registration

Given that each raw image (both T2 weighted and diffusion tensor image (DTI) modalities) from the scanner contained a 2 x 3 matrix of brains, the initial processing step was the parsing of the raw data into individual brain volumes via manual segmentation using fslroi (FSL, Oxford, UK). In accordance with the FSL DTI pipeline, individual masks were generated for each mouse brain in the matrix using the Brain Extraction Toolkit (BET) (FSL, www.fmrib.ox.ac.uk/fsl) to isolate the brain from the background. Because BET is intended to extract the brain from the skull and the mouse skulls were not present (see Fixation Procedure), the fractional intensity threshold for extraction was determined empirically (a reduction in the threshold by 0.05 recursively till the extraction successfully isolated the brain from background) to be 0.05 from the default 0.5. Masks were subsequently edited manually to correct any remaining errors in the masking process. A study-specific high-resolution mouse template was generated by nonlinearly registering each mouse brain to a single reference image. The default FSL non-linear parameters were used, with the exception that the reference mask was based on the selected reference brain. The mouse brain with the best orientation, signal to noise, and contrast between white and grey matter was used for this purpose. Non-linear registration was validated by checking for correct alignment of the surface of the brain and internal alignment of the anterior commissure, corpus callosum, and cerebellum. An averaged image of the registered brains was then constructed and used as the reference image for subsequent analysis (FNIRT and FSLMATHS, respectively, www.fmrib.ox.ac.uk/fsl), and transformation matrices were generated between the reference image and individual mouse brain data sets using FNIRT (FSL, www.fmrib.ox.ac.uk/fsl). In this study results from 10 mice are presented of the 18 scanned. The initial two tubes of 6 brains had two problems that cost 4 brains from each tube. The first problem was that brain volumes were clipped or aliased (as a byproduct of trying to use a minimal FOV to cut down the imaging time), the solution was to reduce the distance between the brains measuring the embedding matrix to ensure it was smaller than the selected field of view. The second problem that arose was an issue with centering the tube in the coil, which led to a few brains with notable signal loss in the cerebellum which compromised the registration algorithm. The final tube, which had the brains placed in a tighter 2 x 6 matrix, and which was accurately centered with an iterative flash tripilot approach and a 3 plane positional scan resulted in all six brains being used in the analysis. Overall, this methodology is quite similar to those commonly employed in group level MRI imaging as described here (Lerch, Sled et al. 2011)

5.3.7 Probabilistic Tractography

Diffusion-based probabilistic tractography was performed using the FSL imaging suite on a Linux workstation. As part of the standard FSL pipeline, the IL and PL ROIs drawn on T2 weighted high-resolution space were transformed into each individual mouse's DTI space. Tractography was then computed for each voxel within the seed mask (using n=5000 streamline fibers/voxel and curvature threshold of 0.2) and then back-transformed into the high-resolution mouse-standard space. For all tractography, a multi-fiber reconstruction algorithm was employed allowing the reconstruction of more geometrically complex pathways, including regions of crossing fibers (Behrens, Berg et al. 2007).

5.3.8 Determining Connectivity of the IL/PL

Connectivity, based on the probabilistic tractography results, was determined in two separate but complimentary ways. First, a single mouse was chosen as a representative sample from the group (middle column of **Figure 5.3-3a,b**), and that individual's tractography was transformed into the high-resolution standard mouse space. The raw tractography was thresholded to exclude voxels that received less than 10 total tracts from the seed ROI. Using anatomical landmarks, including the corpus collosum, the ventricles (lateral, 3rd and 4th ventricles, plus the aqueduct) and the hippocampus, it was possible to review MRI slices and assign the voxels with tractography results to a particular area of the brain labeled in the Paxinos & Franklin atlas.

In another analysis, the tracts from all 10 mice were placed in the standard space analogous to the methodology describe above, and then were averaged (right hand most column of **Figure 5.3-3a,b** for IL and PL respectively) together yielding an average number of tracts passing through the voxels in the standard mouse space, which could be similarly assigned anatomic labels by referencing the Paxinos & Franklin Atlas.

5.3.9 Intra-mice Comparison of IL/PL Connectivity

To disambiguate regions of overlapping connectivity from the IL/PL seeds, a strategy to exploit the relative probability of connectivity between IL and PL was employed. Conceptually, for each individual brain the tractography results of both the IL and PL were compared for each voxel. If the number of tracts from the IL seed were greater in a voxel relative to those from the PL seed, that voxel was classified as IL dominant, and vice versa. For each animal, a binarized map of where the IL or the PL connectivity was dominant was generated. By subsequently merging the individual binarized maps, a map indicating the proportion of animals which showed tracts passing through that voxel that were dominant for either the IL or the PL (**Figure 5.3-4**).

5.3.10 Anterograde Tracer Injection of BDA into the Mouse IL/PL

To have a within-species classical tracing study for comparison to the DTI, we stereotactically (Kopf, Tujunga, Ca) injected with a pump (World Precision Instruments, Inc. Sarasota, Fl) either 0.25 µl of BDA (10,000 MW) into the PL or 0.15 µl of BDA into the IL (a smaller target) of the mouse anesthetized with 0.15 ml of Ketamine/Medetomidine (Domitor), using a 5 µl Hamilton syringe (30 gauge beveled needle). The coordinates were determined using the Paxinos and Franklin mouse atlas (PL, 1.7 mm anterior of bregma, 0.3 mm lateral, and 3 mm ventral; IL 1.6 mm anterior of bregma, 0.3 mm lateral, and 3.3 mm ventral). Fifteen minutes after the delivery of the BDA, the syringe was removed over the course of 2 minutes to minimize the drag of DBA through the injection site. The mice were allowed to recover for 5 days before they were perfused, analogous to those prepared for MRI. After 24 hours post fixation, the brains were placed in 30% sucrose solution for cryoprotection. The following day the brains were then sectioned (35 μm) using a freezing microtome and the free-floating sections were rinsed with PBS-T (2% Tween). Then sections were incubated in 1% hydrogen peroxide (H2O2) in PBS-T for 30 minutes to quench peroxidase activity. The sections were then subsequently incubated in avidin-biotin-peroxidase complex (Vector Elite ABC kit) for 4 hours. Color development was then conducted with 3,3'-diaminobenzidine (DAB, Dako, Carpinteria, CA) for 30 minutes. The sections were then mounted onto poly-Lysine-coated coverslips, allowed to dry overnight, and were dehydrated and cover-slipped for dark field and phase analysis via a light microscope (Nikon Eclipse, E800)

5.4 Results

5.4.1 Probabilistic Tractography (PT)

The probabilistic tractography results from seeding the infralimbic and the prelimbic areas are presented in **Figure 5.3-3a,b**. A tabulation of the areas that are covered by the probabilistic tracts, sorted by IL/PL, is presented in **Table 5.4-1**. In **Figure 5.3-3**, connectivity is compared between the results described in Vertes (Vertes 2004) using anterograde HRP injections into IL/PL into the rat brain, the results of computed tractography from a single example mouse brain [middle], along with a tractography map generated by identifying patterns of consistent connectivity demonstrated between at least 7 of the 10 mice at the voxel level [right].

5.4.2 IL Connectivity via PT

Robust frontal projections included the frontal cortex, the olfactory bulbs, and the dorsal tenia tecta. Furthermore, the tractography also showed connections to the medial and the ventral orbital cortices. Continuing caudally within the cortical regions, there were connections to the prelimbic cortex and the cingulate cortices, the agranular insular cortex, the ectorhinal and entorhinal cortex and the endopiriform cortex. Of note, there was less strength of connectivity apparent in the medial agranular cortex corresponding to secondary motor area. Subcortically, tractography was consistent with connections to the nucleus accumbens, including both the core and the shell. There were robust connections throughout the medial aspects near the septum, including components of the basal forebrain (medial septal nucleus, the vertical and horizontal diagonal band nucleus), the lateral septum (dorsal, intermediate and ventral), the septohippocampal nucleus, the septofimbrial nucleus, the subfornical nucleus, and the ventral pallidum.

Focusing at the level of the mid-septum, there were cortical projections to the secondary motor cortex and the cingulate cortex, with subcortical projections to the bed nucleus of the stria terminalis (BNST, all major divisions), the substantia innominata, the horizontal limb of the diagonal band, the caudate-putamen, the lateral septal nuclei, the endopiriform cortex, and the magnocellular and lateral preoptic nucleus.

At the level of the hippocampus, the cortical projections were notable at the cingulate cortex and the adjoining retrosplenial agranular and granular cortices. In the subcortical regions, there were projections to the lateral geniculate nucleus, and also robustly to the basolateral, basomedial, lateral, and central amygdala, and both the retrosplenial agranular and granular cortex. There was a notable scarcity of connectivity to the thalamic and hypothalamic regions, though low probability connectivity was noted in the anteromedial nucleus of the thalamus, the lateral geniculate nucleus, the lateral habenula, the laterodorsal nucleus, the reticular and the Reunions nucleus. There were also minor tracts in the hypothalamus include the anterior nucleus, the dorsomedial nucleus and the lateral nucleus.

The probability of connection fell off sharply in the more caudal regions of the brain, as is apparent both in **Figure 5.3-3a** and also **Table 5.4-1** at the level of the thalamus, hypothalamus, and the brain stem. Of note, there were some isolated tracts that reached the substantia nigra reticularis and the dorsal raphe nucleus.

5.4.3 PL Connectivity via PT

Raw tractography results for the PL are largely similar to those presented for the IL seed; however, there were some notable differences. First, the PL connectivity results were quantitatively less robust (in any given voxel of overlap between IL and Pl connectivity, the IL usually had more streamlines passing through any given voxel). Qualitatively, however, there was nearly the same area of coverage. Most notably, the PL seed did not show connections to the agranular and dysgranular insular cortex (dorsal portion), the medial septal nucleus, and the anterior and dorsomedial hypothalamic nuclei. Conversely, the PL showed connectivity to the infralimbic cortex, the rhomboid nucleus and the nucleus pontis oralis.

5.4.4 Direct Contrast of IL and PL Connectivity - Preferential IL Connectivity

A contrast analysis to identify voxels that showed greater probability of connectivity from IL vs PL seeds was also conducted (**Figures 5.3-3, 5.3-4**and **Table 5.4-1**). Overall the IL seed showed stronger relative connectivity, showing strong connectivity (moving rostral to caudal) in most of the frontal cortex (excluding the more ventral areas), the orbital cortex (lateral, medial, ventral and ventrolateral), the secondary motor cortex, the piriform cortex, the insular cortex (agranular and dysgranular), the dorsal peduncular cortex, the cingulate cortex, minor tracts were seen in the somatosensory cortex (both primary and secondary), the retrosplenial cortex, the perirhinal cortex, the ectorhinal cortex, and the entorhinal cortex.

Progressing to the subcortical areas of the telencephalon, from rostral to caudal, there was stronger connectivity in the anterior olfactory nucleus, ventral tenia tecta, the dorsal endopiriform nucleus, the nucleus accumbens (shell and core), the dorsal tenia tecta, the caudate putamen, the septohippocampal nucleus, semilunar nucleus, the claustrum, the ventral pallidum, islands of Calleja, the lateral septum (including the dorsal, intermediate and ventral) nucleus, the medial septal nucleus, the septofimbrial nucleus the diagonal band nucleus (both horizontal and vertical), the BNST, the magnocellular, medial and lateral preoptic area, all portions of the amygdala (anterior, basolateral, basomedial, central, medial and lateral) (e.g., **Figure 5.4-1**), the globus pallidus, and the very most anterior portion of the hippocampus.

Neither seed showed robust connectivity to the diencephalon, though there were several regions common across the IL contrast. In brief, the following thalamic nuclei showed connectivity, the anteromedial, anteroventral, lateral geniculate, lateral dorsal, lateroposterior, mediodorsal, reticular, reunions, rhomboid, and ventral anterior lateral thalamic nuclei, and the medial and lateral habenula. There were also three nuclei of the hypothalamus that showed tracts, the anterior nucleus, the dorsomedial nucleus, and the lateral nucleus. Finally, the only area of the brainstem that showed results was the ventral tegmental area.

5.4.5 Direct Contrast of IL and PL Connectivity - Preferential PL Connectivity

The PL tracts, although showing less robust *preferential* connectivity than IL throughout the brain, still had several notable areas of connection (**Figures 5.3-3, 5.3-4** and **Table 5.4-1**). Starting with the cortical areas and moving rostral to caudal, there were tracts in the ventral aspect of the frontal cortex, the orbital cortex (lateral, medial, ventral and ventrolateral), the secondary motor cortex, the piriform cortex, the insular cortex (agranular and dysgranular), the dorsal peduncular cortex, the cingulate cortex, the retrosplenial cortex, the perirhinal cortex.

Progressing to the subcortical areas of the telencephalon, from rostral to caudal, there was connectivity in the anterior olfactory nucleus, the nucleus accumbens (shell and core), the dorsal tenia tecta, the caudate putamen (e.g., **Figures 5.4-1**), the septohippocampal nucleus, semilunar nucleus, the ventral pallidum, islands of Calleja, the lateral septum (including the dorsal, intermediate and ventral) nucleus, the septofimbrial nucleus, the horizontal diagonal band nucleus, the BNST, the magnocellular, medial and lateral preoptic area, most portions of the amygdala (basolateral, basomedial, central, medial and lateral), the globus pallidus, and the very most anterior portion of the hippocampus.

The diencephalon results for the PL seed mirrored those of the IL seed, with a significant drop off in the number of tracts passing through this area. The following thalamic nuclei were linked to the PL seed, the anteromedial, anteroventral, lateral geniculate, lateral dorsal, lateroposterior, reticular, reunions, rhomboid, and ventral anterior lateral thalamic nuclei, and the lateral habenula. Like the IL, there were also three nuclei of the hypothalamus that were showing tracts, the anterior nucleus, the dorsomedial nucleus, and the lateral nucleus. Finally, the PL showed no results in the region of the brainstem.

5.4.6 BDA Anterograde Tracing of IL/PL Connectivity

Of the four mice selected for PL injections (representative PL injection site shown in **Figures 5.3-1**), three mice had an injection site that included PL. The fourth animal did not yield staining either in the injection site or any of the tracts seen in the other three animals. With the more difficult IL injection site, only 3 of the 20 mice had injection (representative IL injection site shown in **Figures 5.3-1**) sites that were inclusive of the IL. Among the 17 animals where the injection site deviated from the intended IL target, three main problems were noted. First was injection into the ventricles, the second was a miss injection hitting more of corpus callosum and cingulate, the third was a null or poorly DAB staining injection. Overall the patterns of connectivity of the IL/PL of the mouse were largely consistent with those of the rat presented in Vertes (2004). More pertinent to the goal of this paper, the DTI probabilistic tractography results and BDA anterograde projections of the IL/PL had a qualitatively high degree of concordance, as shown in **Figures 5.4-2 and 5.4-3** when compared to **Figures 5.3-3**. In particular, these figures are highlighting certain areas of interest including the insula, the amygdala, and the cingulate. Each of these areas is an important component of the circuit regulated by the IL and the PL. Importantly, and in accordance with the rat tracing results, the mouse IL/PL injection did show more medial projections that were missed, for the most part, by DTI, and highlighted in **Figures 5.4-3**. Furthermore, the IL injections did have less robust classical tracing results when compared to the PL, see **Figures 5.4-2 and 5.4-3**.

5.5 Discussion

In this work we have developed a high-throughput DTI imaging methodology in the mouse and were able to delineate connectivity of the infralimbic and prelimbic cortex in the mouse, regions separated by less than one mm. These regions have been shown to be critically involved in regulation of emotion regulation (1-11), and new approaches which can examine connectivity of these mPFC regions to areas like the cingulate, insula and the amygdala in a hypothesis-neutral fashion are critical to furthering understanding of their function. Our methodology provided a good balance of tissue contrast, SNR, resolution, and throughput allowing us to perform high-resolution DTI on 6 mouse brains in about 55 hours. Our results are largely consistent with both previously published gold standard HRP-staining techniques (Vertes 2004) and also our own mouse IL/PL tracing using DAB for anterograde tracing. The contrasting method employed in this paper, similar to those used in our previous work (Gutman, Holtzheimer et al. 2009) was a critical first step in highlighting the unique connectivity of these two regions that lie in close proximity. Despite the potential confounds, including the adjacency of these regions working within a standardized space and potential issues related to partial voluming, this contrast-based approach was able to differentiate regions more connected to the IL vs. PL seeds.

A readily apparent feature of the raw data is the large degree of overlap in terms of the projections from the IL and PL (as expected from previous anatomical tracing work in rats and also seen in the mouse work presented here), though there are known differential projections. In order to parse out differences in connectivity it was important to understand how differences may be lost. In the probabilistic tractography method used in this paper, each seed voxel generates tracts, which in this case will pass through the adjacent seed in some instances and replicate the most likely tracts generated through that area (IL tracts passing through the PL and taking on tracts similar to those of the PL, and vice versa). Therefore, one potential solution was to compare the number of tracts passing through a voxel for the IL and PL and assigning the voxel to either the IL or PL depending on which seed generated the highest number of tracts in that area. This notion of a voxel containing more tracts from one seed versus the other seed has been referred to as “stronger connectivity”, however, it is important to note that it has not yet been established that this corresponds to stronger connectivity in terms of classical tracing studies (a higher density of axons terminating on a particular brain region). This was done for all 10 brains used in the analysis, and the tracts were overlaid on one another with a scale of 0-10 brains showing that assignment in that voxel (see **Figures 5.3-4)**. We have also presented preliminary BDA tracing work in both the mouse Il and PL showing both that there was agreement between mouse and rat IL/PL projections, and also that the DTI was able to recapitulate these results, particularly with connectivity to areas including the insula, amygdala, and cingulate known to have a strong role in the circuit postulated to regulate emotional activity. With regards to the IL and PL classical connectivity strength it should be noted that the results from the IL appear less robust in **Figures 5.4-2 and 5.4-3**, however given the smaller size of IL we reduced the injection volume of BDA from 0.25 to 0.15 microliters potentially reducing the amount of tracer that was available for uptake. Furthermore, the IL BDA injection results shows some hippocampal projections, which is inconsistent with known anatomical connections, we ascribed these connections to a group of neurons in the lateral septum that also showed tracer uptake in the mouse selected for analysis (for the rat see Kohler et al., 1984).

One of the key developments that made this study feasible was the method for obtaining high-resolution DTI data from multiple brains during a single scan. High spatial resolution and many diffusion-weighted directions are imperative for DTI studies in small animals. The high spatial resolution reduces partial volume effects that reduce the signal from small white matter tracts, and the greater number of diffusion weight directions combined with the probabilistic tractography algorithm facilitates the identification of twisting white matter pathways. However, to obtain the desired resolution, scan times become prohibitively long (~55 hours). We designed our protocol to take advantage of the fact that acquiring more data points in the readout direction is nearly free in terms of enhancing acquisition time, so that an entire tube of six brains (as opposed to two) could be scanned over a single weekend. It should be noted in the particular setup utilized in this study the limit to the resolution was a slice thickness of 161 micron, which limited the in-plane resolution to 161 micron by 161 μm to ensure the voxels were isotropic. Therefore, scanning one brain will reduce the time for imaging (by half), but it would not have increased the isotropic resolution or signal-to-noise of the individually imaged brain. Furthermore, techniques like a two-coil system utilizing both a receiver coil and transmitter coil that were available at the imaging center, while increasing the signal-to-noise, also limit the depth of imaging before signal dropout. As a result the two-coil system could not provide the whole brain coverage available in this study.

While *in vivo* experiments obviously have some inherent advantages, in particular the ability to look at longitudinal changes, the associated logistical challenges including keeping the animals warm, use of anesthesia, movement artifacts, as well as difficulty in moving live animals from different animal facilities for scanning even within a given academic environment, are some clear advantages of *ex vivo* approaches. Also the technique as described is readily amenable to post-imaging analysis as the agarose can be easily removed allowing the brains to be sectioned and stained for further higher-resolution analysis. In fact a key motivation for the development and implementation of our approach was to allow the addition of MRI imaging to the traditional workflow used in our lab in as rapid a fashion as possible; thus we avoided the use of additional contrast agents that could potentially have affected downstream assays and also took the brains out of the skull. While this step induces cortical shape change, the resulting MRI images will share similar morphology/dimensions to histological sections that would be used for correlative analysis.

A number of high-throughput setups have been employed in the community to facilitate this type of research, and our work is heavily influenced by these sorts of schemes. Schneider and Bhattacharya (2004) have demonstrated that up to 32 *ex-vivo* embryos can be scanned in a single overnight session. Special setups that allow multiple animals (e.g., 16 mice), under generalized anesthesia to be scanned *in vivo* have also been developed (Henkelman 2010, Lerch, Sled et al. 2011).

In silico tractography results have been validated in a number of species. Using a porcine brain as a model, comprehensive analysis was performed directly comparing histological tract tracing results using standard methods with post-mortem DWI imaging, as well as MEMRI techniques (22). The results of both biotinylated dextran amine (BDA) and MEMRI techniques produced results that are consistent with those obtained *ex vivo* via tractography, although there were some significant differences in some of the circuits evaluated (Dyrby, Sogaard et al. 2007). Dauguet et al have also shown good visual concordance between DTI and 3D histological tract tracing in the macaque (Dauguet, Peled et al. 2006, Dauguet, Peled et al. 2007), and similar studies have also been done in the rat (Leergaard, White et al. 2010). Recent work from Calamante and colleagues (2011) have also recently validated their novel track density imaging methodology in the mouse showing high concordance between mouse histology and computed tract structure. Our work largely builds on this past study, suggesting valid results can still be obtained in the much smaller mouse brain, allowing whole brain structure and connectivity analysis in this widely used genetic and behavioral model. Future approaches examining differential mouse IL/PL connectivity as a function of genetic background and stress should further our understanding emotion regulation and improve translational approaches to human mPFC functioning.

Figure 5.3-1 High-Throughput Layout Utilized to Scan 6 Brains *Ex Vivo*

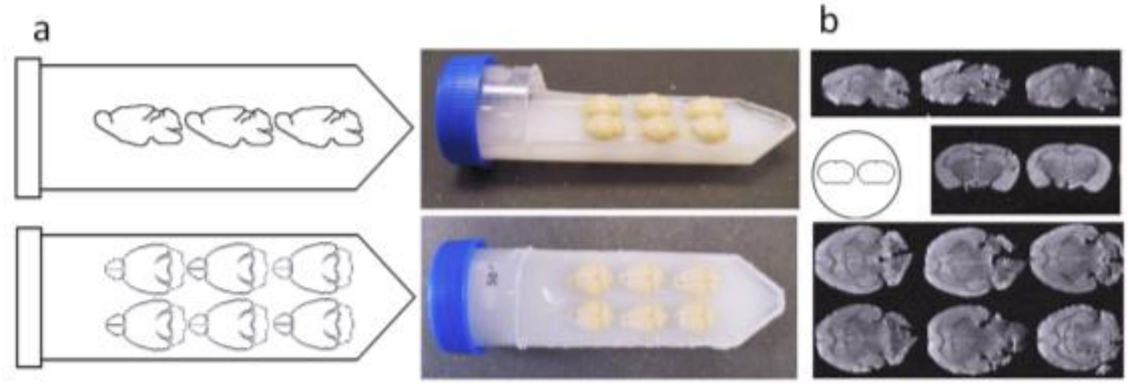

(**a**) Shows the dimensions and the scale used to maximize the volume of sensitivity of the gradient coil. (**b**) Shows the corresponding images that are acquired with optimized T2 weight parameters.

Figure 5.3-2 IL and PL MRI seeds for DTI Tractography and BDA Injection Sites

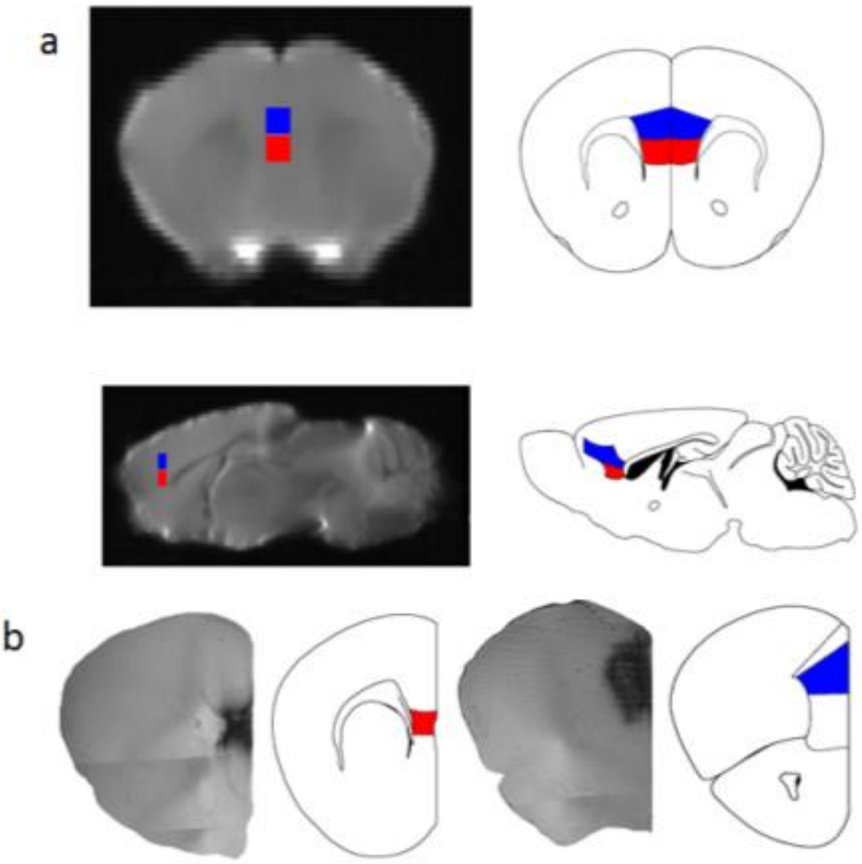

Each brain was placed in a standard space that was also matched (same dimensions, with the ability to overlay the same rulers place on the atlas, to stereotactically determine regions of interest) to the Paxinos and Franklin Mouse Atlas used to determine areas of connectivity from the IL (shown in red) and Pl (shown in blue) seeds. (**a**). Presented is a representation of the MRI images matched to slices in the atlas, as determined by specific anatomical landmarks (particularly the white matter tracts of the corpus callosum, the lateral and third ventricles and the aqueduct to the 4th ventricle, the internal capsule, and the hippocampus). (**b**) Shows the injection site of the BDA/ABC/DAB in the PL and IL area at 4x magnification using phase contrast. The representative atlas slice is shown to the right with IL highlighted in red and Pl highlighted in blue, for the PL injection the cingulate outlined more dorsally and the medial orbital cortex outlined below.

Figure 5.3-3 Tractography Data for the IL and PL Compared to Vertes (2004)

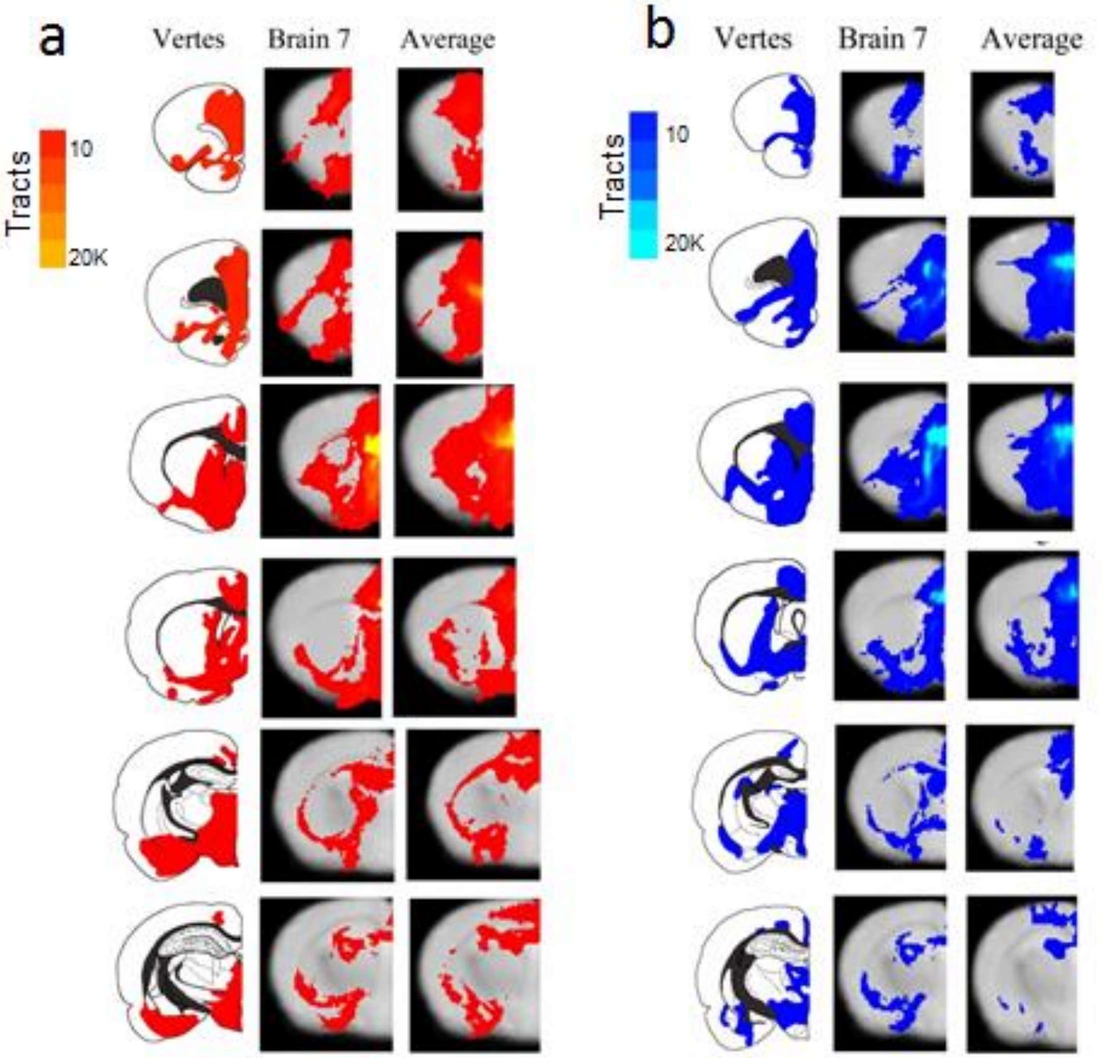

(**a**) Comparison of infralimbic cortex results between the Vertes retrograde tracing study using a rat, the probtrack results from a representative brain, and the probtrack results from all 10 brains placed into standard space and averaged. The images for the probtrack results presented in the right two columns are thresholded to at least 10 tracts passing through a voxel to help ameliorate results from voxels with few passing tracts in only one or two brains. Notice there is considerable overlap between the rat and mouse connectivity results, and also between the representative mouse and all the mice averaged together. (**b**) Comparisons of prelimbic cortex results of the connectivity between the Vertes (2004) Retrograde tracing study using a rat, the probtrack results from a representative brain, and the probtrack results from all 10 brains placed into standard space and averaged. The images for the probtrack results presented in the right two columns are thresholded to at least 10 tracts passing through a voxel to help reduce results from voxels with few passing tracts in only one or two brains. Notice there is considerable overlap between the rat and mouse connectivity results, and also between the representative mouse and all the mice averaged together.

Figure 5.3-4 Relative IL and PL Connectivity

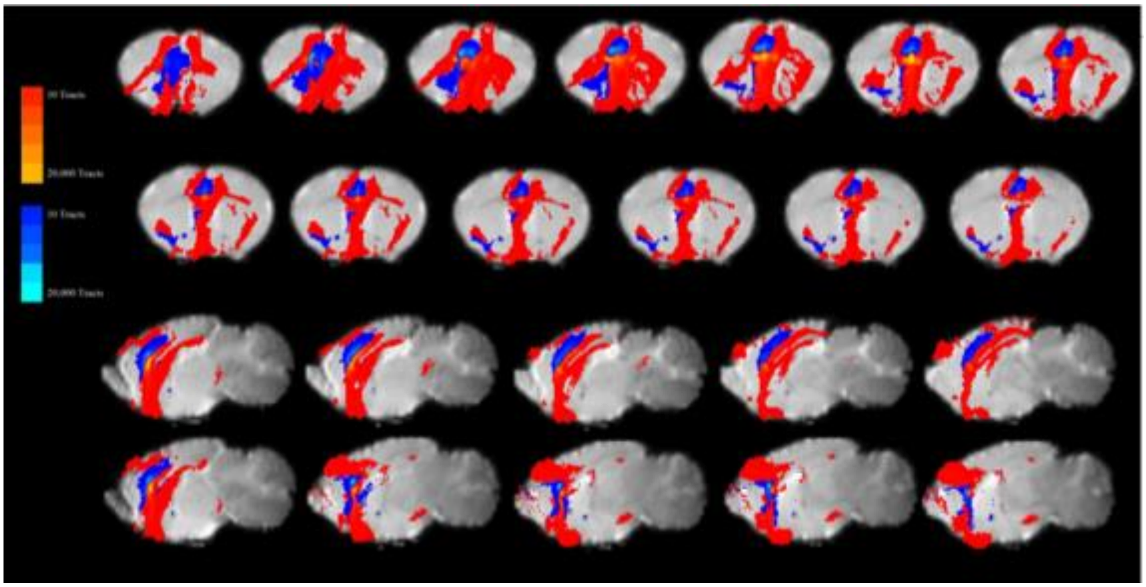

Given the large amount of overlap of probtrack results, the data from the average of the 10 mice were categorized as either Pl or IL dominant, by comparing the magnitude of tracts per voxel in the IL and the PL results, if the number of tracts passing through a voxel was greater for the probtrack results from the IL seed (Red), compared to the PL seed (Blue), the voxel was classified as an IL seed (and vice versa). The images above display the classification within the same standard space to directly compare the relative strengths of the connections. Most notable is the rather dominant character of the IL connectivity when compared to the PL.

Figure 5.4-1 Combined Results for IL to Amygdala and PL to Striatum

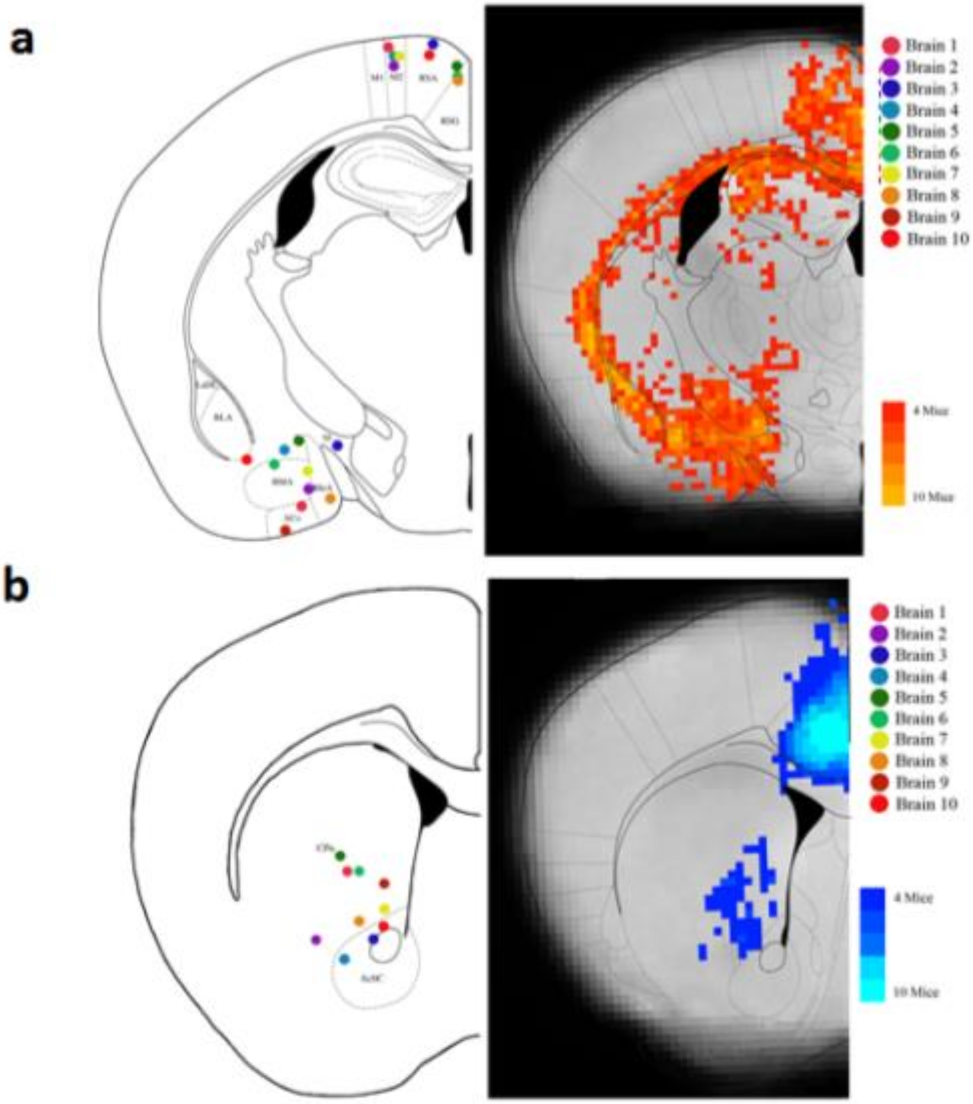

(**a**) The IL results in terms of the number of mice showing voxels with at least 10 tracts passing through. The probtrack results from the IL seed were thresholded at 10 or more tracts and where binarized (voxels showing connectivity of greater than ten tracts were set to a value of 1, those with no tracts or less than 10 tracts were set to a value of 0), the binarized results from each mouse were then summed creating a density map of the number of mice showing tracts in that voxel. This schematic was selected to show the connectivity to the BLA, BMA, and BLV. Additionally, for each brain individually, areas of interest, (like the RSA/RSG and BLA/BMA), were examined individually, and the voxel with the highest number of tracts passing through that area was plotted on the corresponding anatomical atlas image (on the left). (**b**) The PL results in terms of the number of mice showing voxels with at least 10 tracts passing through. This schematic was selected to show the connectivity to the Caudate-Putamen and the Cingulate.

Figure 5.4-2 Comparison of the BDA Projections of IL/PL.

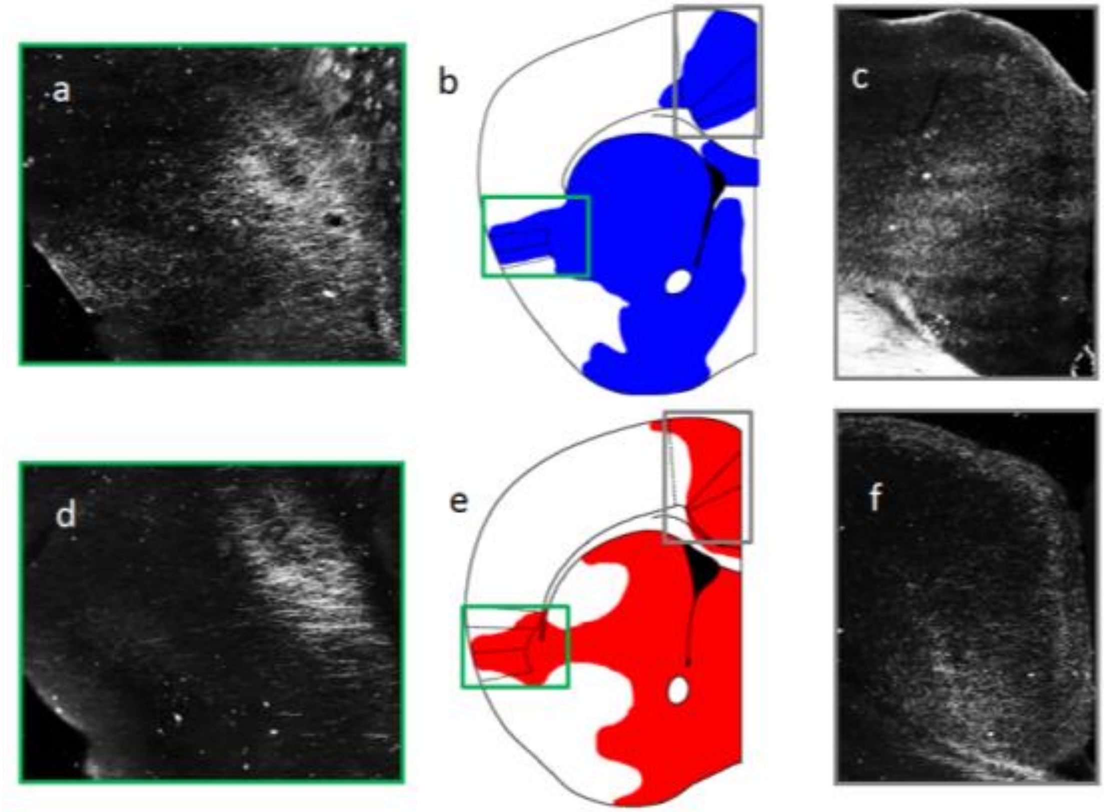

(**a**) Shows the BDA/ABC/DAB dark-field image composite of 20x images around the insula. (b) Shows a representative image of the areas showing BDA/ABC/DAB projections from the PL, the green box surrounds the insula represented in (**a**), while the grey box shows the cingulate projections highlighted in Part (**c**). (**c**) Shows the BDA/ABC/DAB dark field image composite of 20x images of the cingulate. (**d-f**) Shows the same approximate slices but with the IL injection site.

Figure 5.4-3. Comparison of the BDA Projections of IL/PL.

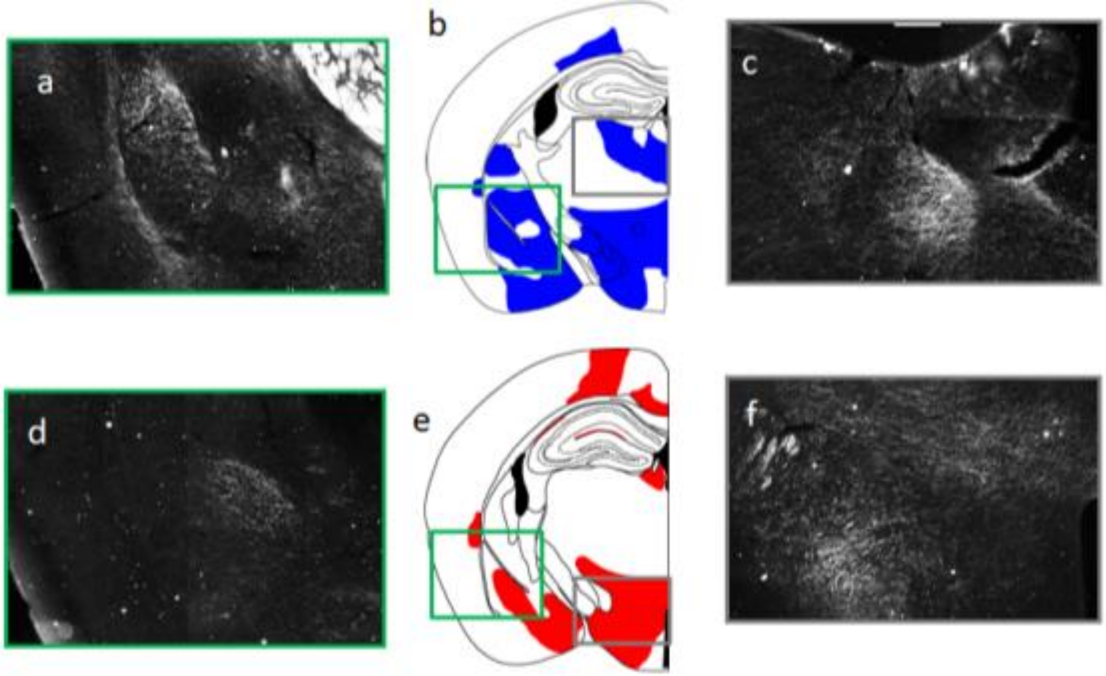

(**a**) Shows the BDA/ABC/DAB dark-field image composite of 20x images around the amygdala. (**b**) Shows a representative image of the areas showing BDA/ABC/DAB projections from the PL, the green box surrounds the amygdala represented in (**a**), while the grey box shows the tracts projecting to the mediodorsal thalamic nucleus highlighted in (**c**). (**c**) Shows the BDA/ABC/DAB dark field image composite of 20x images of the mediodorsal thalamic nucleus. (**d-f**) Shows the same approximately representative slices of the BDA/ABC/DAB staining from the IL injection site, with the exception that the grey box highlights the posterior hypothalamic regions and the dorsomedial hypothalamic nucleus.

Table 5.4-1 Compilation of the Tractography Data for IL and PL

Structure	Vertes IL	Brain 17 IL	Subtraction IL	Vertes PL	Brain 17 PL	Subtraction PL
Telencephalon						
Cortex						
Cingulate	+++	✓	✓+	+++	✓	✓
Ectorhinal	+	--	✓	--	--	--
Entorhinal	++	✓	✓	++	✓	--
Frontal						
Medial	+++	✓	✓+	+++	✓	✓
Lateral	--	-	-	--	-	-
Infralimbic	+++	✓	✓	+++	✓	✓
Insular						
Agranular	+	✓	✓	+++	✓	✓
Dysgranular	++	✓	✓	+++	--	✓
Granular	+	✓	--	--	--	--
Lateral Agranular (Motor)	--	--	--	--	--	--
Medial Agranular (Motor)	+	✓	✓+	+	✓	✓
Occipital	--	--	--	--	--	--
Orbital						
Lateral	+	✓	✓	+	✓	✓
Medial	+++	✓	✓+	+++	✓	✓
Ventral	+	✓	✓	+	✓	✓
Ventrolateral	+	✓	✓	+	✓	✓
Perirhinal	+	✓	✓	++	✓	✓
Piriform						
Anterior	--	✓	✓	+	✓	✓
Posterior	++	✓	✓	--	✓	✓
Prelimbic	+++	✓	✓	+++	✓	✓
Retrosplenial	+	✓	✓	+	✓	✓
Somatosensory I	--	--	✓	--	--	--
Somatosensory II	--	--	✓	--	--	--
Temporal	--	--	--	--	--	--
Nucleus Accumbens						
Shell	+	✓	✓+	+++	✓	✓
Core	+	✓	✓	+++	✓	✓+
Amygdala						
Anterior	++	✓	✓+	--	✓	--
Basolateral	+	✓	✓+	+++	✓	✓
Basomedial	+++	✓	✓+	+	✓	✓
Central	+++	✓	✓+	+++	✓	✓
Cortical	++			--		
Medial	+++	✓	✓+	--	✓	✓
Lateral	+	✓	✓+	+	✓	✓
Posterior	+			--		
Anterior Olfactory Nucleus	+++	✓	✓	+++	✓	✓+
Bed Nucleus of the Stria Terminalis	+++	✓	✓	--	✓	✓
Caudate-Putamen	++	✓	✓	++	✓	✓
Claustrum	--	✓	✓	+++	✓	--
Diagonal Band Nucleus						
Horizontal	+++	✓	✓+	+	✓	✓
Vertical	++	✓	✓	--	✓	--
Endopiriform Nucleus	++	✓	✓+	--	✓	--
Globus Pallidus	--	--	✓	--	--	✓+
Hippocampus						
Ammon's Horn	--	--	✓+	--	--	✓
Dentate Gyrus	--	--	✓+	--	--	✓
Subiculum	--	--	✓+	--	--	✓
Lateral Septum						
Dorsal Nucleus	++	✓	✓+	--	✓	✓
Intermediate Nucleus	+	✓	✓+	--	✓	✓
Ventral Nucleus	+++	✓	✓+	+	✓	✓
Lateral Preoptic Area	+++	✓	✓+	+	✓	✓
Magnocellular Preoptic Area	+	✓	✓+	+	✓	✓
Medial Preoptic Area	+++	✓	✓+	+	✓	✓
Median Preoptic Nucleus	++			--		
Medial Septal Nucleus	+	✓	✓	--	--	--
Olfactory Tubercle	++	✓	✓	+++	✓	✓+
Septofimbrial Nucleus	--	✓	✓+	--	✓	✓
Septohippocampal Nucleus	++	✓	✓+	--	✓	✓
Substantia Innominata	+++	✓	✓+	+	✓	✓
Tania Tecta						
Dorsal	++	✓	✓+	++	✓	✓
Ventral	+	✓	✓	--	✓	--
Ventral Pallidum	+	✓	✓	--	✓	--
Concordance to Vertes		=53/57 (0.93)	= 47/57 (0.825)		=44/57 (0.772)	=44/57 (0.772)

Diencephalon						
Thalamus						
Anterodorsal Nucleus	--	--	--	--	--	--
Anteromedial Nucleus	+	✓	✓	++	✓	✓+
Anteroventral Nucleus	--	--	✓	--	--	✓
Central Lateral Nucleus	--	--	--	+	--	--
Central Medial Nucleus	++	--	--	++	--	--
Interanteromedial Nucleus	++	--	--	+++	--	--
Intermediodorsal Nucleus	+++	--	✓	+++	--	✓+
Lateral Geniculate Nucleus	--	✓	✓	--	✓	✓
Lateral Habenula	+	✓	✓	+	✓	✓
Laterodorsal Nucleus	+	✓	✓	+	✓	✓
Lateroposterior Nucleus	+	-	✓	+	-	✓
Medial Geniculate Nucleus	--	✓	--	--	✓	--
Medial Habenula	--	--	✓	--	--	--
Mediodorsal Nucleus	++	--	✓	+++	--	--
Paracentral Nucleus	--	--	--	--	--	--
Parafasicicular Nucleus	+	--	--	-+	--	--
Paratential Nucleus	+++			+++		
Paraventricular Nucleus	+++	--	--	+++	--	--
Posterior Nucleus	--	--	--	---	--	--
Reticular Nucleus	--	✓	✓	--	✓	✓
Reuniens Nucleus	+++	✓	✓+	+++	✓	✓
Rhomboid Nucleus	++	--	✓	+	✓	✓+
Submedial Nucleus	--	--	--	--	--	--
Ventral Anterior-lateral Nucleus	--	--	✓	--	--	✓
Ventral Basal Complex	--			--		
Concordance to Vertes		= 12/24 (0.50)	= 14/24 (0.583)		= 12/24 (0.50)	= 13/24 (0.54)
Hypothalamus						
Anterior Nucleus	++	✓	✓+	--	--	✓
Dorsal Hypothalamic Area	++			+		
Dorsomedial Nucleus	+++	✓	✓+	+	--	✓
Lateral Nucleus	+++	✓	✓+	++	✓	✓
Mammillary Bodies	+	--	--	--	--	--
Paraventricular Nucleus	--	--	--	--	--	--
Perifornical Area	+++	--	--	++	--	--
Posterior Nucleus	+++	--	--	+	--	--
Premammillary Nucleus	+	--	--	--	--	--
Supramammillary Nucleus	++	--	--	++	--	--
Ventromedial Nucleus	--	--	--		--	--
Concordance to Vertes		= 5/10 (0.50)	= 5/10 (0.50)		=5/9 (0.555)	= 5/9 (0.555)
Subthalamus						
Fields of Forel	+	--	--	--	--	--
Zona Incerta	+	--	✓	--	--	--
		= 0/2 (0.00)	= ½ (0.5)		= 2/2 (1.00)	= 2/2 (1.00)
Brain Stem						
Anterior Pretectal Nucleus	--	--	--	--	--	--
Barrington's Nucleus	+	--	--	+	--	--
Cuneiform Nucleus	--	--	--	+	--	--
Dorsal Motor Nucleus (Vagus)	+	--	--	--	--	--
Dorsal Raphe Nucleus	+	✓	--	+++	✓	--
Dorsal Tegmental Nucleus	--	--	--	--	--	--
Interpeduncular Nucleus	++	✓	--	+	✓	--
Laterodorsal Tegmental Nucleus	+	--	--	+	--	--
Locus Coeruleus	+	--	--	--	--	--
Mesencephalic Reticular Formation	+	--	--	+	--	--
Nucl+eus Ambiguus	--	--	--	--	--	--
Nucleus Incertus	+	--	--	++	--	--
Nucleus Gigantocellularis	--	--	--	+	--	--
Nucleus Pons	--	✓	--	--	✓	--
Nucleus Pontis Caudalis	--	--	--	--	--	--
Nucleus Pontis Oralis	--	--	--	--	✓	--
Nucleus Solitary Tract	+	--	--	--	--	--
Parabrachial Nucleus	++	✓	--	--	✓	--
Pedunculopontine Tegmental Nucleus	++	--	--	+	--	--
Periaquaductal Gray Matter	+	--	--	+++	--	--
Peripeduncular Nucleus	+++	--	--	+	--	--
Reticular Tegmental Nucleus	+	✓	--	--	✓	--
Retrorubral Areas	--	--	--	+	--	--
Rostro-ventrolateral Medulla	--	--	--	--	--	--
Surpalemniscal Nucleus	--			++	--	--
Superior Colliculus	--	--	--	--	--	--
Ventral Tegmental Area	++	✓	✓	++	✓	--
Ventral Tegmental Nucleus	--	--	--	--	--	--
Concordance with Vertes		= 16/27 (0.592)	= 13/27 (0.481)		= 13/27 (0.481)	= 14/27 (0.519)
Total Concordance		= 86/120 (0.717)	= 80/120 (0.667)		= 76/119 (0.639)	= 78/119 (0.655)

True Detect		55	56		40	39
True No Detect		31	24		36	39
False Detect		7	14		19	16
False No Detect		27	26		24	25
TD/(TD+FD)		=55/62 (0.890)	=56/70 (0.80)		=40/59 (0.678)	= 39/55 (0.709)
TND/(TND+FND)		=31/58 (0.534)	=24/50 (0.480)		= 36/60 (0.60)	= 39/64 (0.609)

Key To Table
Vertes: +++ robust
Vertes: ++ strong
Vertes: + Weak
Vertes: – None
Probtrack: ✓✓voxel of probtrack present in that area
Probtrack: ✓+ voxel of probtrack present in that area (but so is the other seed, but this area shows more voxels than other area)
Probtrack: – No voxels in that area

Chapter 6:

A Comparative Analysis of Mouse and Human Medial Geniculate Nucleus Connectivity: A DTI and Classical Tracing Study

6.1 Context, Author Contribution, and Acknowledgement of Reproduction

The following chapter presents the application of *ex vivo* DWI probabilistic tractography to the mouse brain to study the projections of the posterior thalamic nuclei, especially the closely situated medial genicular nucleus, suprageniculate nucleus, and paraintralaminar nucleus. The results of the probabilistic tractography were compared to a parallel study using the anterograde tracer biotinylated dextran amine in the posterior thalamic nuclei. Further, the *ex vivo* DWI probabilistic tractography results were compared to *in vivo* probabilistic tractography results in human participants. The dissertation author contributed to the paper by preparing the *ex vivo* brains, imaging those brains with the DWI scan, pre-processing and analyzing the data, conducting the injections of the anterograde tracer and the follow-up tracing work, analyzing the DWI tractography in humans, and was a main contributor to the writing of the paper. The chapter is reproduced with minor edits from Keifer Jr, O.P., Gutman, D.A., Hecht, E.E., Keilholz, S.D., Ressler, K.J. (Revise and Resubmit). “A Comparative Analysis of Mouse and Human Medial Geniculate Nucleus Connectivity: A DTI and Classical Tracing Study”. *Neuroimage*

6.2 Introduction

The thalamic nuclei are critical for interfacing and organizing cortical and subcortical connectivity and functioning. Traditionally, thalamic nuclei like the medial and lateral geniculate have been described as relay stations for auditory and visual information, respectively. For example, the most studied function of the medial geniculate nucleus

(MGN) is its role in passing auditory information from the inferior colliculus to the auditory cortex (Monakow 1914, Poliak 1926, Walker 1937, Tunturi 1946, Mesulam and Pandya 1973, Ryugo and Killackey 1974, Jones 1985, Redies, Brandner et al. 1989, Budinger, Heil et al. 2000, Llano and Sherman 2008, Crippa, Lanting et al. 2010, Geiser, Notter et al. 2012, Horie, Tsukano et al. 2013). However, there is also evidence the MGN has a far broader role in multisensory processing (Wepsic 1966, Love and Scott 1969, Blum, Abraham et al. 1979, Brinkhus, Carstens et al. 1979, Carstens and Yokota 1980). Further, there is growing evidence that the MGN does not operate in isolation from other posterior thalamic nuclei (i.e., the posterior intralaminar, suprageniculate, and peripeduncular nuclei) which are in very close proximity and may be part of a more collective functional system(Winer and Morest 1983, Linke and Schwegler 2000). Interestingly, in addition to the thalamocortical pathway, there is preliminary evidence that the MGN and surrounding nuclei ('MGN/S',) project to the amygdala (Carter and Fibiger 1977, Ottersen and Ben-Ari 1979, LeDoux, Ruggiero et al. 1985, LeDoux, Sakaguchi et al. 1985, Shinonaga, Takada et al. 1994), insula/parainsular area (Guldin and Markowitsch 1984, Clasca, Llamas et al. 1997, Linke and Schwegler 2000), caudate/putamen(LeDoux, Ruggiero et al. 1985), globus pallidus(Moriizumi and Hattori 1992), the hypothalamus(LeDoux, Sakaguchi et al. 1984, LeDoux, Ruggiero et al. 1985), the thalamus(LeDoux, Sakaguchi et al. 1984, LeDoux, Ruggiero et al. 1985), and the midbrain(Moriizumi and Hattori 1992). Additionally, the MGN/S receives input from the globus pallidus(Shammah-Lagnado, Alheid et al. 1996), the auditory cortex(Roger and Arnault 1989) (Winer, Diehl et al. 2001), the insula(Cranford, Ladner et al. 1976), the cerebellum(Raffaele, Sapienza et al. 1969) (Zimny, Sobusiak et al. 1981) , and the inferior colliculus(Benevento and Fallon 1975).

Because the MGN/S plays a central role in sensory processing, a thorough understanding of its anatomy and function are important for understanding certain disorders. For example, the function of the MGN/S has been well-established in auditory fear learning (LeDoux, Sakaguchi et al. 1984, LeDoux, Ruggiero et al. 1985, LeDoux, Sakaguchi et al. 1985, LeDoux, Sakaguchi et al. 1986). Further, recent studies have suggested that thalamic auditory processing may play a role in tinnitus(Muhlau, Rauschecker et al. 2006, Landgrebe, Langguth et al. 2009, Crippa, Lanting et al. 2010, Aldhafeeri, Mackenzie et al. 2012, Su, Luo et al. 2012), attention deficit disorder(Schweitzer, Lee et al. 2004, Xia, Li et al. 2012, Hart, Radua et al. 2013), and schizophrenia(Dorph-Petersen, Caric et al. 2009, Smith, Wang et al. 2011). However, the broad network connectivity of the MGN/S is not currently well-established nor is the role of these connections. The majority of the cited work above has focused on the rat model. Given that the mouse model offers opportunities for neuro-genetics research, and work in human patient populations can directly address the role of the MGN/S in disease studies, studying both is imperative to future progress.

Unfortunately, there is a paucity of studies addressing these issues. Furthermore, existing MGN/S connectivity work uses different methodologies in mice versus humans - mouse MGN/S connections were studied using injection tract tracing(Llano and Sherman 2008, Horie, Tsukano et al. 2013), while human MGN/S connections to the amygdala and the inferior colliculus used diffusion tensor imaging (DTI)(Devlin, Sillery et al. 2006, Crippa, Lanting et al. 2010, Javad, Warren et al. 2013). Furthermore, given that anatomy and physiology differ in some systems between humans and other species (Preuss 2000, Manger, Cort et al. 2008, Smulders 2009, Carlson 2012), verification of homologous MGN/S connectivity across species is an important foundational step for translational research.

Here we present a whole-brain exploration and comparison of the general patterns of connectivity of the mouse and human MGN/S using DTI. Importantly, DTI is often cited as a translationally useful tool and it has been successfully used for comparative analyses of connectivity in humans and other primates (Rilling, Glasser et al. 2008, Thiebaut de Schotten, Dell'Acqua et al. 2012, Zhang, Guo et al. 2012, Hecht, Gutman et al. 2013). However, there is a dearth of studies linking small animal models (e.g., mouse) to humans. Therefore, the objectives of the following paper are to address the broad patterns of connectivity of the human and murine MGN/S, to provide evidence for the comparative utility of DTI, and to validate the results of small animal DTI results with classical tracing. First, we hypothesized that humans and mice would show connectivity patterns between MGN/S and the amygdala, auditory cortex, caudate/putamen, globus pallidus, thalamus, hypothalamus, cerebellum, and insula. Additionally, we sought to further validate(Gutman, Keifer et al. 2012) the mouse probabilistic tractography results by comparing them to anterograde tracing results in the MGN/S. We hypothesized that the mouse probabilistic tractography results would parallel the patterns of connectivity evaluated using anterograde tracing.

6.3 Materials & Methods

6.3.1 Human Participants

All study procedures were approved by the institutional review board of Emory University. A total of 10 African American women and 3 African American men, aged 20-52 (mean age of 38 years old) were recruited under a broader, on-going neuroimaging study of risk factors for PTSD in civilians(Fani, King et al. 2012, Fani, Gutman et al.

2013). The participants selected for the current student were randomly sampled from the control arm of the study. All participants underwent a screening procedure to ensure there was no active use of psychotropic medication, no current alcohol or substance abuse, no history of psychiatric disorders, no history of head injury or other neurological disorders. All female participants received a pregnancy test to ensure that they were not pregnant prior to the imaging session.

6.3.2 Animal Studies

All imaging was conducted on 8 week old C57BL/6J male mice (n=10) that had received no prior handling or training The, 10 mice were placed under anesthesia using ketamine/ dexmedetomidine, were perfused with 10mls Phosphate Buffered Saline (PH 7.4), followed by 10mls 4% paraformaldehyde (PF)/PBS and then post-fixed (for 24 hours) in the same 4% PF/PBS, then rinsed in PBS and stored at 4˚C in PBS until they were embedded in an agarose-gadolinium (III) oxide matrix for imaging. Previous work has shown the validity and utility of using this method (Gutman, Keifer et al. 2012).

A total of five 8 week old C57BL/6J male mice were used for the classical tracing (using 10,000 MW biotinylated dextran amine, BDA) arm of the study. The details of the BDA method are presented in our previously published work(Gutman, Keifer et al. 2012). In brief, injections of 0.15 microliters of BDA were placed into the mouse MGN using a Stoelting *Just for Mice* Stereotax (Wood Dale, Illinois) with a Hamilton Neuros 5 microliter syringe driven by a World Precision Instruments UMC4-J pump controller and UMP3 pump (Sarasota, Fl). The targeting of the MGN was -3.0mm AP, +/- 2.2 mm ML, - 3.2 mm DV from Bregma. The duration of injection was approximately 1 minute with the syringe left in place for 10 minutes and withdrawn over the course of 1 minute.

6.3.3 Magnetic Resonance Imaging - Human

All human MRI scanning was conducted on a research-dedicated Siemens 3-Tesla TIM-Trio Scanner located at the Emory University Hospital as part of the Biomedical Imaging Technology Core (BITC). Details of the parameters used for the diffusion weighted imaging scans are found in previous work (Fani, King et al. 2012). In brief, the volumes had a slice thickness of 2mm, imaging matrix, of 128 x 128, and a field of view of 256 mm x 256 mm, TE = 154 ms, TR 13500 ms, and b = 1000 s/mm^2. There were 60 diffusion weighted gradients volumes with 3 b0 volumes. Additionally, T1 anatomical scans were acquired with an MPRAGE sequence with a slice thickness of 1mm, imaging matrix 256 x 256, FOV = 256 mm x 256 mm, TE = 3.02 ms and TR = 2600 ms.

6.3.4 Magnetic Resonance Imaging – Mouse

All mouse MRI scanning was conducted on a research dedicated Bruker 9.4 Tesla MRI scanner. All brains were scanned using our previously designed *ex vivo* procedure (Gutman, Keifer et al. 2012, Gutman, Magnuson et al. 2013). In brief, perfused mouse brains were embedded in a gadolinium agarose matrix and scanned at multiples of 6 with a T2 Rare sequence and a 60 direction DTI sequence. T2-weighted images were first acquired at 161 micron isotropic resolution (TE = 26ms, matrix 256 x 512, 20 averages, scan time ~ 16 hours). Diffusion Tensor images were then acquired using a 2-D spin-echo based sequence with 200 micron isotropic resolution. (TE = 26.9 ms, TR=10000 ms, matrix size of 256 x 128, 60 axial slices collected/tube, 60 gradient directions with a diffusion weighting b=2000 s/mm^2, and 3 b0 images).

6.3.5 Diffusion Tensor Imaging Analysis

All post acquisition processing was conducted as analogously as possible between the human and mouse data sets; differences in processing are noted. Initially, the mouse volumes were isolated from the raw imaging volume that contained six mouse brains as previously described(Gutman, Keifer et al. 2012). From there, the human and mouse diffusion volumes were processed by isolating them either from the skull (human) or the embedding matrix (mouse), using the Brain Extraction Toolkit (BET(Smith 2002), http://fsl.fmrib.ox.ac.uk/fsl/fslwiki/BET). Both human and mouse brains were then processed using the FSL DTI pipeline in preparation for probabilistic tractography (FDT) (Behrens, Johansen-Berg et al. 2003, Behrens, Berg et al. 2007), http://fsl.fmrib.ox.ac.uk/fsl/fslwiki/FDT).

The MGN/S seeds were based on anatomical localization with the use of the Atlas of the Human Brain (with guidance from (Devlin, Sillery et al. 2006)) and the Paul Allen mouse reference atlas (Lein, Hawrylycz et al. 2007). These anatomically placed seeds were then cross referenced with tractography results from seeds placed within the auditory cortex and inferior colliculus (**Figure 6.3-1**). In particular, the MGN/S regions of interest (ROIs) were drawn in T1 (humans) weighted high-resolution space (e.g., the MGN/S is ventral to the ventral posterolateral thalamic nucleus and anterior pulvinar nucleus, dorsal to the cerebral peduncle, medial to the lateral geniculate, and lateral to the dorsal trigemino-thalamic tract). In parallel, seeds of the primary auditory cortex, primary visual cortex, and the inferior colliculus were used to generate probabilistic connectivity maps. These diffusion-space tractography maps were then registered to the higher resolution anatomical space. The anatomically defined MGN/s seed was checked against the tracts from the auditory cortex and inferior colliculus. The visual cortex tracts were also generated and used to ensure that the MGN/S was isolated from the lateral geniculate nucleus. The mouse MGN/S seeds were analogously generated and checked, though their anatomical identification is significantly easier given the anterior to posterior displacement of the nuclei (e.g., posterior to the LGN, medial to the hippocampus, lateral to the midbrain). Probabilistic tractography, with multi-fiber reconstruction, was then generated for each voxel within the MGN/S seed mask (changes from default settings include the use of fractional anisotropy constrained tracking, Euler streamlining and a curvature threshold of 0.1). A priori exclusions masks were placed in the occipital lobe and pre/postcentral gyrus to help mitigate spurious tractography results from the lateral geniculate and ventrolateral nuclei which are located adjacent to the medial geniculate. The results were then back-transformed into the high-resolution mouse T2 or human T1 space and transformed into a common imaging space (e.g., Montreal Neurological Institutes 152 Brain 6th Generation(Grabner, Janke et al. 2006) for humans or our own standard mouse space template(Gutman, Keifer et al. 2012, Gutman, Magnuson et al. 2013)). The resulting tract distributions were then set from a minimum threshold 0.1% to a maximum of 1% for clarity of data presentation (e.g., if the highest number of tracts passing through a single voxel across the whole brain was 25,000 the threshold was set at a minimum of 25 tracts passing through a voxel)(Devlin, Sillery et al. 2006). These results were then binarized and summed (providing a measure of how many participants/animals showed tracts in that area) and/or averaged for analysis (showing the average number of tracts passing through that area). The human results were submitted to FSL Atlasquery function to determine the areas of the brain were the MGN connectivity mapped onto the MNI152 space. The mouse results were compared to the Paul Allen Brain mouse reference atlas (Allen Institute for Brain Science, Allen Mouse Brain Atlas (Lein, Hawrylycz et al. 2007), http://mouse.brain-map.org/static/atlas) to determine areas of connectivity.

6.4 Results

6.4.1 Isolation of Human MGN/S

The results presented in **Figure 6.3-1** illustrate the anatomical localization of the medial geniculate in each human participant (**Figure 6.3-1 a**) based on the Mai, Paxinos and Voss Atlas of the Human Brain(Mai, Paxinos et al. 2008). As a form of validation for the accuracy of these seed placements, these localizations where crossed referenced to projections from the inferior colliculus (**Figure 6.3-1b**) and the primary auditory. The visual cortex connectivity distribution was used to confirm the differentiation of the medial geniculate nucleus from the lateral geniculate nucleus (**Figure 6.3-1 c**). Each individual human brain (shown in a consistent position across **Figure 6.3-1's** surrounding border, with the male participants shown on the lower right three brains) showed the same pattern of the auditory cortex connecting more medially (shown in the red to yellow overlay) when compared to the visual cortex projections which had more lateral projections (shown in the light to dark blue overlay). Importantly, all of the anatomically defined MGN/S seeds fell within the pathway of the inferior colliculus and auditory cortex and did not require modification.

6.4.2 MGN/S Probabilistic Connectivity in Humans

Following MGN/S isolation and seed generation, the connectivity of the human MGN/s was analyzed and the results are presented in **Figure 6.4-1.** The results (**Figure 6.4-1,a**) highlight the human probabilistic connectivity between the MGN/S and the amygdala, caudate, putamen, and globus pallidus. Moving more posteriorly, **Figure 6.4-1b** details the connections between the MGN/S and the auditory cortex, middle temporal cortex, insula, thalamus, hypothalamus, and portions of the midbrain. Moving most posteriorly, **Figure 6.4-1c** shows the connectivity of the MGN/S and the cerebellum. All results presented in the **Figure 6.3-1** and **Figure 6.4-1** are using modified images from the high-resolution brain atlas (www.thehumanbrain.info, Dusseldorf, Germany). The cerebellar atlas used in **Figure 6.4-1c**, is included in the FSL atlas resources(Diedrichsen, Balsters et al. 2009). The results are tabulated in the second column of **Table6.4-1** with the number of participants showing the pattern of connectivity. It is interesting to note that though a seed in the auditory cortex was used as an accuracy check of the atlas based placement of the MGN/S seed, the consequential seeding of the MGN/S did not show equally robust projections to the auditory cortex. Overall, the tractography results were highly consistent across participants despite differences in age and gender (nearly all projections were in 100% of the participants)

6.4.3 MGN/S Probabilistic Connectivity in Mice

Paralleling the results found in humans, the results of the probabilistic connectivity of the MGN/S in mice are presented in **Figure 6.4-2**. Moving from anterior to posterior, **Figure 6.4-2a** highlights the connectivity of the MGN with the caudate/putamen. In **Figure 6.4-2b**, the connectivity maps show connections to the auditory cortex, amygdala, thalamus, hypothalamus, and portions of the midbrain. Because there is extensive connectivity shown in this panel, both a summed and threshold image plus the average results are presented in the central left figure. **Figure 6.4-2c** shows the connections between the MGN and the cerebellum. For **Figure 6.4-2**, all presented atlas sections are from modified from the Allen Brain Atlas (www.brain-map.org). The results are also presented in **Table6.4-1** for comparisons to the results in human participants. Like the human results, the mice showed remarkable consistency across the animals imaged. Further the patterns of connectivity of the MGN/S were concordant with those found in the Human participants.

6.4.4 Mouse Anterograde Tracing Results

Of the five mice used for the study, three mice had injections in and around the area encompassing MGN/S. Of the three, one showed the most concordance with the MGN/S seed used for the mouse data. The results from the anterograde tracer injections for that mouse are summarized in **Table6.4-1** and **in Figure 6.4-3.** In agreement with the mouse tractography results there were fibers of passage and termination through the thalamus, hypothalamus, and midbrain. Additionally, there were dense projections that terminated in the auditory cortex, amygdala, and the caudate/putamen. The other two mice showed comparable patterns of connectivity though less dense because the injection site for these animals was not as large (data not shown).

6.5 Discussion

Though the classical role of the MGN is to relay information to the auditory cortex, the numerous other projections from the MGN and surrounding area need further exploration. Here we have shown that the connections previously found in rats also exist in both humans and mice. These results have extensively expanded our understanding of both mouse and human MGN connectivity over previous work. Further, these results suggest a common pattern of connectivity between mice, rats, and humans, suggesting that these connections are likely evolutionarily conserved throughout the mammalian family tree. Additionally, we have further expanded the corroboration of DTI based probabilistic tractography in mice with the use of the anterograde tracing molecules biotinylated dextran amine(Gutman, Keifer et al. 2012).

Our comparison of the broad patterns of probabilistic tractography in mice and humans revealed connections between the MGN/S and the auditory cortex, amygdala, globus pallidus, caudate/putamen, hypothalamus, thalamus, and cerebellum. Interestingly, we also saw connections with the middle temporal cortex and posterior cingulate (e.g., retrosplenial cortex) that have not been previously reported (discussed further below). A review of the literature reveals that the functional role of these specific connections is not apparent. Of the medial geniculate connections, the most studied is the reciprocal connection between the amygdala (central and lateral) and MGN. Early work by Ledoux and colleagues showed that the connection between the auditory thalamus and the amygdala, but not necessarily the auditory cortex to the amygdala, was important for auditory fear conditioning in the rat (LeDoux, Sakaguchi et al. 1984). Further exploration of the connections from the MGN provided evidence that disruptions of the MGN - amygdala tracts, but not to the caudate/putamen, resulted in diminished fear conditioning responses (LeDoux, Ruggiero et al. 1985, Iwata, LeDoux et al. 1986, LeDoux, Sakaguchi et al. 1986). However, whether this pathway serves a broader role in cognition and behavior is still unclear.

With regards to the connections with the caudate-putamen, our results are also consistent with past work in the rat(Ryugo and Killackey 1974, LeDoux, Sakaguchi et al. 1984) that showed the primary source of these projections were the ventral and dorsal subdivisions of the MGN (Ryugo and Killackey 1974). Beyond tract tracing, there is converging evidence for the connection in the form of evoked unit responses in striatal neurons when electrical stimulation is applied to the medial geniculate nucleus(Clugnet, LeDoux et al. 1990). With the pallidum there is evidence in the rat that there are reciprocal projections between the medial portion of the medial geniculate and the globus pallidus (Moriizumi and Hattori 1992, Shammah-Lagnado, Alheid et al. 1996). The role of the connection between the MGN and globus pallidus is unclear. Clearly there is a lack of research on the role of the direct connections between the MGN and the caudal portions of the caudate-putamen and globus pallidus. However, looking more broadly, there is accumulating evidence for the basal ganglia in processing auditory information, including projections from the auditory cortex(McGeorge and Faull 1989). Such work is now coalescing into a broadly accepted theory that the basal ganglia is involved in temporal auditory perception (e.g., beat perception)(Grahn and Brett 2007), in the synchronization of auditory and visual sensory information(Freeman, Ipser et al. 2013), in the processing of language(Lieberman, Friedman et al. 1990), and in vocal learning and perception in song birds(Hessler and Doupe 1999) (Brainard and Doupe 2000). Inputs from the MGN/s (and vice versa) into the basal ganglia may sub-serve important roles in these facets of cognition and behavior.

The connections between the hypothalamus and the MGN/S implicate a potential neuroendocrine role. Both the BDA tracing results and the DTI results suggest that there is a fair degree of connectivity between the MGN/S and the hypothalamus (albeit the BDA staining density is lower than seen in the other areas). Of the results presented here with humans and mice there is a match to previous work in rats showing a projection from the immediately adjacent area of the MGN to the ventromedial hypothalamus (LeDoux, Sakaguchi et al. 1984). A study of this connection has shown that lesions to the MGN, and potentially surrounding nuclei, drastically reduce the release of corticosterone released in response to audiogenic stress (restraint and ether stress resulted in normal corticosterone release)(Campeau, Akil et al. 1997). Interestingly, with MGN lesioning, there was also a commiserate decrease in the c-fos activity of the paraventricular hypothalamus. Notably the paraventricular hypothalamus lies immediately adjacent to the ventromedial hypothalamus. While the authors of the study proposed their own pathway for activation of the paraventricular nucleus, they did not include the ventromedial hypothalamus as part of the pathway. However, a more recent study has shown that there is direct input, including input from glutamatergic neurons, from the ventromedial nucleus into the paraventricular nucleus potentially explaining their findings (Ulrich-Lai, Jones et al. 2011). Further, the results of the BDA staining here showed a direct connection between the MGN/S and the paraventricular nucleus providing a further pathway to consider. Overall, like the direct connections of the MGN to the striatum, little work has focused on the connection the MGN/S to the hypothalamus.

Regarding the connectivity between the MGN/S and the rest of the thalamus, there is evidence that the immediately adjacent areas around the MGN/S send projections to the subparafasicular nucleus in rats (LeDoux, Sakaguchi et al. 1984, LeDoux, Ruggiero et al. 1985, Wang, Palkovits et al. 2006). We show the same connections using our classical tracing study in mice. Interestingly, very little is known about the subparafasicular nucleus, though it is known that it is the point of convergence of input from medial prefrontal, insular, and ectorhinal cortices, as well as the lateral septum, amygdala, portions of the hypothalamus, periaqueductal gray, and several other nuclei(Wang, Palkovits et al. 2006). Based on the source of these afferent inputs it has been postulated that the area is involved in reproductive, visceral, nociceptive, and auditory functions. Looking more broadly at **Table6.4-1** and the results in the **Figure 6.4-1**, **2**, **3**, it would appear that there are numerous other connections between the MGN/S and thalamus that should be explored.

Overall, the probabilistic tractography results show that there are large similarities in the broad patterns of connectivity between mice and humans. These similarities suggest that these connections have functional utility though these functions are still poorly understood. Interestingly, there are points of discordance in the comparison between the two species. The mouse data shows projections to the middle temporal cortex (unilaterally) and the also the retrosplenial cortex (part of the posterior cingulate cortex). Neither of these areas has known direct connectivity to MGN or adjacent nuclei. Further analysis will be necessary to determine whether these are previously unknown connections or the result of probabilistic tractography picking up robust tracts adjacent to the connectivity of the MGN/S. An example of the later problem would be if the algorithm picked up the well-known robust reciprocal connections between the anterior thalamus and retrosplenial cortex (Rose and Woolsey 1948, Domesick 1969, Niimi 1978) . The human data showed connectivity between the MGN/S and the insula, which is concordant with other species (as aforementioned); however the mouse data did not show this finding. The lack of a finding in the mouse likely reflects large robust tracts adjacent to the MGN/S (e.g., internal capsule), dominating the majority of the tractography results and mitigating other projections to cortical areas.

There is significant evidence presented here for the convergence of DTI based probabilistic tractography and the classical tracing findings. While previous work exists identifying a few points of specific corroboration between classical tracing and probabilistic tractography (Gutman, Keifer et al. 2012), here we provide a more comprehensive comparison between the two methods. In our data, probabilistic tractography highlight the major fasciculi that contain the projections from the MGN/S seed including the internal capsule, medial lemniscus, and cerebral peduncle. Notably, these same major white matter projections were also noted in the classical tracing data. Furthermore, the conjunction of the two techniques reveals that DTI was able to pick up fibers passing through large portions of the midbrain, thalamus and hypothalamus, which are heterogeneous mixtures of white and grey matter. Finally, the results from the both techniques highlighted many of the patterns of connectivity seen in the rat. Importantly, the corroboration of the probabilistic tractography with the classical tracing helps to validate the MRI based techniques while the comparison with human data provides strong evidence for its use as a translational tool. It should also be considered that the tracing employed in the study was only anterograde, and there are likely extensive projections to the MGN/S that are captured by the probabilistic tractography but not our classical tracing.

In terms of study limitations there are few notable points that need addressed with regards to human participant selection, differences in image acquisition, and finally overall data interpretation limitations. First, the human arm of the study was conducted with all African Americans, mostly with female participants and the average age was older than most imaging studies. Looking at the patterns of the three men versus the ten women in all figures suggest that there is not an obvious gender difference. Likewise, age effects were not readily apparent when looking at connectivity between the participants in their 20s and 50s. With regards to race, there is no evidence readily available suggesting it would affect connectivity, but future studies are encouraged to investigate the question further. With regards to imaging acquisition, it should be remarked that the mouse DTI volumes were collected *ex vivo* while the human volumes were collected *in vivo*. Our previous work has suggested that the *ex vivo* images reliably recapitulate the results seen with classical tracing, as does this current study(Gutman, Keifer et al. 2012). Whether systematic differences exist between *in vivo* and *ex vivo* studies remains unanswered, though both appear to recapitulate classical tracing results. Finally, with regards to the analysis, the use of DTI imaging naturally limits the resolution and hence resolving power of the analysis and is also not predictive of direction (e.g., anterograde vs. retrograde). Therefore, it is not possible to further elucidate which of the MGN or surrounding nuclei are contributing to the different paths of connectivity with our current data sets. Additionally, the collection of higher resolution data using conventional imaging requires prohibitively long scan times, though advances are growing in the field to ameliorate some of these concerns(Muller, Vernikouskaya et al. 2012). Looking more broadly, DTI is used widely to make conclusions concerning human patterns of connectivity and also changes in the diffusion measurements of fractional anisotropy and mean diffusivity. Understanding what these measurements are showing requires the use of well validated animal models, as in the case of this study.

Overall, the preceding discussion and findings provide a foundation against which to study the role of these conserved but poorly understood patterns of MGN/S connectivity. Given the growing literature that implicates the auditory thalamic nuclei in disorders as diverse as tinnitus and schizophrenia there is a need to study these pathways and their function. Additionally, excellent work has begun to demonstrate the role of mice in understanding stress related brain structure and function (Golub, Kaltwasser et al. 2011, Grunecker, Kaltwasser et al. 2013). Our data provide a precedent for the use of DTI tractography in a comparative and translationally meaningful way with small animal model. Furthermore, we present at least two lines of evidence that DTI tractography in mice recapitulates the patterns of connectivity seen with classical tracing techniques. These findings provide a foundation for future experimental work examining aberrations in connectivity with experimental small animal genetically tractable models like the mouse.

Figure 6.3-1 Probabilistic Connections of the Visual Cortex and Auditory Cortex.

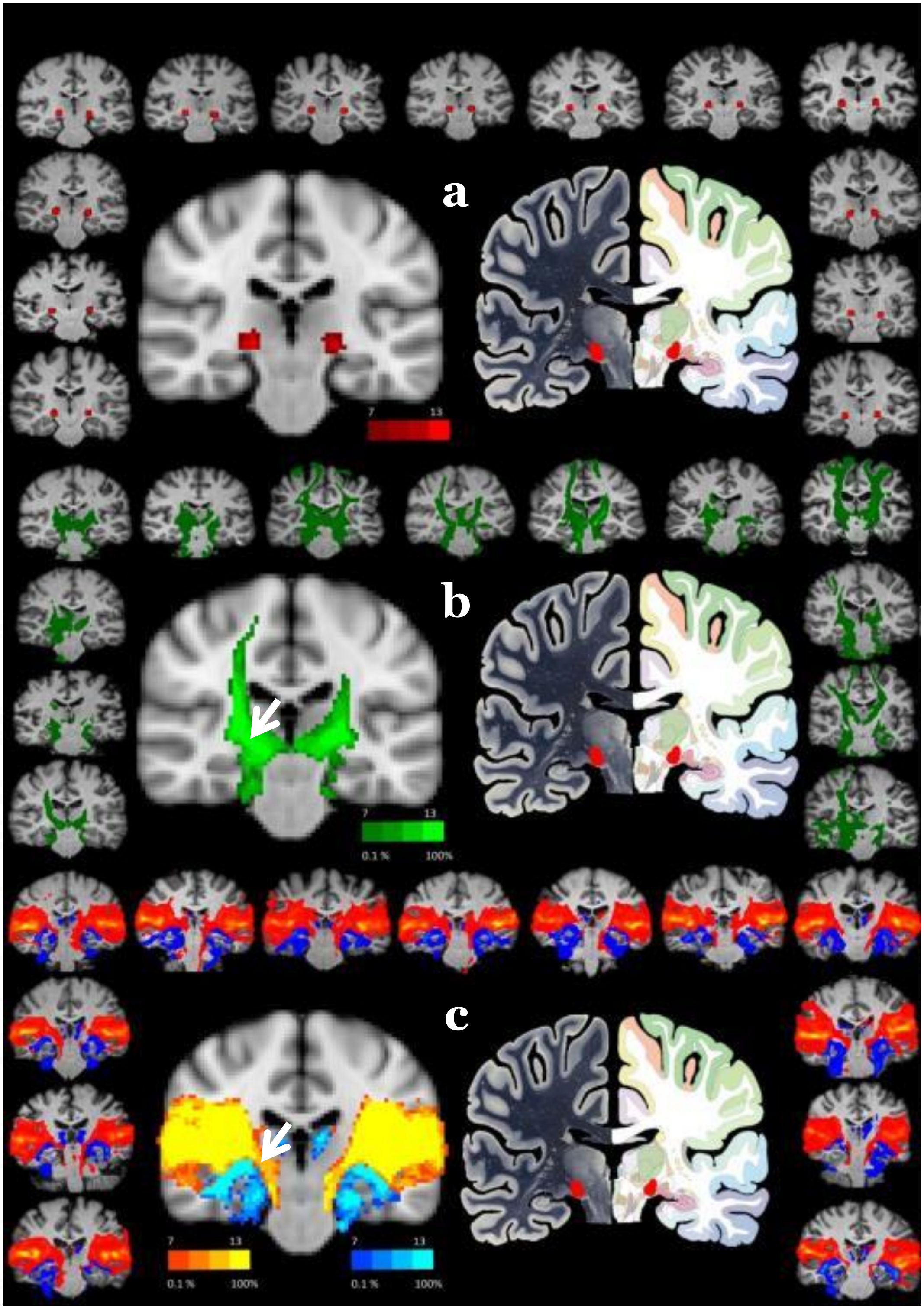

(**a**) Shows the placement of the MGN/S seed (red) on a standard MNI template (center left) with the atlas image (central right, www.thehumanbrain.info) provided for comparison. The surrounding brains show the placement of the seed on the T1 anatomical image for each participant. (**b**) shows the patterns of connectivity (in green) for the inferior colliculus seed. The central left brain shows the summation of all participants in MNI152 space (threshold set 0.1% tracts and to a minimum of 7 of the 13 brains showing the results as indicated on the top of the color key). (**c**) shows the connections of the primary visual cortex are shown in dark blue to bright blue and are contrasted with the projections of the primary auditory cortex shown in red to yellow. The MGN/S seed center of mass is represented by the white arrow presented on the left hemisphere of the left central brain for (**b**) and (**c**).

Figure 6.4-1 The Probabilistic Connections of the Human Medial Geniculate Nucleus.

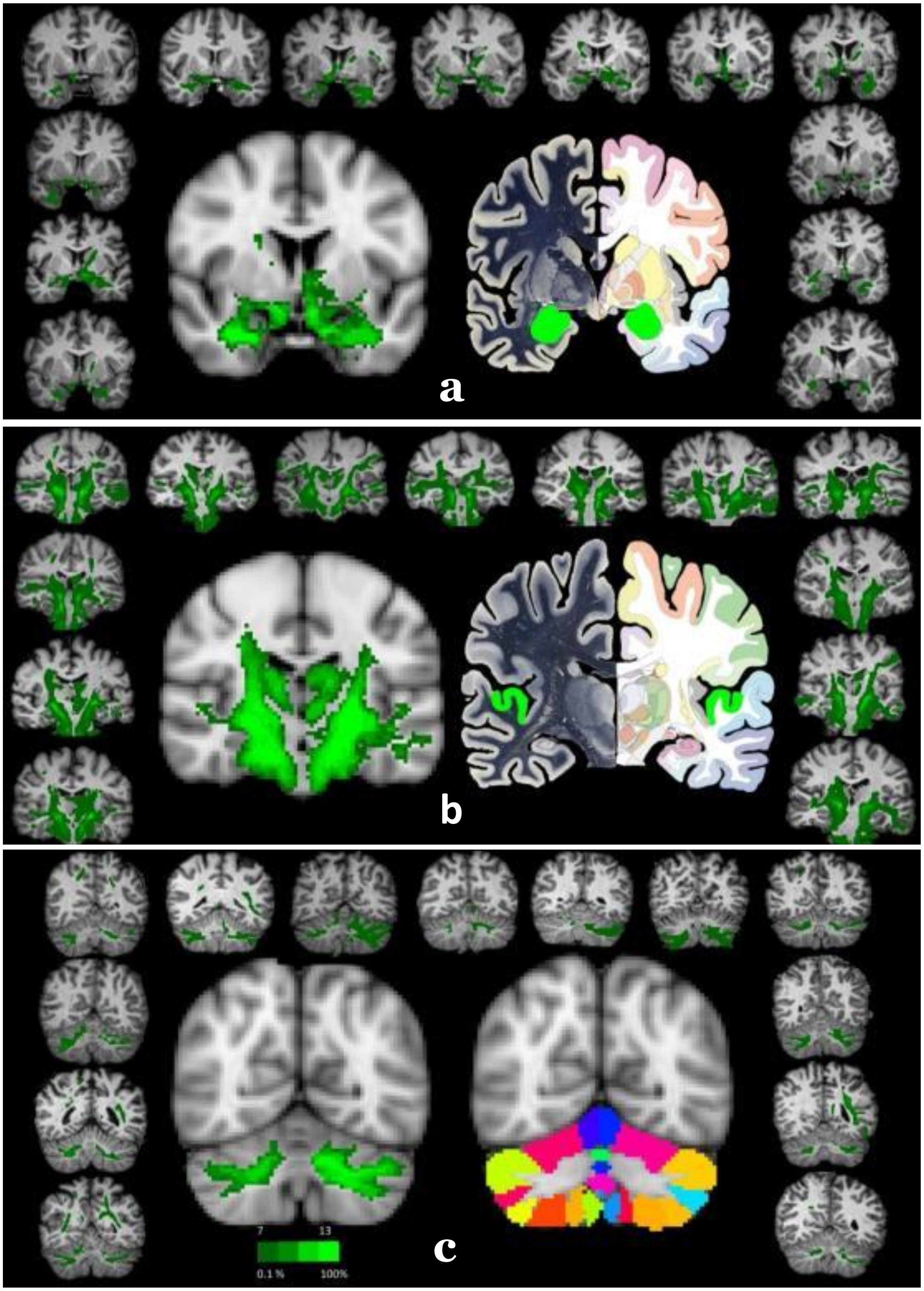

(**a**) The dark to light green in (**a**) shows the connectivity of the medial geniculate nucleus to the amygdala (highlighted above on the central right figure in bright green) and also portions of the caudate, putamen, and globus pallidus. The left central figure is the summation of the results from all participants overlaid onto the MNI152 brain (threshold set at 0.1% tracts and 7 of the 13 participants showing the connectivity). The surrounding brains are the individual results (matched in position to **Figure 6.3-1**). (**b**) shows the connectivity of the medial geniculate to the thalamus, hypothalamus, auditory cortex, middle temporal cortex and portions of the midbrain and spinal tracts. (**c**) shows the connectivity of MGN and cerebellum, with the right central imaging representing a probabilistic cerebellar atlas.

Figure 6.4-2 The Probabilistic Connections of the Mouse Medial Geniculate Nucleus.

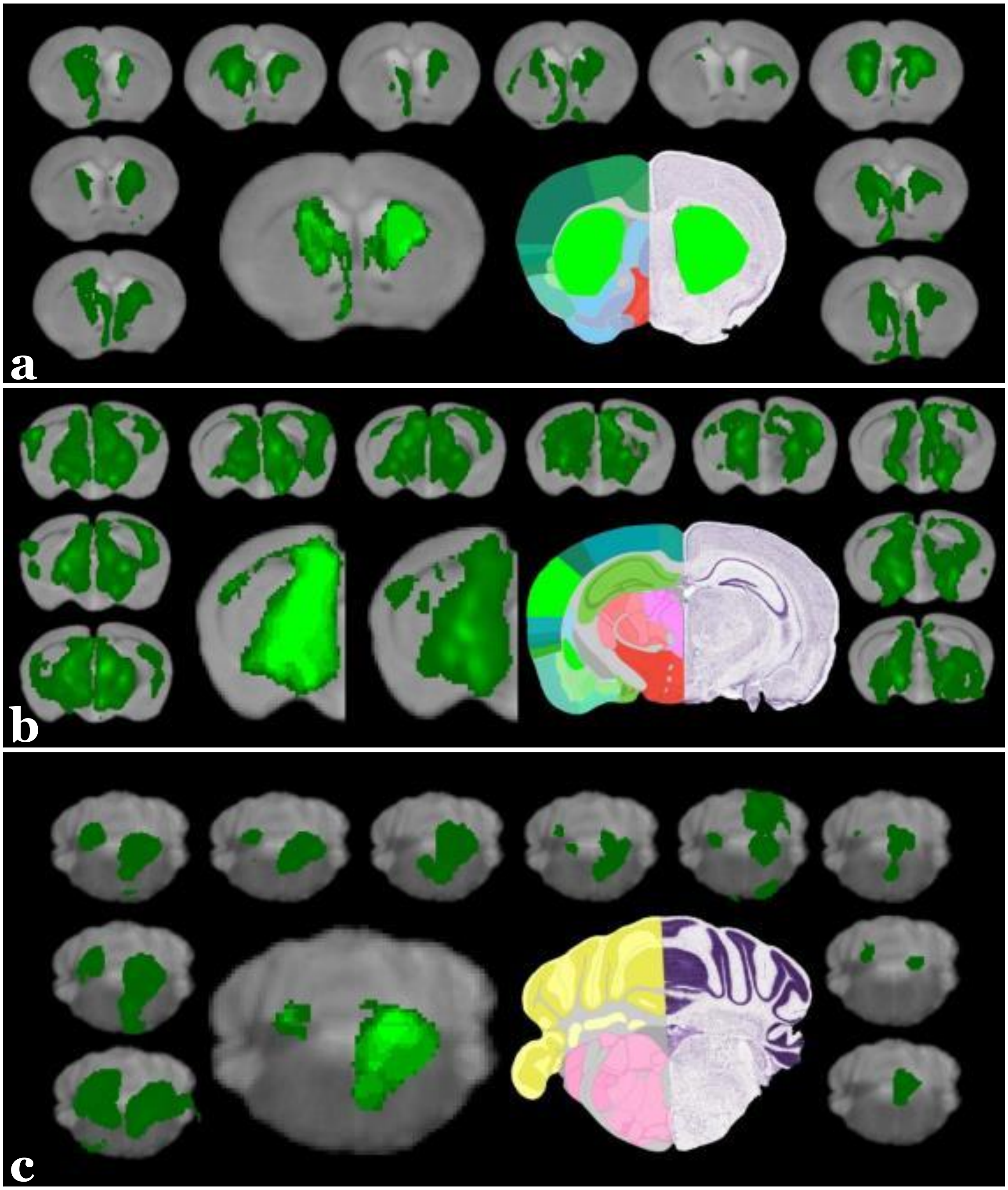

The dark to light green overlay in panel (**a**) shows the connectivity of the MGN/S and the caudate/putamen (highlighted above on the central right figure in bright green). The left central figure is the summation of the results from all participants overlaid onto our standard 24 average mouse brain (threshold set at 1% tracts and 5 of the 10 participants showing the connectivity). The surrounding brains are the individual results overlaid onto the standard mouse brain (matched in position to remaining panels). (**b**) shows the connectivity of the medial geniculate and the thalamus, hypothalamus, auditory cortex, portions of the midbrain and spinal tracts. (**c**) shows the connectivity of MGN and cerebellum, with the right central imaging representing a probabilistic cerebellar atlas.

Figure 6.4-3 The Anterograde Classical Tracing Results of the Mouse MGN/S.

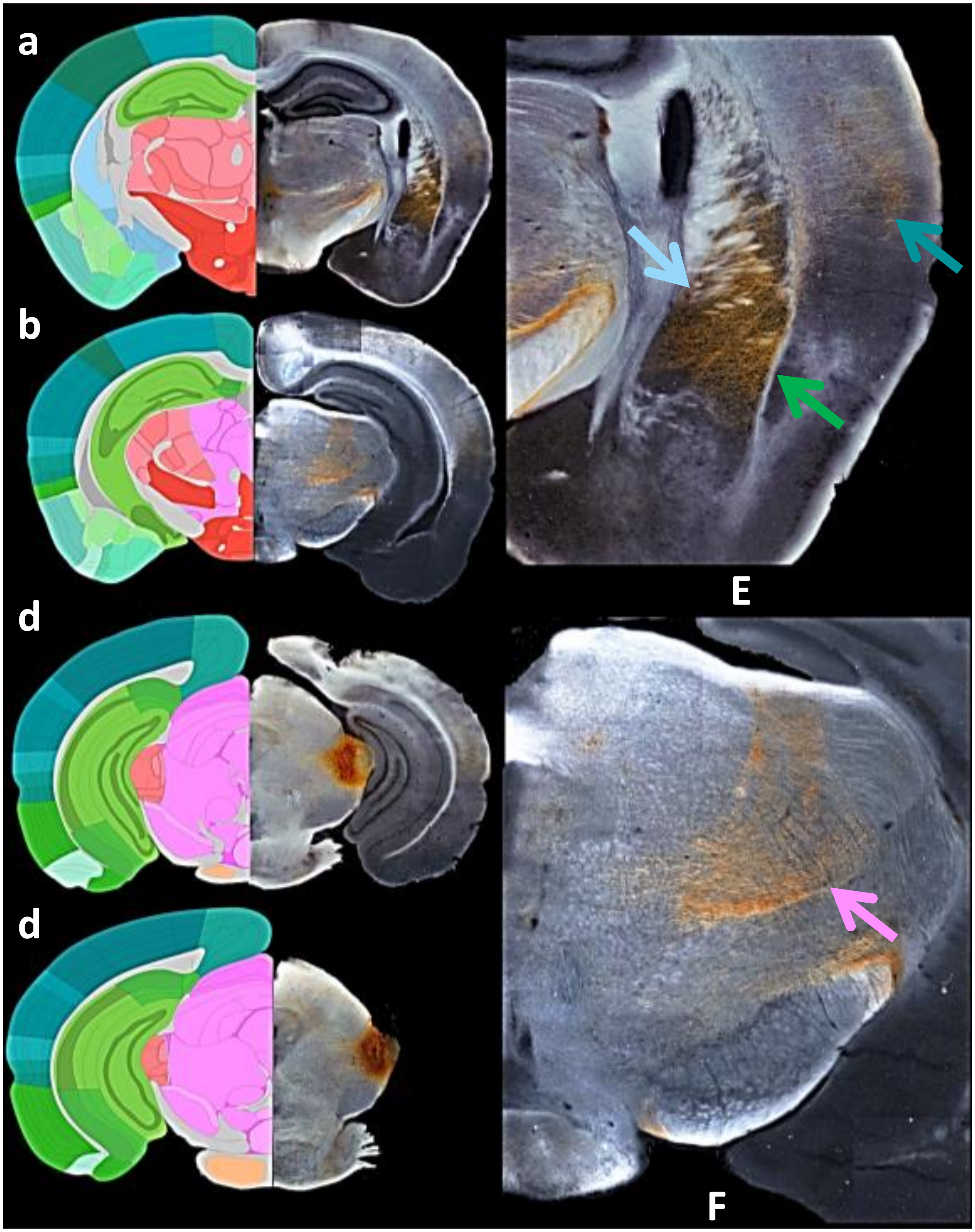

The whole brain sections on the left (**a-d**) are a composite of the most representative slice from one mouse starting with the most anterior section (**b**) showing extensive **amygdala** (color of brain area corresponds to Allen Brain Atlas Color Scheme) and **caudate-putamen** projections and also notable projections to regions of the **hypothalamus** and **thalamus** to the most posterior (**d**) showing the injection site the predominantly resides in the MGN/S (last two sections have the thalamus color which encompasses the MGN and surrounding nuclei). The right two sections (**e & f**) are magnifications of the amygdala/caudate putamen plus **auditory cortex** on top from the upper left section and the magnification of the high density of fibers of termination and passage through the thalamus, hypothalamus, and **midbrain** from the upper middle section. Note that even in the magnification many of the fine and less dense fibers are not easily visualized.

Table 6.4-1 Comparison of MGN/S Connectivity in Mice and Humans

Brain Area	Human DTI Tractography	Mouse DTI Tractography	Mouse BDA Case Study Anterograde Tracing
Auditory Cortex	✓ (12 of 13)	✓ (7 of 10)	✓ (Very Dense)
Insular Cortex	✓ (13 of 13)	-	✓ (Very Sparse)
Amygdala Complex	✓ (13 of 13)	✓ (7 of 10)	Central, Medial, Lateral Nuclei
Pallidum	✓ (13 of 13)	✓ (10 of 10)	Substantia Innominata, Globus Pallidus
Caudate Putamen	✓(13 of 13)	✓ (10 of 10)	✓
Thalamus	✓(13 of 13)	✓ (10 of 10)	Lateral Posterior, Subparafasicular, Interomedial Dorsal, and Ventral Posterior areas/nuclei and Posterior Complex
Hypothalamus	✓(13 of 13)	✓ (10 of 10)	Anterior Hypothalamic Nucleus, Subparaventricular Zone, Peri and Paraventricular Nuclei, Zona Incerta, Subthalamic nucleus
Pons	✓ (13 of 13)	✓ (10 of 10)	Pontine grey
Midbrain	✓ (13 of 13)	✓ (10 of 10)	Periaqueductal grey and Superior/inferior colliculus
Cerebellum	✓ (13 of 13)	✓ (10 of 10)	Not Observed

Chapter 7:

Parallel Macroscopic and Microscopic Increase in Brain Structure after Learning: Voxel-Based Morphometry Predicts Shifts in Dendritic Spine Density and Morphology with Auditory Fear Conditioning

7.1 Context, Author Contribution, and Acknowledgement of Reproduction

The following chapter presents the use of *ex vivo* T2 high-resolution structural scans for voxel-based morphometry analysis between mice that have undergone auditory conditioning and handled controls to study the long term structural changes in the brain. To complement the VBM analysis and help to elucidate the underlying neurobiological mechanisms that may account for VBM signal, the study also had a confocal analysis arm that focused on dendritic spine density and morphology in areas showing significant differences in the VBM study. The chapter is reproduced with minor edits from Keifer Jr, O.P., Hurt, R., Gutman, D.A., Keilholz, S.D., Gourley, S.L., and Ressler, K.J. (Revise and Resubmit). "Parallel Macroscopic and Microscopic Growth After Learning: Voxel-Based Morphometry Predicts Shifts In Dendritic Spine Density and Morphology with Auditory Fear Conditioning." *Nature Neuroscience*.

7.2 Introduction

The use of various MRI techniques (e.g., functional magnetic resonance imaging, voxel based morphometry, and diffusion weighted/tensor imaging) to understand human neurological physiology and pathology is now ubiquitous. With the exception of functional magnetic resonance imaging(Logothetis, Pauls et al. 2001), few of these methods have undergone rigorous study to determine the underlying causes for signal or signal change(Dauguet, Peled et al. 2007, Gutman, Keifer et al. 2012). For example, voxel-based morphometry (VBM) is a process by which high-resolution structural volumes of brains undergo statistical comparison to draw conclusions about differences in brain regions between groups(Ashburner and Friston 2000). This approach has been used widely in neuropsychiatric disorders; for example, a number of fear-related disorders such as posttraumatic stress and panic disorder, among others, have been associated with regional alterations using VBM(Yamasue, Kasai et al. 2003, Uchida, Del-Ben et al. 2008, Carlson, Beacher et al. 2012, Kuhn and Gallinat 2013) . Such techniques provide the tremendous advantage of *in vivo,* non-invasive analysis of human brains in health and disease. However, as a natural consequence, there is only speculation regarding what cellular changes underlie the changes in the structural imaging signal(Good, Johnsrude et al. 2001). Hypotheses about the mechanisms associated with these MRI signals range from altered neurogenesis and glial proliferation to shifts in dendritic spine size and density changes. Yet, despite this lack of understanding, there are a tremendous number of influential papers that have shown effects using MRI-based techniques(Taki, Goto et al. 2004, Chetelat, Landeau et al. 2005, Prinster, Quarantelli et al. 2006, Dauguet, Peled et al. 2007, Valfre, Rainero et al. 2008).

The main hindrance to studying the underlying mechanisms of MRI-based signal changes is the frequent application to human studies, but its relatively sparse use in animal model studies in which more mechanistic approaches can be employed. This is surprising to some degree because the translational potential of MRI studies is unparalleled. In a partial readdress, our previous work has focused on developing DTI-based imaging in the mouse model, which has allowed for the development of an imaging and analysis protocol to examine mechanisms of MRI based structural change in this study(Gutman, Keifer et al. 2012, Gutman, Magnuson et al. 2013). We use these tools to address some of the potential cellular mechanisms that may account for the changes in MRI signal detected by VBM.

Because VBM is most often used for a comparison between two groups, we elected to use fear conditioning as our experimental model. Fear conditioning is a robust paradigm used world-wide to study mechanisms of emotional memory formation and regulation(Maren 2001). Although a tremendous amount of work has focused on amygdala-dependent mechanisms of fear conditioning, fewer studies have examined the neural mechanisms underlying structural plasticity within cortical sensory areas associated with paradigms such as auditory fear conditioning(Romanski and LeDoux 1992, Quirk, Armony et al. 1997). In this study, we used our high-throughput *ex vivo* imaging protocol to acquire T2 high-resolution structural volumes of *Thy1*-YFP-expressing transgenic mice that underwent an auditory fear conditioning paradigm. Following the acquisition of high-resolution scans, a subset of the mouse brains were then sectioned and prepared for confocal imaging of the auditory cortex, one of the cortical areas that consistently showed significant VBM signal change. The metrics of confocal analyses focused on the proposed mechanisms of VBM signal change, including spine density, spine width, spine length, the ratio of width to length, and cell nuclei width and density. The measurements of spine density, spine width, length and the ratio of width and length were used to draw preliminary conclusions about the hypothesis that VBM signal change is related to changes in the spines on dendrites. The nuclei widths and densities were used to evaluate the potential for proliferation of glia cells or neurons (though unlikely) to account for the increases in VBM signal. Final analyses included the correlation of confocal analyses with VBM morphometry metrics to assess which cellular structural change best accounted for the VBM signal.

Remarkably, we found that, of the metrics evaluated, the auditory fear conditioning group had a higher density of wider, though shorter, dendritic spines in the auditory cortex. Additionally, the density of spines significantly correlated with increases in auditory fear conditioning-induced VBM signal in the auditory cortex. Importantly, there was not a significant difference between the nuclei densities or widths between the groups, and there was no significant correlation between cell nuclei density and VBM signal. These results begin to address the tremendous gap in our current understanding of the cellular underpinnings of VBM. Additionally, they highlight the feasibility and large potential for the emerging field of small-animal MRI imaging (a.k.a. magnetic resonance microscopy) as a scientifically and translationally powerful tool.

7.3 Results

7.3.1 Auditory Fear Conditioning

To facilitate comparisons of the VBM results with underlying cellular measures, *Thy1*-YFP expressing mice were selected as the experimental model. *Thy1*-YFP-expressing mice have robust fluorescent signal (**Figure 7.3-1**) - most notably in cortical layer V pyramidal neurons (Feng, Mellor et al. 2000). Given the role of sensory cortex in memory(Miyashita 1988, Braver, Barch et al. 2001, Weinberger 2004) and our interest in long-term structural changes underlying emotional memory, our auditory fear conditioning paradigm follows previous work related to fear incubation(Pickens, Golden et al. 2009). Additionally, prior evidence from our lab suggests that a number of immediate-early and synaptic plasticity genes are expressed in the sensory cortex during the consolidation period following auditory fear conditioning (Ressler, Paschall et al. 2002). In the current studies, *Thy1*-YFP-expressing mice underwent 5 days of conditioning with 10 tone-shock pairings each day. The resulting fear acquisition curves are presented in **Figure 7.3-2a** for day 1 and day 5. The curves show the expected acquisition across days, suggesting that the animals acquired the pairing of the tone with the electrical shock. The control group was handled identically except tones and shocks were withheld.

7.3.2 Magnetic Resonance Imaging – Voxel Based Morphometry Analysis.

Two weeks after training, mice were placed under deep anesthesia, perfused with 4% paraformaldehyde in phosphate buffered solution, the brains extracted and post-fixed overnight. The brains were then embedded into an agarose-gadolinium (III) oxide matrix for our high throughput (9 for this study, though 16 is possible, **Figure 7.3-2b,c**) *ex vivo* imaging method (Gutman, Keifer et al. 2012, Gutman, Magnuson et al. 2013). The two groups (n=27 per group) were distributed through 6 rounds of high-resolution RARE T2-weighted image acquisitions on a Bruker 9.4 Tesla scanner (Billerica, MA). All MRI brain volumes were examined for any signs of damage or artifact in the cortex (the brains were inspected before embedding so no major damage or artifacts were noted).

The brains were parsed from the imaging volume of nine brains and preprocessed for VBM analysis using the FSL Imaging Analysis Suite (FSL, Oxford). As a component of this analysis, the brains were segmented into white matter and grey matter. The grey matter skeleton of the 54 brains is presented in **Figure 7.3-2d**. The study was designed to split the 54 brains into two groups to allow for an initial analysis, a replicate, and then a combined analysis. The initial analysis of half of the brains is shown in **Figure 7.3-3a** (group 1), followed by analysis of group 2 presented in **Figure 7.3-3b**, the combined analysis inclusive of both groups is shown in **Figure 7.3-3c**. Based on the auditory fear conditioning literature, several cortical areas were investigated in an *a priori* manner. Masks were created that were inclusive of the ROI and the adjacent cortex including the infralimbic and prelimbic cortices (IL and PL), insular cortex (In), auditory cortex (AC), medial, basolateral/lateral, and central amygdala (MeA, BLA/LA, CeA respectively), anterior cingulate cortex/retrosplenial cortex (ACC/RSC) and a control region of the rhinal cortex. Of these areas, 1 (auditory cortex) showed significant differences between groups all three iterations of the analysis. But five areas (auditory cortex, medial amygdala, central amygdala, and basolateral/lateral amygdala, and insula) showed significance in at least two of the analyses including the most robust and powerful combined analysis. The bar graphs in **Figure 7.3-3d** represent the VBM signal (grey matter voxel intensity multiplied by the Jacobian) of the significant voxels in the auditory cortex, with analysis 1 and 2 revealing an 18.8% increase in signal in the auditory fear conditioning group compared to controls and the overall analysis revealing a 16.5% increase. These results indicate that, among other areas, auditory fear conditioning leads to increased grey matter density within the mouse auditory cortex consistently across all three VBM analyses. The control seed in the rhinal cortex and the *a priori* hypothesized mPFC area never reached significance, nor did they trend towards significance ($0.051<P\leq0.1$). The ACC and the RSC did show trending significance (max $P = 0.06$) in Analysis 1 but Analysis 2 and the Combined Analysis both resulted in P-values in the range of 0.20.

7.3.3 Confocal Microscopy – Dendritic Spine Density, Width, and Length

In order to understand the underlying cellular mechanisms that may account for the VBM changes in the auditory cortex, following the acquisition of the MRI volumes, brains were un-embedded and sectioned into 35 μm sections on a Microm HM450 freezing sliding microtome (ThermoFisher Scientific HM 450, Waltham, MA) . A preliminary comparison with fluorescence microscopy of a post-MRI brain to a brain that did not undergo embedding and imaging (compare **Figure 7.3-1a to 1b, 1c to 1d**, and 1e to 1f) ensured that the embedding methodology did not compromise cellular integrity or fluorescence signal. Of the 54 brains imaged and selected for VBM analysis, we randomly sampled a third of the brains from each group (9 brains) for analysis based on previous work (Gourley, Olevska et al. 2012, Gourley, Swanson et al. 2012, Gourley, Swanson et al. 2013).

Of the cortical areas that were significantly different between groups in the VBM portion of the study, we selected to further analyze the auditory cortex. The auditory cortex was advantageous in many ways including its significance across all three VBM analyses, its relative size in the coronal plane (allowing for a larger collection area), the ease of identification on coronal sections relative to known anatomical landmarks, and the density and intensity of the *Thy1*-YFP neurons in that portion of the cortex. The confocal analyses focused on second- and third-order dendrites and quantification of dendritic spine density, length and head diameter. Additionally, brains were stained using Hoechst stain to perform nuclei density and width analysis of the auditory cortical areas where dendrites were sampled.

Figure 7.3-4a represents the comparison of overall spine density measurements, treating each mouse (as opposed to each dendrite) as an independent sample. Dendritic spines in the auditory cortex for the auditory fear conditioned group were 18% more dense than the control group (*t* test, n = 9 auditory fear conditioning, n = 9 control, $p<0.05$, $t_{16} = 2.79$). A cumulative density analysis of the average dendritic spine density per dendritic length revealed a rightward shift in the cumulative distribution [Kolmogorov-Smirnov (K-S) test, n= 290 and 300 dendrites for auditory fear conditioned and control group respectively, $p < 0.0005$, $D = 0.185$]. Representative dendrites are presented in **Figure 7.3-4c**, corresponding with the minimum, maximum, and mid-point densities. These data suggest that the overall distribution of densities is shifted to the right, with overall increased densities of spines across the full distribution range for the auditory fear conditioned group when compared to controls. Overall, auditory fear conditioning results in higher dendritic spines densities in the auditory cortex. Additionally, the data show some of the first evidence that dendritic spine density differences could serve as a cellular mechanism for signal differences detected by VBM.

Looking to the morphology of the dendritic spines themselves, **Figure 7.3-5a,b** show the overall average and cumulative distribution function for spine head diameter. Notably, the dendritic spines from the auditory fear condition group were approximately 5% wider when compared to control mice (*t* test, n = 9 auditory fear conditioning, n = 9 control, $P \leq 0.05$, $t_{16} = 2.23$). The cumulative distribution of the average dendritic spine head diameter per dendritic length shows a significant rightward shift (wider spine diameter across the distribution) for the auditory fear conditioning group when compared to controls (K-S test, n= 290 and 300 for auditory fear conditioned and control group respectively, $P \leq 0.0001$, $D = 0.182$). **Figure 7.3-5c** depicts dendritic spine heads in the range of the maximum, minimum, and midpoint diameters observed between groups.

Similarly, **Figure 7.3-5d-f** reports the average dendritic spine length per dendritic length between the groups. In particular, auditory fear conditioning shortens dendritic spines (5%), further substantiated by a leftward shift in the cumulative distribution curve (*t* test, n = 9 auditory fear conditioning, n = 9 control, $P \leq 0.05$, $t_{16} = 2.17$; K-S test, n= 290 and 300 for auditory fear conditioned and control group respectively, $P \leq 0.05$, $D = 0.123$). Overall, auditory fear conditioning results in dendrites that are shorter but wider in the auditory cortex. This further suggests dendritic spine morphology differences could serve as a cellular mechanism for signal differences detected by VBM.

Figure 7.3-5g-i reports the ratio of head diameter to dendritic spine length, highlighting a relatively similar distribution of dendrite spines with smaller head to length ratios, which then quickly diverges around 0.3, with the auditory conditioned group having significantly higher ratio values. The shorter but wider morphology may reflect more mature spines being found in the auditory cortex of auditory fear conditioned mice. On average, the auditory conditioned group has a 10.6% greater spine head diameter to length ratio compared to the controls (*t* test, n = 9 auditory fear conditioning, n = 9 control, P≤0.01, $t_{16} = 2.92$; K-S test, n= 290 and 300 for auditory fear conditioned and control group respectively, P≤0.0005, $D = 0.2178$). Overall, these findings are consistent with shorter but wider spines following auditory fear conditioning.

7.3.4 Confocal Microscopy – Nuclei/Cell Density

Given the hypothesis that increases in either neuron or glial count may account for the increased signal detected with VBM, we directly addressed this question using Hoechst dye to stain the nuclei of all the cells. Images were collected from the same subset of brains used for the dendritic spine analyses from the same regions where dendritic spines were imaged. Using previously published and validated counting methods, we assessed nuclei density, as well as the diameter of those nuclei(Williams and Rakic 1988). These results are presented in **Figure 7.3-6**. Throughout, we identified no differences using parametric statistical approaches (note that n =8 for each group as one slide from each group did not have adequate Hoechst staining). (P>0.05). Further, neither of the K-S analyses reached significance (P > 0.05). Representative Hoechst images are shown in **Figure 7.3-6c**. Together these data suggest that the VBM signal changes, while associated with spine density and morphology, are not associated with any changes in cell density, across the range of cell sizes, including neuronal populations with large nuclei and glial populations with smaller nuclei.

7.3.5 Correlational Metrics between VBM and Confocal Analysis

While the VBM and confocal analyses findings provide compelling evidence for changes in brain structure after exposure to a fear conditioning protocol, we sought to further quantify the relationship between each mode of analysis with correlational analysis. To assess the relationship we covaried the average VBM signal in the auditory cortex used for permutation testing by FSL (grey matter voxel intensity, GMVI, multiplied by the Jacobian of the warp field) with the corresponding brain's spine density, head diameter, and length metrics. **Figure 7.3-7a** reports a significant ($P<0.05$) and strong correlation ($r=0.46$) between the VBM signal and dendritic spine density. The correlations with spine head diameter, dendritic spine length, and the diameter/length ratio were $r= 0.12$, $r= -0.29$, and $r=0.24$, though none reached significance ($P>0.05$, data not shown). **Figure 7.3-7c** represents the correlational analysis of GMVI x Jacobian and the nuclei density per imaging volume. The correlation was $r=0.29$ and not significant ($p>0.05$). Together, these data show that dendritic spine density strongly and significantly correlates with VBM signal differences, providing even further evidence that this could provide a cellular mechanism to account for the signal differences detected by VBM.

7.4 Discussion

The large VBM literature in human subjects and the smaller but growing literature using animal models have highlighted the utility of MRI-based techniques to address meaningful questions regarding brain structure and function(Sawiak, Wood et al. 2009, Sawiak, Wood et al. 2013). These reports must, however, only speculate as to the underlying cellular changes that may explain shifts in VBM signal. Here we assessed at least two of the major hypotheses in the field regarding the mechanism underlying VBM signal changes – shifts in dendritic spine density and character, or shifts in *cellular* density (often attributed to glia). We generated evidence that support the first hypothesis – that VBM signal is tightly coupled with regional dendritic spine density. Specifically, auditory fear conditioning increased VBM signal in the auditory cortex (on the order of 16-18%) of mice, and this was associated with an 18% increase in dendritic spine density, a 5% increase in spine head diameter, and a 5% shortening of spine length. Conversely, we found no evidence supporting the hypothesis that VBM signal changes reflect a proliferation of glia or neurons. While our work in the auditory cortex provides the first evidence of long-term changes in the dendritic spine density and morphology, it is corroborated by Moczulska and colleagues, who used two-photon imaging to track the dynamics of dendritic spine changes in the auditory cortex during auditory fear conditioning. Their findings show that there is dynamic formation and elimination of dendritic spines in the auditory cortex with auditory fear conditioning (Moczulska, Tinter-Thiede et al. 2013).

Auditory fear conditioning decreased the length of dendritic spines in the auditory cortex. This is particularly provocative because dendritic spine morphology is closely associated with maturity and the likelihood that the spine contains an active synapse

(Yuste and Bonhoeffer 2001, Bourne and Harris 2008, Bhatt, Zhang et al. 2009). Immature spines are characterized a long, filopodia-like shape with a narrow head. These filopodic dendritic spines are extremely dynamic in their environment, and some will stabilize, at which point they shorten and widen -- forming a “mushroom-shaped” dendritic spine, reflecting a more mature, synapse-containing state. Thus, it is then possible that denser, shorter and wider dendritic spines following auditory fear conditioning reflect a maturation of dendritic spines in the auditory cortex. This in turn would support an overarching hypothesis that cortical areas play an important role in long-term memory.

Further considering the VBM signal, it should be noted that the voxel sizes are on the order of 100 x 100 x 100 μm^3. To detect signal changes at this level, it may be surprising that dendritic spine density can account for 20% of the variance of the signal. However, **Figure 7.4-1** demonstrates the plausibility of such an assertion. The volumetric (assuming a dendritic spine is a cylinder with a sphere on top) increases, with respect to increased spine density and increased head diameter, far outweigh that of decreasing the neck lengths alone. Further, the change in spine density alone leads to an increase in overall spine volume on the order of 21%; if combined with both the wider diameter heads and shorter lengths, the gross volumetric change is on the order of 31%. Considering a simplified and idealized case, if the density of neurons is approximately 90 x 10^3 neurons per mm^3 with an approximate total dendritic length of 1000 μm(Schuz and Palm 1989, Ma and Vacca-Galloway 1991), then there are 90 neurons per voxel and 90000 μm of total dendritic length. In turn, this would yield approximately 126,000 dendritic spines in control mice and 153,000 dendritic spines in the auditory fear conditioning group. Therefore, the dendritic spines in auditory conditioned mice will occupy about 8100 μm^3, compared to 6170 μm^3 for the controls, an overall increase in

~31% of neuronal dendritic spine volume. While this is compelling, it is also likely not the whole story and further consideration must be paid towards other potential volume changes that can co-occur. For example, if we assume there is a commiserate increase in the pre-synaptic side (synaptic boutons), that would double the volumetric increase. Further, because increases in dendritic spines likely increase the metabolic demand of the neurons, increases in neuronal and glial size is another possible factor. Additionally, it is also plausible there is an increase in the dendritic arborization and axonal branching patterns that co-occur with increases in dendritic spine density changes (Gourley, Swanson et al. 2013). All of which would further contribute to the "greyness" of an area.

Considering the other areas that showed either significant or trending significant results, existing literature suggests similar patterns of dendritic density changes with fear conditioning. The VBM results presented here showed significant increases in the VBM signal in several nuclei of the amygdala (medial, basolateral and lateral, and central amygdala) with auditory fear conditioning. Are these areas also associated with long term changes in dendritic spine density? Using auditory fear conditioning, Heinrichs et al reported that neurons in the basolateral amygdala were associated with an increase in second and third order dendritic spine density (on the order of 20-30%) with auditory fear conditioning when compared to naïve controls(Heinrichs, Leite-Morris et al. 2013). These results were echoed by Pignataro et al, who examined spine density changes with context conditioning and auditory fear conditioning and reported, in both cases, that dendritic spine density increased in the BLA and hippocampus (the hippocampus is discussed further below).

With regards to the ACC, IL, and PL there are a few studies looking at dendritic spine densities in these areas that may account the inconsistent VBM findings. Restivo et al have shown that there is a difference in the dendritic density in the anterior cingulate cortex at 36 days after contextual fear conditioning, but not 24 hours. Interestingly, the percent change in dendritic spine density was slightly smaller than that in the auditory cortex (~16% for apical dendrite spine density)(Restivo, Vetere et al. 2009). This suggests at least two potential explanations for our ACC findings. The first is that a dendritic spine density change around 16% maybe at the cusp of detectability with our VBM methodology. Further, because we only waited 14 days in our behavior paradigm before euthanizing the animals, it is possible that our time table was too short, and waiting 36 days would result in more consistent and significant results in the ACC. Our *a priori* selection of the IL and PL was based on the growing literature that suggests a regulatory role in fear conditioning and extinction (Morgan and LeDoux 1995, Milad and Quirk 2002). Yet interestingly, neither the PL nor the IL showed significant change in VBM signal with auditory fear conditioning. The discrepancy may reflect two aspects worthy of consideration. First, for the infralimbic cortex, Vetere reported that contextual fear conditioning increased spine density and head size in the ACC and infralimbic cortex when compared to pseudo-conditioned animals. The percent change in dendritic spine density for these areas was on the order of 10-15% change in spine density in apical dendrites in layer II/III(Vetere, Restivo et al. 2011). Clearly, like the ACC results reported above, this percent difference in dendritic spine density was smaller than found here in the auditory cortex, and additionally, this was in a different layer of cells. Perhaps more interestingly, other studies have also suggested a *decrease* in dendrite terminal branches in the IL with repeated stress (like our 5 day training paradigm) (Izquierdo, Wellman et al. 2006). Thus, a decrease in the number of dendrites and a smaller percentage increase in dendritic spine density with auditory fear conditioning could explain a lack of consistent VBM findings in the IL. With regards to the PL there was not definitive study on the changes of dendritic spine density with auditory fear conditioning so we are unable to draw any conclusions.

We did not identify VBM signal changes in the hippocampus, but that follows from Restivos work that, like Pignataro, showed spine density changes in the hippocampus 24 hours after conditioning, but, importantly, not 36 days later(Pignataro, Middei et al. 2013). These findings, along with ours, suggests an important temporary increase of spine density in the hippocampus that later reverts because our samples were collected 2 weeks after conditioning.

Overall, this study establishes a strong evidence for the hypothesis that dendritic spine density may be the cellular mechanisms that underlies changes in brain structure that is detected by voxel based morphometry. Follow up work should focus on providing further evidence for this hypothesis and should additionally look at post-synaptic density, dendrite arborization, and glial or neuronal volume. Additionally, we have shown that using magnetic resonance imaging techniques on animal models is a very powerful translational tool, because many of the areas detected by VBM in our AFC group parallel findings in human studies of psychiatric pathology (particularly those that are fear-related, such as post-traumatic stress disorder). Further work should focus on developing the full translational utility of these techniques. Finally, this study highlights the technical feasibility of utilizing MRI imaging of animal models to better understand the biological and cellular underpinnings of MRI techniques - a tremendously needed effort to better understand the neurobiological basis for MRI studies.

7.5 Methods

7.5.1 Mice

All experiments were conducted on *Thy1*-YFP expressing mice (B6.Cg-Tg HJrs/J-*Thy1*-YFP, Jackson Labs, Bar Harbor, Maine). All male mice were 8 weeks of age when the fear conditioning was initiated. After concluding the 5 days of training the mice were returned to their normal housing conditions in the Yerkes National Primate Research Center for 2 weeks before they were deeply anaesthetized with ketamine and dexmedetomidine and perfused with paraformaldehyde. The mice were housed with a 12-h light/dark cycle grouped in cages (≤5/cage) with *ad libitum* access to food and water. All conditioning was conducted during the light half of the cycle during the same time of day. All procedures were approved by the Institutional Animal Care and Use Committee of Emory University.

7.5.2 Auditory Fear Conditioning

Mice were conditioned to pair an auditory tone with a mild foot shock. To do so, we employed the SR-Lab Startle-Response system (San Diego Instruments, San Diego California). The mice were trained on 5 consecutive days, with each training day consisting of 10 trials of an auditory tone (12 kHz) presentation of 30s co-terminating with a 0.50-s 1.0-mA foot shock with an inter-trial interval of 60 s. The controls were handled analogously with the exception that that SR-Lab conditioning program was not initiated during the time the mice were in the startle-response cradles.

7.5.3 Magnetic Resonance Imaging

All MRI scanning was conducted on a research dedicated Bruker 9.4 Tesla MRI Scanner (Bruker, Billerica, MA). All brains were scanned using our previously designed *ex vivo* procedure (Gutman, Keifer et al. 2012, Gutman, Magnuson et al. 2013). In brief, perfused mouse brains were embedded in a gadolinium agarose matrix and scanned at multiples of 9 with a T2 RARE sequence. T2-weighted images were first acquired at 0.081 x 0.081 x 0.162 µm^3 resolution (TE = 28.6ms, matrix 1024 x 512 x 65, 10 averages, scan time ~ 14 hours).

7.5.4 Voxel-Based Morphometry Analysis

The acquired mouse structural volumes were parsed into individual brain volumes (each of the 6 scans that contained 9 brain volumes was cut into 9 individual brain volumes). The structural data was then analyzed with a modified version (the built in version is optimized for human data, we replaced the human MNI template with a mouse template of our own creation) of FSL(Douaud, Smith et al. 2007) (http://fsl.fmrib.ox.ac.uk/fsl/fslwiki/FSLVBM, Oxford, UK), an optimized VBM protocol(Good, Johnsrude et al. 2001) carried out with FSL tools(Smith, Jenkinson et al. 2004). First, structural images were brain-extracted (from the minor background noise created by the gadolinium agarose matrix) and grey matter-segmented before being registered to our mouse standard space using non-linear registration. The resulting images were averaged and flipped along the x-axis to create a left-right symmetric, study-specific grey matter template. Second, all native grey matter images were non-linearly registered to this study-specific template and "modulated" to correct for local expansion (or contraction) due to the non-linear component of the spatial transformation. The modulated grey matter images were then smoothed with an isotropic Gaussian kernel with a sigma of 0.25 mm. Finally, voxel wise GLM was applied using permutation-based non-parametric testing, correcting for multiple comparisons across space. Results were displayed as a gradient of trending significance ($p = 0.10$) to significance ($p < 0.01$).

7.5.5 Dendritic Spine Density and Morphology Analyses

Once the mouse brains were imaged, they were placed in 30% sucrose solution overnight and then sectioned into 35-μm-thick coronal sections on a freezing microtome held at −18°C. Sections were then mounted onto slides using Mowiol mounting medium (Mowiol 40-88, Sigma-Aldrich, St. Louis, MO) and were de-identified to ensure the experimenter was blinded. The auditory cortex was identified using anatomical landmarks (anterior to posterior section required the presence of the stria terminalis (section 75 of 132 on the Paul Allen Reference Atlas –as for the VBM significant signal), the dorsal border corresponded the level of the dentate gyrus of the hippocampus, the ventral border was at the level of the ventral portion of the lateral ventricle and fimbria, medial border was the corpus callosum and lateral border was the edge of the cortex. For each animal, at least 10 unobstructed secondary and tertiary apical dendritic segments (with in 160 µm of the soma) running parallel to the surface of the section were imaged on a spinning disk confocal (VisiTech International, Sunderland, UK) on a Leica DM5500 B microscope (laser $\lambda = 488$ nm, Leica, Solms, Germany). Z-stacks were collected with a 100x 1.4NA objective using a 0.1 µm step size, sampling above and below the dendrite. After imaging, we confirmed at 10X that the image was collected from the intended regions. The auditory cortex of both hemispheres was sampled equally for each animal (at least 5 dendrites from each hemisphere).

Collapsed *z*-stacks were analyzed using FIJI – (http://fiji.sc/Fiji). Protrusions ≤4 μm were considered spines(Peters and Kaiserman-Abramof 1970) and counted. Additionally, spine lengths (from the base of the dendritic spine to the tip) and head widths (at the widest point) were measured. If a spine bifurcated, only the longest arm was measured and counted. Individual planes were also evaluated to detect protrusions extending perpendicular to the collapsed *z*-stack. Total spine number for each segment was normalized to the length of the dendritic segment (≥ 20 µm but ≤ 25 µm) to generate density values. All scoring was conducted by a single blinded rater.

7.5.6 Nuclei Density/Width Analysis

Analysis of nuclei density/width was conducted in accordance with previous work(Williams and Rakic 1988). In brief, in addition to collecting z-stacks of the *Thy1*-YFP dendrites, 12 stacks (6 left and 6 right) of the Hoechst-stained neurons were also collected per brain (laser λ = 350 nm). The Hoechst images were pre-processed by finding the center of the Z-stack (defined with respect to the portion of the z-stack containing nuclei), selecting the images that composed 5 µm around the center (total z-stack depth of 10 µm), and creating a maximum projection across the stack. The no count boundaries of the stack were the top image of the z-stack and the right and top border of the collapsed z-stack.

Figure 7.3-1 Comparison of *Thy1*-YFP Signal between MR Imaged and Naïve Mouse

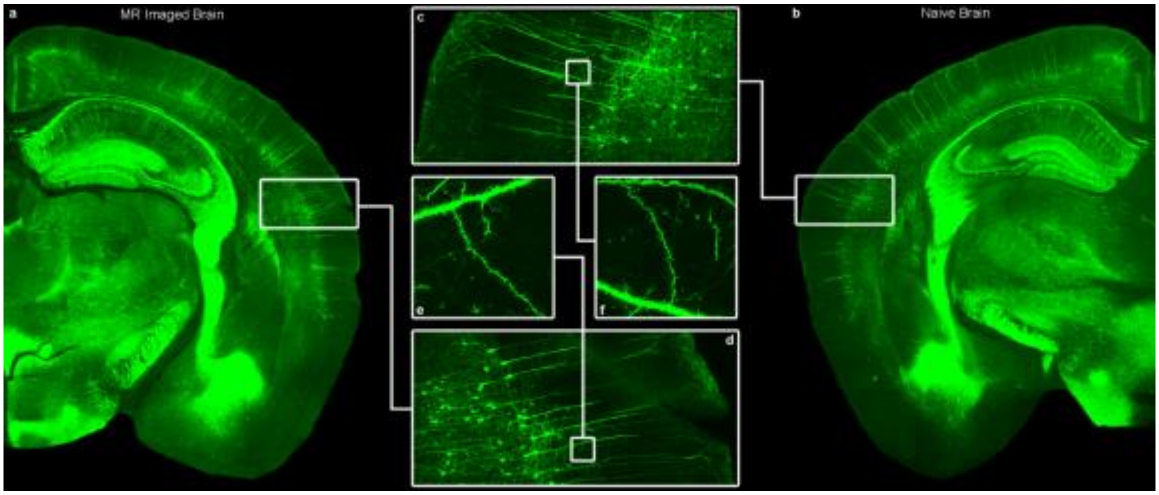

(**a,b**) Composite images (4x) of the *Thy1*-YFP expressing neurons for a mouse that underwent the training, perfusion, embedding, MR imaging and then confocal sectioning and analysis versus one that only underwent perfusion, and confocal sectioning. (**c,d**) These images show a magnified (20x) composite section of the auditory cortex for both the MR imaged and naïve brain. (**e,f**) Selection of a specific dendritic length (100x) to show no difference in the signal and imaging quality between brains having undergone the MRI embedding procedure and those that had not.

Figure 7.3-2 Auditory Fear Conditioning/High Throughput *Ex Vivo* Structural MRI

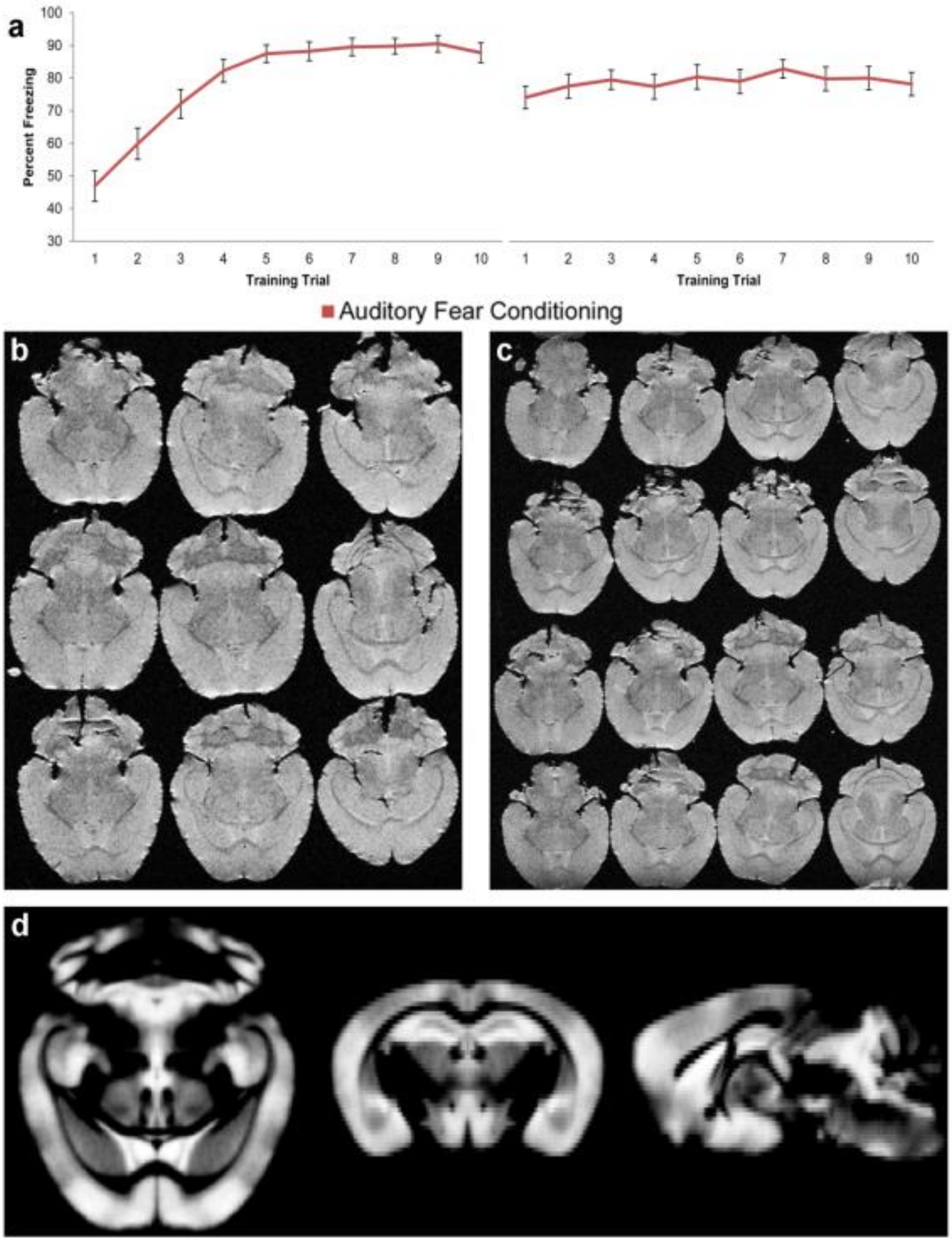

(**a**)The two graphs illustrate the acquisition of auditory fear conditioning (illustrated with percent total freezing during the tone conditioned cue during each training trial) over the course of 5 days (days 1 and 5 shown). The left graph shows the acquisition of fear during the first day as indicated by the increased freezing behavior during the presentation of the tone. The right graph shows the freezing behavior of the group during the last day of training which has plateaued at about 80% freezing during the presentation of the tone. (**b,c**)The middle two images show the T2 RARE high-resolution *ex vivo* acquisition of both 9 (**b**) and 16 brains (**c**) based on our *ex vivo* technique. (**d**)The result of segmenting the grey matter from each mouse MRI volume to create a grey matter skeleton template (n =54 brains) used in the present study.

Figure 7.3-3. VBM Analysis of Auditory Fear Conditioning

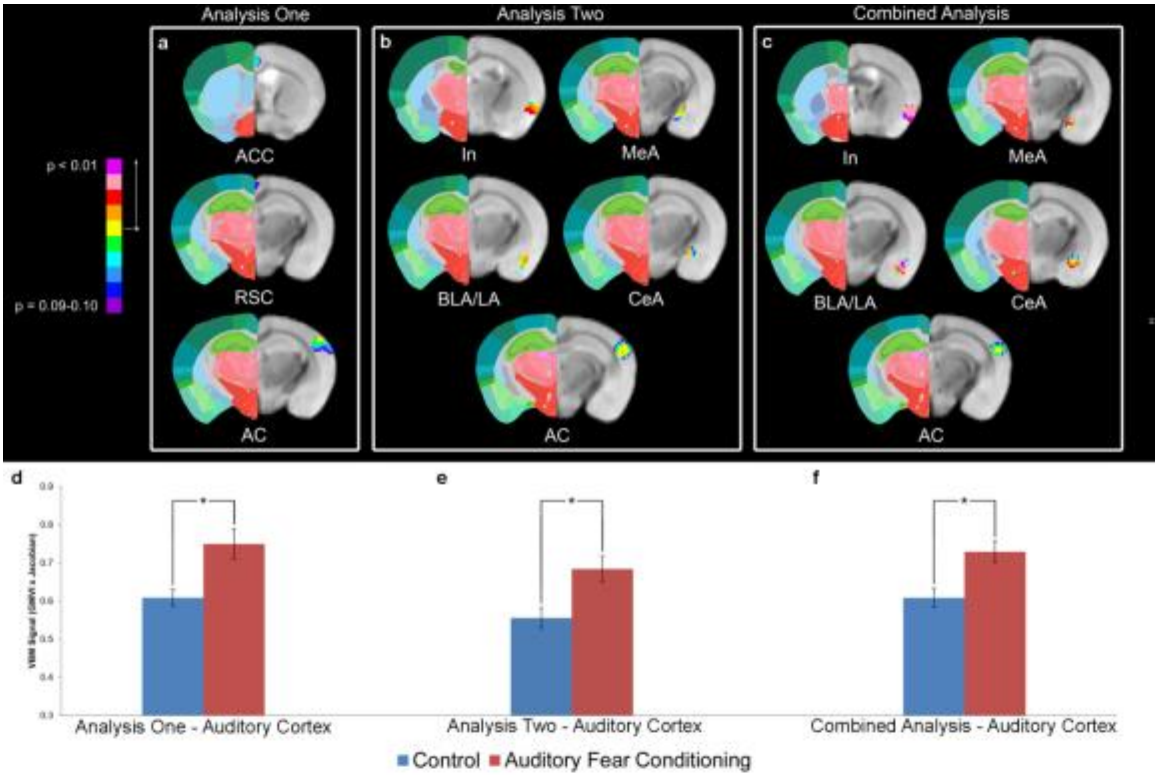

(**a**) The results of the VBM analysis of the first 26 (n =13 auditory fear conditioning, n=13 controls) brains acquired in the series (ACC – anterior cingulate cortex, RSC – retrosplenial cortex, AC – auditory cortex). The top of panel (**a**) demonstrates results trending towards significance ($0.051<P\leq0.1$) in the ACC and RSC. The bottom of (**a**) shows the significant ($P\leq0.05$) differences in the AC between control and auditory fear conditioned mice. (**b**) The results of the analysis of the next 28 brains (n =14 auditory fear conditioning, n=14 controls) in the series, with the significant results ($P\leq0.05$) in the insula (In), medial amygdala (MeA), basolateral and lateral amygdala (BLA/LA), central amygdala (CeA), and auditory cortex (AC). Note that for the first analysis, many of the areas were significant for analysis 2 had p-values that ranged between P = 0.2 and p = 0.11 and therefore are not displayed. This is relevant when considering the significant results ($P\leq0.05$) of combing the two groups for a final analysis (**c**). The fact that the significant results were in the same areas and same direction of analysis two suggests

that the results of analysis one were in the same direction with similar strength as the effects presented in analysis two. (**d-f**) Sampling from only the voxels that showed significance ($P \leq 0.05$) in the auditory cortex, the bar graphs presented show the difference in VBM signal (grey matter voxel intensity multiplied by the Jacobian) between the auditory fear conditioned group and controls. Data are presented as mean ± s.e.m. * $P \leq 0.05$

Figure 7.3-4. Dendritic Spine Density in the Auditory Cortex

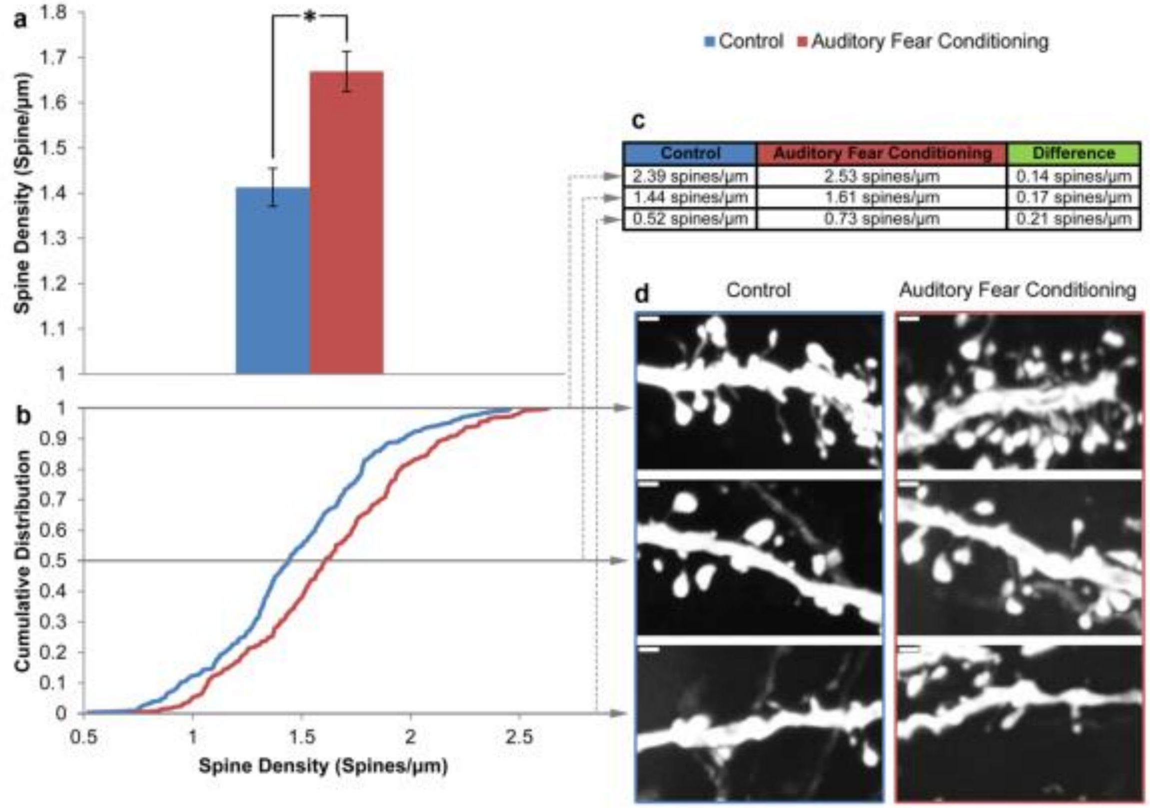

Control	Auditory Fear Conditioning	Difference
2.39 spines/µm	2.53 spines/µm	0.14 spines/µm
1.44 spines/µm	1.61 spines/µm	0.17 spines/µm
0.52 spines/µm	0.73 spines/µm	0.21 spines/µm

(**a**)The bar graph shows the significant difference in average spine density between the auditory fear conditioning group and control (*t* test, n = 9 auditory fear conditioning, n = 9 control, $p<0.05$, $t_{16} = 2.79$). (**b**)The cumulative distribution of the average spine densities for each dendrite length shows a significant rightward shift (higher spine densities across the distribution) for the auditory fear conditioned group (K-S test, n= 290 and 300 for auditory fear conditioned and control group respectively, $p < 0.0005$, $D = 0.185$). (**c-d**) The maximum, mid-point, and minimum densities from the distribution the auditory fear conditioning group and control are presented in the table (**c**) with commiserate confocal images of representative densities (**d**). Data are presented as mean ± s.e.m. * $P \leq 0.05$

Figure 7.3-5. Dendritic Spine Width, Length, and their Ratio in the Auditory Cortex.

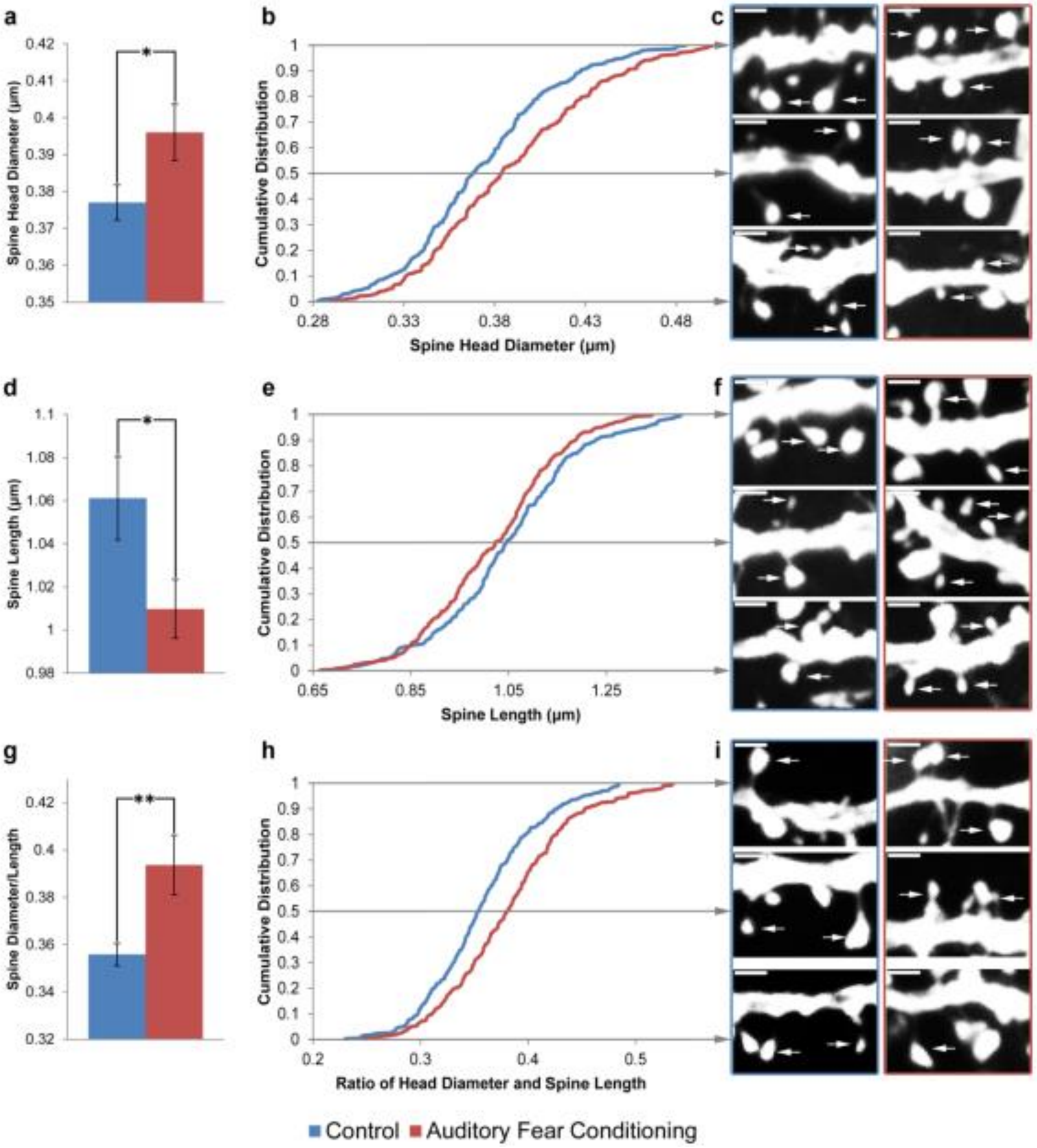

(**a**) The bar graph shows the significant difference in average spine diameter between the auditory fear conditioning group and control (*t* test, n = 9 auditory fear conditioning, n = 9 control, P≤0.05, $t_{16} = 2.23$). (**b**)The cumulative distribution of the spine head diameter for each dendritic spine shows a significant rightward shift (wider spine diameter across the distribution) for the auditory fear conditioning group when compared to controls (K-

S test, n= 290 and 300 for auditory fear conditioned and control group respectively, $P \leq 0.0001$, $D = 0.182$). (**c**) The maximum, mid-point, and minimum diameters from the distribution for the auditory fear conditioning and control groups are shown in representative confocal images. (**d-f**) These figures show the same analysis of those of spine diameter but for the length of the spines (*t* test, n = 9 auditory fear conditioning, n = 9 control, $P \leq 0.05$, $t_{16} = 2.17$) and (K-S test, n= 290 and 300 for auditory fear conditioned and control group respectively, $P \leq 0.05$, $D = 0.123$). These tests reveal that the auditory fear conditioning group has significantly shorter dendritic spine lengths than the control. The bottom panel shows the same panel for the ratio of the spine diameter and length ($P \leq 0.05$ for the overall comparison and $P \leq 0.0001$ for the K-S analysis). (**g-i**) These figures show the same analysis of those of spine diameter and length but for the ratio of the diameter to the length of the spines (*t* test, n = 9 auditory fear conditioning, n = 9 control, $P \leq 0.01$, $t_{16} = 2.92$) and (K-S test, n= 290 and 300 for auditory fear conditioned and control group respectively, $P \leq 0.0005$, $D = 0.2178$). These tests reveal that the auditory fear conditioning group has dendritic spines with a significantly larger ratio of head diameter to length when compared to controls. Data in bar graphs are presented as mean ± s.e.m. Data in the line graphs are the average of that noted measure (head diameter, length, and the ratio) per dendritic length presented as a cumulative distribution. Dendritic spine images are from maximum projections used in the analysis (100x). * $P \leq 0.05$ ** ≤ 0.01

Figure 7.3-6. Nuclei Density and Width Measurements in the Auditory Cortex.

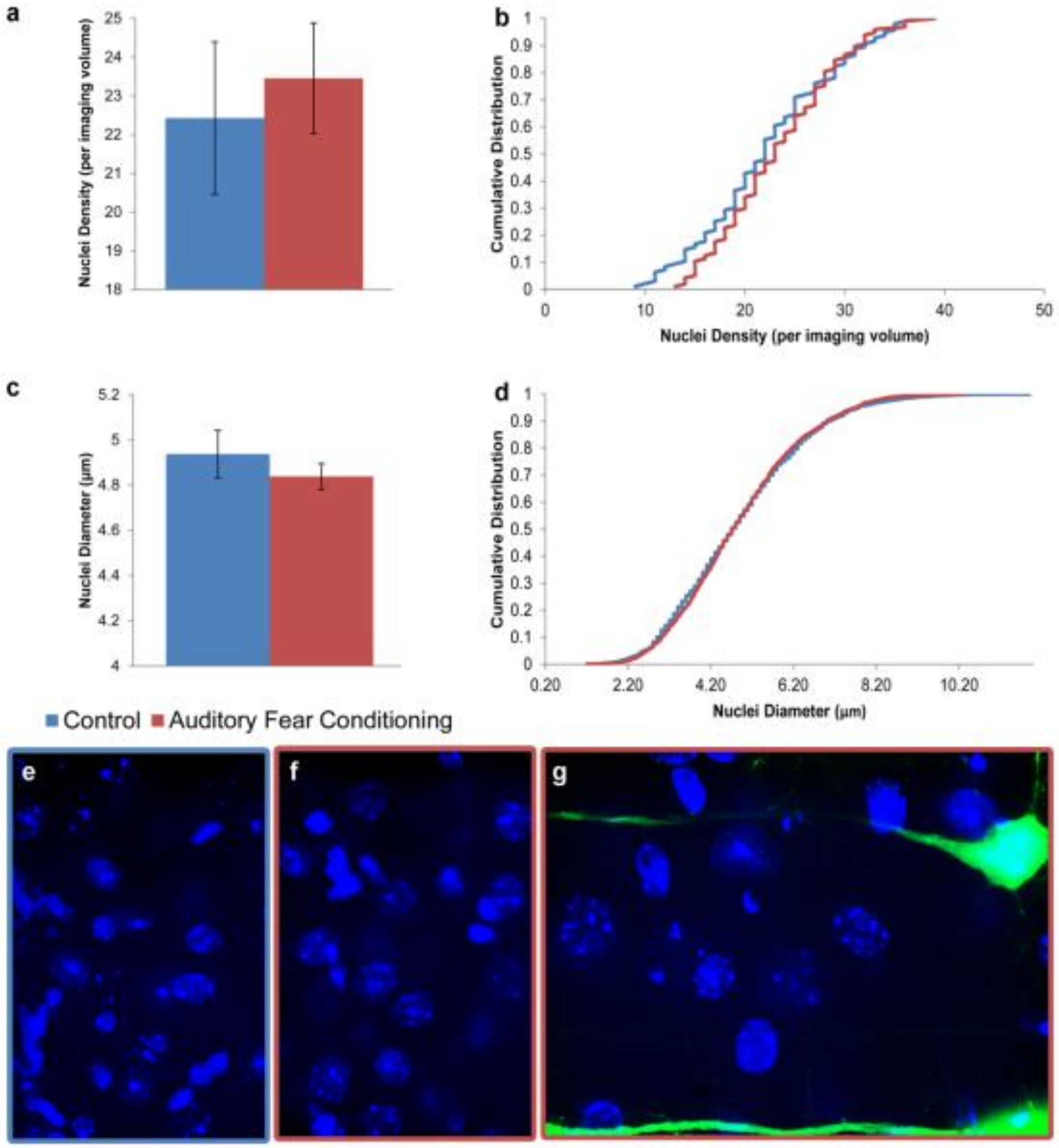

(**a**) The comparison of the nuclei density between the auditory fear conditioning and control groups did not show a significant difference (*t* test, n = 8 per group, P = 0.68, t_{14} = 0.422). (**b**) Further, the respective cumulative distribution of the cell nuclei density measures also did not show a significant difference (K-S test, n = 96 per group, P = 0.68, *D* = 0.1046). (**c**) Likewise, there was an overall lack of a significant difference between the auditory fear conditioning group and the control group for nuclei diameter (t-test, n

= 8 per group, P = 0.42, t_{14} = 0.830). (**d**) Additionally, the cumulative distribution of nuclei diameters was not significantly different across groups (K-S test, n = 2042 for auditory fear conditioning, n = 1828 for control, P = 0.45, *D* = 0.0269). (**e-g**) The pictures show representative images of the Hoechst staining for the control group (**e**), auditory fear conditioning group (**f**), and a combined overlay with the *Thy1*-YFP expressing neurons (**g**). Data in bar graphs are presented as mean ± s.e.m. Data in the line graphs are the average of the noted measure (e.g., density or width).

Figure 7.3-7. Correlations of VBM and Dendritic Spine/Nuclei Density Analysis

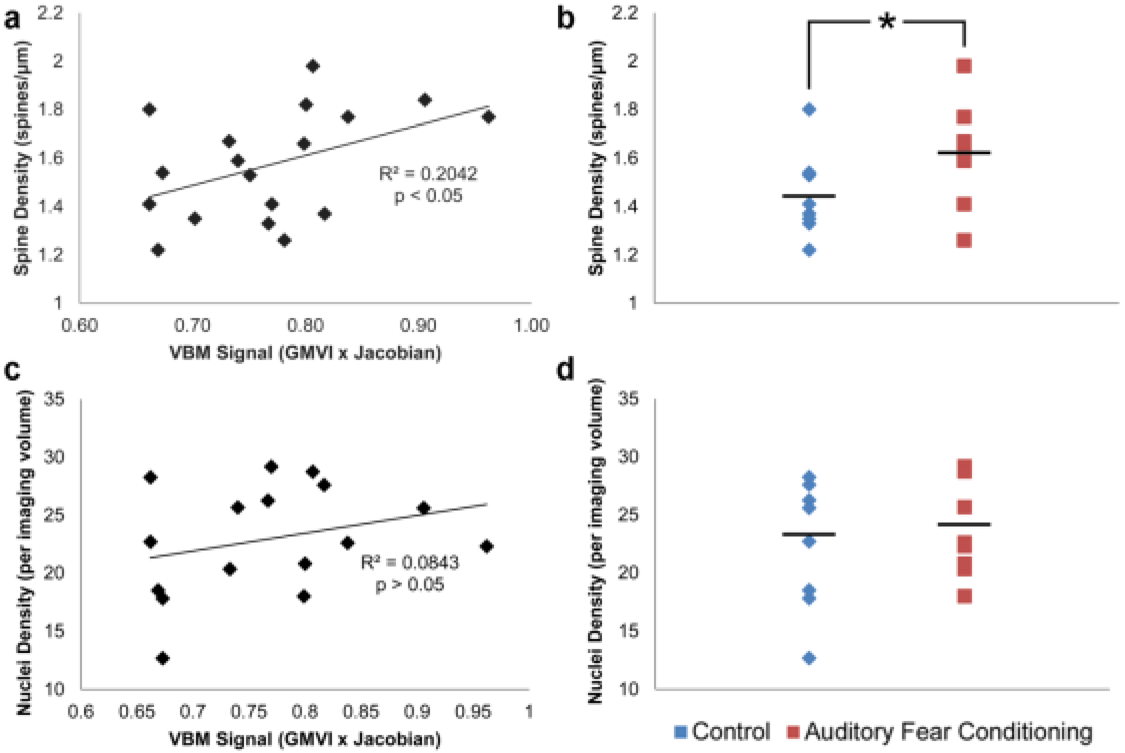

(**a**) A scatter plot of the total data showing an overall significant correlation of spine density values to the VBM signal used for comparison between the auditory fear conditioned group and the control group (Pearson's correlation, n=9 per group, one way analysis, $P \leq 0.05$, $R^2 = 0.2042$). (**b**) A plot of the difference in dendritic spine density for the 18 animals used for the analysis (*t* test, n = 9 auditory fear conditioning, n = 9 control, $P \leq 0.05$, $t_{16} = 2.23$). (**c**)The overall correlation between the nuclei density and VBM signal was not significant (Pearson's correlation, n=8 per group, one way analysis, P = 0.138, $R^2 = 0.0843$). The respective data used for the correlation is parsed in the top right and bottom right graphs. (**b**) A plot of the difference in nuclei density for the 16 animals used for the analysis (*t* test, n = 8 per group, P = 0.68, $t_{14} = 0.422$).

Figure 7.7.4-1 Schematic of Volume Changes with Dendritic Spine Changes

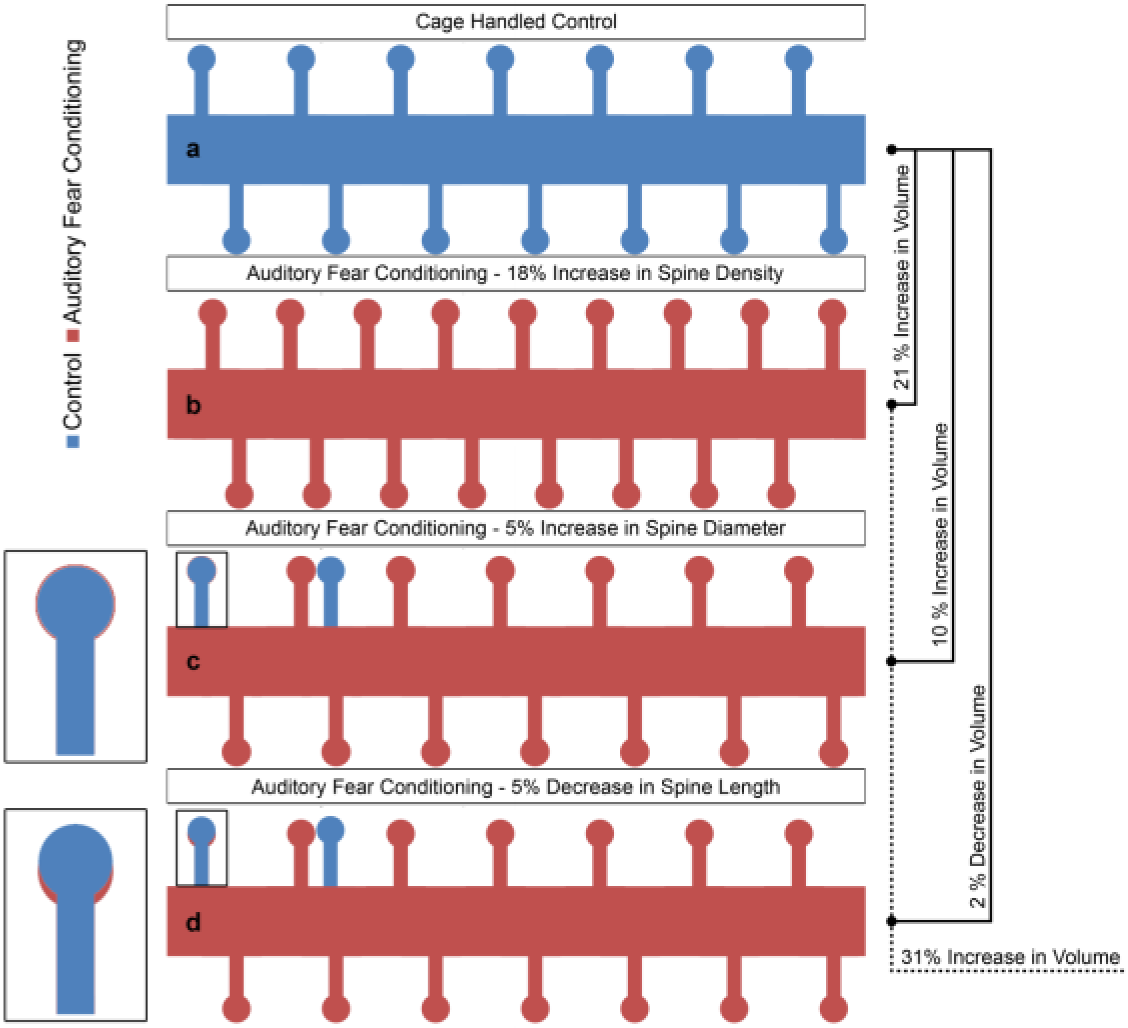

(**a**) A schematic representation of the control group's average dendritic width, length, and density (scaled to represent a 10 micron length of dendrite). By assuming a spine to be a sphere atop a cylinder we are able to approximate the impact of changes of density and morphology on overall volumetric changes at the macro scale. (**b**)The representation of an auditory dendrite shows an 18% increase in density of spines only (keeping all other variables constant), which results in a commiserate 21% increase in volume. (**c**)The second red dendrite shows a 5% increase in the diameter of spines holding all of the variables constant – the result is a 10% increase in volume. (**d**)Looking at the third and final red dendrite a 5% decrease in length of a spine there is commiserate loss of only 2%

of the volume. Changing all three variables, to reflect the totality of our findings here, results in a 31% increase of volume occupied by spines of the auditory fear conditioning group versus the control group. Representative magnifications of a single spine are shown next to the 2nd and 3rd red dendrite to get a sense of the effect of 5% difference.

Chapter 8:

Overall Discussion and Future Directions

8.1 General Discussion

As discussed in the introduction, the work in this dissertation lies broadly within the field of emotion and memory. Within those two very large fields, lies fear conditioning and extinction, which is a behavioral paradigm that really operates at the intersection of memory and emotion. Within that subfield is the study of the neurobiological and neuroanatomical basis of fear conditioning and extinction. It is in this realm that this dissertation makes its most prominent scientific contributions. In particular, the majority of the work is focused on examining the circuitry that is proposed to underlie fear conditioning and extinction using *ex vivo* diffusion weighted probabilistic tractography and anterograde biotinylated dextran amine tracing. The later work has also focused on understanding the long term structural brain changes cause by auditory fear conditioning by employing *ex vivo* based voxel-based morphometry methods with complementary confocal analysis of dendritic spine density and morphology.

The mouse model has risen to become one of the most prominently used experimental animals – especially in the context of genetic and molecular manipulations. However, there is a paucity of work focusing on the neuroanatomical structure of the mouse brain (the mouse model would come to prominence after neuronal tracing reached its zenith, so it is normally assumed that the mouse brain follows the structure of the rat brain). Here, several of the chapters here (4-6) have helped to fill this gap in knowledge through studying the connections of the olfactory bulb, the posterior thalamic nuclei including the medial geniculate nucleus, and the infralimbic and prelimbic cortices, especially with respect to the proposed fear circuit. Further, chapter 6 has established a much-needed precedence for using MRI techniques to do translationally and comparatively meaningful studies between humans and small animal models like the mouse. Chapter 7 changes approaches slightly and investigates the long term structural changes in the mouse brain due to auditory fear conditioning, in doing so it attempts to understand the role of the auditory cortex in auditory fear conditioning. A question that is particularly relevant, as chapter 3 and 6 point out, because there are multiple inputs of auditory information to the amygdala and their roles are still not well characterized.

From a technical standpoint, the work of the dissertation accomplished many things. It provides a broadly usable method for conducting *ex vivo* MRI studies. The method is especially powerful because it is affordable, reliable, and high-throughput. Because MRI scanner time is often limited and expensive, the ability to scan at least 16 brains in one session allows for very powerful studies to be undertaken (e.g., Chapter 7). Further, it provides technical developments, including adding studies to the literature that further establish the underlying mechanisms of MRI techniques. Chapter 3-6 all complement the MRI based probabilistic methods with other confirmatory measures including MEMRI and anterograde tracing. In doing so they help to confirm the underlying assumption the water diffuses along the length of axons and therefore can be used to predict the connectivity of the brain through the use of diffusion weighted MRI imaging. Likewise, chapter 7 provides a much needed analysis of the potential cellular underpinnings of the voxel-based morphometry. The strong and significant correlation between increases in the VBM signal of the auditory cortex with increases in dendritic spine density after auditory fear conditioning finally provides evidence for a neural basis for VBM signal change. At the same time the lack of a correlation with the nuclear density and VBM signal in the auditory cortex helps provide evidence against the hypothesis that glial or neuronal proliferation account for VBM signal change.

8.2 Future Directions

The future directions from the work of this dissertation are to some extent unlimited. However, there are several categories of future studies that should be noted with the appropriate examples. These include further analysis of the mechanisms underlying MRI techniques, further scientific exploration of the role of the auditory cortex, further comparative work between humans and mice, and working with collaborators to further expand the use of the *ex vivo* methods.

8.2.1 Researching Mechanisms of MRI Techniques

Future directions in researching the neurobiological mechanisms of MRI techniques could be an entire career. However, first and foremost, replication of the combined VBM/confocal study using another behavioral paradigm (e.g., appetitive learning) would provide extremely strong evidence for the role of dendritic spine density fluctuations to account for differences in the VBM signal. In the same stroke, experimental manipulations designed to affect the VBM signal and dendritic spines should be conducted to further bolster the VBM signal – spine density correlation. One could hypothesize, for example, that an animal undergoing extinction training may show reduced dendritic spine density and VBM signal in the auditory cortex. Likewise, within chapter 7 was also the discussion of other factors that could account for changes in VBM signals, these include changes in post-synaptic density, neuronal or glial size, or dendrite arborization. All of these could be evaluated scientifically, with immunohistochemistry methods either using the *Thy1*-YFP mouse, or alternative mouse lines. Looking to another technique, diffusion weighted imaging allows for not only probabilistic tractography but also tract-based spatial statistic (TBSS). Tract based spatial statistics is used to determine if there are differences in white matter between two groups. By employing that technique in mice, it would then be possible to better understand what change in white matter may account for the observed signal differences.

8.2.2 Further Scientific Exploration of the Role of the Auditory Cortex

The VBM and confocal results that showed long-term structural changes in the auditory cortex with auditory fear conditioning provide evidence that it may be involved in the long term memory of the auditory conditioning. Follow-up work could include a range of approaches. A simple lesioning study at different time points after conditioning would provide a temporal understanding of when the changes to the auditory cortex occur and whether they mediate long term memory. Similarly, using techniques that block plasticity in the auditory cortex would provide a mechanistic understanding of what is causing the structural shifts and would also provide evidence for the role of the auditory cortex. Employing the use of *Thy1-ChR2* mice – that is those who have channel rhodopsin on the same neurons that showed dendritic density and morphology differences with auditory fear conditioning – would allow for direct control and elucidation of the role of those particular neurons in the auditory cortex through the use of optogenetics approaches.

8.2.3 Further Comparative Work between Humans and Mice

One of the strengths of MRI based techniques is the ability to use them in both humans and mice. Employing methods like DWI based probabilistic tractography between humans and mice would allow for a greater understanding of the connectivity of each species' brain, which would then allow for a better understanding of where the mouse brain is a good model for the human brain and where it fails. From a pathophysiological perspective, there are many human diseases that are modeled with genetically modified mice – using MRI techniques would allow for a chance to see if brain structures between the model and the patient are similar or different (again leading to a better understanding of how applicable a model the mouse is for humans and human conditions).

8.2.4 Work with Collaborators to Expand the Use of Ex Vivo Imaging

As presented in Chapter 2, several collaborating scientists have already brought these approaches to address future work. Projects are currently underway to acquire ultra-high-resolution of human brain sections, which are then being sectioned and processed for an extensive histological undertaking. In doing so it is hoped that the source of signal across many different imaging sequences can be compared and correlated with various histological measures. The fox work, presented in chapter 2, is attempting to use MRI approaches to better understand how domestication changes brain structure and connectivity. The hamster brains are currently being used to generate a much-needed MRI atlas. Finally, the work on the sea lions is attempting to use MRI based methods to better understand how certain types of toxicity alter the structure and connectivity of the brain.

Appendix

A-1. Scientific Publications Outside of the Scope of the Dissertation

This appendix section is designed to highlight other work completed during the duration of the dissertation that did not fall within the scope of the dissertation. These works are as detailed below:

Keifer Jr., O.P., O'Connor, D.M., and Boulis, N.M. (2014) Gene and protein therapies utilizing VEGF for ALS. Pharmacology & Therapeutics 141 (3), 261-271

Keifer Jr., O.P., Riley, J.P., Boulis, N.M. (2014) Deep Brain Stimulation for Chronic Pain – Intracranial Targets, Clinical Outcomes, and Trial Design Considerations. *Neurosurgical Clinics of North America*, *Submitted*

Keifer, Jr., O.P., Hurt, R.C., Ressler, K.J, and Marvar, P.J. (2014) The Role of the Angiotensin Receptor Type 1 on Corticotropin-Releasing Factor Expressing Neurons in Auditory Fear Conditioning. *Biological Psychiatry*, *In Preparation*.

References

Aggleton, J. P., M. J. Burton and R. E. Passingham (1980). "Cortical and subcortical afferents to the amygdala of the rhesus monkey (Macaca mulatta)." Brain Res **190**(2): 347-368.

Aldhafeeri, F. M., I. Mackenzie, T. Kay, J. Alghamdi and V. Sluming (2012). "Neuroanatomical correlates of tinnitus revealed by cortical thickness analysis and diffusion tensor imaging." Neuroradiology **54**(8): 883-892.

Anaby, D., I. D. Duncan, C. M. Smith and Y. Cohen (2013). "White matter maturation in the brains of Long Evans shaker myelin mutant rats by ex-vivo QSI and DTI." Magn Reson Imaging **31**(7): 1097-1104.

Apergis-Schoute, A. M., J. Debiec, V. Doyere, J. E. LeDoux and G. E. Schafe (2005). "Auditory fear conditioning and long-term potentiation in the lateral amygdala require ERK/MAP kinase signaling in the auditory thalamus: a role for presynaptic plasticity in the fear system." J Neurosci **25**(24): 5730-5739.

Archibald, R. and A. Gelb (2002). "A method to reduce the Gibbs ringing artifact in MRI scans while keeping tissue boundary integrity." IEEE Trans Med Imaging **21**(4): 305-319.

Armony, J. L., D. Servan-Schreiber, L. M. Romanski, J. D. Cohen and J. E. LeDoux (1997). "Stimulus generalization of fear responses: effects of auditory cortex lesions in a computational model and in rats." Cereb Cortex **7**(2): 157-165.

Ashburner, J. and K. J. Friston (2000). "Voxel-based morphometry--the methods." Neuroimage **11**(6 Pt 1): 805-821.

Badea, A. and G. A. Johnson (2012). "Magnetic resonance microscopy." Anal Cell Pathol (Amst) **35**(4): 205-227.

Bakin, J. S. and N. M. Weinberger (1990). "Classical conditioning induces CS-specific receptive field plasticity in the auditory cortex of the guinea pig." Brain Res **536**(1-2): 271-286.

Beaulieu, C. F., X. Zhou, G. P. Cofer and G. A. Johnson (1993). "Diffusion-weighted MR microscopy with fast spin-echo." Magn Reson Med **30**(2): 201-206.

Behrens, T. E., H. J. Berg, S. Jbabdi, M. F. Rushworth and M. W. Woolrich (2007). "Probabilistic diffusion tractography with multiple fibre orientations: What can we gain?" Neuroimage **34**(1): 144-155.

Behrens, T. E., H. Johansen-Berg, M. W. Woolrich, S. M. Smith, C. A. Wheeler-Kingshott, P. A. Boulby, G. J. Barker, E. L. Sillery, K. Sheehan, O. Ciccarelli, A. J. Thompson, J. M. Brady and P. M. Matthews (2003). "Non-invasive mapping of connections between human thalamus and cortex using diffusion imaging." Nat Neurosci **6**(7): 750-757.

Behrens, T. E., M. W. Woolrich, M. Jenkinson, H. Johansen-Berg, R. G. Nunes, S. Clare, P. M. Matthews, J. M. Brady and S. M. Smith (2003). "Characterization and propagation of uncertainty in diffusion-weighted MR imaging." Magn Reson Med **50**(5): 1077-1088.

Belyaev, D. K., I. Z. Plyusnina and L. N. Trut (1985). "Domestication in the silver fox (Vulpes fulvus Desm): Changes in physiological boundaries of the sensitive period of primary socialization." Applied Animal Behaviour Science **13**(4): 359-370.

Benevento, L. A. and J. H. Fallon (1975). "The ascending projections of the superior colliculus in the rhesus monkey (Macaca mulatta)." J Comp Neurol **160**(3): 339-361.

Benveniste, H. and S. Blackband (2002). "MR microscopy and high-resolution small animal MRI: applications in neuroscience research." Prog Neurobiol **67**(5): 393-420.

Benveniste, H., K. Kim, L. Zhang and G. A. Johnson (2000). "Magnetic resonance microscopy of the C57BL mouse brain." Neuroimage **11**(6 Pt 1): 601-611.

Besson, J. A., P. V. Best and E. R. Skinner (1992). "Post-mortem proton magnetic resonance spectrometric measures of brain regions in patients with a pathological diagnosis of Alzheimer's disease and multi-infarct dementia." Br J Psychiatry **160**: 187-190.

Bhatt, D. H., S. Zhang and W. B. Gan (2009). "Dendritic spine dynamics." Annu Rev Physiol **71**: 261-282.

Blanchard, D. C. and R. J. Blanchard (1972). "Innate and conditioned reactions to threat in rats with amygdaloid lesions." J Comp Physiol Psychol **81**(2): 281-290.

Blanchard, R. J. and D. C. Blanchard (1969). "Passive and active reactions to fear-eliciting stimuli." J Comp Physiol Psychol **68**(1): 129-135.

Blum, P. S., L. D. Abraham and S. Gilman (1979). "Vestibular, auditory, and somatic input to the posterior thalamus of the cat." Exp Brain Res **34**(1): 1-9.

Boatman, J. A. and J. J. Kim (2006). "A thalamo-cortico-amygdala pathway mediates auditory fear conditioning in the intact brain." Eur J Neurosci **24**(3): 894-900.

Bobinski, M., M. J. de Leon, J. Wegiel, S. Desanti, A. Convit, L. A. Saint Louis, H. Rusinek and H. M. Wisniewski (2000). "The histological validation of post mortem magnetic resonance imaging-determined hippocampal volume in Alzheimer's disease." Neuroscience **95**(3): 721-725.

Bourne, J. N. and K. M. Harris (2008). "Balancing structure and function at hippocampal dendritic spines." Annu Rev Neurosci **31**: 47-67.

Brainard, M. S. and A. J. Doupe (2000). "Interruption of a basal ganglia-forebrain circuit prevents plasticity of learned vocalizations." Nature **404**(6779): 762-766.

Braver, T. S., D. M. Barch, W. M. Kelley, R. L. Buckner, N. J. Cohen, F. M. Miezin, A. Z. Snyder, J. M. Ollinger, E. Akbudak, T. E. Conturo and S. E. Petersen (2001). "Direct comparison of prefrontal cortex regions engaged by working and long-term memory tasks." Neuroimage **14**(1 Pt 1): 48-59.

Brinkhus, H. B., E. Carstens and M. Zimmermann (1979). "Encoding of graded noxious skin heating by neurons in posterior thalamus and adjacent areas in the cat." Neurosci Lett **15**(1): 37-42.

Buchanan, S. L., R. H. Thompson, B. L. Maxwell and D. A. Powell (1994). "Efferent connections of the medial prefrontal cortex in the rabbit." Exp Brain Res **100**(3): 469-483.

Buck, L. and R. Axel (1991). "A novel multigene family may encode odorant receptors: a molecular basis for odor recognition." Cell **65**(1): 175-187.

Budinger, E., P. Heil and H. Scheich (2000). "Functional organization of auditory cortex in the Mongolian gerbil (Meriones unguiculatus). IV. Connections with anatomically characterized subcortical structures." Eur J Neurosci **12**(7): 2452-2474.

Budinger, E., A. Laszcz, H. Lison, H. Scheich and F. W. Ohl (2008). "Non-sensory cortical and subcortical connections of the primary auditory cortex in Mongolian gerbils: bottom-up and top-down processing of neuronal information via field AI." Brain Res **1220**: 2-32.

Buonanno, F. S., I. L. Pykett, J. P. Kistler, J. Vielma, T. J. Brady, W. S. Hinshaw, M. R. Goldman, J. H. Newhouse and G. M. Pohost (1982). "Cranial anatomy and detection of ischemic stroke in the cat by nuclear magnetic resonance imaging." Radiology **143**(1): 187-193.

Burgos-Robles, A., I. Vidal-Gonzalez and G. J. Quirk (2009). "Sustained conditioned responses in prelimbic prefrontal neurons are correlated with fear expression and extinction failure." J Neurosci **29**(26): 8474-8482.

Burgos-Robles, A., I. Vidal-Gonzalez, E. Santini and G. J. Quirk (2007). "Consolidation of fear extinction requires NMDA receptor-dependent bursting in the ventromedial prefrontal cortex." Neuron **53**(6): 871-880.

Callaway, E. M. (2008). "Transneuronal circuit tracing with neurotropic viruses." Curr Opin Neurobiol **18**(6): 617-623.

Campeau, S., H. Akil and S. J. Watson (1997). "Lesions of the medial geniculate nuclei specifically block corticosterone release and induction of c-fos mRNA in the forebrain associated with audiogenic stress in rats." J Neurosci **17**(15): 5979-5992.

Campeau, S. and M. Davis (1995). "Involvement of the central nucleus and basolateral complex of the amygdala in fear conditioning measured with fear-potentiated startle in rats trained concurrently with auditory and visual conditioned stimuli." J Neurosci **15**(3 Pt 2): 2301-2311.

Canals, S., M. Beyerlein, A. L. Keller, Y. Murayama and N. K. Logothetis (2008). "Magnetic resonance imaging of cortical connectivity in vivo." NeuroImage **40**(2): 458-472.

Carlson, B. A. (2012). "Diversity matters: the importance of comparative studies and the potential for synergy between neuroscience and evolutionary biology." Arch Neurol **69**(8): 987-993.

Carlson, J. M., F. Beacher, K. S. Reinke, R. Habib, E. Harmon-Jones, L. R. Mujica-Parodi and G. Hajcak (2012). "Nonconscious attention bias to threat is correlated with anterior cingulate cortex gray matter volume: a voxel-based morphometry result and replication." Neuroimage **59**(2): 1713-1718.

Carstens, E. and T. Yokota (1980). "Viscerosomatic convergence and responses to intestinal distension of neurons at the junction of midbrain and posterior thalamus in the cat." Exp Neurol **70**(2): 392-402.

Carter, D. A. and H. C. Fibiger (1977). "Ascending projections of presumed dopamine-containing neurons in the ventral tegmentum of the rat as demonstrated by horseradish peroxidase." Neuroscience **2**(4): 569-576.

Cassell, M. D. and D. J. Wright (1986). "Topography of projections from the medial prefrontal cortex to the amygdala in the rat." Brain Res Bull **17**(3): 321-333.

Chetelat, G., B. Landeau, F. Eustache, F. Mezenge, F. Viader, V. de la Sayette, B. Desgranges and J. C. Baron (2005). "Using voxel-based morphometry to map the structural changes associated with rapid conversion in MCI: a longitudinal MRI study." Neuroimage **27**(4): 934-946.

Chiba, T., T. Kayahara and K. Nakano (2001). "Efferent projections of infralimbic and prelimbic areas of the medial prefrontal cortex in the Japanese monkey, Macaca fuscata." Brain Res **888**(1): 83-101.

Choi, D. C., K. A. Maguschak, K. Ye, S. W. Jang, K. M. Myers and K. J. Ressler "Prelimbic cortical BDNF is required for memory of learned fear but not extinction or innate fear." Proc Natl Acad Sci U S A **107**(6): 2675-2680.

Chuang, K.-H. and A. P. Koretsky (2009). "Accounting for nonspecific enhancement in neuronal tract tracing using manganese enhanced magnetic resonance imaging." Magnetic Resonance Imaging **27**(5): 594-600.

Clasca, F., A. Llamas and F. Reinoso-Suarez (1997). "Insular cortex and neighboring fields in the cat: a redefinition based on cortical microarchitecture and connections with the thalamus." J Comp Neurol **384**(3): 456-482.

Clugnet, M. C., J. E. LeDoux and S. F. Morrison (1990). "Unit responses evoked in the amygdala and striatum by electrical stimulation of the medial geniculate body." J Neurosci **10**(4): 1055-1061.

Cook, P., C. Reichmuth and F. Gulland (2011). "Rapid behavioural diagnosis of domoic acid toxicosis in California sea lions." Biol Lett **7**(4): 536-538.

Cooper, L. A., J. Kong, D. A. Gutman, F. Wang, J. Gao, C. Appin, S. Cholleti, T. Pan, A. Sharma, L. Scarpace, T. Mikkelsen, T. Kurc, C. S. Moreno, D. J. Brat and J. H. Saltz

(2012). "Integrated morphologic analysis for the identification and characterization of disease subtypes." J Am Med Inform Assoc **19**(2): 317-323.

Corcoran, K. A. and G. J. Quirk (2007). "Activity in prelimbic cortex is necessary for the expression of learned, but not innate, fears." J Neurosci **27**(4): 840-844.

Cousens, G. and T. Otto (1998). "Both pre- and posttraining excitotoxic lesions of the basolateral amygdala abolish the expression of olfactory and contextual fear conditioning." Behav Neurosci **112**(5): 1092-1103.

Cranford, J. L., S. J. Ladner, C. B. Campbell and W. D. Neff (1976). "Efferent projections of the insular and temporal neocortex of the cat." Brain Res **117**(2): 195-210.

Crippa, A., C. P. Lanting, P. van Dijk and J. B. Roerdink (2010). "A diffusion tensor imaging study on the auditory system and tinnitus." Open Neuroimag J **4**: 16-25.

Cross, D. J., S. Minoshima, Y. Anzai, J. A. Flexman, B. P. Keogh, Y. Kim and K. R. Maravilla (2004). "Statistical mapping of functional olfactory connections of the rat brain in vivo." Neuroimage **23**(4): 1326-1335.

D'Arceuil, H. E., S. Westmoreland and A. J. de Crespigny (2007). "An approach to high-resolution diffusion tensor imaging in fixed primate brain." Neuroimage **35**(2): 553-565.

Dauguet, J., S. Peled, V. Berezovskii, T. Delzescaux, S. K. Warfield, R. Born and C. F. Westin (2006). "3D histological reconstruction of fiber tracts and direct comparison with diffusion tensor MRI tractography." Med Image Comput Comput Assist Interv **9**(Pt 1): 109-116.

Dauguet, J., S. Peled, V. Berezovskii, T. Delzescaux, S. K. Warfield, R. Born and C. F. Westin (2007). "Comparison of fiber tracts derived from in-vivo DTI tractography with 3D histological neural tract tracer reconstruction on a macaque brain." Neuroimage **37**(2): 530-538.

Devlin, J. T., E. L. Sillery, D. A. Hall, P. Hobden, T. E. Behrens, R. G. Nunes, S. Clare, P. M. Matthews, D. R. Moore and H. Johansen-Berg (2006). "Reliable identification of the auditory thalamus using multi-modal structural analyses." Neuroimage **30**(4): 1112-1120.

Dhenain, M., J. L. Michot, N. Privat, J. L. Picq, F. Boller, C. Duyckaerts and A. Volk (2000). "MRI description of cerebral atrophy in mouse lemur primates." Neurobiol Aging **21**(1): 81-88.

Dhenain, M., S. W. Ruffins and R. E. Jacobs (2001). "Three-dimensional digital mouse atlas using high-resolution MRI." Dev Biol **232**(2): 458-470.

Diamond, I. T., K. L. Chow and W. D. Neff (1958). "Degeneration of caudal medial geniculate body following cortical lesion ventral to auditory area II in the cat." J Comp Neurol **109**(3): 349-362.

Diamond, I. T. and W. D. Neff (1957). "Ablation of temporal cortex and discrimination of auditory patterns." J Neurophysiol **20**(3): 300-315.

Dias, B. G. and K. J. Ressler (2014). "Parental olfactory experience influences behavior and neural structure in subsequent generations." Nat Neurosci **17**(1): 89-96.

Diedrichsen, J., J. H. Balsters, J. Flavell, E. Cussans and N. Ramnani (2009). "A probabilistic MR atlas of the human cerebellum." Neuroimage **46**(1): 39-46.

Domesick, V. B. (1969). "Projections from the cingulate cortex in the rat." Brain Res **12**(2): 296-320.

Doron, N. N. and J. E. Ledoux (1999). "Organization of projections to the lateral amygdala from auditory and visual areas of the thalamus in the rat." J Comp Neurol **412**(3): 383-409.

Dorph-Petersen, K. A., D. Caric, R. Saghafi, W. Zhang, A. R. Sampson and D. A. Lewis (2009). "Volume and neuron number of the lateral geniculate nucleus in schizophrenia and mood disorders." Acta Neuropathol **117**(4): 369-384.

Douaud, G., S. Jbabdi, T. E. Behrens, R. A. Menke, A. Gass, A. U. Monsch, A. Rao, B. Whitcher, G. Kindlmann, P. M. Matthews and S. Smith (2011). "DTI measures in crossing-fibre areas: increased diffusion anisotropy reveals early white matter alteration in MCI and mild Alzheimer's disease." Neuroimage **55**(3): 880-890.

Douaud, G., S. Smith, M. Jenkinson, T. Behrens, H. Johansen-Berg, J. Vickers, S. James, N. Voets, K. Watkins, P. M. Matthews and A. James (2007). "Anatomically related grey and white matter abnormalities in adolescent-onset schizophrenia." Brain **130**(Pt 9): 2375-2386.

Driehuys, B., J. Nouls, A. Badea, E. Bucholz, K. Ghaghada, A. Petiet and L. W. Hedlund (2008). "Small animal imaging with magnetic resonance microscopy." ILAR J **49**(1): 35-53.

Dulac, C. and R. Axel (1995). "A novel family of genes encoding putative pheromone receptors in mammals." Cell **83**(2): 195-206.

Dyrby, T. B., W. F. Baare, D. C. Alexander, J. Jelsing, E. Garde and L. V. Sogaard (2011). "An ex vivo imaging pipeline for producing high-quality and high-resolution diffusion-weighted imaging datasets." Hum Brain Mapp **32**(4): 544-563.

Dyrby, T. B., L. V. Sogaard, G. J. Parker, D. C. Alexander, N. M. Lind, W. F. Baare, A. Hay-Schmidt, N. Eriksen, B. Pakkenberg, O. B. Paulson and J. Jelsing (2007). "Validation of in vitro probabilistic tractography." Neuroimage **37**(4): 1267-1277.

Ebner, F. F. (1967). "Medial geniculate nucleus projections to telencephalon in the opossum." The Anatomical Record **157**: 238-239.

Elfenbein, H. A., R. F. Rosen, S. L. Stephens, R. C. Switzer, Y. Smith, J. Pare, P. D. Mehta, R. Warzok and L. C. Walker (2007). "Cerebral beta-amyloid angiopathy in aged squirrel monkeys." Histol Histopathol **22**(2): 155-167.

Fani, N., D. Gutman, E. B. Tone, L. Almli, K. B. Mercer, J. Davis, E. Glover, T. Jovanovic, B. Bradley, I. D. Dinov, A. Zamanyan, A. W. Toga, E. B. Binder and K. J. Ressler (2013). "FKBP5 and attention bias for threat: associations with hippocampal function and shape." JAMA Psychiatry **70**(4): 392-400.

Fani, N., T. Z. King, T. Jovanovic, E. M. Glover, B. Bradley, K. Choi, T. Ely, D. A. Gutman and K. J. Ressler (2012). "White matter integrity in highly traumatized adults with and without post-traumatic stress disorder." Neuropsychopharmacology **37**(12): 2740-2746.

Farb, C. R. and J. E. LeDoux (1997). "NMDA and AMPA receptors in the lateral nucleus of the amygdala are postsynaptic to auditory thalamic afferents." Synapse **27**(2): 106-121.

Farb, C. R. and J. E. Ledoux (1999). "Afferents from rat temporal cortex synapse on lateral amygdala neurons that express NMDA and AMPA receptors." Synapse **33**(3): 218-229.

Farinelli, M., O. Deschaux, S. Hugues, A. Thevenet and R. Garcia (2006). "Hippocampal train stimulation modulates recall of fear extinction independently of prefrontal cortex synaptic plasticity and lesions." Learn Mem **13**(3): 329-334.

Feng, G., R. H. Mellor, M. Bernstein, C. Keller-Peck, Q. T. Nguyen, M. Wallace, J. M. Nerbonne, J. W. Lichtman and J. R. Sanes (2000). "Imaging neuronal subsets in transgenic mice expressing multiple spectral variants of GFP." Neuron **28**(1): 41-51.

Ford, C. C., T. L. Ceckler, J. Karp and R. M. Herndon (1990). "Magnetic resonance imaging of experimental demyelinating lesions." Magn Reson Med **14**(3): 461-481.

Freeman, E. D., A. Ipser, A. Palmbaha, D. Paunoiu, P. Brown, C. Lambert, A. Leff and J. Driver (2013). "Sight and sound out of synch: Fragmentation and renormalisation of audiovisual integration and subjective timing." Cortex.

Garcia, R., C. H. Chang and S. Maren (2006). "Electrolytic lesions of the medial prefrontal cortex do not interfere with long-term memory of extinction of conditioned fear." Learn Mem **13**(1): 14-17.

Geiser, E., M. Notter and J. D. Gabrieli (2012). "A corticostriatal neural system enhances auditory perception through temporal context processing." J Neurosci **32**(18): 6177-6182.

Gewirtz, J. C., W. A. Falls and M. Davis (1997). "Normal conditioned inhibition and extinction of freezing and fear-potentiated startle following electrolytic lesions of medical prefrontal cortex in rats." Behav Neurosci **111**(4): 712-726.

Goldstein, T., J. A. Mazet, T. S. Zabka, G. Langlois, K. M. Colegrove, M. Silver, S. Bargu, F. Van Dolah, T. Leighfield, P. A. Conrad, J. Barakos, D. C. Williams, S. Dennison, M. Haulena and F. M. Gulland (2008). "Novel symptomatology and changing epidemiology of domoic acid toxicosis in California sea lions (Zalophus californianus): an increasing risk to marine mammal health." Proc Biol Sci **275**(1632): 267-276.

Golub, Y., S. F. Kaltwasser, C. P. Mauch, L. Herrmann, U. Schmidt, F. Holsboer, M. Czisch and C. T. Wotjak (2011). "Reduced hippocampus volume in the mouse model of Posttraumatic Stress Disorder." J Psychiatr Res **45**(5): 650-659.

Good, C. D., I. Johnsrude, J. Ashburner, R. N. Henson, K. J. Friston and R. S. Frackowiak (2001). "Cerebral asymmetry and the effects of sex and handedness on brain structure: a voxel-based morphometric analysis of 465 normal adult human brains." Neuroimage **14**(3): 685-700.

Good, C. D., I. S. Johnsrude, J. Ashburner, R. N. Henson, K. J. Friston and R. S. Frackowiak (2001). "A voxel-based morphometric study of ageing in 465 normal adult human brains." Neuroimage **14**(1 Pt 1): 21-36.

Gourley, S. L., A. Olevska, M. S. Warren, J. R. Taylor and A. J. Koleske (2012). "Arg kinase regulates prefrontal dendritic spine refinement and cocaine-induced plasticity." J Neurosci **32**(7): 2314-2323.

Gourley, S. L., A. M. Swanson, A. M. Jacobs, J. L. Howell, M. Mo, R. J. Dileone, A. J. Koleske and J. R. Taylor (2012). "Action control is mediated by prefrontal BDNF and glucocorticoid receptor binding." Proc Natl Acad Sci U S A **109**(50): 20714-20719.

Gourley, S. L., A. M. Swanson and A. J. Koleske (2013). "Corticosteroid-induced neural remodeling predicts behavioral vulnerability and resilience." J Neurosci **33**(7): 3107-3112.

Grabner, G., A. L. Janke, M. M. Budge, D. Smith, J. Pruessner and D. L. Collins (2006). "Symmetric atlasing and model based segmentation: an application to the hippocampus in older adults." Med Image Comput Comput Assist Interv **9**(Pt 2): 58-66.

Grahn, J. A. and M. Brett (2007). "Rhythm and beat perception in motor areas of the brain." J Cogn Neurosci **19**(5): 893-906.

Graybiel, A. M. (1973). "The thalamo-cortical projection of the so-called posterior nuclear group: a study with anterograde degeneration methods in the cat." Brain Res **49**(2): 229-244.

Griffiths, P. D., M. N. Paley and E. H. Whitby (2005). "Post-mortem MRI as an adjunct to fetal or neonatal autopsy." Lancet **365**(9466): 1271-1273.

Grunecker, B., S. F. Kaltwasser, A. C. Zappe, B. T. Bedenk, Y. Bicker, V. I. Spoormaker, C. T. Wotjak and M. Czisch (2013). "Regional specificity of manganese accumulation and clearance in the mouse brain: implications for manganese-enhanced MRI." NMR Biomed **26**(5): 542-556.

Guldin, W. O. and H. J. Markowitsch (1984). "Cortical and thalamic afferent connections of the insular and adjacent cortex of the cat." J Comp Neurol **229**(3): 393-418.

Gutman, D. A., L. A. Cooper, S. N. Hwang, C. A. Holder, J. Gao, T. D. Aurora, W. D. Dunn, Jr., L. Scarpace, T. Mikkelsen, R. Jain, M. Wintermark, M. Jilwan, P. Raghavan, E. Huang, R. J. Clifford, P. Mongkolwat, V. Kleper, J. Freymann, J. Kirby, P. O. Zinn, C. S. Moreno, C. Jaffe, R. Colen, D. L. Rubin, J. Saltz, A. Flanders and D. J. Brat (2013). "MR imaging predictors of molecular profile and survival: multi-institutional study of the TCGA glioblastoma data set." Radiology **267**(2): 560-569.

Gutman, D. A., P. E. Holtzheimer, T. E. Behrens, H. Johansen-Berg and H. S. Mayberg (2009). "A tractography analysis of two deep brain stimulation white matter targets for depression." Biol Psychiatry **65**(4): 276-282.

Gutman, D. A., O. P. Keifer, Jr., M. E. Magnuson, D. C. Choi, W. Majeed, S. Keilholz and K. J. Ressler (2012). "A DTI tractography analysis of infralimbic and prelimbic connectivity in the mouse using high-throughput MRI." Neuroimage **63**(2): 800-811.

Gutman, D. A., M. Magnuson, W. Majeed, O. P. Keifer, Jr., M. Davis, K. J. Ressler and S. Keilholz (2013). "Mapping of the mouse olfactory system with manganese-enhanced magnetic resonance imaging and diffusion tensor imaging." Brain Struct Funct **218**(2): 527-537.

Hart, H., J. Radua, T. Nakao, D. Mataix-Cols and K. Rubia (2013). "Meta-analysis of functional magnetic resonance imaging studies of inhibition and attention in attention-deficit/hyperactivity disorder: exploring task-specific, stimulant medication, and age effects." JAMA Psychiatry **70**(2): 185-198.

Hecht, E. E., D. A. Gutman, T. M. Preuss, M. M. Sanchez, L. A. Parr and J. K. Rilling (2013). "Process versus product in social learning: comparative diffusion tensor imaging of neural systems for action execution-observation matching in macaques, chimpanzees, and humans." Cereb Cortex **23**(5): 1014-1024.

Hecht, E. E., L. E. Murphy, D. A. Gutman, J. R. Votaw, D. M. Schuster, T. M. Preuss, G. A. Orban, D. Stout and L. A. Parr (2013). "Differences in neural activation for object-directed grasping in chimpanzees and humans." J Neurosci **33**(35): 14117-14134.

Heinrichs, S. C., K. A. Leite-Morris, M. D. Guy, L. R. Goldberg, A. J. Young and G. B. Kaplan (2013). "Dendritic structural plasticity in the basolateral amygdala after fear conditioning and its extinction in mice." Behav Brain Res **248**: 80-84.

Henkelman, R. M. (2010). "Systems biology through mouse imaging centers: experience and new directions." Annu Rev Biomed Eng **12**: 143-166.

Herry, C. and R. Garcia (2002). "Prefrontal cortex long-term potentiation, but not long-term depression, is associated with the maintenance of extinction of learned fear in mice." J Neurosci **22**(2): 577-583.

Herzog, A. G. and G. W. Van Hoesen (1976). "Temporal neocortical afferent connections to the amygdala in the rhesus monkey." Brain Res **115**(1): 57-69.

Herzog, C. and T. Otto (1997). "Odor-guided fear conditioning in rats: 2. Lesions of the anterior perirhinal cortex disrupt fear conditioned to the explicit conditioned stimulus but not to the training context." Behav Neurosci **111**(6): 1265-1272.

Herzog, C. and T. Otto (1998). "Contributions of anterior perirhinal cortex to olfactory and contextual fear conditioning." Neuroreport **9**(8): 1855-1859.

Hessler, N. A. and A. J. Doupe (1999). "Singing-related neural activity in a dorsal forebrain-basal ganglia circuit of adult zebra finches." J Neurosci **19**(23): 10461-10481.

Hilpert, P. (1928). "Der Mandelkern des Menschen. I. Cytoarchitektonik und Faserverbindungen. ." Journal für Psychologie und Neurologie **36**: 44-74.

Hitchcock, J. and M. Davis (1986). "Lesions of the amygdala, but not of the cerebellum or red nucleus, block conditioned fear as measured with the potentiated startle paradigm." Behav Neurosci **100**(1): 11-22.

Horie, M., H. Tsukano, R. Hishida, H. Takebayashi and K. Shibuki (2013). "Dual compartments of the ventral division of the medial geniculate body projecting to the core region of the auditory cortex in C57BL/6 mice." Neurosci Res.

Hugues, S., O. Deschaux and R. Garcia (2004). "Postextinction infusion of a mitogen-activated protein kinase inhibitor into the medial prefrontal cortex impairs memory of the extinction of conditioned fear." Learn Mem **11**(5): 540-543.

Hurley, K. M., H. Herbert, M. M. Moga and C. B. Saper (1991). "Efferent projections of the infralimbic cortex of the rat." J Comp Neurol **308**(2): 249-276.

Iwata, J., J. E. LeDoux, M. P. Meeley, S. Arneric and D. J. Reis (1986). "Intrinsic neurons in the amygdaloid field projected to by the medial geniculate body mediate emotional responses conditioned to acoustic stimuli." Brain Res **383**(1-2): 195-214.

Izquierdo, A., C. L. Wellman and A. Holmes (2006). "Brief uncontrollable stress causes dendritic retraction in infralimbic cortex and resistance to fear extinction in mice." J Neurosci **26**(21): 5733-5738.

Javad, F., J. D. Warren, C. Micallef, J. S. Thornton, X. Golay, T. Yousry and L. Mancini (2013). "Auditory tracts identified with combined fMRI and diffusion tractography." Neuroimage.

Johansen-Berg, H. and T. E. Behrens (2006). "Just pretty pictures? What diffusion tractography can add in clinical neuroscience." Curr Opin Neurol **19**(4): 379-385.

Johnson, G. A., H. Benveniste, R. T. Engelhardt, H. Qiu and L. W. Hedlund (1997). "Magnetic resonance microscopy in basic studies of brain structure and function." Ann N Y Acad Sci **820**: 139-147; discussion 147-138.

Jones, E. G. (1985). Comparative Anatomy of the Thalamus. The Thalamus. E. G. Jones. Plenum Press, New York, Springer US.

Jones, S. V., D. C. Choi, M. Davis and K. J. Ressler (2008). "Learning-dependent structural plasticity in the adult olfactory pathway." J Neurosci **28**(49): 13106-13111.

Jones, S. V., S. A. Heldt, M. Davis and K. J. Ressler (2005). "Olfactory-mediated fear conditioning in mice: simultaneous measurements of fear-potentiated startle and freezing." Behav Neurosci **119**(1): 329-335.

Jones, S. V., L. Stanek-Rattiner, M. Davis and K. J. Ressler (2007). "Differential regional expression of brain-derived neurotrophic factor following olfactory fear learning." Learn Mem **14**(12): 816-820.

Kapp, B. S., M. Gallagher, M. D. Underwood, C. L. McNall and D. Whitehorn (1982). "Cardiovascular responses elicited by electrical stimulation of the amygdala central nucleus in the rabbit." Brain Res **234**(2): 251-262.

Keegan, P. M., O. P. Keifer, Jr.,, I. L. Parker, S. D. Keilholz and M. O. Platt (2013). "Spontaneous Strokes In Sickle Cell Transgenic Mice Captured Ex Vivo With Magnetic Resonance Imaging." Stroke. **44**: ATP261.

Kleinschmidt-DeMasters, B. K., C. A. Anderson and D. Rubinstein (1997). "Asymptomatic pontine lesions found by magnetic resonance imaging: are they central pontine myelinolysis?" J Neurol Sci **149**(1): 27-35.

Kluver, H. and P. C. Bucy (1937). ""Psychic blindness" and other symptoms following bilateral temporal lobectomy in Rhesus monkeys." American Journal of Physiology **119**: 352-353.

Knapska, E. and S. Maren (2009). "Reciprocal patterns of c-Fos expression in the medial prefrontal cortex and amygdala after extinction and renewal of conditioned fear." Learn Mem **16**(8): 486-493.

Koretsky, A. P. and A. C. Silva (2004). "Manganese-enhanced magnetic resonance imaging (MEMRI)." NMR Biomed **17**(8): 527-531.

Kosmal, A., M. Malinowska and A. Woznicka (1997). "Diversity of connections of the temporal neocortex with amygdaloid nuclei in the dog (Canis familiaris)." Acta Neurobiol Exp (Wars) **57**(4): 289-314.

Krettek, J. E. and J. L. Price (1978). "A description of the amygdaloid complex in the rat and cat with observations on intra-amygdaloid axonal connections." J Comp Neurol **178**(2): 255-280.

Kuhn, S. and J. Gallinat (2013). "Gray matter correlates of posttraumatic stress disorder: a quantitative meta-analysis." Biol Psychiatry **73**(1): 70-74.

Kukekova, A. V., L. N. Trut, I. N. Oskina, A. V. Kharlamova, S. G. Shikhevich, E. F. Kirkness, G. D. Aguirre and G. M. Acland (2004). "A marker set for construction of a genetic map of the silver fox (Vulpes vulpes)." J Hered **95**(3): 185-194.

LaLumiere, R. T., K. E. Niehoff and P. W. Kalivas "The infralimbic cortex regulates the consolidation of extinction after cocaine self-administration." Learn Mem **17**(4): 168-175.

Landgrebe, M., B. Langguth, K. Rosengarth, S. Braun, A. Koch, T. Kleinjung, A. May, D. de Ridder and G. Hajak (2009). "Structural brain changes in tinnitus: grey matter decrease in auditory and non-auditory brain areas." Neuroimage **46**(1): 213-218.

Lanens, D., A. Van der Linden, P. O. Gerrits and E. J. s-Gravenmade (1994). "In vitro NMR micro imaging of the spinal cord of chronic relapsing EAE rats." Magn Reson Imaging **12**(3): 469-475.

Laurent, V. and R. F. Westbrook (2009). "Inactivation of the infralimbic but not the prelimbic cortex impairs consolidation and retrieval of fear extinction." Learn Mem **16**(9): 520-529.

Lebron, K., M. R. Milad and G. J. Quirk (2004). "Delayed recall of fear extinction in rats with lesions of ventral medial prefrontal cortex." Learn Mem **11**(5): 544-548.

LeDoux, J. E. (1993). "Emotional memory: in search of systems and synapses." Ann N Y Acad Sci **702**: 149-157.

LeDoux, J. E. (2000). "Emotion circuits in the brain." Annu Rev Neurosci **23**: 155-184.

LeDoux, J. E. (2014). "Coming to terms with fear." Proc Natl Acad Sci U S A **111**(8): 2871-2878.

LeDoux, J. E., P. Cicchetti, A. Xagoraris and L. M. Romanski (1990). "The lateral amygdaloid nucleus: sensory interface of the amygdala in fear conditioning." J Neurosci **10**(4): 1062-1069.

LeDoux, J. E., C. Farb and D. A. Ruggiero (1990). "Topographic organization of neurons in the acoustic thalamus that project to the amygdala." J Neurosci **10**(4): 1043-1054.

LeDoux, J. E. and C. R. Farb (1991). "Neurons of the acoustic thalamus that project to the amygdala contain glutamate." Neurosci Lett **134**(1): 145-149.

LeDoux, J. E., C. R. Farb and T. A. Milner (1991). "Ultrastructure and synaptic associations of auditory thalamo-amygdala projections in the rat." Exp Brain Res **85**(3): 577-586.

LeDoux, J. E., C. R. Farb and L. M. Romanski (1991). "Overlapping projections to the amygdala and striatum from auditory processing areas of the thalamus and cortex." Neurosci Lett **134**(1): 139-144.

LeDoux, J. E., J. Iwata, P. Cicchetti and D. J. Reis (1988). "Different projections of the central amygdaloid nucleus mediate autonomic and behavioral correlates of conditioned fear." J Neurosci **8**(7): 2517-2529.

LeDoux, J. E., J. Iwata, D. Pearl and D. J. Reis (1986). "Disruption of auditory but not visual learning by destruction of intrinsic neurons in the rat medial geniculate body." Brain Res **371**(2): 395-399.

LeDoux, J. E., D. A. Ruggiero and D. J. Reis (1985). "Projections to the subcortical forebrain from anatomically defined regions of the medial geniculate body in the rat." J Comp Neurol **242**(2): 182-213.

LeDoux, J. E., A. Sakaguchi, J. Iwata and D. J. Reis (1985). "Auditory emotional memories: establishment by projections from the medial geniculate nucleus to the posterior neostriatum and/or dorsal amygdala." Ann N Y Acad Sci **444**: 463-464.

LeDoux, J. E., A. Sakaguchi, J. Iwata and D. J. Reis (1986). "Interruption of projections from the medial geniculate body to an archi-neostriatal field disrupts the classical conditioning of emotional responses to acoustic stimuli." Neuroscience **17**(3): 615-627.

LeDoux, J. E., A. Sakaguchi and D. J. Reis (1984). "Subcortical efferent projections of the medial geniculate nucleus mediate emotional responses conditioned to acoustic stimuli." J Neurosci **4**(3): 683-698.

Lee, S. P., M. F. Falangola, R. A. Nixon, K. Duff and J. A. Helpern (2004). "Visualization of beta-amyloid plaques in a transgenic mouse model of Alzheimer's disease using MR microscopy without contrast reagents." Magn Reson Med **52**(3): 538-544.

Leergaard, T. B., J. G. Bjaalie, A. Devor, L. L. Wald and A. M. Dale (2003). "In vivo tracing of major rat brain pathways using manganese-enhanced magnetic resonance imaging and three-dimensional digital atlasing." NeuroImage **20**(3): 1591-1600.

Leergaard, T. B., N. S. White, A. de Crespigny, I. Bolstad, H. D'Arceuil, J. G. Bjaalie and A. M. Dale (2010). "Quantitative histological validation of diffusion MRI fiber orientation distributions in the rat brain." PLoS One **5**(1): e8595.

Lein, E. S., M. J. Hawrylycz, N. Ao, M. Ayres, A. Bensinger, A. Bernard, A. F. Boe, M. S. Boguski, K. S. Brockway, E. J. Byrnes, L. Chen, L. Chen, T. M. Chen, M. C. Chin, J. Chong, B. E. Crook, A. Czaplinska, C. N. Dang, S. Datta, N. R. Dee, A. L. Desaki, T. Desta, E. Diep, T. A. Dolbeare, M. J. Donelan, H. W. Dong, J. G. Dougherty, B. J. Duncan, A. J. Ebbert, G. Eichele, L. K. Estin, C. Faber, B. A. Facer, R. Fields, S. R. Fischer, T. P. Fliss, C. Frensley, S. N. Gates, K. J. Glattfelder, K. R. Halverson, M. R. Hart, J. G. Hohmann, M. P. Howell, D. P. Jeung, R. A. Johnson, P. T. Karr, R. Kawal, J. M. Kidney, R. H. Knapik, C. L. Kuan, J. H. Lake, A. R. Laramee, K. D. Larsen, C. Lau, T. A. Lemon, A. J. Liang, Y. Liu, L. T. Luong, J. Michaels, J. J. Morgan, R. J. Morgan, M. T. Mortrud, N. F. Mosqueda, L. L. Ng, R. Ng, G. J. Orta, C. C. Overly, T. H. Pak, S. E. Parry, S. D. Pathak, O. C. Pearson, R. B. Puchalski, Z. L. Riley, H. R. Rockett, S. A. Rowland, J. J. Royall, M. J. Ruiz, N. R. Sarno, K. Schaffnit, N. V. Shapovalova, T. Sivisay, C. R. Slaughterbeck, S. C. Smith, K. A. Smith, B. I. Smith, A. J. Sodt, N. N. Stewart, K. R. Stumpf, S. M. Sunkin, M. Sutram, A. Tam, C. D. Teemer, C. Thaller, C. L. Thompson, L. R. Varnam, A. Visel, R. M. Whitlock, P. E. Wohnoutka, C. K. Wolkey, V. Y. Wong, M. Wood, M. B. Yaylaoglu, R. C. Young, B. L. Youngstrom, X. F. Yuan, B. Zhang, T. A. Zwingman and A. R. Jones (2007).

"Genome-wide atlas of gene expression in the adult mouse brain." Nature **445**(7124): 168-176.

Lemos, J. I., L. B. Resstel and F. S. Guimaraes (2010). "Involvement of the prelimbic prefrontal cortex on cannabidiol-induced attenuation of contextual conditioned fear in rats." Behav Brain Res **207**(1): 105-111.

Lerch, J. P., J. G. Sled and R. M. Henkelman (2011). "MRI phenotyping of genetically altered mice." Methods Mol Biol **711**: 349-361.

Letzkus, J. J., S. B. Wolff, E. M. Meyer, P. Tovote, J. Courtin, C. Herry and A. Luthi (2011). "A disinhibitory microcircuit for associative fear learning in the auditory cortex." Nature **480**(7377): 331-335.

Li, L., T. M. Preuss, J. K. Rilling, W. D. Hopkins, M. F. Glasser, B. Kumar, R. Nana, X. Zhang and X. Hu (2010). "Chimpanzee (Pan troglodytes) precentral corticospinal system asymmetry and handedness: a diffusion magnetic resonance imaging study." PLoS One **5**(9): e12886.

Li, X. F., G. E. Stutzmann and J. E. LeDoux (1996). "Convergent but temporally separated inputs to lateral amygdala neurons from the auditory thalamus and auditory cortex use different postsynaptic receptors: in vivo intracellular and extracellular recordings in fear conditioning pathways." Learn Mem **3**(2-3): 229-242.

Lieberman, P., J. Friedman and L. S. Feldman (1990). "Syntax comprehension deficits in Parkinson's disease." J Nerv Ment Dis **178**(6): 360-365.

Lin, C.-P., W.-Y. I. Tseng, H.-C. Cheng and J.-H. Chen (2001). "Validation of Diffusion Tensor Magnetic Resonance Axonal Fiber Imaging with Registered Manganese-Enhanced Optic Tracts." NeuroImage **14**(5): 1035-1047.

Lin, C. P., V. J. Wedeen, J. H. Chen, C. Yao and W. Y. Tseng (2003). "Validation of diffusion spectrum magnetic resonance imaging with manganese-enhanced rat optic tracts and ex vivo phantoms." Neuroimage **19**(3): 482-495.

Lin, Y. K., A.P. (1997). "Manganese ion enhances T1-weighted MRI during brain activation: an approach to direct imaging of brain function." Magn Reson Med **38**(3): 378-388.

Linke, R. and H. Schwegler (2000). "Convergent and complementary projections of the caudal paralaminar thalamic nuclei to rat temporal and insular cortex." Cereb Cortex **10**(8): 753-771.

Llano, D. A. and S. M. Sherman (2008). "Evidence for nonreciprocal organization of the mouse auditory thalamocortical-corticothalamic projection systems." J Comp Neurol **507**(2): 1209-1227.

Logothetis, N. K., J. Pauls, M. Augath, T. Trinath and A. Oeltermann (2001). "Neurophysiological investigation of the basis of the fMRI signal." Nature **412**(6843): 150-157.

Love, J. A. and J. W. Scott (1969). "Some response characteristics of cells of the magnocellular division of the medial geniculate body of the cat." Can J Physiol Pharmacol **47**(10): 881-888.

Luskin, M. B. and J. L. Price (1983). "The laminar distribution of intracortical fibers originating in the olfactory cortex of the rat." J Comp Neurol **216**(3): 292-302.

Ma, W. Y. and L. L. Vacca-Galloway (1991). "Reduced branching and length of dendrites detected in cervical spinal cord motoneurons of Wobbler mouse, a model for inherited motoneuron disease." J Comp Neurol **311**(2): 210-222.

Macchi, G. and R. P. Cioffi (1992). "An in vivo and post mortem MRI study in multiple sclerosis with pathological correlation." Ital J Neurol Sci **13**(9 Suppl 14): 97-103.

Maddux, J. M. and P. C. Holland (2011). "Effects of dorsal or ventral medial prefrontal cortical lesions on five-choice serial reaction time performance in rats." Behav Brain Res **221**(1): 63-74.

Magnitsky, S., D. J. Watson, R. M. Walton, S. Pickup, J. W. Bulte, J. H. Wolfe and H. Poptani (2005). "In vivo and ex vivo MRI detection of localized and disseminated neural stem cell grafts in the mouse brain." Neuroimage **26**(3): 744-754.

Mai, J. K., G. Paxinos and T. Voss. (2008). "Atlas of the human brain." 3rd. from http://firstsearch.oclc.org/WebZ/DCARead?standardNoType=1&standardNo=9780123736031:srcdbname=worldcat:fromExternal=true&sessionid=0 cover art.

Manger, P. R., J. Cort, N. Ebrahim, A. Goodman, J. Henning, M. Karolia, S. L. Rodrigues and G. Strkalj (2008). "Is 21st century neuroscience too focussed on the rat/mouse model of brain function and dysfunction?" Front Neuroanat **2**: 5.

Marburg, O. (1948). "The amygdaloid complex. ." Confinia Neurologica **9**: 211-216.

Maren, S. (2001). "Neurobiology of Pavlovian fear conditioning." Annu Rev Neurosci **24**: 897-931.

Maren, S. (2008). "Pavlovian fear conditioning as a behavioral assay for hippocampus and amygdala function: cautions and caveats." Eur J Neurosci **28**(8): 1661-1666.

Markham, C. M., S. L. Taylor and K. L. Huhman (2010). "Role of amygdala and hippocampus in the neural circuit subserving conditioned defeat in Syrian hamsters." Learn Mem **17**(2): 109-116.

Marte Thuen, T. E. S., Tina Bugge Pedersen, Olav Haraldseth, Martin Berry, Axel Sandvig, Christian Brekken, (2005). "Manganese-enhanced MRI of the optic visual pathway and optic nerve injury in adult rats." Journal of Magnetic Resonance Imaging **22**(4): 492-500.

Maurer, J., T. Mitrovics, I. Schlecht, F. Knollmann and R. Felix (1998). "An experimental high-resolution MR coil for the imaging of pathological findings in the post mortem brain stem." Acta Radiol **39**(5): 487-489.

McCann, K. E. and K. L. Huhman (2012). "The effect of escapable versus inescapable social defeat on conditioned defeat and social recognition in Syrian hamsters." Physiol Behav **105**(2): 493-497.

McDonald, A. J., F. Mascagni and L. Guo (1996). "Projections of the medial and lateral prefrontal cortices to the amygdala: a Phaseolus vulgaris leucoagglutinin study in the rat." Neuroscience **71**(1): 55-75.

McGeorge, A. J. and R. L. Faull (1989). "The organization of the projection from the cerebral cortex to the striatum in the rat." Neuroscience **29**(3): 503-537.

McLaughlin, J., H. Skaggs, J. Churchwell and D. A. Powell (2002). "Medial prefrontal cortex and pavlovian conditioning: trace versus delay conditioning." Behav Neurosci **116**(1): 37-47.

Medina, J. F., J. C. Repa, M. D. Mauk and J. E. LeDoux (2002). "Parallels between cerebellum- and amygdala-dependent conditioning." Nat Rev Neurosci **3**(2): 122-131.

Mesulam, M. M. and D. N. Pandya (1973). "The projections of the medial geniculate complex within the sylvian fissure of the rhesus monkey." Brain Res **60**(2): 315-333.

Milad, M. R. and G. J. Quirk (2002). "Neurons in medial prefrontal cortex signal memory for fear extinction." Nature **420**(6911): 70-74.

Milad, M. R., I. Vidal-Gonzalez and G. J. Quirk (2004). "Electrical stimulation of medial prefrontal cortex reduces conditioned fear in a temporally specific manner." Behav Neurosci **118**(2): 389-394.

Miller, K. L., J. A. McNab, S. Jbabdi and G. Douaud (2012). "Diffusion tractography of post-mortem human brains: optimization and comparison of spin echo and steady-state free precession techniques." Neuroimage **59**(3): 2284-2297.

Miyamichi, K., F. Amat, F. Moussavi, C. Wang, I. Wickersham, N. R. Wall, H. Taniguchi, B. Tasic, Z. J. Huang, Z. He, E. M. Callaway, M. A. Horowitz and L. Luo (2011). "Cortical representations of olfactory input by trans-synaptic tracing." Nature **472**(7342): 191-196.

Miyashita, Y. (1988). "Neuronal correlate of visual associative long-term memory in the primate temporal cortex." Nature **335**(6193): 817-820.

Moczulska, K. E., J. Tinter-Thiede, M. Peter, L. Ushakova, T. Wernle, B. Bathellier and S. Rumpel (2013). "Dynamics of dendritic spines in the mouse auditory cortex during memory formation and memory recall." Proc Natl Acad Sci U S A **110**(45): 18315-18320.

Moldrich, R. X., K. Pannek, R. Hoch, J. L. Rubenstein, N. D. Kurniawan and L. J. Richards (2010). "Comparative mouse brain tractography of diffusion magnetic resonance imaging." Neuroimage **51**(3): 1027-1036.

Mombaerts, P., F. Wang, C. Dulac, S. K. Chao, A. Nemes, M. Mendelsohn, J. Edmondson and R. Axel (1996). "Visualizing an olfactory sensory map." Cell **87**(4): 675-686.

Monakow, C. v. (1914). "Die Lokalisation im Grosshirn und der Abbau der Funktion durch kortikale Herde." Wiesbaden.: S. 800.

Morgan, M. A. and J. E. LeDoux (1995). "Differential contribution of dorsal and ventral medial prefrontal cortex to the acquisition and extinction of conditioned fear in rats." Behav Neurosci **109**(4): 681-688.

Morgan, M. A., J. Schulkin and J. E. LeDoux (2003). "Ventral medial prefrontal cortex and emotional perseveration: the memory for prior extinction training." Behav Brain Res **146**(1-2): 121-130.

Mori, S., R. Itoh, J. Zhang, W. E. Kaufmann, P. C. van Zijl, M. Solaiyappan and P. Yarowsky (2001). "Diffusion tensor imaging of the developing mouse brain." Magn Reson Med **46**(1): 18-23.

Moriizumi, T. and T. Hattori (1992). "Ultrastructural morphology of projections from the medial geniculate nucleus and its adjacent region to the basal ganglia." Brain Res Bull **29**(2): 193-198.

Muhlau, M., J. P. Rauschecker, E. Oestreicher, C. Gaser, M. Rottinger, A. M. Wohlschlager, F. Simon, T. Etgen, B. Conrad and D. Sander (2006). "Structural brain changes in tinnitus." Cereb Cortex **16**(9): 1283-1288.

Muller, H. P., J. Kassubek, I. Vernikouskaya, A. C. Ludolph, D. Stiller and V. Rasche (2013). "Diffusion tensor magnetic resonance imaging of the brain in APP transgenic mice: a cohort study." PLoS One **8**(6): e67630.

Muller, H. P., I. Vernikouskaya, A. C. Ludolph, J. Kassubek and V. Rasche (2012). "Fast diffusion tensor magnetic resonance imaging of the mouse brain at ultrahigh-field: aiming at cohort studies." PLoS One **7**(12): e53389.

Narkiewicz, O., M. J. de Leon, A. Convit, A. E. George, J. Wegiel, J. Morys, M. Bobinski, J. Golomb, D. C. Miller and H. M. Wisniewski (1993). "Dilatation of the lateral part of the transverse fissure of the brain in Alzheimer's disease." Acta Neurobiol Exp (Wars) **53**(3): 457-465.

Nauta, W. J. and D. G. Whitlock (1956). "Subcortical projections from the temporal neocortex in Macaca mulatta." J Comp Neurol **106**(1): 183-212.

Nemeth, C. L., D. A. Gutman, W. Majeed, S. D. Keilholz and G. N. Neigh (2014). "Microembolism induces anhedonia but no detectable changes in white matter integrity in aged rats." PLoS One **9**(5): e96624.

Ngai, J., A. Chess, M. M. Dowling, N. Necles, E. R. Macagno and R. Axel (1993). "Coding of olfactory information: topography of odorant receptor expression in the catfish olfactory epithelium." Cell **72**(5): 667-680.

Nieuwenhuis, I. L. and A. Takashima (2011). "The role of the ventromedial prefrontal cortex in memory consolidation." Behav Brain Res **218**(2): 325-334.

Niimi, M. (1978). "Cortical projections of the anterior thalamic nuclei in the cat." Exp Brain Res **31**(3): 403-416.

Nijeholt, G. J., E. Bergers, W. Kamphorst, J. Bot, K. Nicolay, J. A. Castelijns, J. H. van Waesberghe, R. Ravid, C. H. Polman and F. Barkhof (2001). "Post-mortem high-resolution MRI of the spinal cord in multiple sclerosis: a correlative study with conventional MRI, histopathology and clinical phenotype." Brain **124**(Pt 1): 154-166.

Nishi, R. A., H. Liu, Y. Chu, M. Hamamura, M. Y. Su, O. Nalcioglu and A. J. Anderson (2007). "Behavioral, histological, and ex vivo magnetic resonance imaging assessment of graded contusion spinal cord injury in mice." J Neurotrauma **24**(4): 674-689.

Osechinskiy, S. and F. Kruggel (2009). "Quantitative comparison of high-resolution MRI and myelin-stained histology of the human cerebral cortex." Conf Proc IEEE Eng Med Biol Soc **2009**: 85-89.

Ottersen, O. P. (1982). "Connections of the amygdala of the rat. IV: Corticoamygdaloid and intraamygdaloid connections as studied with axonal transport of horseradish peroxidase." J Comp Neurol **205**(1): 30-48.

Ottersen, O. P. and Y. Ben-Ari (1979). "Afferent connections to the amygdaloid complex of the rat and cat. I. Projections from the thalamus." J Comp Neurol **187**(2): 401-424.

Otto, T., G. Cousens and C. Herzog (2000). "Behavioral and neuropsychological foundations of olfactory fear conditioning." Behav Brain Res **110**(1-2): 119-128.

Otto, T., F. Schottler, U. Staubli, H. Eichenbaum and G. Lynch (1991). "Hippocampus and olfactory discrimination learning: effects of entorhinal cortex lesions on olfactory learning and memory in a successive-cue, go-no-go task." Behav Neurosci **105**(1): 111-119.

Øystein, O., T. Marte, B. Martin, K. Vassili, P. Maria, G. Pål Erik, S. Axel, H. Olav and B. Christian (2008). Axon tracing in the adult rat optic nerve and tract after intravitreal injection of MnDPDP using a semiautomatic segmentation technique. **27:** 34-42.

Papez, J. W. (1945). "Fiber tracts of the amygdaloid region in the human brain, from a graphic reconstruction of fiber connections and nuclear masses." The Anatomical Record **91**: 294.

Papp, E. A., T. B. Leergaard, E. Calabrese, G. A. Johnson and J. G. Bjaalie (2014). "Waxholm Space atlas of the Sprague Dawley rat brain." Neuroimage **97**: 374-386.

Pautler, R. G. (2004). "In vivo, trans-synaptic tract-tracing utilizing manganese-enhanced magnetic resonance imaging (MEMRI)." NMR Biomed **17**(8): 595-601.

Pautler, R. G., A. C. Silva and A. P. Koretsky (1998). "In vivo neuronal tract tracing using manganese-enhanced magnetic resonance imaging." Magn Reson Med **40**(5): 740-748.

Pavlov, I. P. (1927). Conditioned Reflexes: An Investigation of the Physiological Activity of the Cerebral Cortex. Translated and Edited by G. V. Anrep. . London, Oxford University Press.

Pavlov, I. P. (2003). Conditioned Reflexes Courier Dover Publications.

Paxinos, G. and G. Franklin (2004). The Mouse Brain in Stereotaxic Coordinates, Elsevier.

Peter, M., H. Scheuch, T. R. Burkard, J. Tinter, T. Wernle and S. Rumpel (2012). "Induction of immediate early genes in the mouse auditory cortex after auditory cued fear conditioning to complex sounds." Genes Brain Behav **11**(3): 314-324.

Peters, A. and I. R. Kaiserman-Abramof (1970). "The small pyramidal neuron of the rat cerebral cortex. The perikaryon, dendrites and spines." Am J Anat **127**(4): 321-355.

Peters, J., R. T. LaLumiere and P. W. Kalivas (2008). "Infralimbic prefrontal cortex is responsible for inhibiting cocaine seeking in extinguished rats." J Neurosci **28**(23): 6046-6053.

Pickens, C. L., S. A. Golden, T. Adams-Deutsch, S. G. Nair and Y. Shaham (2009). "Long-lasting incubation of conditioned fear in rats." Biol Psychiatry **65**(10): 881-886.

Pignataro, A., S. Middei, A. Borreca and M. Ammassari-Teule (2013). "Indistinguishable pattern of amygdala and hippocampus rewiring following tone or contextual fear conditioning in C57BL/6 mice." Front Behav Neurosci **7**: 156.

Pinard, C. R., F. Mascagni and A. J. McDonald (2012). "Medial prefrontal cortical innervation of the intercalated nuclear region of the amygdala." Neuroscience **205**: 112-124.

Poliak, S. (1926). "Untersuchungen am Octavus-system der Saugetiere und an den mit diesen koordinierten motorischen Apparaten des Hirnstamms." Journal für Psychologie und Neurologie **32**: S.170.

Powell, D. A., H. Skaggs, J. Churchwell and J. McLaughlin (2001). "Posttraining lesions of the medial prefrontal cortex impair performance of Pavlovian eyeblink conditioning but have no effect on concomitant heart rate changes in rabbits (Oryctolagus cuniculus)." Behav Neurosci **115**(5): 1029-1038.

Preuss, T. M. (2000). "Taking the measure of diversity: comparative alternatives to the model-animal paradigm in cortical neuroscience." Brain Behav Evol **55**(6): 287-299.

Prinster, A., M. Quarantelli, G. Orefice, R. Lanzillo, A. Brunetti, C. Mollica, E. Salvatore, V. B. Morra, G. Coppola, G. Vacca, B. Alfano and M. Salvatore (2006). "Grey matter loss in relapsing-remitting multiple sclerosis: a voxel-based morphometry study." Neuroimage **29**(3): 859-867.

Quirk, G. J., J. L. Armony and J. E. LeDoux (1997). "Fear conditioning enhances different temporal components of tone-evoked spike trains in auditory cortex and lateral amygdala." Neuron **19**(3): 613-624.

Quirk, G. J. and D. Mueller (2008). "Neural mechanisms of extinction learning and retrieval." Neuropsychopharmacology **33**(1): 56-72.

Quirk, G. J., C. Repa and J. E. LeDoux (1995). "Fear conditioning enhances short-latency auditory responses of lateral amygdala neurons: parallel recordings in the freely behaving rat." Neuron **15**(5): 1029-1039.

Quirk, G. J., G. K. Russo, J. L. Barron and K. Lebron (2000). "The role of ventromedial prefrontal cortex in the recovery of extinguished fear." J Neurosci **20**(16): 6225-6231.

Raffaele, R., S. Sapienza and A. Urbano (1969). "[Fastigial nucleus projections in the pars magnocellularis of the medial geniculate body of the cat]." Boll Soc Ital Biol Sper **45**(20): 1296-1298.

Raju, D. V. and Y. Smith (2006). "Anterograde axonal tract tracing." Curr Protoc Neurosci **Chapter 1**: Unit 1 14.

Rasmusson, A. M. and D. S. Charney (1997). "Animal models of relevance to PTSD." Ann N Y Acad Sci **821**: 332-351.

Redies, H., S. Brandner and O. D. Creutzfeldt (1989). "Anatomy of the auditory thalamocortical system of the guinea pig." J Comp Neurol **282**(4): 489-511.

Ressler, K. J., G. Paschall, X. L. Zhou and M. Davis (2002). "Regulation of synaptic plasticity genes during consolidation of fear conditioning." J Neurosci **22**(18): 7892-7902.

Ressler, K. J., S. L. Sullivan and L. B. Buck (1993). "A zonal organization of odorant receptor gene expression in the olfactory epithelium." Cell **73**(3): 597-609.

Ressler, K. J., S. L. Sullivan and L. B. Buck (1994). "Information coding in the olfactory system: evidence for a stereotyped and highly organized epitope map in the olfactory bulb." Cell **79**(7): 1245-1255.

Restivo, L., G. Vetere, B. Bontempi and M. Ammassari-Teule (2009). "The formation of recent and remote memory is associated with time-dependent formation of dendritic spines in the hippocampus and anterior cingulate cortex." J Neurosci **29**(25): 8206-8214.

Rilling, J. K., M. F. Glasser, T. M. Preuss, X. Ma, T. Zhao, X. Hu and T. E. Behrens (2008). "The evolution of the arcuate fasciculus revealed with comparative DTI." Nat Neurosci **11**(4): 426-428.

Roberts, G. W. and C. J. Bruton (1990). "Notes from the graveyard: neuropathology and schizophrenia." Neuropathol Appl Neurobiol **16**(1): 3-16.

Robia G. Pautler, R. M., Russell E. Jacobs, (2003). "In vivo trans-synaptic tract tracing from the murine striatum and amygdala utilizing manganese enhanced MRI (MEMRI)." Magnetic Resonance in Medicine **50**(1): 33-39.

Rodrigues, S. M., J. E. LeDoux and R. M. Sapolsky (2009). "The influence of stress hormones on fear circuitry." Annu Rev Neurosci **32**: 289-313.

Rodriguez-Romaguera, J., F. Sotres-Bayon, D. Mueller and G. J. Quirk (2009). "Systemic propranolol acts centrally to reduce conditioned fear in rats without impairing extinction." Biol Psychiatry **65**(10): 887-892.

Roger, M. and P. Arnault (1989). "Anatomical study of the connections of the primary auditory area in the rat." J Comp Neurol **287**(3): 339-356.

Romanski, L. M., M. C. Clugnet, F. Bordi and J. E. LeDoux (1993). "Somatosensory and auditory convergence in the lateral nucleus of the amygdala." Behav Neurosci **107**(3): 444-450.

Romanski, L. M. and J. E. LeDoux (1992). "Bilateral destruction of neocortical and perirhinal projection targets of the acoustic thalamus does not disrupt auditory fear conditioning." Neurosci Lett **142**(2): 228-232.

Romanski, L. M. and J. E. LeDoux (1992). "Equipotentiality of thalamo-amygdala and thalamo-cortico-amygdala circuits in auditory fear conditioning." J Neurosci **12**(11): 4501-4509.

Romanski, L. M. and J. E. LeDoux (1993). "Information cascade from primary auditory cortex to the amygdala: corticocortical and corticoamygdaloid projections of temporal cortex in the rat." Cereb Cortex **3**(6): 515-532.

Room, P., F. T. Russchen, H. J. Groenewegen and A. H. Lohman (1985). "Efferent connections of the prelimbic (area 32) and the infralimbic (area 25) cortices: an anterograde tracing study in the cat." J Comp Neurol **242**(1): 40-55.

Roozendaal, B., J. M. Koolhaas and B. Bohus (1991). "Central amygdala lesions affect behavioral and autonomic balance during stress in rats." Physiol Behav **50**(4): 777-781.

Rose, J. E. and C. N. Woolsey (1948). "Structure and relations of limbic cortex and anterior thalamic nuclei in rabbit and cat." J Comp Neurol **89**(3): 279-347.

Rose, J. E. and C. N. Woolsey (1949). "The relations of thalamic connections, cellular structure and evocable electrical activity in the auditory region of the cat." J Comp Neurol **91**(3): 441-466.

Russchen, F. T. (1982). "Amygdalopetal projections in the cat. I. Cortical afferent connections. A study with retrograde and anterograde tracing techniques." J Comp Neurol **206**(2): 159-179.

Russchen, F. T. (1982). "Amygdalopetal projections in the cat. II. Subcortical afferent connections. A study with retrograde tracing techniques." J Comp Neurol **207**(2): 157-176.

Ryugo, D. K. and H. P. Killackey (1974). "Differential telencephalic projections of the medial and ventral divisions of the medial geniculate body of the rat." Brain Res **82**(1): 173-177.

Saleem, K. S., J. M. Pauls, M. Augath, T. Trinath, B. A. Prause, T. Hashikawa and N. K. Logothetis (2002). "Magnetic resonance imaging of neuronal connections in the macaque monkey." Neuron **34**(5): 685-700.

Santini, E., H. Ge, K. Ren, S. Pena de Ortiz and G. J. Quirk (2004). "Consolidation of fear extinction requires protein synthesis in the medial prefrontal cortex." J Neurosci **24**(25): 5704-5710.

Santini, E., R. U. Muller and G. J. Quirk (2001). "Consolidation of extinction learning involves transfer from NMDA-independent to NMDA-dependent memory." J Neurosci **21**(22): 9009-9017.

Sawiak, S. J., N. I. Wood, G. B. Williams, A. J. Morton and T. A. Carpenter (2009). "Voxel-based morphometry in the R6/2 transgenic mouse reveals differences between genotypes not seen with manual 2D morphometry." Neurobiol Dis **33**(1): 20-27.

Sawiak, S. J., N. I. Wood, G. B. Williams, A. J. Morton and T. A. Carpenter (2013). "Voxel-based morphometry with templates and validation in a mouse model of Huntington's disease." Magn Reson Imaging **31**(9): 1522-1531.

Scalia, F. and S. S. Winans (1975). "The differential projections of the olfactory bulb and accessory olfactory bulb in mammals." J Comp Neurol **161**(1): 31-55.

Schneider, J. E. and S. Bhattacharya (2004). "Making the mouse embryo transparent: identifying developmental malformations using magnetic resonance imaging." Birth Defects Res C Embryo Today **72**(3): 241-249.

Schuz, A. and G. Palm (1989). "Density of neurons and synapses in the cerebral cortex of the mouse." J Comp Neurol **286**(4): 442-455.

Schweitzer, J. B., D. O. Lee, R. B. Hanford, C. F. Zink, T. D. Ely, M. A. Tagamets, J. M. Hoffman, S. T. Grafton and C. D. Kilts (2004). "Effect of methylphenidate on executive functioning in adults with attention-deficit/hyperactivity disorder: normalization of behavior but not related brain activity." Biol Psychiatry **56**(8): 597-606.

Shammah-Lagnado, S. J., G. F. Alheid and L. Heimer (1996). "Efferent connections of the caudal part of the globus pallidus in the rat." J Comp Neurol **376**(3): 489-507.

Shinonaga, Y., M. Takada and N. Mizuno (1994). "Direct projections from the non-laminated divisions of the medial geniculate nucleus to the temporal polar cortex and amygdala in the cat." J Comp Neurol **340**(3): 405-426.

Shipley, M. T. and G. D. Adamek (1984). "The connections of the mouse olfactory bulb: a study using orthograde and retrograde transport of wheat germ agglutinin conjugated to horseradish peroxidase." Brain Res Bull **12**(6): 669-688.

Smith, B. R., G. A. Johnson, E. V. Groman and E. Linney (1994). "Magnetic resonance microscopy of mouse embryos." Proc Natl Acad Sci U S A **91**(9): 3530-3533.

Smith, M. J., L. Wang, W. Cronenwett, D. Mamah, D. M. Barch and J. G. Csernansky (2011). "Thalamic morphology in schizophrenia and schizoaffective disorder." J Psychiatr Res **45**(3): 378-385.

Smith, S. M. (2002). "Fast robust automated brain extraction." Hum Brain Mapp **17**(3): 143-155.

Smith, S. M., M. Jenkinson, M. W. Woolrich, C. F. Beckmann, T. E. Behrens, H. Johansen-Berg, P. R. Bannister, M. De Luca, I. Drobnjak, D. E. Flitney, R. K. Niazy, J. Saunders, J. Vickers, Y. Zhang, N. De Stefano, J. M. Brady and P. M. Matthews (2004). "Advances in functional and structural MR image analysis and implementation as FSL." Neuroimage **23 Suppl 1**: S208-219.

Smulders, T. V. (2009). "The relevance of brain evolution for the biomedical sciences." Biol Lett **5**(1): 138-140.

Sosulski, D. L., M. L. Bloom, T. Cutforth, R. Axel and S. R. Datta (2011). "Distinct representations of olfactory information in different cortical centres." Nature **472**(7342): 213-216.

Sotres-Bayon, F., C. K. Cain and J. E. LeDoux (2006). "Brain mechanisms of fear extinction: historical perspectives on the contribution of prefrontal cortex." Biol Psychiatry **60**(4): 329-336.

Sotres-Bayon, F. and G. J. Quirk (2010). "Prefrontal control of fear: more than just extinction." Curr Opin Neurobiol **20**(2): 231-235.

Su, Y. Y., B. Luo, Y. Jin, S. H. Wu, E. Lobarinas, R. J. Salvi and L. Chen (2012). "Altered neuronal intrinsic properties and reduced synaptic transmission of the rat's medial geniculate body in salicylate-induced tinnitus." PLoS One **7**(10): e46969.

Takagishi, M. and T. Chiba (1991). "Efferent projections of the infralimbic (area 25) region of the medial prefrontal cortex in the rat: an anterograde tracer PHA-L study." Brain Res **566**(1-2): 26-39.

Takashi Watanabe, J. F., Thomas Michaelis, (2004). "Functional mapping of neural pathways in rodent brain <I>in vivo</I> using manganese-enhanced three-dimensional magnetic resonance imaging." NMR in Biomedicine **17**(8): 554-568.

Taki, Y., R. Goto, A. Evans, A. Zijdenbos, P. Neelin, J. Lerch, K. Sato, S. Ono, S. Kinomura, M. Nakagawa, M. Sugiura, J. Watanabe, R. Kawashima and H. Fukuda (2004). "Voxel-based morphometry of human brain with age and cerebrovascular risk factors." Neurobiol Aging **25**(4): 455-463.

Thiebaut de Schotten, M., F. Dell'Acqua, R. Valabregue and M. Catani (2012). "Monkey to human comparative anatomy of the frontal lobe association tracts." Cortex **48**(1): 82-96.

Thuen, M., T. E. Singstad, T. B. Pedersen, O. Haraldseth, M. Berry, A. Sandvig and C. Brekken (2005). "Manganese-enhanced MRI of the optic visual pathway and optic nerve injury in adult rats." J Magn Reson Imaging **22**(4): 492-500.

Tsvetkov, E., W. A. Carlezon, F. M. Benes, E. R. Kandel and V. Y. Bolshakov (2002). "Fear conditioning occludes LTP-induced presynaptic enhancement of synaptic transmission in the cortical pathway to the lateral amygdala." Neuron **34**(2): 289-300.

Tunturi, A. R. (1946). "A study on the pathway from the medial geniculate body to the acoustic cortex in the dog." Am J Physiol **147**: 311-319.

Turner, B. H., M. Mishkin and M. Knapp (1980). "Organization of the amygdalopetal projections from modality-specific cortical association areas in the monkey." J Comp Neurol **191**(4): 515-543.

Uchida, R. R., C. M. Del-Ben, G. F. Busatto, F. L. Duran, F. S. Guimaraes, J. A. Crippa, D. Araujo, A. C. Santos and F. G. Graeff (2008). "Regional gray matter abnormalities in panic disorder: a voxel-based morphometry study." Psychiatry Res **163**(1): 21-29.

Ugolini, G. (2010). "Advances in viral transneuronal tracing." J Neurosci Methods **194**(1): 2-20.

Ulrich-Lai, Y. M., K. R. Jones, D. R. Ziegler, W. E. Cullinan and J. P. Herman (2011). "Forebrain origins of glutamatergic innervation to the rat paraventricular nucleus of the hypothalamus: differential inputs to the anterior versus posterior subregions." J Comp Neurol **519**(7): 1301-1319.

Valfre, W., I. Rainero, M. Bergui and L. Pinessi (2008). "Voxel-based morphometry reveals gray matter abnormalities in migraine." Headache **48**(1): 109-117.

Van der Linden, A., M. Verhoye, V. Van Meir, I. Tindemans, M. Eens, P. Absil and J. Balthazart (2002). "In vivo manganese-enhanced magnetic resonance imaging reveals connections and functional properties of the songbird vocal control system." Neuroscience **112**(2): 467-474.

Vassar, R., S. K. Chao, R. Sitcheran, J. M. Nunez, L. B. Vosshall and R. Axel (1994). "Topographic organization of sensory projections to the olfactory bulb." Cell **79**(6): 981-991.

Veening, J. G. (1978). "Subcortical afferents of the amygdaloid complex in the rat: an HRP study." Neurosci Lett **8**(3): 197-202.

Venot, A., J. F. Lebruchec, J. L. Golmard and J. C. Roucayrol (1983). "An automated method for the normalization of scintigraphic images." J Nucl Med **24**(6): 529-531.

Vertes, R. P. (2004). "Differential projections of the infralimbic and prelimbic cortex in the rat." Synapse **51**(1): 32-58.

Vetere, G., L. Restivo, G. Novembre, M. Aceti, M. Lumaca and M. Ammassari-Teule (2011). "Extinction partially reverts structural changes associated with remote fear memory." Learn Mem **18**(9): 554-557.

Vidal-Gonzalez, I., B. Vidal-Gonzalez, S. L. Rauch and G. J. Quirk (2006). "Microstimulation reveals opposing influences of prelimbic and infralimbic cortex on the expression of conditioned fear." Learn Mem **13**(6): 728-733.

Walker, A. E. (1937). "The Projection of the Medial Geniculate Body to the Cerebral Cortex in the Macaque Monkey." J Anat **71**(Pt 3): 319-331.

Wang, J., M. Palkovits, T. B. Usdin and A. Dobolyi (2006). "Afferent connections of the subparafascicular area in rat." Neuroscience **138**(1): 197-220.

Wang, R., T. Benner, A. G. Sorensen and V. J. Wedeen (2007). Diffusion Tookit: A Software Package for Diffusion Imaging Data Processing and Tractography. ISMRM.

Watanabe, T., T. Michaelis and J. Frahm (2001). "Mapping of retinal projections in the living rat using high-resolution 3D gradient-echo MRI with Mn2+-induced contrast." Magn Reson Med **46**(3): 424-429.

Wedeen, V. J., R. P. Wang, J. D. Schmahmann, T. Benner, W. Y. Tseng, G. Dai, D. N. Pandya, P. Hagmann, H. D'Arceuil and A. J. de Crespigny (2008). "Diffusion spectrum magnetic resonance imaging (DSI) tractography of crossing fibers." Neuroimage **41**(4): 1267-1277.

Weinberger, N. M. (2004). "Specific long-term memory traces in primary auditory cortex." Nat Rev Neurosci **5**(4): 279-290.

Weinberger, N. M. (2011). "The medial geniculate, not the amygdala, as the root of auditory fear conditioning." Hear Res **274**(1-2): 61-74.

Weiskrantz, L. (1956). "Behavioral changes associated with ablation of the amygdaloid complex in monkeys." J Comp Physiol Psychol **49**(4): 381-391.

Welzl, H., P. D'Adamo and H. P. Lipp (2001). "Conditioned taste aversion as a learning and memory paradigm." Behav Brain Res **125**(1-2): 205-213.

Wepsic, J. G. (1966). "Multimodal sensory activation of cells in the magnocellular medial geniculate nucleus." Exp Neurol **15**(3): 299-318.

Werner, M., A. Chott, A. Fabiano and H. Battifora (2000). "Effect of formalin tissue fixation and processing on immunohistochemistry." Am J Surg Pathol **24**(7): 1016-1019.

Williams, R. W. and P. Rakic (1988). "Three-dimensional counting: an accurate and direct method to estimate numbers of cells in sectioned material." J Comp Neurol **278**(3): 344-352.

Winer, J. A., J. J. Diehl and D. T. Larue (2001). "Projections of auditory cortex to the medial geniculate body of the cat." J Comp Neurol **430**(1): 27-55.

Winer, J. A. and D. K. Morest (1983). "The medial division of the medial geniculate body of the cat: implications for thalamic organization." J Neurosci **3**(12): 2629-2651.

Xia, S., X. Li, A. E. Kimball, M. S. Kelly, I. Lesser and C. Branch (2012). "Thalamic shape and connectivity abnormalities in children with attention-deficit/hyperactivity disorder." Psychiatry Res **204**(2-3): 161-167.

Yamasue, H., K. Kasai, A. Iwanami, T. Ohtani, H. Yamada, O. Abe, N. Kuroki, R. Fukuda, M. Tochigi, S. Furukawa, M. Sadamatsu, T. Sasaki, S. Aoki, K. Ohtomo, N. Asukai and N. Kato (2003). "Voxel-based analysis of MRI reveals anterior cingulate gray-matter volume reduction in posttraumatic stress disorder due to terrorism." Proc Natl Acad Sci U S A **100**(15): 9039-9043.

Yan, Y., L. Li, T. M. Preuss, X. Hu, J. G. Herndon and X. Zhang (2014). "In vivo evaluation of optic nerve aging in adult rhesus monkey by diffusion tensor imaging." Quant Imaging Med Surg **4**(1): 43-49.

Yopak, K. E. and L. R. Frank (2009). "Brain size and brain organization of the whale shark, Rhincodon typus, using magnetic resonance imaging." Brain Behav Evol **74**(2): 121-142.

Yukie, M. (2002). "Connections between the amygdala and auditory cortical areas in the macaque monkey." Neurosci Res **42**(3): 219-229.

Yuste, R. and T. Bonhoeffer (2001). "Morphological changes in dendritic spines associated with long-term synaptic plasticity." Annu Rev Neurosci **24**: 1071-1089.

Zhang, D., L. Guo, D. Zhu, K. Li, L. Li, H. Chen, Q. Zhao, X. Hu and T. Liu (2012). "Diffusion tensor imaging reveals evolution of primate brain architectures." Brain Struct Funct.

Zhang, J., L. J. Richards, P. Yarowsky, H. Huang, P. C. van Zijl and S. Mori (2003). "Three-dimensional anatomical characterization of the developing mouse brain by diffusion tensor microimaging." Neuroimage **20**(3): 1639-1648.

Zhang, J., P. C. van Zijl and S. Mori (2002). "Three-dimensional diffusion tensor magnetic resonance microimaging of adult mouse brain and hippocampus." Neuroimage **15**(4): 892-901.

Zimny, R., T. Sobusiak, A. Kotecki and A. Deja (1981). "The medial geniculate body afferents from the cerebellum in the rabbit as studied with the method of orthograde degeneration." J Hirnforsch **22**(5): 573-585.